Volume 72A
Number 2
Mar.–Apr. 1968

Physics and Chemistry

U.S. DEPARTMENT OF COMMERCE

SECTION A

JOURNAL OF RESEARCH

NATIONAL BUREAU OF STANDARDS

Journal of Research

of the

National Bureau of Standards

A. Physics and Chemistry

Mar.–Apr. • 1968

VOLUME • 72A

NUMBER • 2

Editor: C. W. Beckett

Associate Editors: D. D. Wagman
J. M. Richardson

Publication dates:
Feb. 1, Apr. 1, June 1, Aug. 1, Oct. 1, Dec. 1, 1968

JOURNAL OF RESEARCH

The National Bureau of Standards Journal of Research reports research and development in the fields of activity shown at right. Also included from time to time are survey articles on topics closely related to the Bureau's scientific and technical program.

The Journal is published in three separate sections as follows:

A. Physics and Chemistry

Contains papers of interest primarily to scientists working in these fields. Issued six times a year. Annual subscription: domestic, $5.00; foreign, $6.00. Single copy, $1.00.

B. Mathematical Sciences

Presents studies and compilations designed mainly for the mathematician and the theoretical physicist. Issued quarterly. Annual subscription: domestic, $2.25; foreign, $2.75. Single copy, 75c.

C. Engineering and Instrumentation

Reports research and development results of interest chiefly to the engineer and the applied scientist. Issued quarterly. Annual subscription: domestic, $2.75; foreign, $3.50. Single copy, 75c.

The National Bureau of Standards is a principal focal point in the Federal Government for assuring maximum application of the physical and engineering sciences to the advancement of technology in industry and commerce. Its responsibilities include development and maintenance of the national standards of measurement, and the provision of means for making measurements consistent with those standards; determination of physical constants and properties of materials; development of methods for testing materials, mechanisms, and structures, and making such tests as may be necessary, particularly for government agencies; cooperation in the establishment of standard practices for incorporation in codes and specifications; advisory service to government agencies on scientific and technical problems; invention and development of devices to serve special needs of the Government; assistance to industry, business and consumers in the development and acceptance of commercial standards and simplified trade practice recommendations; administration of programs in cooperation with United States business groups and standards organizations for the development of international standards of practice; and maintenance of a clearinghouse for the collection and dissemination of scientific, technical and engineering information. The scope of the Bureau's activities is suggested in the following listing of its three Institutes and their organizational units.

Institute for Basic Standards. Applied Mathematics. Electricity. Metrology. Mechanics. Heat. Atomic Physics. Physical Chemistry. Radiation Physics. Laboratory Astrophysics.* Radio Standards Laboratory.* Radio Standards Physics & Radio Standards Engineering. Office of Standard Reference Data.

Institute for Materials Research. Analytical Chemistry. Metallurgy. Reactor Radiations. Polymers. Inorganic Materials. Cryogenics.* Office of Standard Reference Materials.

Institute for Applied Technology. Building Research. Electronic Instrumentation. Technical Analysis. Center for Computer Sciences and Technology. Textile and Apparel Technology Center. Office of Weights and Measures. Office of Engineering Standards Services. Office of Invention and Innovation. Office of Vehicle Systems Research. Clearinghouse for Federal Scientific and Technical Information.** Materials Evaluation Laboratory. NBS/GSA Testing Laboratory.

*Located at Boulder, Colo. 80302.
**Located at 5285 Port Royal Road, Springfield, Va. 22151.

U.S. DEPARTMENT OF COMMERCE
C. R. Smith, Secretary

NATIONAL BUREAU OF STANDARDS
A. V. Astin, Director

Order all publications from the Superintendent of Documents
U.S. Government Printing Office, Washington, D.C. 20402

Use of funds for printing this publication approved by the Director of the Bureau of the Budget (June 22, 1966).

JOURNAL OF RESEARCH of the National Bureau of Standards—A. Physics and Chemistry
Vol. 72A, No. 2, March–April 1968

Constant Pressure Flame Calorimetry With Fluorine
II. The Heat of Formation of Oxygen Difluoride*

Reatha C. King and George T. Armstrong

Institute for Basic Standards, National Bureau of Standards, Washington, D.C. 20234

(December 27, 1967)

The heats of the following reactions were measured directly in an electrically calibrated flame calorimeter operated at one atm pressure and 303 °K.

$$OF_2(g) + 2H_2(g) + 99H_2O(l) \rightarrow 2[HF \cdot 50H_2O](l)$$

$$F_2(g) + H_2(g) + 100H_2O(l) \rightarrow 2[HF \cdot 50H_2O](l)$$

$$\tfrac{1}{2}\,O_2(g) + H_2(g) \rightarrow H_2O(l)$$

The reactants and products were analyzed for each of the reactions. From these heats we calculated the corresponding heats of formation, as follows:

$$OF_2(g)\ \Delta H^\circ_{f298.15} = +24.52 \pm 1.59 \text{ kJ mol}^{-1}\ (+5.86 \pm 0.38 \text{ kcal mol}^{-1})$$
$$HF \cdot 50H_2O(l)\ \Delta H^\circ_{f298.15} = -320.83 \pm 0.38 \text{ kJ mol}^{-1}\ (-76.68 \pm 0.09 \text{ kcal mol}^{-1})$$
$$H_2O(l)\ \Delta H^\circ_{f298.15} = -285.85 \pm 0.33 \text{ kJ mol}^{-1}\ (-68.32 \pm 0.08 \text{ kcal mol}^{-1})$$

The uncertainties indicated are the estimates of the overall experimental errors. The value of the average O—F bond energy in OF_2 was calculated to be 191.29 kJ mol^{-1} (45.72 kcal mol^{-1}).

Key Words: Bond energy (O—F), flame calorimetry, flow calorimetry, fluorine, heat of formation, heat of reaction, hydrogen fluoride (aqueous), oxygen, oxygen difluoride, reaction calorimetry, water.

1. Introduction

Thermochemical data for the fluorine oxidizers are very important for their present-day applications. This group of oxidizers includes elemental fluorine, and its compounds such as OF_2, ClF_3, ClF_5, and BrF_3. These substances are typically very reactive and combine with most other elements and compounds, yielding large heats of reaction and in many cases the highest valence state of the oxidized element. Two important uses of these oxidizers are for the production of fluorides, and as possible ingredients in rocket propellants and explosive systems. Because of their reactivity, they make possible chemical reactions which have not been investigated, e.g., reactions at extremely low temperatures.

Until a few years ago, very few thermochemical studies involving these materials had been conducted. This lack of work was caused mainly by the nonexistence of corrosion-resistant construction materials and the unavailability of sufficiently pure samples the fluorides. In recent years several of the problems hindering earlier research have been solved, and precise calorimetry has been demonstrated to be possible.

For measuring heats of reactions of the fluorine oxidizers, a new flame calorimetric apparatus has been set up in this laboratory. An earlier version of this apparatus has already been described [1, 2].[1] An investigation of the heat of formation of oxygen difluoride is the first study carried out with the new apparatus and is described in this presentation.

For many years there has been interest in the heat of formation of oxygen difluoride. In 1930, von Wartenberg and Klinkott [3], and Ruff and Menzel [4], reported two different thermochemical studies on this compound. In various reviews of thermochemical properties [5–8], the data from these studies have been reevaluated repeatedly in attempts to derive a selected "best" value for the heat of formation of this compound. For some time, the selected value for

*This research was sponsored by the Air Force Office of Scientific Research under Order No. OAR ISSA 65–8. For the first paper of this series see Reference [1].

[1] Figures in brackets indicate the literature references at the end of this paper.

$\Delta H^\circ_{f298.15}[OF_2]$ was +7.6 kcal mol^{-1} [5]. In 1965 Bisbee, et al. [9] reported on a more recent study from which they derived $\Delta H^\circ_{f298.15}[OF_2] = -4.06$ kcal mol^{-1}. In spite of the large amount of earlier work, there thus remained considerable uncertainty in the heat of formation of oxygen difluoride and, at the start of this work, it was not clear whether the compound was exothermic or endothermic. The results of the earlier experimental work are compared with those from the present study in another section of this paper. For comparison with the present experiments, it is important to mention here the reactions which were studied in the earlier investigations.

The measurements of von Wartenberg and Klinkott were carried out in a flow system in which they reacted OF_2 (g) with (1) KOH (excess KOH aq 40%), (2) [6KI + 2HF] (in excess aq), and (3) HBr (excess HBr, aq 45%). They measured the heats of reaction and derived a value for the heat of formation of oxygen difluoride based on each reaction. Ruff and Menzel used a flame calorimeter to measure the heat of the overall reaction of combustion of OF_2 with hydrogen and neutralization of the product HF in NaOH (aq). In the same apparatus they also measured the heats of the $F_2 - H_2 - NaOH$ and the $O_2 - H_2$ reactions. The latter measurements provide the auxiliary heat data needed for calculating $\Delta H^\circ_f[OF_2]$. Bisbee, et al. reacted oxygen difluoride with hydrogen in a combustion bomb, which contained water for solution of the product HF. For calculating $\Delta H^\circ_f[OF_2]$ they obtained their auxiliary data for the HF (aq) from the literature. It is interesting to note that in the earlier work, three different calorimetric methods were used. With well-developed procedures, suitably selected reactions for study, and pure reaction materials, it seems possible that each of the above calorimetric methods could lead to a reliable value for $\Delta H^\circ_f[OF_2]$. However, it appears that these methods were not used to their best advantage in the earlier work.

There are few known reactions of oxygen difluoride which are suitable for a thermochemical study for deriving $\Delta H^\circ_f[OF_2]$. Because the magnitude of this heat-of-formation value is small, it is desirable to derive it from a reaction with a small heat effect. Such reactions with oxygen difluoride unfortunately tend to lead to multiple products, which are not readily recovered and separated for quantitative analysis. Under ordinary conditions fluorine and oxygen do not combine directly to form oxygen difluoride.

With the above points in mind, the $OF_2 - H_2 - H_2O$ reaction was selected for this study despite the large heat effects to be expected. This reaction leads to only a few products, goes readily to completion, is amenable to analysis of reactants and products, and requires auxiliary data that can be measured in the same apparatus. Oxygen difluoride was reacted with hydrogen in a flame, and then the product hydrogen fluoride was dissolved in water present in the reaction vessel. Using the same apparatus and similar procedures, heat measurements were made also for the $F_2 - H_2 - H_2O$ and $O_2 - H_2$ reactions.

The reliability of the heat-of-formation value derived is increased by several factors inherent in this experimental plan. (1) The hydrogen fluoride is dissolved in water, yielding a well-defined thermodynamic state for the acid. (2) Dissolving the hydrogen fluoride inside the calorimeter lessens the possibility of loss of the acid by corrosion and retains it for later quantitative analyses. (3) Because the auxiliary data are measured in the same way as the principal reaction, several of the systematic errors cancel in the calculation of $\Delta H^\circ_f[OF_2]$. This plan is similar to that used by Ruff and Menzel. Our work differs from theirs mainly in the solution of the hydrogen fluoride in water instead of aqueous sodium hydroxide, and in the design of the reaction vessel.

2. Experimental Apparatus and Procedures

2.1. The Samples

a. Hydrogen

A commercially available high purity grade of hydrogen was used. A mass spectrometric analysis was performed directly on the contents of the cylinder and the composition (mole percent) of the gas was: H_2, 99.9; H_2O, 0.04 ± 0.02; and N_2, 0.05 ± 0.01. The hydrogen was used directly from the cylinder.

b. The Oxidizer Gases

Commercially available samples of oxygen, fluorine, and oxygen difluoride were used. Each of the samples was transferred from the large cylinder to a spherical weighable container for the analyses and calorimetric experiments. The design of the sample containers has already been described [1, 2]. They were constructed of Monel and equipped with either Monel or 316-stainless-steel valves with Teflon packing. The weight of a typical bulb was approximately 150 g. Extensive analyses were carried out for each of the gases and the procedures used are described in detail in the Appendix.

Oxygen. The oxygen was of high purity and is the grade used in this laboratory for bomb combustion experiments. The purity was reported by the supplier to be greater than 99.99 percent. It was analyzed for argon and nitrogen by mass spectrometry and gas chromatography, respectively. The composition of the sample is estimated to be oxygen, 99.987; nitrogen, 0.009; and argon, 0.004 weight percent.

Fluorine. The fluorine sample was of ordinary commercial quality and therefore not of the high purity desirable for a definitive thermochemical study of the hydrogen-fluorine reaction. While being sampled, the gas was passed over activated sodium fluoride for removal of hydrogen fluoride.

The total analysis of the fluorine sample was obtained using a combination of analytical methods. The total mole percent fluorine was determined by the mercury absorption technique and the relative amounts of the constituents of the residual gas were measured with mass spectrometry and gas chromatography. The chromatographic method was developed to provide a check on the results from the mass spectrometric method, which we have usually used

for analysis of the residual gas. The results from the two methods were in good agreement (see appendix). Table 1 gives the complete analysis of the fluorine sample.

TABLE 1. *Analysis of the fluorine sample*

Constituent	Mole percent total impurities [a]		Mole percent in fluorine sample	Weight percent
	I [b]	II	(based on II)	
F_2			98.75	98.92
N_2	61.8	62.0	0.77	0.54
O_2	28.6	31.3	.39	.33
Ar	0.2	0.2	.0025	.003
CO_2	3.4	1.2	.015	.017
CF_4	5.0	4.4	.055	.128
SiF_4		0.03	.0004	.001
SO_2F_2	0.3	.3	.0037	.010
C_2F_6		.28	.0035	.013
SF_6		.08	.0010	.004
C_3F_8		.08	.0010	.005
C_4F_8 (unsat.)		.07	.0009	.005
Remaining fluorocarbons	0.6	.06	.0007	

[a] Mass spectrometric analysis of volatile impurities after removal of F_2 by reaction with mercury.

[b] Sample pressure of I was factor of ten less than that of II. Analysis of I serves only for comparison of the analysis for major impurities.

Oxygen difluoride. The supplier's analysis of the oxygen difluoride sample showed it to contain: OF_2, 99.25; O_2, 0.69; and CO_2, 0.06 weight percent, and 0.01 volume percent CF_4. The gas was reported to contain no free fluorine. Kesting, et al. [10] compared the methods of gas chromatography, iodimetry and infrared spectroscopy for analysis of OF_2 and their tests show that gas chromatography yields the most reproducible and accurate results.

Because of the importance of the analysis to the accuracy of the calorimetric data, the oxygen difluoride sample was reanalyzed in this laboratory by gas chromatography, following procedures similar to those described by Kesting. The results from two of the analyses are shown below.

	Analysis I	Analysis II	Av
	Mole %		wt. %
OF_2	99.07	99.10	99.36
O_2	0.76	0.73	0.45
CF_4	.06	.07	.11
CO_2	.10	.10	.08

For qualitative identification, an infrared spectrum of the sample was obtained and is shown in figure 11 (appendix).

2.2. Reaction Vessel and Flow System Designs

a. The Reaction Vessel

The general method is to react the oxidizer in a flowing atmosphere of excess hydrogen and then to form the aqueous acid solution of the products. The overall design is illustrated in figure 1. In the upper chamber (A) the oxidizer and hydrogen (excess) are mixed, ignited, and reacted in a flame. The effluent

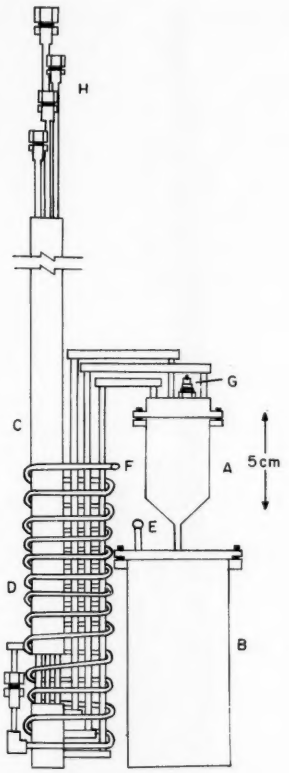

FIGURE 1. *Burner for fluorine flame calorimetry.*

A, Combustion chamber; B, Primary solution vessel; C, Heat exchanger; D, Cooling coil; E, To secondary solution vessel; F, From secondary solution vessel; G, Igniter; H, Inlet and Outlet connectors.

hydrogen removes the reaction products to the lower chamber (B), which is the primary solution vessel and contains 100 cm^3 of water. A gas dispersion system forces the gas mixture as fine bubbles through the aqueous solution, to cause complete removal of the hydrogen fluoride from the flowing hydrogen, and simultaneously to mix the solution making it homogeneous in concentration and temperature.

The gases are brought to the burner from the exterior of the calorimeter system by Monel tubes passing through the heat exchanger (C). The exit gas enters from the coiled tube (D) into the lower end of the outer tube of the heat exchanger, and while leaving the calorimeter, circulates among the small tubes which contain the entering gases. The outlet (E) on the primary solution vessel connects to a smaller vessel which is seen in the foreground in the complete burner assembly shown in figure 2. For an experiment this secondary vessel contains 20 cm^3 of water. As can be seen by reference to figures 1 and 2, the effluent gases leave the secondary solution vessel at F and pass through a helix of Monel tubing before entering the heat exchanger. Except for the primary solution vessel, the reaction vessel is composed almost entirely of

FIGURE 2. *Assembly of reaction vessel.*

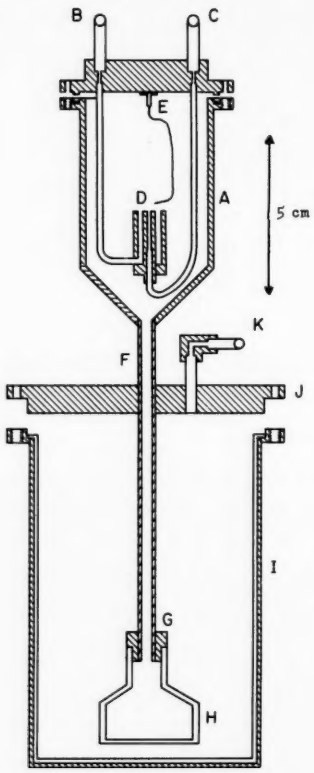

FIGURE 3. *Combustion chamber and primary solution vessel.*
A, Combustion chamber; B, Hydrogen inlet; C, Oxidizer inlet; D, Flame position; E, Spark electrode; F, Platinum tubing; G, Teflon adapter; H, Polyethylene gas disperser; I, Primary solution chamber; J, Lid for solution vessel; K, To secondary solution vessel.

Monel and silver-soldered at all of the permanent joints.

Details of the combustion chamber are shown in figure 3. The inlet tubes for the reacting gases, the igniter, and the flame tip are attached to the lid of the combustion chamber so that they are readily accessible when the lid is removed. The oxidizer is introduced through inlet C, and the major part of the hydrogen atmosphere enters through inlet B. Additional hydrogen is introduced through a third gas inlet (not shown). The joint between the cover and the combustion chamber is made by a Teflon gasket placed in a groove on the flange of the cup.

The reaction is initiated with an electric spark from a high voltage electrode which is a nickel rod, insulated by Teflon from a Monel sheath. A calcium fluoride disk is placed over the electrode (E) to further shield it from the reaction heat and product hydrogen fluoride.

The platinum tube (F) leading into the solution chamber is fitted with a polyethylene cap having a porous lower surface. The cap is held in place with a small Teflon adapter (G). The primary solution vessel is made of nickel-plated copper and has a Teflon liner. The flange on the liner makes the seal when the vessel is closed.

The water in the secondary solution vessel removes any hydrogen fluoride from the effluent gas that may be transferred from the primary solution. This provision assures also that upon leaving the burner the effluent gas flows through a solution for which the partial pressure of HF does not change during the experiment. In the primary solution vessel, the liquid contains no HF during the fore-period, but contains about two weight percent hydrogen fluoride in the final drift. The vapor pressure of hydrogen fluoride over the final solution is about 0.048 mm Hg at 25 °C [11]. Consequently, very little hydrogen fluoride is transferred to the secondary solution.

b. The Flow System

The layout of the gas flow system is similar to that used previously for flame calorimetric work in this laboratory [1, 2]. The components of the flow system are schematically shown in figure 4. Preceding the calorimeter are three flow lines which connect to inlet ports on the reaction vessel. These consist of the two flow lines for hydrogen, and one for the oxidizer.

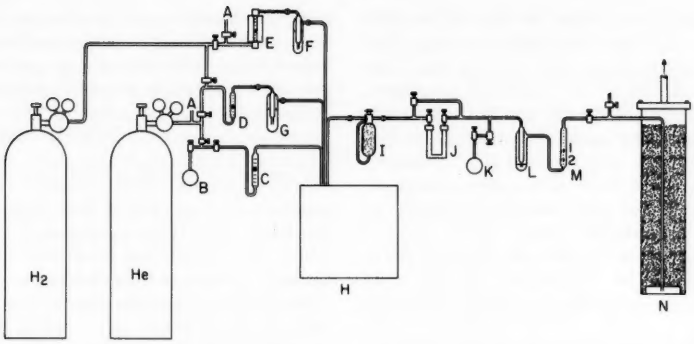

FIGURE 4. *Flow system.*

A, Flow inlet (helium); B, Oxidizer sample container; C, Flowmeter (oxidizer); D, Flowmeter (hydrogen, II); E, Flowmeter (hydrogen, I); F, Saturator (I); G, Saturator (II); H, Calorimeter; I, Absorber (magnesium perchlorate); J, Absorber (sodium fluoride); K, Sampling bulb; L, Bubbler (Kel-F oil); M, Flowmeter (effluent gas); N, Fluorine absorption tower.

The oxidizer line begins with the spherical sample bulb at B. Not shown in the diagram is an absorber of magnesium perchlorate placed immediately after the helium cylinder. Predrying of the helium is desired for the helium that enters the fuel line, but as is explained below, dried helium is not necessary for the hydrogen lines. The flow rate of the oxidizer was regulated by manual adjustment of the valves.

Each hydrogen line includes a flowmeter and weighable "saturator." The saturator is Pyrex and with the water, weighs about 69 grams. The hydrogen entering the reaction vessel is saturated with water to compensate for the water removed by the effluent hydrogen.

The items after the calorimeter used in these experiments are the absorption bulb (I), the sampling bulb (K), the bubbler (L), and the flowmeter (M). The absorption bulb contains magnesium perchlorate and is used to measure the amount of water removed from the reaction vessel by the effluent hydrogen. The final flowmeter is useful in monitoring the reaction. The remaining items serve the same purpose as described earlier [1].

2.3. The Calorimeter and Its Operation

The calorimeter is similar in design to the Dickinson Calorimeter [12], with modifications which were introduced by Prosen, et al. [13]. It is enclosed in a constant-temperature submarine-shield in the surrounding water bath. The calorimeter can is separated from the enclosure by a ½-in air space. It is supported by three metal pegs and has a volume of 5.5 liters. The calorimeter lid has three holes for bringing out the platinum resistance thermometer, the leads to the electrical calibration heater, and the flow lines to the reaction vessel. The reaction vessel and most of the heat exchanger are immersed in the stirred water of the calorimeter. The water is stirred at a rate of 300 rpm. The reaction vessel is placed on a small brass platform, supported by three small cones. This positions the bottom of the reaction vessel about ¼ in above the bottom of the calorimeter can.

In the manner customary in this laboratory, temperature measurements were made with a calibrated platinum resistance thermometer, used in conjunction with a G–2 Mueller bridge and a high-sensitivity galvanometer. A displacement of 0.5 mm on the galvanometer scale represented 10 $\mu\Omega$ on the bridge or one-tenth millidegree. At 0 °C the thermometer has a resistance of 25.4668 Ω.

The temperature of the jacket water was kept constant at 32 °C by an automatic regulating system consisting of a thermistor sensing element, linear dc microvolt amplifier, strip-chart recorder (-5 to $+5$ μV), current-adjusting-type controller, and a 50-W magnetic power amplifier [14]. The jacket bath has two heaters, a 14-Ω heater for raising the jacket temperature to 32 °C, and a 131-Ω heater for temperature control. A 500-mA meter is connected between the magnetic amplifier and the control heater. The thermistors form two opposite arms of a Wheatstone bridge circuit of which the two remaining arms are formed by adjustable temperature-insensitive resistors. Each thermistor arm of the bridge consists of four bead thermistors of about 1000 Ω each. The thermistors are encased in flattened thin-wall copper tubing and are immersed in the jacket water near the heaters and stirrer. A 1.5-V mercury cell supplies a current of 0.040 mA to the bridge. The current is kept very small so that self heating of the thermistor elements remains below 0.001 °C. The temperature was usually controlled to better than ± 0.0015 °C.

a. Electrical Calibration System

The calibration heater was made from B&S gage No. 30 Advance wire covered with a double layer of glass insulation. The current leads were 22-gage copper wire and the heater sheath was thin copper tubing flattened onto the resistance wire. The resistance of the heater was 23 Ω. The heater was formed in a 1-in o.d. coil which was suspended from the calorimeter lid. The ends of the sheath passed through a small copper plug which was fastened securely to a ring on the lid.

The potential leads are attached so that there is a negligible disturbance in the current leads [15]. The first potential lead is soldered to the current lead just inside of the copper sheath at the physical boundary of the calorimeter. The three leads are then brought up to a copper plate and the second potential lead is attached at the point where the current lead contacts the copper plate. Then all four wires are coiled on the lower side of the plate and cemented firmly in place. By means of a bakelite rod, which passes through a tube in the submarine lid, the copper plate is secured firmly against the lower side of the submarine lid to achieve good thermal contact with the calorimeter shield.

The power for the electrical calibration was obtained from a precision regulated power supply. The unit has a power output of about 500 W maximum, with a current range from 0–5 A and a voltage range from 0–103 V. The supply was operated in the constant current mode.

With the parameters and switching arrangement in these experiments, operation in the current mode gave more constant current and voltage readings. The double-pole, double-throw switch which connects the calibration heater and a dummy heater of similar resistance alternately into the circuit posed a problem in the calibrations. While interchanging the heaters, a transient voltage appeared. In a separate investigation [16] the magnitude and decay time of this transient voltage were observed. Because the transients were over in about ten seconds, while the heating periods were usually about sixteen minutes long, we believe that this effect does not significantly affect the accuracy of the calibrations performed. Current and voltage readings were made on alternate minutes. The time interval for the electrical heating was measured with an electronic counter, with an internal quartz oscillator generating at 100 kHz, which gave the time readings to 10^{-5} second. The timer was actuated by the switching arrangement which initiated the heating to the calorimeter.

Other equipment used in measuring the electrical energy input consisted of a 0.01 Ω standard resistor, a volt box with a ratio of 20,000 to 20 Ω, a thermostated standard cell, and a Wolff Diesselhorst potentiometer. During the calibration experiments the calibration of the potentiometer was checked daily. Details on a similar calibration circuit are given by Churney and Armstrong [16]. The resistors, potentiometer, and standard cells were calibrated at the National Bureau of Standards.

b. The Ignition System

A high voltage coil was used for the igniter and the sparking was timed with an electric clock connected in the ignition circuit. The sparking power was measured in blank experiments to be 1.4 J sec^{-1}.

c. Conduct of an Experiment

Preliminary Actions. Before and after each experiment, the oxidizer-sample container, saturators, and magnesium perchlorate absorber (see figure 4) are weighed to 0.1 mg. In preparing the reaction vessel, the sparking lead is positioned over the flame position and demineralized water is added to the primary and secondary solution vessels and then the reaction vessel is assembled. The weight of the calorimeter can with water is adjusted to 5950 ± 0.0005 g on a 6-kg capacity balance. This weight also includes the support for the reaction vessel. Immediately the reaction vessel is positioned and the calorimeter is covered with its lid from which is suspended the calibration heater. Then the remaining assembly of the calorimeter and its accessories is completed.

Reactions. The three inlet flow lines are purged with helium to remove air and a flowing hydrogen atmosphere is established in the hydrogen inlets. The total flow rate of hydrogen varied, depending on the reaction being studied, from about 350 to 450 cm^3 min^{-1}. Though the oxidizer line is initially flushed with helium, no gas is flowing through this line during the initial drift period. After a fore drift period of about 20 min, during which time-temperature readings of the calorimeter are made, the reaction is initiated by simultaneously initiating the sparking and releasing gas from the sample bulb. The sparking is discontinued when there is certainty that the fuel has ignited. This is usually after 10 to 15 seconds of sparking. The increase in the rate of the temperature rise of the calorimeter and the decrease in the flow rate of effluent gas are the main signals that the reaction is taking place smoothly.

In most experiments, a 2.5–2.7 deg temperature rise was achieved in a 15- to 18-minute reaction period. Near the end of the reaction period the oxidizer sample container is closed and the material remaining in the flow line is flushed into the burner with helium. The helium flow is reduced and continued for the remainder of the experiment while hydrogen flows through the other lines. After the reaction experiments the solution in the primary solution vessel is transferred, with washings, to a weighed 250-cm^3 polyethylene bottle. The secondary solution (20 cm^3) is also recovered for titration.

Calibrations. The procedure for conducting the calibration experiments is similar to that used for the reactions. The solution vessels contain 100 and 20 cm^3 water, respectively. A hydrogen flow through the bubblers is maintained at a rate comparable to that used for the reactions. The regulation of the helium flow in the oxidizer flow line constitutes the main difference between the gas handling procedures for the calibration and reaction experiments. In the calibrations a small flow of helium is maintained in the oxidizer line throughout the experiment, whereas for the reactions the helium flow is begun at the end of the reaction period.

d. Calculations

All of the values for the corrected temperature rise were calculated on an electronic computer with a computer program developed by Shomate [17]. For the calculation, it was necessary to give the computer the following data: (1) dial corrections for the Mueller bridge; (2) time and resistance readings taken during

the reaction and drift periods of the experiment; and (3) constants for the platinum resistance thermometer. A comparison of some hand-calculated and computer-calculated values showed that the program satisfactorily calculates the corrected resistance change, ΔR(corr); the initial and final drifts; the conversion factor, $\frac{dR}{dt}$; the initial and final temperatures for the reaction; the correction to the temperature rise, Δt(corr); the corrected temperature rise, Δt_c; and the cooling constant.

The definition, 1 cal = 4.184 J, was used for expressing the results in calories. All atomic weights were taken from the 1961 Table of Atomic Weights based on Carbon 12, adopted by the International Union of Pure and Applied Chemistry [18]. The heat capacity data used for the gases and liquid water are tabulated below. The heat of vaporization of water was taken as 2,439 and 2,428 J/g at 298.15 and 303.15 °C, respectively [19]. Values for the heat capacity of aqueous hydrogen fluoride were obtained from the work of Thorvaldson and Bailey [20].

Substance	$C_{p298.15}$ J mol^{-1} deg^{-1}	Reference
F_2(g)	31.30	[8]
O_2(g)	29.355	[8]
OF_2(g)	43.30	[8]
H_2(g)	28.823	[8]
H_2O(l)	75.2911	[8]

e. Water Removal from the Reaction Vessel

One general problem encountered in all the experiments was to account for and minimize loss of water from the reaction vessel. This was done by using a weighable drying tube on the outlet of the calorimeter and weighable saturators on the inlet tubes. The water entering and leaving the calorimeter could thus be monitored and the net change kept to a small value. The largest part of the residual heat effect due to condensation or evaporation could be presumed to form part of the causes of the initial and final drift rates, along with heat of stirring and heat transfer by conduction between the calorimeter and jacket. However, by keeping the net change in the amount of water small, it is believed that the uncertainty introduced by assuming the associated heat effects were constant would also be small. With this assumption, the results which are given in table 2, do not require further discussion. However, it is interesting to note the consistency in the signs of the differences for a given set of experiments.

A net removal of water is observed for all of the calibration experiments. This is consistent with the use of the helium in the oxidizer line throughout the experiment. Because the helium is not passed through a saturator, it causes a removal of water from the reaction vessel. The signs in the changes of water in the reaction vessel during the reaction experiments nearly correlate with the amounts of excess hydrogen used. The stoichiometric and actually used reactant ratios are summarized below.

TABLE 2. *Water changes in reaction vessel*

Expt. No.	Water removed g	Water carried in g	Increase g
Electrical calibrations			
4	0.8033	0.5246	−0.2787
5	.8084	.4813	−0.3271
6	.7025	.4644	−0.2381
7	.7478	.4637	−0.2841
Oxygen-hydrogen reaction			
1	0.6680	0.6483	−0.0197
2	.6483	.7264	+0.0781
3	.8313	1.0051	+0.1738
4	.8676	0.8887	+0.0211
5	.9486	.9740	+0.0245
6	.9345	.9461	+0.0116
Oxygen difluoride-hydrogen reaction			
7	0.5466	0.5656	+0.0190
8	.7458	.7135	−0.0323
9	.7069	.7288	+0.0219
10	.6102	.6805	+0.0703
11	.5034	.6186	+0.1152
Fluorine-hydrogen reaction			
1	1.4000	1.0715	−0.3285
2	1.2908	1.0127	−0.2781
3	1.1670	1.0396	−0.1274
5	0.9910	0.8310	−0.1591
6	1.0987	1.0397	−0.0590
7	0.8431	0.7853	−0.0578
8	1.0606	.9651	−0.0955
9	0.9137	.8323	−0.0814
10	.8322	.7700	−0.0622

reaction		stoichiometric	actual
O_2-H_2	n_{H_2}/n_{O_2}	2	2.8–3.4
F_2-H_2	n_{H_2}/n_{F_2}	1	4
OF_2-H_2	n_{H_2}/n_{OF_2}	2	4

A much larger excess of hydrogen was used in the fluorine reactions. This shows in the net removal of water from the reaction vessel, compared to the deposition of water observed for the other reactions.

3. Electrical Calibration Results

A series of seven electrical calibration experiments was conducted and the data are given in table 3. Included in this table are the experiment number; the average calorimeter temperature, t(av); the correction to the temperature rise, Δt(corr); the corrected temperature rise, Δt_c; the average current; average voltage; heating time; electrical energy; and the energy equivalent of the calorimeter. For the seven experiments the average value for the energy equivalent was 21887.9 J (°C)$^{-1}$ with a standard deviation of the mean of 0.006 percent.

TABLE 3. *Calibration of the calorimeter*

Expt. No.	1	2	3	4	5	6	7
t (av)....°C...	30.37	30.36	30.38	30.39	30.37	30.38	30.48
Δt (corr)....°C...	0.04724	0.04976	0.04658	0.04332	0.04878	0.04709	0.04368
Δt_c....°C...	2.73616	2.75413	2.72360	2.71066	2.74159	2.77289	2.55693
Current....A...	1.62580	1.62770	1.62706	1.62711	1.62770	1.62817	1.62737
Voltage....V...	37.3949	37.4378	37.4236	37.4280	37.4385	37.4483	37.4282
Time....sec...	984.857	989.160	979.206	974.077	984.874	995.612	918.805
q....J...	59875.9	60276.9	59624.3	59320.7	60016.8	60704.6	55964.0
E....J(°C)$^{-1}$...	21883.2	21886.0	21891.7	21884.2	21891.2	21892.2	21887.2

4. Examination of the Reaction Products

The corrosivity of fluorine and hydrogen fluoride is a general problem to be minimized and checked in these experiments. This was partly accomplished by using Monel as the construction material for the flow line and combustion chamber. Prior to the experiments these parts of the flow system were exposed to a flowing fluorine atmosphere to condition the surfaces. Consequently, all of the fluorine released from the weighed sample bulb should enter into the reaction with hydrogen.

Most of the corrosion problem in these experiments was caused by the product hydrogen fluoride. The appearance of the combustion chamber after the experiments suggested that more corrosion resulted from the hydrogen fluoride in the F_2-H_2 reaction than from the HF-H_2O mixture in the OF_2-H_2 reaction.

The solutions and washings from the primary solution vessel were transferred to a weighed polyethylene bottle from which weighed aliquots were taken for titration with standard sodium hydroxide solution. After the analyses for H^+, samples of these solutions were analyzed by atomic spectrophotometry for Cu^{++}, Ca^{++}, Ni^{++} and Ag^+. These results for the F_2-H_2-H_2O and OF_2-H_2-H_2O reactions are given in table 4.

TABLE 4. *Quantities of metal ions in hydrofluoric acid solutions*

Expt. No.	Ag	Ca	Cu	Ni	n_{HF} equiv
	μ moles				(total)
F_2-H_2-H_2O Reaction					
1	<0.05	<0.3	7.4	20.0	0.00005
2	<.05	<.3	9.0	16.1	.00005
3	<.05	<.3	2.2	9.1	.00003
4	<.05	<.3	1.5	3.9	.00001
5	<.05	<.3	1.5	4.5	.00001
6	<.05	<.3	3.2	8.4	.00002
7	<.05	<.3	0.6	3.9	.00001
8	<.05	<.3	<.1	4.7	.00001
9	<.05	<.3	1.2	7.7	.00002
10	<.05	<.3	3.5	10.0	.00003
OF_2-H_2-H_2O Reaction					
1	0.3	1.4	16.1	32.9	0.00010
4	<.05	0.9	15.1	23.4	.00008
7	<.05	.9	16.8	29.2	.00009
Blank	<.05	<.1	<0.1	<0.2	

For the fluorine reaction, the solution from each experiment was analyzed, and in the OF_2 reaction solutions from three selected experiments were tested. The blank is a sample of the demineralized water used for the solutions. Because the blank showed no ions (outside the uncertainty intervals), we concluded that the metal ions resulted from the corrosion of the reaction vessel.

The total amount of corrosion cannot be determined from these tests. The total quantity of aqueous fluoride salts amounts to less than 10 percent of the deficiency of HF. (Compare n_{HF}(equiv) in table 4 with Δn_{HF}(obs-calc) in tables 7 and 9.) However, the tests do reveal some interesting features about the reactions.

The solutions from the fluorine reaction contain a smaller concentration of the metal ions, in spite of the more corroded appearance of the reaction vessel. It is possible that only the metal fluorides that exist in the vapor phase near the flame position are flushed downward by the effluent gas in this reaction. On the other hand, the product HF(aq) in the oxygen difluoride reaction may dissolve some metal fluorides and serve as a transport medium to the solution. Approximately 1 g of water was formed in each experiment, more than enough to wet the surfaces of the combustion chamber. Much more erosion of the CaF_2 disk was observed for the OF_2 reaction. This is consistent with the larger amount of Ca^{++} present in the solution, and suggests that the CaF_2 is slightly dissolved by the HF(aq), and then transferred to the solution.

5. Reaction Heat Measurements

5.1. Oxygen-Hydrogen Reaction

For six of the nine experiments on this reaction (series I) the contents of the calorimeter were the same as for the electrical calibrations. In the other three experiments (series II), the water in the solution vessel was omitted, so that the product water could be weighed and compared with the amount calculated from the weighed quantity of oxygen reacted. In these three experiments the water was flushed from the reaction vessel with helium and absorbed in magnesium perchlorate outside the calorimeter [21]. The data for the experiments are given in table 5.

m_g is the mass of sample and m_{O_2} is the mass of oxygen, based on the analysis given in section 2.1.b. m_{H_2O}(obs) is the measured mass of water formed in the reaction and m_{H_2O}(obs)/m_{H_2O}(calc) is the ratio of the observed to calculated quantities of water. t(av) is the average temperature of the calorimeter during the reaction and is the reference temperature for the reaction. Δt(corr) and Δt_c are respectively, the correction to the temperature rise and the corrected temperature rise.

TABLE 5. O_2-H_2 *reaction*

a. Heat measurements

Expt. No.	Series I 1	2	3	4	5	6	Series II 7	8	9
m_s.....g...	3.3032	3.3850	3.4945	3.2208	3.2248	3.2376	3.2342	3.2325	3.1527
m_{O_2}.....g...	3.3028	3.3846	3.4941	3.2204	3.2244	3.2372	3.2338	3.2321	3.1523
m_{H_2O}(obs).....g...	[a]	[a]	[a]	[a]	[a]	[a]	3.6417	[b]	3.5517
m_{H_2O}(obs)/m_{H_2O}(calc).....							1.0001		1.0006
t_{av}.....°C...	30.36	30.38	30.43	30.31	30.32	30.32	30.34	30.34	30.37
Δt(corr).....°C...	0.06586	0.06620	0.05722	0.04966	0.05286	0.05159	0.07163	0.06773	0.06378
Δt_c.....°C...	2.70570	2.77304	2.86490	2.64052	2.64704	2.64914	2.67368	2.67882	2.61481
m_{H_2O}(in soln vessels).....g...	119.64	119.64	119.64	119.64	119.64	119.64	0	0	0
Δe_1.....J(°C)$^{-1}$...	7.8	7.5	8.2	7.6	7.6	7.6	7.6	7.6	7.4
Δe_2.....J(°C)$^{-1}$...	0	0	0	0	0	0	−499.9	−499.9	−499.9
E(calorim).....J(°C)$^{-1}$...	21895.7	21895.4	21896.1	21895.5	21895.5	21895.5	21395.6	21395.6	21395.4
q(obs).....J...	59243.2	60716.8	62730.1	57815.5	57958.3	58004.2	57205.0	57315.0	55944.9
n_{H_2}/n_{O_2}.....	2.81	2.88	3.02	3.35	3.35	3.23	2.96	2.96	3.20

b. Corrections to the heat measurements

q(ign).....J...	23.2	16.0	11.5	19.6	22.4	18.2	16.4	10.5	17.1
q(temp).....J...	−37.5	−40.3	−25.1	−42.0	−28.0	−38.9	−18.4	−46.4	−38.5
q'(vap).....J...	271.5	278.1	371.1	256.6	279.5	265.3			
q''(vap).....J...	36.3	39.6	29.1	26.2	26.1	26.1			
q'''(vap).....J							−366.9	−227.6	−181.6
q^{iv}(vap).....J							−33.9	−33.8	−33.8
Total.....J...	293.5	293.4	386.6	260.4	300.0	270.7	−402.8	−297.3	−236.8
q_{O_2}.....J...	58949.7	60423.4	62343.5	57555.1	57658.3	57733.5	57607.8	57612.3	56181.7
n_{H_2O}.....mol...	0.20644	0.21154	0.21838	0.20128	0.20154	0.20234	0.20212	0.20202	0.19702
q_{O_2}/n_{H_2O}.....kJ mol^{-1}...	285.55	285.64	285.48	285.95	286.09	285.33	285.02	285.18	285.16

[a] Water formed was not measured.
[b] Attempt to measure water was unsuccessful.

m_{H_2O}(in soln vessels) is the total mass of water in the solution vessels. Δe_1 is the correction to the energy equivalent for the water formed in the reaction (the heat capacity of half the water formed). Δe_2 is the correction for the omission of water from the solution vessel. E(calorim) is the energy equivalent of the calorimeter corrected for the deviations from the standard calorimeter. q(obs) is the observed heat effect.

q(ign) and q(temp) correct for the ignition energy and the energy required to temper the reacting gases from room temperature to t(av), the average calorimetric temperature during the reaction. q(ign) was calculated from the sparking power, 1.4 J sec^{-1} and the measured sparking times. q(temp) was calculated from the heat capacities and the measured amounts of the gases reacted.

q'(vap) is a correction for the addition of water to the reaction vessel during the reaction period by the reacting hydrogen. The hydrogen that enters into reaction is saturated with water, which condenses and is not carried out of the calorimeter. The amount of water added to the calorimeter is calculated from the volume of hydrogen reacted (based on stoichiometry of reaction) and the vapor pressure of water at the room temperature. q'(vap) is then the heat of condensation of this water at t(av).

In contrast, the helium used for purging the oxidizer line causes a net removal of water from the solution vessel. We reason that if the gas flow were begun at the time when one-half of the temperature increase is achieved, no correction would be needed for the vaporization of the water because the heat effect would then be properly accounted for by the final drift rate measurements. q''(vap) is a correction for the energy of vaporization of the additional water that would have been removed from the solution vessel had the helium flow been started at t_m at the rate that was continued through the final drift period. q'(vap) and q''(vap) apply to all experiments with water in the solution vessel, whereas the corrections q'''(vap) and q^{iv}(vap) pertain only to the experiments in which the product water was measured. q'''(vap) is the amount of heat required to vaporize the water removed from the reaction vessel by the hydrogen and helium during the reaction. This quantity of water was measured by weighing the absorber immediately after the experiment, and using another weighed absorber for collecting the water remaining in the reaction vessel. q^{iv}(vap) is the heat of vaporization of the water in the vapor phase in the reaction vessel.

We have assumed that the nitrogen impurity present in the hydrogen and the oxygen sample does not react and therefore no correction was applied. Under the conditions the nitrogen impurity may react to give NH_3. No test was made for NH_3 in these experiments. In similar calorimetric work Rossini [21] reported the presence of nitrogen in his oxygen sample. For some of his experiments in which oxygen was burned in a hydrogen atmosphere, he tested the product gases for NH_3 and found the amount present to be negligibly small.

The heat of the oxygen-hydrogen reaction is given in table 6. The values given represent averages for the number of experiments shown in parentheses. The data are given for 303.4 °K and 298.15 °K. The factor, σ, is the standard deviation of the mean. As mentioned above, the series II measurements were conducted mainly for confirming the amount of reaction. Because water was not contained in the solution vessels for these measurements, we believe that the heat

TABLE 6. *Heat of the oxygen-hydrogen reaction*

$H_2(g) + \frac{1}{2}O_2(g) = H_2O(l)$			
	$-\Delta H°_{303.4}$	$-\Delta H°_{298.15}$	σ
Series I (6) ..... kJ mol^{-1} ...	285.67	285.84	0.12
Series II (3) ..... kJ mol^{-1} ...	285.12	284.30	.....
Series I (6) ..... kcal mol^{-1} ...	68.28	68.32	0.03
Series II (3) ..... kcal mol^{-1} ...	68.14	68.18	.....

σ is the standard deviation of the mean.

data are less reliable than the series I data. The fact that they are less negative suggests that all of the heat from the reaction was not dissipated by the effluent gas. We do not propose the value found here, $\Delta H°_{298.15} = -68.32$ kcal mol^{-1}, as a replacement for Rossini's determination [21], but use the agreement with the earlier work as an indication of the general validity of these and other experiments conducted in this study.

5.2. Fluorine-Hydrogen-Water Reaction

Ten experiments were conducted for the F_2-H_2-H_2O reaction. For the first five experiments only the oxidizer flow line was conditioned with fluorine, whereas in the remaining experiments the flow line and combustion chamber were conditioned. On this basis the data for the experiments are presented in two series.

The data for these experiments are given in table 7. The heat measurement data have been explained for the oxygen reaction. Δe is a correction to the energy equivalent for the hydrogen fluoride formed in the reaction (one half the heat capacity of the hydrogen fluoride). n_{H_2O}/n_{HF} is the ratio of the moles water in the solution vessel to the moles of hydrogen fluoride formed in the reaction, as determined by the analyses of the solutions.

For the reaction quantities, $n_{HF}(F_2)$ and $n_{HF}(CF_4)$ are the numbers of moles of HF produced from F_2 and CF_4, respectively. They were calculated from the analyses in table 1. The deficiency of HF in these experiments varied greatly. For the ten experiments, the values of $n_{HF}(obs)/n_{HF}(calc)$ ranged from 0.9772 to 0.9964, with a mean of 0.9844. We assume that the deficiency of HF is caused by corrosion. However, the erraticity of the recovery is difficult to explain.

The ignition, vaporization, and gas temperature corrections are the same as described above. q_{O_2}, q_{CF_4}, and q_{CO_2} are corrections for the reactions of the impurities. These corrections were calculated on the basis of eqs (1), (2), and (3).

$$\Delta H_{R,298.15\,°K} \quad [8]$$

$$H_2(g) + \tfrac{1}{2}O_2(g) \rightarrow H_2O(l) \qquad -68.32 \text{ kcal(mol } H_2O)^{-1} \qquad (1)$$

$$2H_2(g) + CF_4(g) + 50H_2(l) \rightarrow 4[HF{:}50H_2O](l) + C(c) \qquad -84.2 \text{ kcal(mol } CF_4)^{-1} \qquad (2)$$

$$2H_2(g) + CO_2(g) \rightarrow C(c) + 2H_2O(l) \qquad -42.59 \text{ kcal(mol } CO_2)^{-1} \qquad (3)$$

TABLE 7. F_2-H_2-H_2O *reaction*

a. Heat measurements

	Series 1					Series 2				
Expt. No.	1	2	3	4	5	6	7	8	9	10
m_F ..... g ...	3.5504	2.7483	2.7084	1.3165	2.7981	2.9859	2.4623	2.6524	3.1136	2.4048
Δt(corr) ..... °C ...	0.05552	0.03351	0.03381	0.07354	0.02279	0.07565	0.02937	0.03237	0.04481	0.05046
Δt_c ..... °C ...	2.71469	2.10439	2.07278	1.01125	2.14415	2.29429	1.89230	2.04004	2.39349	2.61824
t(av) ..... °C ...	30.35	30.73	30.73	30.02	30.74	30.16	30.78	30.69	30.51	30.30
Δe ..... J(°C)$^{-1}$ ...	1.8	1.4	1.4	1.0	1.4	1.6	1.6	1.4	1.6	1.8
E(calorim) ..... J(°C)$^{-1}$ ...	21889.7	21889.3	21889.3	21888.9	21889.3	21889.5	21889.5	21889.3	21889.5	21889.7
q(obs) ..... J ...	59423.7	46063.6	45371.7	22135.2	46933.9	50220.9	41421.5	44655.0	52392.3	57312.5
n_{H_2O}/n_{HF}	30.4	38.9	39.8	82.9	38.2	35.8	44.3	40.9	34.8	31.8

b. Reaction quantities

n_{F_2} ..... mol ...	0.09243	0.07155	0.07051	0.03427	0.07284	0.07773	0.06410	0.06905	0.08111	0.08864
$n_{HF}(CF_4)$ ..... mol ...	.00020	.00016	.00016	.00008	.00016	.00016	.00012	.00016	.00016	.00020
n_{HF}(calc) ..... mol ...	.18506	.14326	.14118	.06862	.14584	.15562	.12832	.13826	.16238	.17748
n_{HF}(obs) ..... mol ...	.18277	.14267	.13965	.06706	.14532	.15502	.12545	.13596	.15938	.17453
Δn_{HF}(obs-calc) ..... mol ...	−.00229	−.00059	−.00153	−.00156	−.00052	−.00060	−.00287	−.00230	−.00300	−.00295
n_{HF}(obs)/n_{HF}(calc)	.9876	.9959	.9891	.9772	.9964	.9961	.9776	.9833	.9815	.9833

c. Corrections to heat data

q(ign) ..... J ...	17.6	30.0	14.8	19.6	23.2	22.4	19.0	23.8	30.2	24.1
q'(vap) ..... J ...	122.6	100.3	100.3	56.9	90.8	120.9	89.9	95.8	109.2	104.0
q'(vap) ..... J ...	31.4	24.3	25.5	14.2	22.4	26.3	21.4	21.3	25.1	30.7
q(temp) ..... J ...	− 15.5	− 7.3	− 13.8	− 1.5	− 25.1	− 11.1	− 15.5	− 14.6	− 19.2	− 34.9
q(O_2) ..... J ...	205.8	159.8	159.8	74.0	165.7	177.0	142.0	154.4	182.8	200.0
q(CF_4) ..... J ...	17.6	14.1	14.1	6.7	14.1	14.1	10.5	14.4	14.1	17.6
q(CO_2) ..... J ...	1.7	1.7	1.7	.8	1.7	1.7	1.7	1.7	1.7	1.7
q(diln) ..... J ...	− 12.2	− 6.5	− 5.3	7.0	− 6.1	− 7.1	− 1.0	− 3.4	− 8.0	− 11.7
Total (1)	369.0	306.4	297.1	163.7	286.7	344.2	268.0	293.4	335.9	331.5
q(corros) ..... J ...	764.	197.	510.	520.	173.	200.	958.	767.	1001.	984.
Total (2)	1133.0	503.4	807.1	683.7	459.7	544.2	1226.0	1060.4	1336.9	1315.6
q_{F_2}(1) ..... J ...	59054.7	45757.2	45074.6	21957.5	46647.2	49876.7	41153.5	44361.6	52056.4	56981.0
q_{F_2}(2) ..... J ...	58290.7	45560.2	44564.6	21437.5	46474.2	49676.	40195.5	43594.6	51055.4	55997.0
$q_{F_2}(1)/n_{HF}(F_2)$ ..... kJ mol^{-1} ...	319.45	319.76	319.63	320.36	320.20	320.83	321.01	321.23	320.90	321.42
$q_{F_2}(1)/n_{HF}$ [a] ..... kJ mol^{-1} ...	323.46	321.08	323.14	327.82	321.35	322.08	328.36	326.67	326.95	326.86
$q_{F_2}(2)/n_{HF}$ ..... kJ mol^{-1} ...	319.28	319.70	319.48	320.06	320.16	320.78	320.72	321.02	320.66	321.21

[a] $n'_{HF} = n_{HF}(obs) - n_{HF}(CF_4)$.

q(diln) corrects for diluting the acid solution from a concentration, HF:nH$_2$O, to HF:50H$_2$O. Total (1) is the sum of the corrections to this point and total (2) includes q(corros), a correction for the corrosion of the combustion chamber. Equation (4) is the corrosion reaction assumed and shows the heat of reaction used for calculating q(corros) [22]. The number of moles of reaction (4) is taken to be n_{HF}(obs-calc)/2.

$$F_2(g) + Ni(c) \rightarrow NiF_2(c) \qquad -159.5 \text{ kcal(mol } F_2)^{-1} \qquad (4)$$

The corrections Total (1) and Total (2), table 7, were applied to the observed heat effect to give $q_{F_2}(1)$ and $q_{F2}(2)$, respectively. We now have three ways of calculating the results. Referring to experiment (1) for example, in the first way the heat of reaction corrected by Total (1) to give $q^{(1)}_{F_2}$ is presumed to be caused by the measured amount of F_2 introduced, giving $q_{F_2}(1)/n_{HF}(F_2) = 319.45$ kJ mol^{-1}. In the second way the same heat of reaction is attributed to reaction of enough fluorine to form the observed amount of HF, giving $q_{F_2}(1)/n_{HF} = 323.46$ kJ mol^{-1}. In the third way the deficiency of HF is attributed to corrosion forming NiF_2(c), introducing an additional energy correction, q(corros), and allowing a new total energy, $q_{F_2}(2)$ to be attributed to the amount of F_2 needed to form the observed HF. This gives $q_{F2}(2)/n'_{HF} = 319.28$ kJ mol^{-1}, which we consider to be the best representation of the data. All experiments are treated each way at the bottom of table 7.

The results of two series of five measurements each are summarized in table 8 in which the results obtained by the three methods are listed in columns (1), (2), and (3), respectively. The calculation in column (3) is preferred for reasons described above and experiments of series 2 are considered to be preferable because of a better conditioning procedure for the reaction vessel. Hence, the value $\Delta H^\circ_{303} = -76.69$ kcal mol^{-1} is selected for use in later calculations. This value, corrected to 298.15° gives

$$\Delta H^\circ_{f298.15}[HF \cdot 50H_2O] = -76.68 \text{ kcal mol}^{-1}.$$

TABLE 8. *Heat of fluorine-hydrogen-water reaction*

$\frac{1}{2}F_2(g) + \frac{1}{2}H_2(g) + 50H_2O(l) = [HF \cdot 50H_2O](l)$

	(1) $-\Delta H^\circ_{303}$	σ	(2) $-\Delta H^\circ_{303}$	σ	(3) $-\Delta H^\circ_{303}$	σ
Series 1 (5).....kJ mol^{-1}...	319.88	0.17	323.37	1.21	319.74	0.15
Series 2 (5).....kJ mol^{-1}...	321.08	0.11	326.18	1.07	320.87	0.11
Series 1 (5).....kcal mol^{-1}...	76.45	0.04	77.29	0.29	76.42	0.04
Series 2 (5).....kcal mol^{-1}...	76.74	0.03	77.96	0.25	76.69	0.03

σ is the standard deviation of the mean.

5.3. The OF_2-Hydrogen-Water Reaction

The data obtained for this reaction are shown in table 9. No new features are involved. The experiments in series 1 were conducted before the electrical cali-

TABLE 9. OF_2-H_2-H_2O *reaction*

a. Heat measurements

	Series 1						Series 2						
Expt. No.	1	2	3	4	5	6	7	8	9	10	11	12	13
m_s.....g...	2.9080	3.4370	3.0869	3.5261	3.4556	3.4512	3.4558	3.4015	3.3549	3.3785	3.4021	3.4929	3.4651
Δt(corr).....°C...	0.05253	0.04624	0.05224	0.04464	0.05456	0.05402	0.05216	0.05179	0.05348	0.05228	0.04842	0.04621	0.04681
Δt_r.....°C...	2.34591	2.77485	2.49106	2.84661	2.78877	2.78491	2.78889	2.74369	2.70657	2.72699	2.74267	2.81633	2.79548
t(av).....°C...	30.16	30.37	30.25	30.41	30.38	30.38	30.39	30.37	30.37	30.36	30.50	30.45	30.42
Δe.....J(°C)$^{-1}$...	3.8	4.0	3.9	4.0	3.9	3.9	3.9	3.9	3.9	3.9	3.9	4.0	4.0
E.....J(°C)$^{-1}$...	21891.7	21891.9	21891.8	21891.9	21891.8	21891.8	21891.8	21891.8	21891.8	21891.8	21891.8	21891.9	21891.9
q(obs).....J...	51356.0	60746.7	54533.8	62317.7	61051.2	60966.7	61053.8	60064.3	59251.7	59698.7	60042.0	61654.8	61198.4
n_{H_2O}/n_{HF}.....	52.6	44.6	49.4	43.2	44.3	44.4	44.4	45.1	45.8	45.5	45.3	43.8	44.3

b. Reaction quantities

n_{OF_2}.....mol...	0.05351	0.06224	0.05680	0.06488	0.06359	0.06351	0.06359	0.06259	0.06173	0.06217	0.06260	0.06427	0.06376
$n_{HF}(CF_4)$.....mol...	.00016	.00016	.00016	.00016	.00016	.00016	.00016	.00016	.00016	.00016	.00016	.00016	.00016
n_{HF}(calc).....mol...	.10718	.12664	.11376	.12992	.12734	.12718	.12734	.12534	.12362	.12450	.12536	.12870	.12768
n_{HF}(obs).....mol...	.10669	.12602	.11380	.13009	.12682	.12634	.12658	.12462	.12266	.12355	.12399	.12811	.12686
Δn_{HF}(obs−calc).....mol...	−.00049	−.00062	+.00004	+.00017	−.00052	−.00084	−.00076	−.00072	−.00096	−.00095	−.00137	−.00059	−.00082
n_{HF}(obs)/n_{HF}(calc).....	.9954	.9951	1.0003	1.0013	.9959	.9934	.9940	.9942	.9922	.9924	.9890	.9954	.9936

c. Corrections to heat measurements

q(ign).....J...	17.1	18.9	19.3	14.0	21.6	21.6	16.8	19.6	18.5	14.8	14.8	19.0	19.9
q'(vap).....J...	140.6	155.0	130.9	162.7	179.1	169.4	148.1	146.1	143.9	154.8	165.7	156.9	148.1
q''(vap).....J...	31.8	55.6	43.6	45.2	53.1	53.1	53.1	45.2	50.6	50.6	49.8	50.6	50.6
q(temp).....J...	−22.8	−36.8	−30.1	−35.6	−22.0	−28.4	−38.2	−42.0	−40.2	−34.2	−29.3	−37.0	−41.5
q(diln).....J...	+1.8	−1.0	−.4	−2.2	−1.0	−1.0	−1.0	−.5	−.5	−.5	−.5	−1.0	−1.0
$q(O_2)$.....J...	234.3	274.0	245.6	285.8	274.0	274.0	274.0	274.0	268.6	268.6	268.6	279.9	279.9
$q(CF_4)$.....J...	14.1	14.1	14.1	14.1	14.1	14.1	14.1	14.1	14.1	14.1	14.1	14.1	14.1
$q(CO_2)$.....J...	8.8	10.5	10.5	10.5	10.5	10.5	10.5	10.5	10.5	10.5	10.5	10.5	10.5
Total (1).....J...	425.7	490.3	433.5	494.5	529.4	513.3	477.4	467.0	465.5	478.7	493.7	493.0	480.6
q(corros).....J...	240.	303.	0	0	254.	411.	372.	352.	469.	465.	670.	288.	401.
Total (2).....J...	665.7	793.3	433.5	494.5	783.4	924.3	849.4	819.0	934.5	943.7	1163.7	781.0	881.6
$q_{OF_2}(1)$.....J...	50930.2	60256.4	54100.2	61823.2	60521.7	60453.4	60576.4	59597.3	58786.2	59220.0	59548.2	61161.8	60717.8
$q_{OF_2}(2)$.....J...	50690.2	59953.4	54100.2	61823.2	60267.7	60042.4	60204.4	59245.3	58317.2	58755.0	58878.2	60873.8	60316.8
$q_{OF_2}(1)/n_{OF_2}$.....kJ(mol)$^{-1}$...	951.79	952.82	952.47	952.88	951.75	951.87	952.61	952.18	952.31	952.55	951.25	951.64	952.29
$q_{OF_2}(1)/n'_{OF_2}$[a].....kJ(mol)$^{-1}$...	956.17	957.51	952.13	951.71	955.66	958.21	958.33	957.69	959.77	959.96	961.85	956.10	958.45
$q_{OF_2}(2)/n'_{OF_2}$.....kJ(mol)$^{-1}$...	951.66	952.70	952.13	951.71	951.64	951.69	952.45	952.04	952.12	952.35	951.03	951.52	952.12

[a] $n'_{OF_2} = [n_{HF}(obs) - n_{HF}(CF_4)]/2$.

brations were performed, and those in series 2 were conducted later. Otherwise, the procedures used were identical. The average recovery of hydrogen fluoride was better than 99.5 percent. q(corros) for this system was calculated from eq (5) using the heat of reaction given there and a number of moles equal to Δn_{HF}(obs-calc)/2.

$$OF_2(g) + Ni(c) + H_2(g) = H_2O(l) + NiF_2(c)$$

$$-233.78 \text{ kcal (mol } OF_2)^{-1} \qquad (5)$$

The treatment is the same as for the fluorine reaction. The three alternative calculations of the reaction energy are shown at the bottom of table 9 and in table 10, of which the preferred one is based upon the amount of energy, adjusted for the energy of corrosion, and the amount of hydrogen fluoride actually observed. This is given as $\Delta H^\circ_{303}(3)$ of table 10.

TABLE 10. *Heat of* OF_2-H_2-H_2O *reaction*

$OF_2 + 2H_2 + 99H_2O = 2[HF \cdot 50H_2O]$ (*l*)

	$-\Delta H^\circ_{303}(1)$	σ	$-\Delta H^\circ_{303}(2)$	σ	$-\Delta H^\circ_{303}(3)$	σ
Series 1.....kJ mol^{-1}...	952.26		955.23		951.92	
Series 2.....kJ mol^{-1}...	952.12		958.88		951.95	
Total (13 expts).....	952.18	0.14	957.20	0.80	951.94	0.14
Series 1 kcal mol^{-1}.	227.60		228.31		227.51	
Series 2 kcal mol^{-1}.	227.56		229.18		227.52	
Total (13 expts).....	227.58	0.033	228.78	0.19	227.52	0.033

σ is the standard deviation of the mean.

6. Discussion of Errors

The uncertainties are summarized in table 11 for the three reactions and for the calculation of the heat of formation of OF_2(g). The observed standard deviation of the OF_2-H_2-H_2O measurements is 0.14 kJ mol^{-1} or 0.015 percent and that for the electrical calibrations is 0.015 percent. Hence the overall imprecision in the experiments expressed in 2-sigma limits is

$$\pm 2\sqrt{(0.015)^2 + (0.015)^2}$$

$$= \pm 0.042 \text{ percent } (0.40 \text{ kJ mol}^{-1}).$$

Systematic errors in calibration are 0.02 percent for "irrelevance" and 0.02 percent for the transient. Systematic errors in the reaction heat measurements are 0.02 percent for uncertainty in the oxygen content of the sample, and 0.02 percent for uncertainty in the correction for corrosion. Each of these sources of error is explained below. Assuming that these errors are independent we apply them as the square root of the sum of the squares and obtain 0.040 percent (0.38 kJ mol^{-1}) as the overall systematic error. The overall uncertainty in the heat of reaction is, therefore the sum of 0.042 and 0.040 or 0.082 percent (0.78 kJ mol^{-1} or 0.19 kcal mol^{-1}).

The error treatments for the two other reactions are summarized in much the same way. The systematic errors for the O_2-H_2 experiments do not include any uncertainties for analysis or corrosion, but do include systematic errors listed for the calibration. To place these on the same basis as the other calculations, we combine these two systematic errors as the square root of the sum of the squares.

In estimating the uncertainty in the heat of formation of OF_2 we combine the contributions in joules for the three reactions in the following way. The random errors and the chemical errors, which are presumed to be independent for the various reactions, are added without regard to sign; and the systematic calibration errors are added with due regard for the sign with which the reaction equations are added, in order to obtain their contributions to the uncertainty in the heat of formation of OF_2. These contributions, listed

TABLE 11. *Summary of errors*

$\Delta H_{R\ 303\ ^\circ K}$ kJ mol^{-1}	951.94		320.88		285.67		
	OF_2-H_2-H_2O		F_2-H_2-H_2O		1/2 O_2-H_2		OF_2
	%	kJ mol^{-1}	%	kJ mol^{-1}	%	kJ mol^{-1}	kJ^{-1}
Random errors:							
Calibration (σ_c).....	0.015	0.14	0.015	0.05	0.015	0.04	.....
Reaction measurement (σ_r).....	.015	.14	.034	.11	.042	.12	.....
Imprecision $2\sqrt{\sigma_c^2 + \sigma_r^2}$.....	0.042	0.40	0.074	0.24	0.089	0.25	1.13
Systematic errors:							
Irrelevance of calib.....	0.02	0.19	0.02	0.06	0.02	0.06	.....
Transient.....	.02	.19	.02	.06	.02	.06	.....
Total systematic calib.....	.028	.27	.028	.09	.028	.08	0.01
Analysis.....	.02	.19	.02	.06	.....	.....	.....
Corrosion.....	.02	.19	.02	.06	.....	.....	.....
Total chemical.....	.028	.27	.028	.09	.....	.....	.45
Overall systematic error.....	0.040	0.38	0.040	0.13	0.028	0.08	0.46
Uncertainty.....	0.082	0.78	0.114	0.37	0.117	0.33	1.59
Uncertainty (kcal mol^{-1}).....	.....	0.19	.....	0.09	.....	0.08	0.38

in the right-hand column of table 11, are added to obtain 1.59 kJ mol^{-1} (0.38 kcal mol^{-1}) for the uncertainty in the heat of formation of OF_2(g).

Recent experiments in this laboratory have indicated that to obtain accurate heat measurements in calorimetric studies such as these, using the Dickinson calorimeter, the chemical energy and the energy from the calibration heater should be liberated at nearly the same position in the calorimeter [16]. This would tend to cancel the effect of temperature gradients on the surface of the calorimeter. In the experiments described in this paper, the heater was near the side of the calorimeter (closer to the thermometer), whereas the reaction vessel was near the center. The earlier investigation shows that the energy equivalent determined from the electrical energy measurements may be inappropriate for the calorimeter as used in the chemical energy measurements. This possible uncertainty in the calibration is listed here as the "irrelevance" error and is estimated to have an upper limit of 0.02 percent for these experiments. It is noted that this error probably affects all of the heat measurements by the same fractional amount. It would thus cause an effect too small to be observed in the heat of formation of OF_2 which is calculated from differences between the measurements reported here; however, it could have an observable effect on the values for $\Delta H^\circ_{f298.15}[HF \cdot 50H_2O[(l)$ and $\Delta H^\circ_{f298.15}[H_2O(l)]$. The close agreement of the value found for the latter quantity with that reported by Rossini suggests that no important error is involved.

The "transient" effect has already been discussed in the description of the calibration procedures. Exact measurements of the effect were not made, but the maximum systematic error that could arise from this source was calculated to be 0.02 percent.

On the basis of earlier work [1, 2], we believe that the error in the analysis of the fluorine sample is 0.02 percent. Assuming that this amount of uncertainty is distributed among the F_2, N_2, and O_2 analyses, different values for n_{HF}(calc), q_{O_2}, and q(corros) are obtained (table 12). The variations amount to less than .02 percent.

We can demonstrate the validity of the overall corrosion correction applied in the following way. In figure 5 we have plotted the heats of reaction, corrected and uncorrected for corrosion, versus the percentage correction for corrosion for the F_2-H_2-H_2O and OF_2-H_2-H_2O reactions. The data plotted are obtained from tables 7 and 9, respectively. The data were fitted to the lines shown by the method of least squares and the equations are shown on the illustration. For both reactions there is a linear variation of the uncorrected heat of reaction with the q(corros) which was essentially eliminated, when q(corros) was applied. This illustration also shows why, in tables 8 and 10, the standard deviation of the mean of $\Delta H(3)$ is much less than for $\Delta H(2)$. The application of q(corros) smooths out an effect present in varying degrees in each of the experiments.

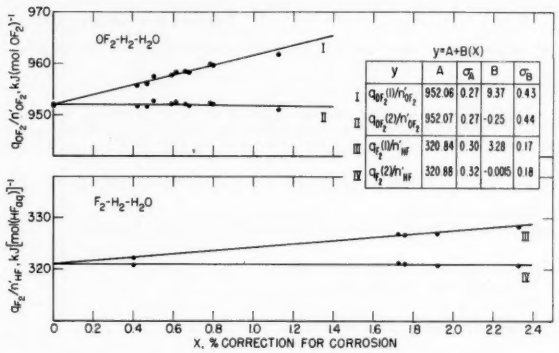

FIGURE 5. *Plot showing the variation of the heats of the* $F_2-H_2-H_2O$ *and* $OF_2-H_2-H_2O$ *reactions versus the percentage correction for corrosion.*

(X = q(corros) × 100/q(1), tables 7 and 9)

7. The Heat of Formation of Oxygen Difluoride. The (O-F) Bond Energy

We summarize the heat measurements and the heat of formation of OF_2 in table 13. The calculated heat of formation at 303.4 °K becomes the same value at 298.15 °K to yield $\Delta H^\circ_{f298.15}[OF_2(g)] = +5.86 \pm 0.38$ kcal mol^{-1}. The uncertainty shown represents the estimated accuracy based on the errors discussed. The value for the average O—F bond energy in OF_2 is calculated from this value for $\Delta H^\circ_f[OF_2(g)]$, using $\Delta H^\circ_f[O(g)] = 59.553$, and $\Delta H^\circ_f[2F(g)] = 37.75$ kcal mol^{-1} [8], to be 45.72 kcal mol^{-1}.

TABLE 12. F_2-H_2-H_2O *reaction*

Expt. #8 wt F_2 sample, 2.6524 g			
Column 1	2	3	4
F_2 (%)	98.92	98.90	98.90
N_2 (%)	0.54	0.56	0.54
O_2 (%)	.33	.33	.35
CF_4 (%)	.13	.13	.13
n_{HF}(calc)	0.13826	0.13824	0.13824
n_{HF}(obs)	.13596	.13596	.13596
Δn_{HF}(obs-calc)	.00230	.00228	.00228
q(corros) J	767.0	761.0	761.0
q_{O_2} J	154.3	154.3	165.7
sum of q(corros) and q_{O_2} J	921.3	915.3	926.7
q(obs) J	44655.0	44655.0	44655.0
% change in ΔH_R		−0.013	+0.012

TABLE 13. *The heat of formation of* OF_2

	$\Delta H_{R,\ 303\ °K}$ kcal	
$OF_2(g) + 2H_2(g) + 99H_2O(l) \longrightarrow 2[HF \cdot 50H_2O](l)$	-227.52 ± 0.19	(6)
$F_2(g) + H_2(g) + 100H_2O(l) \longrightarrow 2[HF \cdot 50H_2O](l)$	-153.38 ± 0.18	(7)
$1/2\ O_2(g) + H_2(g) \longrightarrow H_2O(l)$	-68.28 ± 0.08	(8)
$F_2(g) + 1/2\ O_2(g) \longrightarrow OF_2(g)\ \Delta H^\circ_{f298.15}[OF_2(g)] = +5.86$ kcal ± 0.38		(9)

In table 14 we give the reactions investigated in the earlier work and compare the value reported for $\Delta H^\circ_{f298.15}[OF_2(g)]$ with the value [+5.86 ± 0.38 kcal

TABLE 14. *Earlier thermochemical studies involving* $OF_2(g)$

	Temp °K	$-\Delta H°$ kcal mol^{-1}	$\Delta H_{f298}[OF_2]$	Ref
1. $OF_2(g)+2KOH$ (excess KOH aq 40%)$=[2KF+H_2O]$ (aq KOH)$+O_2(g)$	291	125.75	+6.9	[3, 6, 23]
2. $OF_2(g)+[6KI+2HF]$ (excess aq soln)$=[4KF+2KI_3+H_2O]$ (aq KI + HF soln)	291	176.55	+1.4	[3, 6, 23]
3. $OF_2(g)+4HBr$ (excess HBr aq 45%)$=[2HF+2Br_2]$ (aq HBr)$+H_2O$	291	134.36	+8.8 Av $+5.7\pm2$ [a]	[3, 6, 23]
4. $OF_2(g)+2H_2(g)+2NaOH$ (excess aq 20%)$=2NaF$ (in aq NaOH)$+3H_2O(l)$		254.9		[4, 23]
5. $\frac{1}{2}O_2(g)+H_2(g)=H_2O(l)$		68.5		[4, 23]
6. $F_2(g)+H_2(g)+2NaOH$ (excess aq 20%)$=2NaF$ (in aq NaOH)$+2H_2O(l)$		181.7	$+4.7\pm2$ [a]	[4, 23]
7. $OF_2(g)+H_2(g)$ (excess)$+nH_2O(l)=[2HF+(n+1)H_2O](l)\{n=\infty\}$		222.93	-4.06 ± 2.2 [a]	[9, 23]
8. The present work (see table 13)			$+5.86\pm0.38$	

[a] Estimated overall uncertainty given in original report.

mol^{-1}] derived from the present study. Our value agrees consistently with those reported by von Wartenberg and Klinkott [$+5.7\pm2$ kcal mol^{-1}], and Ruff and Menzel [$+4.7\pm2$ kcal mol^{-1}], but differs from Bisbee's results [-4.06 ± 2.2 kcal mol^{-1}].

In the various reviews which have been conducted on these studies so far, the biggest improvement in the re-evaluation of the original data has been to substitute current auxiliary data for the reactions studied by von Wartenberg and Klinkott. Ruff and Menzel measured the heats of principal reaction (4) and the auxiliary reactions ((5) and (6)) for calculating their value for $\Delta H°_{f298.15}[OF_2]$. Bisbee's value for $\Delta H°_{f298.15}[OF_2]$ will change as improvements are made in the $\Delta H°_{f298.15}$[HF, aq, ∞], the principal auxiliary data on which their results are based. However, it seems unlikely that the $\Delta H°_{f298.15}$[HF, aq, ∞] will ever be revised by an amount that will change the sign of their value for $\Delta H°_{f298.15}[OF_2]$.

No attempt will be made here to review completely the earlier studies. However, in re-examining the work of Bisbee et al., we note several points about their experiments which may lead to a less negative observed heat of reaction, and therefore explain the more negative heat-of-formation value which they reported. They give little information on the (1) analysis of the sample, (2) the technique used to insure mixing of the solution, (3) the corrosion by the product HF, and (4) the quantitative basis for the heat of reaction. Each of these aspects of their experiments is very important in the accuracy of the work. For example, oxygen is a usual impurity in the OF_2 produced by the present-day method (F_2 + NaOH) and would react with H_2 under the conditions of these experiments. These authors mention no test for oxygen and therefore no correction for its heat of reaction.

The measurements were made in a stationary bomb, using a fairly massive internal container for $OF_2(g)$ which was ruptured to initiate reaction with H_2. The reaction products consisted of H_2O and HF in a condensed phase, formed in the presence of excess $H_2O(l)$. The formation of a homogeneous HF(aq) phase was presumed. However, experience in reactions in which condensation occurs in a stationary bomb indicates that much of the condensation would occur on the walls and would form droplets of a solution quite different from the bulk solution. Mixing these two solutions would evolve heat in addition to that which was measured. The massive OF_2 ampoule could also retain significant quantities of heat for an appreciable time, and the complete equilibration of the heat distribution was not described. Both of these processes would appear to act in the same direction, causing the measured amount of heat to be less than could have been evolved if equilibrium had been achieved. If any errors of these types exist in the experiments, a less negative heat of formation would be indicated for OF_2 than was reported.

The authors wish to acknowledge assistance received from several staff members of the National Bureau of Standards. Mr. James Baylor of the Shops Division made several valuable suggestions for the design of the reaction vessel. Mr. William Dorko and Mr. E. E. Hughes performed the mass spectrometric analyses, and Mr. T. C. Rains performed the analyses for metal ions in the hydrofluoric acid solutions.

8. Appendix

8.1. The Analyses of the Oxidizer Gases

a. Oxygen

The oxygen sample was transferred from the large cylinder to the weighing containers with a manifold of a type also used for filling oxygen combustion bombs [16]. Prior to being filled the container was evacuated and then purged three times with 2–3 atm of oxygen. Finally, the container was filled to about 14 atm. Although further purification probably was unnecessary, during the filling procedure the oxygen was passed through a column of CuO, heated to 500 °C, and through successive columns of Ascarite and magnesium perchlorate.

The oxygen in the weighing bulb was analyzed for argon by mass spectrometry. The concentration of argon was found to be 29 ± 10 parts per million. Nitrogen was determined by gas chromatography using the method reported by Kyryacos and Boord [24]. The equipment consisted of a commercially available chromatograph equipped with an electrically

heated column oven, a thermal conductivity cell, and a strip-chart recording potentiometer (−0.2 to +1.0 mV). Molecular Sieve Type 5A was used as column material with helium as carrier gas. The sample was introduced into the column with a commercial gas sampling valve, modified with a 10-cm³ sample loop. Nitrogen could not be detected in smaller samples. The reliability of the method was checked with one-cm³ samples of air.

The conditions are given on the chromatogram in figure 6. The small effect attributed to nitrogen was quite reproducible, and verified by the injection of air.

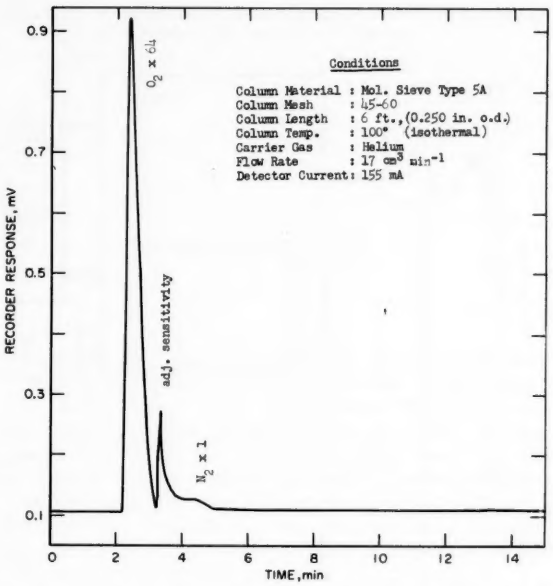

FIGURE 6. *Chromatogram of the oxygen sample on Molecular Sieve Type 5A.*

b. Fluorine

The fluorine was transferred to the spherical sample containers using the manifold and apparatus shown in figure 7. The general procedure for filling the containers consists of (1) evacuating the containers and connecting lines, (2) conditioning and purging the manifold and parts of the connected apparatus with fluorine, (3) filling the bulbs to the desired pressure, and (4) disposing of the fluorine in the connecting lines. To insure that the bulbs were conditioned thoroughly, they were filled repeatedly with a low pressure of fluorine (2 atm), and emptied. Finally they were filled to a working pressure of 13 atm.

Mercury absorption is a well-known technique and has been used extensively for the analysis of fluorine [1, 25, 26]. Although this method appears to be satisfactory, there is some question as to whether the mercury selectively absorbs fluorine from other reactive gases like NF_3 and OF_2 which possibly are present as impurities. These substances may react with mercury under the conditions of the test and produce some N_2 and O_2 which are the major impurities ordinarily contained in fluorine.

The chromatographic procedures developed for analysis of the residual gas are independent of the mass spectrometric method. However, the qualitative identification of the impurities obtained in the latter method is useful for selection of chromatographic column materials.

In addition to the usual chromatographic equipment, the method developed requires (1) a fluorine source, (2) a flask containing mercury for reaction of the fluorine, (3) a loop for containing chromatographic samples of the residual gas, (4) a soda-lime column for disposal of fluorine, and (5) a vacuum source. All of these items were arranged around a manifold as shown in figure 8.

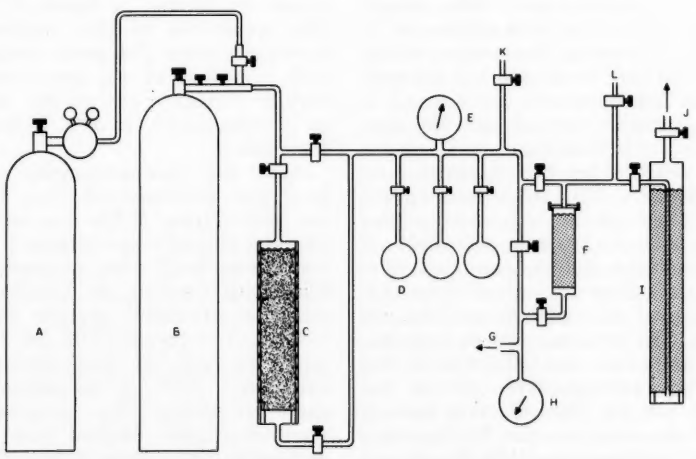

FIGURE 7. *Gas sampling manifold and connected apparatus* (F_2 *and* OF_2).

A, Nitrogen; B, Fluorine or oxygen difluoride; C, Sodium fluoride column; D, Sample bulbs; E, Pressure gauge; F, Fluorine absorption tower; G, Vacuum source; H, Vacuum gauge; I, Fluorine absorption tower; J, Outlet to hood; K, L, to calorimeter flow system.

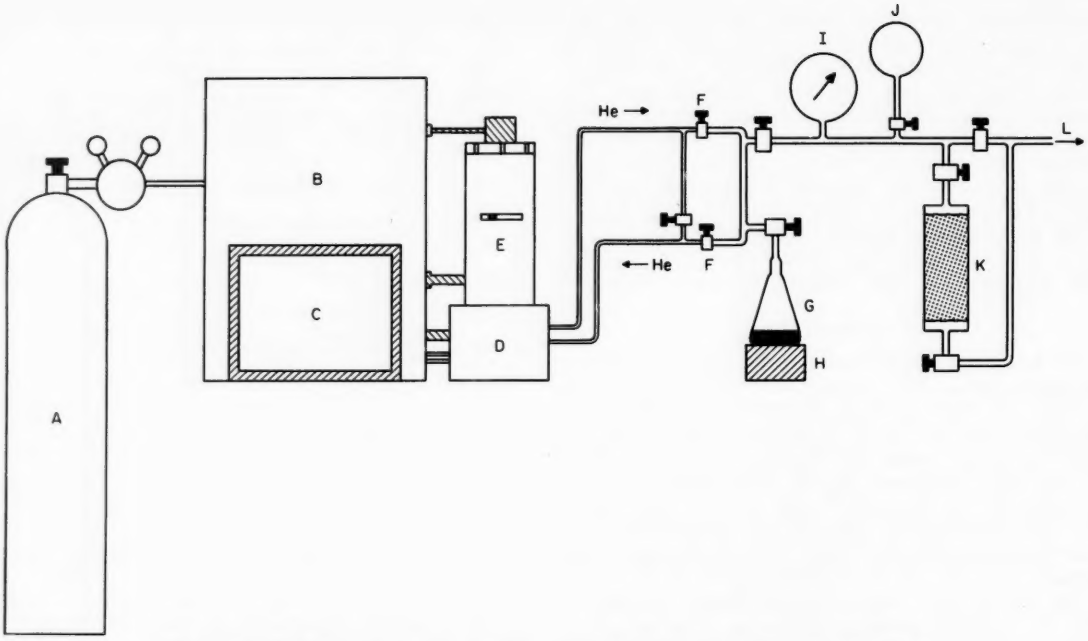

FIGURE 8. *Manifold and apparatus for chromatographic analysis of impurities in fluorine.*
A, Helium; B, Chromatograph; C, Recorder; D, Detector block; E, Column heater; F, Valves; G, Flask with mercury (300-cm³ flask); H, Magnetic stirring motor; I, Vacuum gauge; J, Fluorine sample; K, Fluorine absorption tower; L, Vacuum source.

The equipment preceding valves (F) is ordinarily used in chromatographic analyses and has been described for the oxygen analyses. The steps in the preparation of the system to receive the sample are: (1) close valves (F) and then evacuate remaining parts of system; (2) close flask and admit small amount of fluorine from container (J) for conditioning manifold; and (3) remove fluorine from lines by evacuation through soda-lime column (K). The conditioning procedure is repeated several times. The sample is then introduced by placing one atm of fluorine in the flask. A surface film forms on the mercury which prevents further reaction until the mercury is agitated. The flask contains a Teflon-covered magnet and is placed on a magnetic stirring motor so that the mercury can be agitated with the flask in place. However, to insure complete reaction of the fluorine, it is preferable to disconnect the flask from the manifold so that it can be shaken vigorously by hand. After the fluorine has completely reacted, the flask is reconnected to the manifold and the sample loop is evacuated. Appropriate valves are adjusted so that when the flask is opened the residual gas expands into the sample loop. To introduce the sample into the chromatograph, the valves are adjusted so that the helium from the chromatograph flushes the residual gas into the column. The reaction flask is left in place so that the analyses can be repeated.

Mass spectrometric analyses on other samples of residual gas from commercial fluorine had shown that the major impurities were nitrogen, oxygen, carbon tetrafluoride, and carbon dioxide, with smaller amounts of silicon tetrafluoride, sulfur hexafluoride and fluorocarbons. On this basis Molecular Sieve Type 5A and silica gel were selected for the chromatographic column materials. Molecular Sieve Type 5A, used in the procedure of Kyryacos and Boord [24], separates nitrogen from oxygen, but shows no separation efficiency toward the other impurities. Silica gel [10] separates oxygen plus nitrogen from the carbon tetrafluoride and carbon dioxide. Typical chromatograms are shown in figures 9 and 10, respectively. The conditions for the analyses are given on the chromatograms. The peak components were checked with injections of air, pure carbon tetrafluoride and carbon dioxide. Prior to the analyses both columns were conditioned at 300 °C under a flowing helium atmosphere.

After the chromatographic analyses, the sample loop was disconnected from the chromatograph at the two valves, F. On one valve a Pyrex breakoff-tip type ampoule was attached, and the ampoule and connecting lines were evacuated. The ampoule was filled with residual gas from the flask and sealed. A mass spectrometric analysis was performed on this sample. The results from the two methods are compared in table 15. Considering that these are two completely different techniques, the results are in good agreement. This agreement suggests that the chromatographic method may be developed further and used routinely as a second way of analysing for the impurities in ordinary commerical fluorine, which is usually reported to be of a purity of not better than 98 percent.

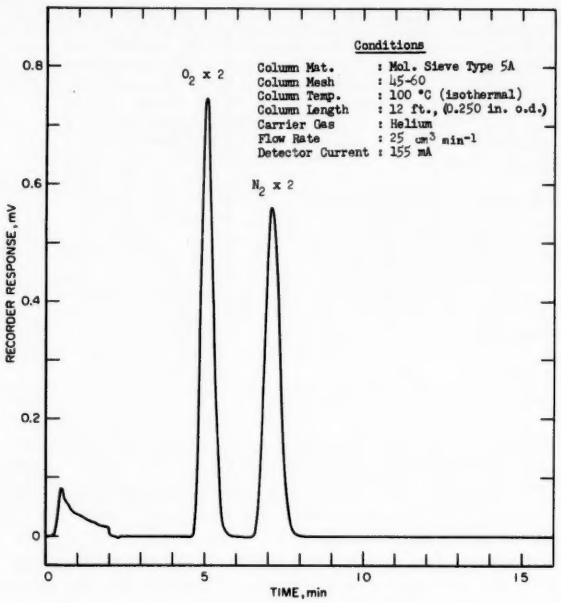
Conditions
Column Mat. : Mol. Sieve Type 5A
Column Mesh : 45-60
Column Temp. : 100 °C (isothermal)
Column Length : 12 ft., (0.250 in. o.d.)
Carrier Gas : Helium
Flow Rate : 25 cm³ min⁻¹
Detector Current : 155 mA
O2 x 2
N2 x 2
RECORDER RESPONSE, mV
TIME, min

FIGURE 9. *Chromatogram of impurities in the fluorine sample on Molecular Sieve Type 5A.*

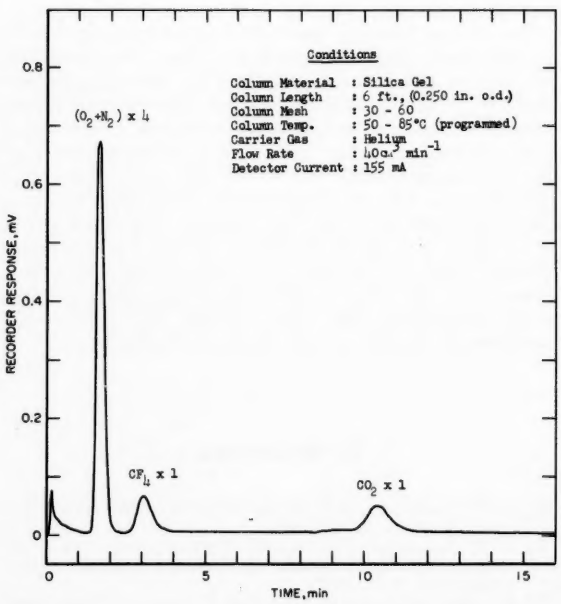
Conditions
Column Material : Silica Gel
Column Length : 6 ft., (0.250 in. o.d.)
Column Mesh : 30 - 60
Column Temp. : 50 - 85°C (programmed)
Carrier Gas : Helium
Flow Rate : 40 cm³ min⁻¹
Detector Current : 155 mA
(O2+N2) x 4
CF4 x 1
CO2 x 1
RECORDER RESPONSE, mV
TIME, min

FIGURE 10. *Chromatogram of Impurities in the fluorine sample on silica gel.*

The data in tables 1 and 15 show a difference between the relative amounts of oxygen and nitrogen in the residual gas in the flask used for chromatography, compared to the residual gas used from the

TABLE 15. *Comparison of chromatographic and mass spectrometric analyses for impurities in fluorine*

Impurity	Mole percent of total impurities	
	Chromatography	Mass spectrometry
N_2	45.	42.6
O_2	47.	47.7
CF_4	3.6	2.8
CO_2	4.6	5.1
SO_2F_2		0.22
Ar		.2
SiF_4		1.1
C_2F_6		0.21
C_3F_8		.04

spherical bulbs. The larger amount of oxygen impurity in the Erlenmeyer flask suggests that some oxygen may have arisen from the mercury because there was 1000g mercury in the Erlenmeyer flask, as compared to 150g of mercury in the flask used for the analysis given in table 1. There is reason to believe that the analysis can be improved by conditioning the mercury and flask surfaces also with a small amount of fluorine, prior to filling the flask with the one atmosphere of gas needed for the analysis.

c. Oxygen Difluoride

The oxygen difluoride was transferred to the sample containers using the same manifold and equipment shown in figure 7. The procedures used were the same as those used in sampling the fluorine, except that the oxygen difluoride was not passed over the sodium fluoride. The sample containers were filled to approximately 8 atm with OF_2.

An infrared spectrum of the oxygen difluoride sample was made and compared with spectra in the literature [27, 28]. The cell was Pyrex with silver chloride windows. The windows were clamped in place and sealed to the cell with Kel-F O-rings. The spectrum is shown in figure 11. An absorption band presumed to be due to the impurity CF_4, is indicated.

The equipment used for the chromatographic analyses already has been described for the oxygen and fluorine analyses. The OF_2 sample container is connected to a loop which can be purged with helium from the chromatograph. Silica gel was used for the column material. Prior to the analyses, the column was conditioned at 350° for one hour under a flowing helium atmosphere. The other conditions for the analyses are given on figures 12 and 13 which show the chromatograms obtained.

In the complete chromatogram, four peaks were obtained. These were verified to be due to O_2 (or air), OF_2, CF_4, and CO_2. Analyses were made with the column temperature at 0° and 50 °C. At 0 °C nearly complete separation was achieved between the O_2 and OF_2 (figure 12), but the CO_2 peak was either very slurred or the fraction did not elute at this temperature. At 50 °C, the separation between the O_2 and OF_2 was poor but separation and elution of CO_2 could be obtained by temperature programming. After elution of the O_2 and OF_2, the column was temperature-programmed to a final temperature of 150 °C for

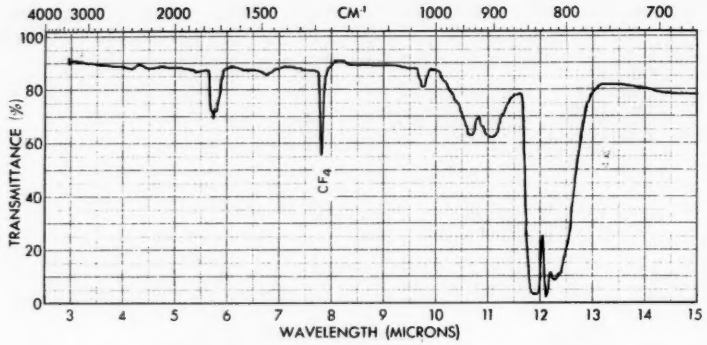

FIGURE 11. *IR spectrum of the* OF_2 *sample.*
Note CF_4 band at 780 microns.

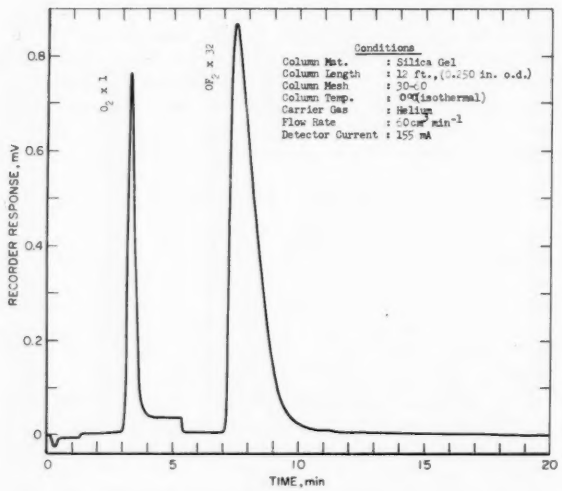

FIGURE 12. *Chromatogram of the* OF_2 *sample on silica gel (0 °C).*

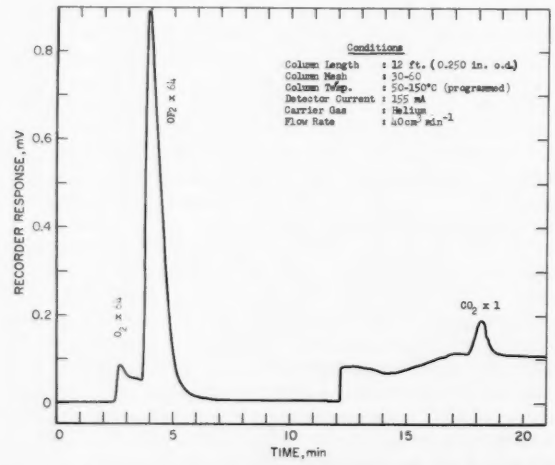

FIGURE 13. *Chromatogram of the* OF_2 *sample on silica gel (50 °C).*
(The column was programmed to 150 °C beginning at 12 mins.)

elution of the CO_2 (fig. 13). In agreement with Kesting's observations [10], the CF_4 eluted on the "tail" of the OF_2 fraction. The CF_4 peak was evaluated from other chromatograms obtained with the instrument set on the most sensitive scale.

Repeated analyses were made on several bulb fillings and the results were quite reproducible. We accepted the findings of Kesting, et al. [10], that the peak area percent for the observed components (OF_2, CO_2, O_2, CF_4) was very nearly equal to mole percent. The peak areas were evaluated both analytically and by counting squares.

Several preliminary analyses were carried out before a procedure was accepted for these experiments. Because of the reactivity of the OF_2, it is conceivable that OF_2 reacts with the silica gel. During preliminary analyses at various column temperatures, it was noted that extraneous peaks appeared at a temperature of 75 °C, and also that even at 50°, the mole percent of OF_2 decreased while the mole percent of O_2 increased. These preliminary analyses suggest that silica gel is not a generally useful column material for chromatographic analyses of the reactive inorganic fluorides. However, under the proper conditions silica gel has good separation efficiency toward OF_2 and inert component impurities such as O_2 and CF_4.

9. References

[1] G. T. Armstrong and R. S. Jessup, J. Res. NBS **64A** (Phys. and Chem.) No. 1, 49 (1960).
[2] G. T. Armstrong, Experimental Thermochemistry, Vol. II., Ch. 7, ed. H. A. Skinner (Interscience Publishers, Inc., New York, N.Y., 1962).
[3] H. v. Wartenberg and G. Z. Klinkott, Z. anorg. u. allgem. Chem. **193,** 409 (1930).
[4] O. Ruff and W. Menzel, Z. anorg. u. allgem. Chem. **190,** 257 (1930).
[5] W. H. Evans, T. R. Munson, and D. D. Wagman, J. Res. NBS **55,** 147 (1955) RP2614.
[6] R. C. King and G. T. Armstrong, Interagency Chemical Rocket Propellant Group, Thermochemistry Working Group, Bulletin of the Fifth Meeting March 15–17, 1967, Vol. 1., Chemical Propulsion Information Agency, Publication CPIA No. 146, pp. 69–96, May 1967.

[7] JANAF Thermochemical Tables, PB 168370, Dow Chemical Co., Midland, Michigan (Clearinghouse for Federal Scientific and Technical Information, Springfield, Va., August 1966).
[8] D. D. Wagman, W. H. Evans, I. Halow, V. B. Parker, S. M. Bailey, and R. H. Schumm, Selected Values of Chemical Thermodynamic Properties, Part 1. Tables for the First Twenty-Three Elements in the Standard Order of Arrangement, NBS Tech. Note 270–1 (U.S. Government Printing Office, Washington, D.C. 20402, 1965).
[9] W. R. Bisbee, J. V. Hamilton, R. Rushworth, T. J. Houser, and J. M. Gerhauser, Advan. Chem. Ser. **54,** 215 (1965).
[10] W. R. Kesting, General Chemical Division, Allied Chem. Corp., Baton Rouge, La., private communication; W. R. Kesting, J. E. Crosslin, and B. W. Bridwell, Analysis of Oxygen Difluoride, Report of the Analytical Chemistry Working Group, 22nd Meeting, ed., John W. Gunn, Jr. (Chemical Propulsion Information Agency, Nov. 3, 1965.)
[11] J. C. Brosheer, F. A. Lenfesty, and K. L. Ellmore, Ind. Eng. Chem. **39,** 423 (1947).
[12] H. C. Dickinson, Bull. BS **11,** 189 (1915).
[13] E. J. Prosen, W. H. Johnson, and F. Y. Pergiel, J. Res. NBS **62,** 43 (1959) RP2927.
[14] E. D. West and D. C. Ginnings, Rev. Sci. Instr. **28,** 1070 (1957).
[15] D. C. Ginnings and E. D. West, Rev. Sci. Instr. **35,** 965 (1964).
[16] K. L. Churney and G. T. Armstrong, submitted for publication J. Res. NBS.
[17] C. H. Shomate, Computer Calculations of Combustion Bomb Calorimetric Data, Technical Progress Report 327, NOTS TP 3288, U.S. Naval Ordnance Test Station, China Lake, Calif., August 1963.
[18] A. E. Cameron and E. Wichers, J. Am. Chem. Soc. **84,** 4175 (1962).
[19] N. S. Osborne, H. F. Stimson, and D. C. Ginnings, J. Res. NBS **23,** 197 (1939) RP1228.
[20] T. Thorvaldson and E. C. Bailey, Can. J. Res. **24,** 51 (1946).
[21] F. D. Rossini, J. Res. NBS **6,** 1 (1931) R.P.259; see also Chapter 4 Experimental Thermochemistry, ed. F. D. Rossini (Interscience Publishers, Inc., New York, N.Y., 1956).
[22] E. Rudzitis, E. H. Van Deventer, and W. N. Hubbard, J. Chem. Eng. Data **12,** 133 (1967).
[23] W. H. Evans, National Bureau of Standards, private communication.
[24] G. Kyryacos and C. E. Boord, Anal. Chem. **29,** 787 (1957).
[25] L. A. Bigelow, Chem. Revs. **40,** 110 (1947).
[26] H. Schmitz and H. J. Schumacher, Z. anorg. u. allgem. Chem. **245,** 221 (1940).
[27] H. J. Bernstein and J. Powling, J. Chem. Phys. **18,** 685 (1950).
[28] E. A. Jones, J. S. Kirby-Smith, P. J. H. Woltz, and A. H. Nielsen, J. Chem. Phys. **19,** 337 (1951).

(Paper 72A2–487)

JOURNAL OF RESEARCH of the National Bureau of Standards—A. Physics and Chemistry
Vol. 72A, No. 2, March–April 1968

The Heat of Formation of Boron Carbide[1]

E. S. Domalski and G. T. Armstrong

Institute for Basic Standards, National Bureau of Standards, Washington, D.C. 20234

(October 28, 1967)

The standard heat of combustion in fluorine of a boron carbide sample having the composition $B_{4.222}C$ was determined from the heats of combustion of polytetrafluoroethylene and of boron carbide-polytetrafluoroethylene mixtures. The energy of the combustion reaction was measured in an isothermal-jacket bomb calorimeter. From the experimental data, we calculate -17.1 kcal mol^{-1} for the heat of formation of boron carbide. By combining all probable errors, we estimate our overall experimental uncertainty to be 2.7 kcal mol^{-1}. The value for the heat of formation of boron carbide is for the phase represented by the formula $B_{4.222}C$.

Key Words: Bomb calorimeter, boron carbide, boron trifluoride, carbon tetrafluoride, heat of combustion, heat of formation, polytetrafluoroethylene.

1. Introduction

The determination of the heat of combustion of boron carbide in oxygen by Smith, Dworkin and van Artsdalen [1] [2] appears to be the only previous work reliable enough to use in deriving a value for the heat of formation of B_4C. Using bomb calorimetric techniques, these authors carried out reaction (1).

$$B_4C(c)+4O_2(g)=2B_2O_3(\text{amorphous})+CO_2(g) \quad (1)$$

They obtained -683.8 ± 2.2 kcal mol^{-1} for the heat of combustion. Using amorphous boron as a reference state and taking -301.75 kcal mol^{-1} for the heat of formation of amorphous B_2O_3 [3] they calculated for $\Delta H^\circ_{f298}[B_4C(c)]$, -13.8 ± 2.7 kcal mol^{-1}. The degree of completeness of combustion was not large, ranging from 21 to 41 percent B_4C burned. They found that when the amounts of B_2O_3 and CO_2 produced in the combustion were measured, a deficiency in the carbon dioxide was observed. The authors assumed that some of the carbon in their boron carbide sample failed to burn and remained behind as free carbon.

More recently several authors have referred the heat of formation to crystalline boron. Several different values for ΔH°_{f298} [$B_4C(c)$] have been suggested, based on the combustion data of Smith, Dworkin, and van Artsdalen, but differing in the values attributed to the heats of transition of amorphous to crystalline boron, and the heat of formation of amorphous B_2O_3. The value -12.2 kcal mol^{-1}, which was for a time widely used, is based on $\Delta H^\circ_{f298}[B(am)]=0.4$ kcal mol^{-1}, and the same value for $\Delta H^\circ_{f298}[B_2O_3(am)]$ as was used by Smith, Dworkin, and van Artsdalen.

The JANAF Thermochemical Tables [3] give -9.3 kcal mol^{-1} for the heat of formation of B_4C using the same combustion data, and other appropriately chosen data from within the JANAF compilation to perform the calculation. Other values have been reported for the heat of formation of B_4C [4–8], but because of their obscurity of source or lack of experimental detail, they cannot be readily discussed here.

We have undertaken the measurement of the heat of combustion of B_4C in fluorine as a route to the determination of its heat of formation. Due to the lack of completeness of combustion in the work of Smith, Dworkin, and van Artsdalen [1], and certain assumptions made in their treatment of the experimental data, we felt a redetermination by another method was warranted. Combustion in fluorine offers the distinct advantage of giving gases for all major reaction products. In addition, a procedure was available for the combustion of refractory compounds which had given a large degree of completeness of combustion for several substances [9].

2. Materials

The sample of boron carbide was obtained from the Carborundum Company as a fine powder having a maximum particle size of 75μ. The sample was analyzed and the results are shown in table 1. The analyses for boron, carbon, and metallic impurities were performed using appropriate wet chemical and instrumental methods. The nitrogen content was

[1] This research was sponsored by the Air Force Aero Propulsion Laboratory, Research and Development Division, Air Force Systems Command, Wright-Patterson Air Force Base, Ohio, under USAF Delivery Order No. 33(615)64-1003, and by the Air Force Office of Scientific Research under Order No. OAR ISSA 65-8.

[2] Figures in brackets indicate literature references at the end of this paper.

[3] $\Delta H^\circ_{f298}[B_2O_3(am)]=-301.75$ kcal mol^{-1} was a preliminary value, and in a later publication [2] was changed to -301.78 kcal mol^{-1}.

TABLE 1. *Analysis of boron carbide (percent by weight)*

Elemental analysis [a]		Assumed composition [b]		
[c] B(78.26%)	78.29	$B_{4.222}C$	99.015	.....
[c] C(21.74%)	20.60	B_4C	.....	94.871
		B	.....	4.144
Al	[d] 0.005	Al	0.005	
Ca	[d] 0.004	Ca	0.004	
Cu	[d] < 0.001	Cu	0.001	
Fe	[d] 0.008	Fe	0.008	
Mg	[d] < 0.001	Mg	0.001	
Mn	[d] < 0.001	Mn	0.001	
Si	0.023	Si	0.023	
Zr	[d] 0.004	Zr	0.004	
Ti	[d] < 0.001	Ti	0.001	
O	[e] 0.375	B_2O_3	0.563	
N	0.21	BN	0.374	
Total	99.523	Total	100.00	

[a] Unless otherwise stated the elemental analyses were performed by the NBS Analysis and Purification Section.
[b] The assumed composition was obtained from the elemental analysis after the latter was normalized.
[c] Theoretical for B_4C.
[d] Analysis by the supplier.
[e] Analysis by Ledoux & Company.

determined by the Kjeldahl method and the oxygen analysis was made by the inert-gas fusion method.

Preliminary analyses of the sample at NBS for boron and carbon showed not only poor agreement among individual determinations but also poor agreement with the analysis provided by the supplier. After a thorough study was made of the past analytical work performed on the sample, a final analysis for boron and carbon was obtained by the NBS Analysis and Purification Section, and appears in the second column of table 1. Three determinations of the boron content had an average deviation of 0.06 percent, and five determinations of carbon had an average deviation of 0.03 percent.

The total elemental analysis of 99.523 was normalized and we assumed the metallic impurities to be present as the elements. The oxygen and nitrogen were assumed to be present as B_2O_3 and BN, respectively. Calculation of the boron to carbon ratio shows the stoichiometry to be $B_{4.222}C$, slightly below carbon-saturated boron carbide. Interpretation of the actual boron carbide phase present will be discussed in Section 8.2.

The B_4C sample was examined using x-ray techniques by the NBS Crystallography Section and was found to have the following hexagonal lattice constants: $a = 5.599$ Å and $c = 12.08$ Å; in good agreement with existing data ($a = 5.60$ Å and $c = 12.12$ Å [10]). Examination of the x-ray pattern at NBS and at another laboratory [4] revealed no lines attributable to graphite or crystalline boron. Samples of boron carbide that are boron rich show significantly larger lattice constants [11] than those observed for our sample, indicating the stoichiometry of our sample to be very close to carbon-saturated boron carbide.

The polytetrafluoroethylene powder ("Teflon 7") and polytetrafluoroethylene film (FEP Fluorocarbon film, type A) used in preparing mixtures for the combustion measurements were described in an earlier publication [12]. Neither the polytetrafluoroethylene powder nor film was modified or treated in any special way prior to use. The energy of combustion, ΔE°_{303}, of the polytetrafluoroethylene film and powder was $-10{,}372.8 \pm 3.1$ J g^{-1}. The uncertainty cited was the overall experimental error. The fluorine used in the heat measurements was found to be 99.40 percent F_2. The analysis was performed by absorbing the fluorine in mercury and observing the pressure of the residual gases [13]. The composition of the residue was determined by examination in a mass spectrometer as previously reported [14].

3. Preparation of Sample Pellets

Attempts to prepare suitable pellets of boron carbide for a combustion measurement without the aid of an auxiliary material were not successful because of the extreme hardness of B_4C. A composite, capable of being pelleted, was obtained by adding polytetrafluoroethylene powder to boron carbide powder which had been introduced into a thermosealable polytetrafluoroethylene bag. The powders were mixed until reasonable homogeneity had been obtained and the bagged mixture was pressed into pellet form. An additional coating of polytetrafluoroethylene was provided around the pellet as a precaution to preclude the possible reaction with fluorine in the combusion bomb prior to the time of ignition. The preparative procedures have been described in detail (methods A and B) in an earlier paper [12].

Much care is needed in keeping track of the cumulative mass of the sample as the polytetrafluoroethylene and boron carbide powders are added because some losses are always observed and their distribution affects the results of the experiment significantly. Average masses for the components of a coated pellet were as follows: polytetrafluoroethylene bag, 0.3 g; polytetrafluoroethylene powder, 1.90 g; B_4C powder, 0.18 g; polytetrafluoroethylene coating, 0.7 g; loss of polytetrafluoroethylene in sealing the bag, 0.21 mg; loss of mixture in pelleting, 0.20 mg.

The densities used for the polytetrafluoroethylene film, polytetrafluoroethylene powder, and B_4C in making buoyancy corrections were 2.15, 2.16, and 2.52 g cm^{-3} [15], respectively. Weighings of pelleted mixtures and intermediate stages were made to 0.01 mg.

4. Calorimetric System

No major changes had been made in the bomb calorimeter, thermometric system or combustion bomb since our earlier work [12] which was carried out with the same apparatus. The apparatus will be discussed here only briefly.

[4] We thank P. W. Gilles, University of Kansas, Lawrence, Kansas, for his assistance in the x-ray examination of our sample for graphite (Aug. 1966).

An isothermal-jacket, stirred-water calorimeter was used for these measurements. The jacket was maintained at a constant temperature near 30 °C to within 0.002 °C. Temperature changes in the calorimeter were measured to 0.0001 °C with a G–2 Mueller bridge in conjunction with a platinum-resistance thermometer. Reactions were carried out in an "A" nickel combustion bomb (volume, 360 cm^3), designed for service with fluorine. Two aluminum electrodes each suspended from the bomb head by a monel rod held a tungsten fuse (0.002 in diam) which contributed about 20 J to the combustion energy, assuming complete combustion. The electrical energy for ignition of the fuse was assumed to be negligible. The quantities of boron carbide and polytetrafluoroethylene in the pellets were adjusted to produce a temperature rise in the calorimeter of about three degrees (27 to 30 °C). For procedures dealing with the loading and emptying of the combustion bomb, and for details of the design and construction of the fluorine manifold, our earlier work should be consulted [16].

5. Products of Combustion

Our previous work [12, 16] has established that polytetrafluoroethylene burns in 15 to 21 atm of fluorine to carbon tetrafluoride as the only major product. Higher fluorocarbons were not detected in amounts greater than 0.02 mole percent. The product gases from representative experiments were analyzed in a mass spectrometer after absorption of the excess fluorine in mercury.

The mass spectrometric examination of product gases from the combustion of a pelleted mixture of boron carbide and polytetrafluoroethylene showed no sign of boron trifluoride. This was similar to the results observed when product gases from the combustion of a pelleted mixture of boron and polytetrafluoroethylene were examined. In both cases, we suspect that under the conditions of the reaction of fluorine with mercury, an interaction of some kind takes place between BF_3 and the mercury fluoride formed during the absorption of fluorine. In other respects the mass spectra appeared comparable to those observed showing carbon tetrafluoride to be the only major product when only polytetrafluoroethylene is burned in fluorine.

Boron trifluoride was identified as a combustion product by infrared spectrometry. Examination in the region 400 to 650 cm^{-1} of a sample of the bomb product gases containing excess fluorine revealed the BF_3 band at 481 cm^{-1} and the CF_4 band at 630 cm^{-1}. Spectra of the evacuated cell and of BF_3 alone were taken over the region mentioned above to substantiate the identification. The cell used was 8 cm long and had polyethylene windows 0.0625 in thick.

6. Calibration Experiments

Twenty calibration experiments were performed in which benzoic acid (Standard Sample 39i) was burned in 30 atm of oxygen and with one cm^3 of distilled water in the nickel combustion bomb. Their consistency and reproducibility have been discussed in our earlier paper [12]. The average energy equivalent was calculated to be 14,803.27 ±2.07 J deg^{-1}. The uncertainty cited was obtained by multiplying the standard deviation of the mean by the appropriate factor in the Student t distribution at the 95 percent confidence level. The energy equivalent is that of the standard initial oxygen-combustion calorimeter which included the nickel combustion bomb with 30 atm of oxygen, a platinum crucible and fuse support wires, platinum fuse (2 cm long, 0.01 cm diam), a stainless-steel (type 304) liner, 1 cm^3 of distilled water, monel pellet holder, and no sample. Fastened to the bomb were a heater and ignition leads. The mass of the calorimeter vessel and water was 3750.0 g. The calorimetric data obtained in the calibration experiments were programmed for the IBM 7094 computer according to the procedure outlined by Shomate [17].

With the appropriate heat capacity data, the energy equivalent of the standard oxygen-combustion calorimeter was adjusted to the proper value for the fluorine experiments. This involved allowing for the heat capacities of 30 atm of oxygen, 1 cm^3 of distilled water, the platinum ware, 21 atm of fluorine, and two aluminum electrodes. The application of these corrections gave 14,805.17 J deg^{-1} for the energy equivalent of the standard initial fluorine combustion calorimeter for the temperature range used (27 to 30 °C).

7. Fluorine Combustion Experiments

Eight calorimetric measurements were made in which pellets of boron carbide and polytetrafluoroethylene were burned in 21 atm of fluorine. These measurements are summarized in table 2. In each experiment the sample pellet was placed in the recess of an "A" nickel plate on the bottom of the bomb. The bomb was attached to the fluorine manifold and filled to 21 atm with fluorine by the usual procedure. All bomb parts (bomb base, bomb-head assembly, electrodes, liner and nickel plate) were weighed before the first experiment and after each successive experiment. The bomb parts were washed with water and dried before the weighings were made.

The calorimetric data also included seven experiments, which have been previously reported in detail [12], in which polytetrafluoroethylene was burned in 21 atm of fluorine. The value listed in section 2 for the energy of combustion, ΔE°_{303}, was determined in these experiments.

The numbered entries in table 2 are as follows:

(1a) mass of the boron carbide sample in the pellet, corrected for weight loss in preparation and for recovery of unburned sample.

(1b) mass of polytetrafluoroethylene in the pellet, corrected for weight loss.

(2) pressure of fluorine introduced into the bomb prior to combustion, corrected to 30 °C.

(3) energy equivalent of the calorimeter for a given experiment.

(4) temperature change of the calorimeter thermom-

TABLE 2. *Boron carbide-"Teflon 7" combustion experiments*

Experiment No.	1	2	3	4	5	6	7	8
(1a) $m(B_4C$ sample)....g	0.201948	0.184980	0.178836	0.179005	0.182011	0.172072	0.178745	0.168138
(1b) m("Teflon 7")....g	2.775820	2.738097	2.776954	2.709381	3.028289	2.895316	2.806986	3.123387
(2) $P(F_2)$....atm	21.5	21.7	22.1	21.3	21.4	22.3	21.1	21.3
(3) ϵ....J deg^{-1}	14,800.14	14,804.85	14,804.13	14,799.56	14,805.42	14,800.13	14,804.42	14,804.25
(4) Δt_c....deg	3.27109	3.13267	3.11938	3.07716	3.31773	3.16025	3.14252	3.29554
(5) $(\epsilon)(-\Delta t_c)$....J	−48,412.6	−46,378.7	−46,179.7	−45,540.6	−49,120.4	−46,772.1	−46,523.2	−48,788.0
(6) ΔE(fuse)....J	18.5	17.4	18.6	17.5	20.3	20.4	20.4	18.8
(7) ΔE(gas)....J	13.1	12.9	13.3	12.5	13.9	14.0	12.9	14.5
(8) ΔE°("Teflon 7")....J	28,793.0	28,401.7	28,804.8	28,103.9	31,411.8	30,032.5	29,116.3	32,398.3
(9) $\Delta E^\circ_{303}(B_4C$ sample)....J g^{-1}	−96,995.3	−97,019.7	−96,977.1	−97,241.4	−97,106.2	−97,082.6	−97,197.7	−97,279.6

(10) $\Delta E^\circ_{303}(B_4C$ sample)$= -97{,}112.5$ J g^{-1}
(11) Std. dev. mean $= 40.8$ J $g^{-1} = 0.5$ kcal mol^{-1}
(12) $\Delta E^\circ_{298} - \Delta E^\circ_{303} = 1.1$ J g^{-1}
(13) $\Delta E^\circ_{298}(B_4C$ sample)$= -97{,}111.4$ J g^{-1}

eter, corrected for heat of stirring and heat transfer.
(5) total energy change in the bomb process.
(6) energy liberated by the tungsten fuse assuming the fuse burns according to the reaction:

$$W(c) + 3F_2(g) = WF_6(g).$$

From the heat of formation of WF_6 [18], we calculate 9.44 J mg^{-1} for the energy of combustion of the fuse.
(7) net energy correction for the hypothetical compression and decompression of bomb gases.

$$\Delta E(\text{gas}) = \Delta E^i(\text{gas}) \Big]_0^{P_{i(\text{gas})}} + \Delta E^f(\text{gas}) \Big]_0^{P_{f(\text{gas})}}$$

(8) standard energy of combustion of polytetrafluoroethylene per gram at 30 °C multiplied by the corrected mass of polytetrafluoroethylene in the pellet.
(9) standard energy of combustion of the sample, per gram.
(10) average standard energy of combustion of the sample, per gram.
(11) standard deviation of the mean of the average cited in (10).
(12) correction based on heat capacities, converting the reference temperature to 298 °K.
(13) standard energy of combustion at 298 °K, not corrected for impurities.

The heat capacities at constant pressure, C_p, used in the calculation of entries (3) and (12) are as follows in cal deg^{-1} g^{-1} at 298 °K; boron carbide, 0.23 [3]; and polytetrafluoroethylene, 0.28 [19]. The heat capacities at constant volume, C_v, used in the calculation of entries (3) and (12) were 5.52 [20], 12.62 [21], and 10.04 [22] cal deg^{-1} mol^{-1}, respectively, for fluorine, carbon tetrafluoride, and boron trifluoride at 303 °K.

Washburn corrections, entry (7) were calculated following the procedure outlined by Hubbard [23] for experiments in which fluorine is used as the oxidant. The coefficients $[\partial E/\partial P]_T = -T[dB/dT]$ were found in tables (based on a Lennard-Jones 6–12 potential function) as compiled by Hirschfelder, Curtiss, and Bird [24] using the appropriate force constants. The force constants used for fluorine, carbon tetrafluoride, and boron trifluoride were those determined by White, Hu, and Johnston [25], Douslin [26], and Brooks and Raw [27], respectively. Force constants appropriate to the mixtures of F_2, CF_4 and BF_3 in the reaction products were calculated from those for the pure components.

In calculating the corrections for the combustion of other impurities in the boron carbide sample (see Section 8.2) the following values for the heats of formation of various substances were used, and are given in kcal mol^{-1}: B_2O_3, −304.20 [28]; BN, −60.8 [28]; AlF_3, −361.0 [12, 16]; CaF_2, −290.3 [29]; CuF_2, −126.9 [29]; FeF_3, −235 [30]; MgF_2, −268.7 [31]; MnF_3, −238 [30]; SiF_4, −385.98 [32]; ZrF_4, −456.80 [33]; TiF_4, −394.19 [34].

The combustion experiments were programmed for machine calculation in the same way as the calibration experiments. However, the only valid data calculated by the computer were the corrected temperature rises, Δt_c, because the program had not been modified to accommodate the use of fluorine as the oxidant.

Atomic weights were taken from the 1961 table of atomic weights, based on $^{12}C = 12$, adopted by the International Union of Pure and Applied Chemistry [35]. The unit of energy is the joule and we use the calorie defined as 4.1840 J.

8. Discussion and Results

8.1. Analysis of Combustion Residues

A residue amounting to less than one mg, which was assumed to be unburned polytetrafluoroethylene and/or carbon, was observed in experiments involving polytetrafluoroethylene alone. No correction was applied to any experiment for this residue, and we assumed that the formation of the residue took place in all experiments approximately in proportion to the amount of polytetrafluoroethylene initially present. The heat of combustion per gram of polytetrafluoroethylene would be constant and the error due to residue formation would be eliminated when the energy due to the combustion of polytetrafluoroethylene in the pelleted mixture was subtracted from the total energy released in the combustion.

After a combustion experiment on pelleted mixtures of boron carbide and polytetrafluoroethylene, a residue was found on the nickel support plate. The mass of the residue was determined by weighing the plate

before and after an experiment. The average mass found from these weighings was 1.0 mg, of which 0.13 to 0.19 mg was estimated to be boron carbide on the basis of the amount of boron found in it. The manner in which the residue was gathered from the nickel plate and analyzed for boron was the same as with the boron-polytetrafluoroethylene combustion residues [14]. Analyses of known masses of boron carbide by this method showed good reproducibility and no bias in the determination of boron. Observations made on the nickel plate after combustion residues had been gathered showed small globules of melted tungsten adhering to the plates. We estimate this mass contribution from the spattering of molten tungsten from ignition of the fuse to be 0.8 mg per experiment [12]. Other effects likely to contribute to the composition of the combustion residue are hygroscopicity of the residue and reaction of the nickel plate with fluorine. However, these effects are presumably small and slow, and no corrections have been made for them.

A non-calorimetric combustion of a pelleted mixture of boron carbide and polytetrafluoroethylene was performed after which the residue was analyzed for its carbon content. The amount found was 0.08 mg, which is comparable to the amount of carbon found in a residue when only polytetrafluoroethylene is burned in fluorine [12].

8.2. The Heat of Formation of Boron Carbide

The calculation of the heat of formation of boron carbide is shown in detail in table 3. Two calculations are given. In one we assume that the boron carbide

TABLE 3. *Calculation of the heat of formation of boron carbide*

	$B_{4.222}C$	B_4C
1. stoichiometry of boron carbide		
2. ΔE°_{298} (B_4C sample), J g^{-1}	−97,111.4	−97,111.4
3. Corrections for impurities (except B)	234.2	234.2
4. Correction for excess boron	.....	4,342.0
5. Fraction of sample present as boron carbide	0.99015	0.94871
6. ΔE°_{298} (Reaction 2), J (g, boron carbide)$^{-1}$	−97,840.9	−97,537.9
7. ΔnRT, J (g, boron carbide)$^{-1}$	−133.8	134.6
8. ΔH°_{298} (Reaction 2), J (g, boron carbide)$^{-1}$	−97,974.7	−97,672.5
9. ΔH°_{298} (Reaction 2), kcal mol^{-1}	−1,350.1	−1,289.9
10. ΔH°_{f298} (boron carbide), (Reaction 3), kcal mol^{-1}	−17.1	−17.1
11. ΔH°_{f298} (combustion products), kcal mol^{-1}	−1,367.2	−1,307.0

phase is non-stoichiometric as implied by the chemical analysis ($B_{4.222}C$). In the other we assume that the sample is stoichiometric B_4C with an excess of elemental boron, sufficient to make the total boron to carbon ratio 4.222. The datum in row 2 of table 3 is the uncorrected energy of combustion of the boron carbide sample taken from table 2, entry (13). The corrected energy of combustion of boron carbide of the assigned stoichiometry (row 6) is obtained by subtracting the corrections for the impurities and excess boron (rows 3 and 4) from row 2, and dividing the remainder by the fraction of the sample present as boron carbide (row 5). Addition of the ΔnRT term (row 7) to the corrected energy of combustion gives the heat of combustion (row 8). The combustion processes for the two limiting stoichiometries assigned are given by reactions (2a) and (2b).

$$B_{4.222}C(c) + 8.333\ F_2(g) = 4.222\ BF_3(g) + CF_4(g) \quad (2a)$$

$$B_4C(c) + 8\ F_2(g) = 4\ BF_3(g) + CF_4(g) \quad (2b)$$

$$4.222\ B(c) + C(c, \text{graphite}) = B_{4.222}C(c) \quad (3a)$$

$$4B(c) + C(c, \text{graphite}) = B_4C(c) \quad (3b)$$

The data presented in row 9 are equivalent to that in row 8 except the units are kcal mol^{-1} instead of J g^{-1}. With the aid of our previously determined values for the heats of formation of carbon tetrafluoride, −222.87 kcal mol^{-1} [12] and boron trifluoride, −271.03 kcal mol^{-1} [14], the sum of the heats of formation of the products (row 11) is calculated. The heat of formation of boron carbide (row 10) is obtained as the difference between the sum of the heats of formation of the combustion products (row 11) and the heat of combustion (row 9). The two calculations, referring respectively to reactions (3a) and (3b) give exactly the same result for the heat of formation of boron carbide, −17.1 kcal mol^{-1}, and do not indicate a preferred representation. The identity of the results of the two methods of calculation is due to the fact that excess free elemental boron has a zero heat of formation. This duality in the calculation could be extended to any data on the heats of formation of nonstoichiometric binary compounds in which there is ambiguity with respect to the nature of the nonstoichiometry.

The absence of any lines in the x-ray spectrum of our sample attributable to crystalline boron causes us to reject the calculation involving free elemental boron, and to favor the nonstoichiometric formula, $B_{4.222}C$, as representative of the heat measurements. A quantity as large as 4.144 percent free crystalline boron in the boron carbide sample should have been observed in the x-ray spectrum even though this value is close to the limit of detectability of the method (1 to 3 percent). No definitive remarks are possible regarding the presence of amorphous boron in our sample from the x-ray examination. We have assumed the amorphous phase to be absent in the treatment of the data.

8.3. Sources of Error

Over 90 percent of the impurity correction in table 3, row 3 depends on the oxygen and nitrogen analyses. If both these analyses are in error by absolute amounts of 0.1 percent, a corresponding error of 0.8 kcal mol^{-1} in the heat of formation of boron carbide is possible.

From our chemical analyses of total boron and total carbon, we calculate the average error in the B/C ratio to be 0.1 percent which would contribute an error of 1.0 kcal mol^{-1} in the heat of formation.

The error introduced by the uncertainties in the heats of formation of $BF_3(g)$, 0.51 kcal mol^{-1}, and $CF_4(g)$, 0.38 kcal mol^{-1}, is 2.2 kcal mol^{-1}, if the two uncertainties are independent. This value was obtained by taking the square root of the sum of the squares of the terms (4.222)(0.51) and (1)(0.38) in which the coefficients of the uncertainties are the numbers of

moles of products formed in the combustion reaction. The same calorimetric system and procedures for sample preparation were used in determining the heats of formation of BF_3(g) and CF_4(g) as have been employed in the present work. Hopefully, because of these features, certain systematic errors that could have occurred in the work on BF_3 and CF_4 would also occur in the present study, and would tend to cancel out in the calculation of the heat of formation of boron carbide.

Errors incurred in performing the heat measurements such as the errors from calibration or combustion experiments, losses in sample preparation, analysis of the amount of unburned boron carbide and incomplete fuse combustion are adequately covered by using two times the standard deviation of the mean, or 1.0 kcal mol^{-1}.

An overall experimental error is calculated by taking the square root of the sum of the squares of these four errors. We obtain 2.7 kcal mol^{-1} as the estimated error in the heat of formation of boron carbide.

8.4. Comparison with Other Work

The calculation of the heat of formation of boron carbide from the work of Smith, Dworkin, and van Artsdalen [1] can be placed on a more current reference base for comparison with our data by introducing a more appropriate value for the heat of formation of amorphous boric oxide into their data. If we use ΔH°_{f298} [B_2O_3(amorphous)] = −299.84 kcal mol^{-1} [28], the value of Smith et al., for ΔH°_{f298} [B_4C(c)] becomes −9.9 kcal mol^{-1}.

We feel that our measurements on boron carbide are an improvement over the previous work [1] because of the greater completeness of combustion, the greater attention given to the analysis of the sample, and the probable cancellation of certain systematic errors as a result of having the heats of formation of BF_3 and CF_4 determined in the same calorimetric system. However, inspection of our value and that of Smith, et al. [1] for the heat of formation of boron carbide shows that the difference in these values is somewhat larger than the sum of the reported uncertainties. It is quite possible that this difference is due to the dissimilarity in the stoichiometries of the respective samples.

The heat of formation of boron carbide has been used to calculate the heat of formation of B(g) from measurements of the vaporization of B_4C, reaction (4), using mass spectrometric and effusion techniques.

$$\tfrac{1}{4}B_4C(c) = B(g) + \tfrac{1}{4}C(c) \qquad (4)$$

The direct measurement of the heat of formation of B(g) was made with these two techniques from the vaporization of elemental boron, reaction (5).

$$B(c) = B(g) \qquad (5)$$

The JANAF Thermochemical Tables [21] summarize the vaporization data that are available from studies on reactions (4) and (5) under the heading: Boron, Monatomic, (Ideal Gas). Close examination of this summary shows a possible systematic error in the value calculated for ΔH_{f298}[B(g)] of about 5 kcal mol^{-1} depending upon whether mass spectrometric or effusion techniques were used. A possible solution to this disparity is a larger negative value for ΔH°_{f298} [B_4C(c)]. However, the application of either our value or that of Smith, Dworkin, and van Artsdalen for ΔH°_{f298}[B_4C(c)] to the available vaporization data on B_4C changes ΔH°_{f298} [B(g)] by less than 2 kcal mol^{-1}. It appears, therefore, that other areas ought to be explored in order to resolve the apparent discordance in the heat of formation of B(g).

9. References

[1] D. Smith, A. S. Dworkin, and E. R. van Artsdalen, J. Am. Chem. Soc. **77**, 2654–6 (1955).
[2] E. J. Prosen, W. H. Johnson, and F. Y. Pergiel, J. Res. NBS **62**, 43–7 (1959) RP2927.
[3] Dow Chemical Company, JANAF Thermochemical Tables Addendum. PB 168370–1 (Clearinghouse for Federal Scientific and Technical Information, Springfield, Virginia, 1966).
[4] G. V. Samsonov, Zh. Prikl. Khim. **28**, 1018–21 (1955).
[5] L. Ya. Markovskii, D. L. Orshanskii, and V. P. Pryanishnikov, Khim. Elektrotermiya, Goskhimizdat, 207–215 (1952).
[6] A. V. Tikhonov, Tr. Tsentral. Nauchno-Issled. Lab. Abraz. i Shlifov. No. **6** (1937).
[7] I. S. Gaev, (a) Zh. Neorgan. Khim. **1**, 193–211 (1956); (b) Metalograficheskii altas zheleznykh splavov (Metallurgizdat, Leningrad-Moskva, 1951).
[8] P. A. G. O'Hare, J. L. Settle, and W. N. Hubbard, Trans. Faraday Soc. **62**, 558–565 (1966).
[9] E. S. Domalski and G. T. Armstrong, J. Res. NBS **71A** (Phys. and Chem.), No. 4, 307–315 (1967).
[10] H. K. Clark and J. L. Hoard, J. Am. Chem. Soc. **65**, 2115–9 (1943).
[11] R. D. Allen, J. Am. Chem. Soc. **75**, 3582–3 (1953).
[12] E. S. Domalski and G. T. Armstrong, J. Res. NBS **71A** (Phys. and Chem.), No. 2, 105–118 (1967).
[13] G. T. Armstrong and R. S. Jessup, J. Res. NBS **64A** (Phys. and Chem.), No. 1, 49–59 (1960).
[14] E. S. Domalski and G. T. Armstrong, J. Res. NBS **71A** (Phys. and Chem.), No. 3, 195–202 (1967).
[15] W. Primack and P. Day, Anal. Chem. **26**, 1515–17 (1954).
[16] E. S. Domalski and G. T. Armstrong, J. Res. NBS **69A** (Phys. and Chem.), No. 2, 137–147 (1965).
[17] C. H. Shomate, Computer Calculations of Combustion Bomb Calorimetric Data, Technical Progress Report 327, NOTS TP3288, U.S. Naval Ordnance Test Station, China Lake, California, August 1963.
[18] O. E. Myers and A. P. Brady, J. Phys. Chem. **64**, 591–4 (1960).
[19] W. D. Good, D. W. Scott, and G. Waddington, J. Phys. Chem. **60**, 1080–9 (1956).
[20] W. H. Evans, J. Hilsenrath, and H. W. Woolley, NBS, private communication, July 1, 1960.
[21] Dow Chemical Company, JANAF Thermochemical Tables, PB 168 370 (Clearinghouse for Federal Scientific and Technical Information, Springfield, Virginia, 1965).
[22] W. H. Evans, NBS, private communication, January 1, 1961.
[23] W. N. Hubbard, Fluorine Bomb Calorimetry, ch. 6, Experimental Thermochemistry, Vol. II, H. A. Skinner, editor (Interscience Publishers, Inc., New York, 1962).
[24] J. O. Hirschfelder, C. F. Curtiss, and R. B. Bird, Molecular Theory of Gases and Liquids (John Wiley and Sons, Inc., New York, copyright 1954, Second Printing, 1964).
[25] D. White, J. H. Hu, and H. L. Johnston, J. Chem. Phys. **24**, 1149–52 (1953).
[26] D. R. Douslin, paper No. 11, pp. 135–46, PVT Relations and Intermolecular Potentials for Methane and Carbon Tetrafluoride, in Progress in International Research on Thermodynamic and Transport Properties, J. F. Masi and D. H. Tsai, editors (Academic Press, New York, 1962).
[27] G. L. Brooks and C. J. G. Raw, Trans. Faraday Soc. **54**, 972–4 (1958).

[28] D. D. Wagman, W. H. Evans, I. Halow, V. B. Parker, S. M. Bailey, and R. H. Schumm, NBS Tech. Note 270-3 (Jan. 1968).
[29] F. D. Rossini, D. D. Wagman, W. H. Evans, S. Levine, and I. Jaffe, Selected Values of Chemical Thermodynamic Properties, NBS Circular 500 (U.S. Government Printing Office, Washington, D.C., 1952).
[30] L. Brewer, L. A. Bromley, P. W. Gilles, and N. Lofgren, The Thermodynamic Properties of the Halides, paper 6, Chemistry and Metallurgy of Miscellaneous Materials: Thermodynamics, L. L. Quill, editor (McGraw-Hill Book Co., Inc., New York, 1950).
[31] E. Rudzitis, H. M. Feder, and W. N. Hubbard, J. Phys. Chem. **68,** 2978-81 (1964).
[32] S. S. Wise, J. L. Margrave, H. M. Feder, and W. N. Hubbard, J. Phys. Chem. **67,** 815-21 (1963).
[33] E. Greenberg, J. L. Settle, H. M. Feder, and W. N. Hubbard, J. Phys. Chem. **65,** 1168-72 (1961).
[34] E. Greenberg, J. L. Settle, and W. N. Hubbard, J. Phys. Chem. **66,** 1345-8 (1962).
[35] A. E. Cameron and E. Wichers, J. Am. Chem. Soc. **84,** 4175-97 (1962).

(Paper 72A2-488)

JOURNAL OF RESEARCH of the National Bureau of Standards—A. Physics and Chemistry
Vol. 72A, No. 2, March–April, 1968

Solubility of Tris(hydroxymethyl)aminomethane in Water-Methanol Solvent Mixtures and Medium Effects in the Dissociation of the Protonated Base

Paul Schindler,[1] R. A. Robinson,[2] and Roger G. Bates

Institute for Materials Research, National Bureau of Standards, Washington, D.C. 20234

(November 13, 1967)

The dissociation constant of the protonated form of tris(hydroxymethyl)aminomethane has been measured at 25 °C in water-methanol solvents containing 30, 50, 70, and 90 wt percent methanol by means of potentiometric titrations. The solubility of tris(hydroxymethyl)aminomethane at 15, 25, and 35 °C in water-methanol solvents containing from 0 to 100 percent methanol has been determined. The results are discussed in terms of free energies of transfer and "medium effects" for hydrochloric acid, tris(hydroxymethyl)aminomethane, and tris(hydroxymethyl)aminomethane hydrochloride.

Key Words: Dissociation constant, medium effect, methanol-water solvents, solubility, tris(hydroxymethyl)aminomethane.

1. Introduction

The dissociation of an acid of the charge type A^+B°, such as the ammonium ion or the protonated form of tris(hydroxymethyl)aminomethane,

$$BH^+ + H_2O \rightarrow H_3O^+ + B,$$

is a process in which a solvated hydrogen ion and an uncharged basic molecule are produced from a positively charged acid ion. The process in aqueous solution can be characterized by a dissociation constant, ${}_wK$:

$${}_wK = \frac{m_{H^+} \cdot m_B}{m_{BH^+}} \cdot {}_w\left(\frac{\gamma_{H^+} \cdot \gamma_B}{\gamma_{BH^+}}\right) \qquad (1)$$

where ${}_w\gamma$ designates an activity coefficient. For aqueous solutions, it is convenient to refer these activity coefficients to the hypothetical molal standard state in water; thus the activity coefficients approach unity as the aqueous solution becomes more dilute. The subscript w indicates this choice of the standard state.

In aqueous solution at 25 °C, $-\log {}_wK$ for the protonated form of tris [3] has been found [1, 2] [4] to be 8.072. The increase in free energy corresponding to the reaction:

$$BH^+ + H_2O \rightarrow H_3O^+ + B$$

is:

$$\Delta_w G^\circ = G^\circ_{H^+} + G^\circ_B - G^\circ_{BH^+} = -RT \ln {}_wK, \qquad (2)$$

the free energies of the reactants and the products being measured in their standard states in water. At 25 °C, therefore, $\Delta_w G^\circ$ is 46.07 kJ mol^{-1}.

If the dissociation constant is determined in another solvent medium, 50 wt percent water-methanol, for example, we have:

$${}_sK = \frac{m_{H^+} \cdot m_B}{m_{BH^+}} \cdot {}_s\left(\frac{\gamma_{H^+} \cdot \gamma_B}{\gamma_{BH^+}}\right) \qquad (3).$$

where the subscript s denotes that the activity coefficients are referred to the hypothetical molal standard state in this solvent and approach unity as the solution becomes more dilute without change in the composition of the solvent. It has been found [3] that $-\log {}_sK = 7.818$ for the protonated form of tris at 25 °C in 50 percent methanol. The reaction is:

$$BH^+ + S \rightarrow SH^+ + B$$

where S is a solvent molecule and SH^+ a solvated hydrogen ion. It is not necessary at this point to dis-

[1] Guest worker (1965–66), on leave from the University of Bern, Switzerland.
[2] Present address: Department of Chemistry, State University of New York at Binghamton, Binghamton, New York 13901.
[3] It is convenient to use "tris" as an abbreviation for tris(hydroxymethyl)aminomethane.
[4] Figures in brackets indicate the literature references at the end of this paper.

tinguish between solvation by water and by methanol molecules. The free energy change corresponding to this reaction is 44.62 kJ mol^{-1}.

The two processes, one in aqueous solution and the other in 50 percent methanol, can be regarded as a single transfer process

$$BH^+(s) + H^+(w) + B(w) \rightarrow BH^+(w) + H^+(s) + B(s),$$

in which the protonated form of tris is transferred from 50 percent methanol to water and solvated hydrogen ions and tris molecules are transferred in the opposite direction. The change in Gibbs free energy when this process occurs is the difference between the separate free energy changes, or $\Delta_m G^\circ = -1.45$ kJ mol^{-1}. The subscript m is used to indicate that the process is a "medium effect," being the composite effect of transferring three species from one solvent medium to another. As each species is in its standard state in each solvent, the free energy change is not concentration-dependent.

It is convenient to define medium effects for each species separately,

$$_mG_i^\circ = RT \ln {}_m\gamma_i \tag{4}$$

so that

$$\Delta_m G^\circ = RT\,(\ln {}_m\gamma_B + \ln {}_m\gamma_{H^+} - \ln {}_m\gamma_{BH^+}). \tag{5}$$

This can be expressed in terms of the pK values:

$$p_sK - p_wK = \log {}_m\gamma_B + \log {}_m\gamma_{H^+} - \log {}_m\gamma_{BH^+}. \tag{6}$$

Hereafter, the terms $\Delta_m G_i^\circ$ will be termed "free energies of transfer," and the quantities ${}_m\gamma_i$ will be designated "medium effects."

Of these three medium effects, two are concerned with the transfer of charged particles from one solvent to another of different dielectric constant (ϵ). The Born equation [4]:

$$G^{el} = \frac{Ne^2}{2\epsilon r} \tag{7}$$

should, therefore, give at least an approximation to the energy of transfer of an ion from water ($\epsilon_w = 78.3$) to 50 percent methanol ($\epsilon_s = 56.3$):

$$\Delta_m G_i^\circ \approx {}_sG_i^{el} - {}_wG_i^{el} = \frac{Ne^2}{2}\left(\frac{1}{\epsilon_s} - \frac{1}{\epsilon_w}\right)\frac{1}{r_i} \tag{8}$$

where the superscript *el* indicates that the calculation is based on electrostatic considerations alone. The useful application of eq (8) requires that the radius, r_i, of the ion be known.

The radius of the tris cation was estimated [3] from atom models to be about 4 Å so that, from eq (8), the transfer of a tris cation from water to 50 percent methanol is accompanied by an increase in electrostatic free energy of 0.87 kJ mol^{-1}. There is some difficulty in assigning a radius to the solvated hydrogen ion, but it was estimated [3] that the radius is about 2.8 Å. Hence the transfer of hydrogen ion from water to 50 percent methanol involves an increase of 1.24 kJ mol^{-1} in free energy.

We now have

	$\Delta_m G^\circ$
$BH^+(s) + H^+(w) + B(w) \rightarrow BH^+(w) + H^+(s) + B(s)$	-1.45 kJ mol^{-1}
$H^+(w) \rightarrow H^+(s)$	$+1.24$ kJ mol^{-1}
$BH^+(s) \rightarrow BH^+(w)$	-0.87 kJ mol^{-1}

and hence,

$$B(w) \rightarrow B(s),\ \Delta_m G^\circ = -1.82 \text{ kJ mol}^{-1}.$$

These results suggest, therefore, that there is a rather large effect, amounting to about 2 kJ mol^{-1}, accompanying the transfer of a mole of the neutral tris molecules between water and 50 percent methanol. A more refined treatment by Hepler [5] of a variable dielectric constant in the close vicinity of an ion reinforces the existence of this large transfer energy term for the uncharged base.

In the earlier study [3] of the pK of protonated tris at several temperatures in 50 wt percent methanol, the discrepancy of about 2 kJ mol^{-1} between the calculated and "observed" free energies of dissociation was attributed to a "basicity effect" of the solvent, which was thought to be superimposed on the medium effects calculated from electrostatic considerations alone. This view was taken in the belief that the medium effect of an uncharged species would be so small as to be unable to account for the differences observed between the experimental and calculated free energies of dissociation.

In the present work, the free energy of transfer and the medium effect for the free base have been determined and found to account reasonably well for the "basicity effect" identified in the prior investigation. These conclusions are based on measurements of the solubility of tris in water and in water-methanol solvents and upon a determination of the pK of protonated tris at 25 °C in 30, 50, 70, and 90 wt percent methanol.

2. Outline of Present Method

The condition for equilibrium between solid tris and its saturated aqueous solution is:

$$G\,(\text{solid}) = {}_wG^\circ + RT \ln {}_w\gamma \cdot m_w, \tag{9}$$

where m_w is the molality of the saturated solution and ${}_w\gamma$ is the activity coefficient of tris at this molality relative to unity in the standard state in water. The condition for equilibrium between solid tris and its saturated solution in a water-methanol mixture is:

$$G\,(\text{solid}) = {}_wG^\circ + RT \ln {}_m\gamma \cdot {}_s\gamma \cdot m_s, \tag{10}$$

where m_s is the molality of the saturated solution in the

mixed solvent and ${}_s\gamma$ is the activity coefficient of tris at this molality relative to unity in the standard state in the mixed solvent. The proof of eq (10) is given in the appendix to this paper.

It follows from eq (9) and (10) that

$$\ln {}_m\gamma = \ln m_w/m_s + \ln {}_w\gamma/{}_s\gamma \qquad (11)$$

and hence that the medium effect, ${}_m\gamma$, can be obtained from the ratio of the solubilities of tris in water and in the mixed solvent, provided that ${}_s\gamma/{}_w\gamma$ is unity. The latter condition will hold to a good approximation if the solute is only slightly soluble in each solvent medium. This would be true, for example, for silver chloride in water and water-methanol mixtures, for in dilute solutions ${}_w\gamma$ and ${}_s\gamma$ are, in the main, expressions of the Debye-Hückel (interionic) forces, and these become more nearly negligible as the solution becomes more dilute. *A fortiori*, this is true of the ratio $\ln {}_w\gamma/{}_s\gamma$. Although tris is uncharged, it is very soluble, especially in water, and it might seem that this condition would not apply. It has, however, been shown [6] that the activity coefficient of tris does not depart much from unity even in concentrated solutions. Similar data are not available for water-methanol mixtures, but there is no reason to believe that ${}_s\gamma$ will depart much from unity in these solvents. As will be shown later, m_w/m_s is large, and it would require values of ${}_s\gamma$ very different from unity to reduce ${}_m\gamma$ to a negligible quantity. In the absence of any proof that that ${}_s\gamma$ is markedly different from unity, it will be assumed that m_w/m_s gives an approximation to the medium effect, ${}_m\gamma$. In order to obtain values of ${}_m\gamma$, the solubility of tris in a number of water-methanol mixtures has been measured at 15, 25, and 35 °C and the results are reported in this paper.

Equation (6) can be recast as follows:

$$p_sK - p_wK = \log {}_m\gamma_B + 2 \log {}_m\gamma_{HCl} - 2 \log {}_m\gamma_{B\cdot HCl} \qquad (12)$$

The terms on the left and the first term on the right are obtained from measurements to be described later in this paper. The term in ${}_m\gamma_{HCl}$ corresponds to the free energy change in the transfer of hydrochloric acid from water to a water-methanol mixture and can be obtained from the standard emf of the cell with hydrogen and silver-silver chloride electrodes in water and in the water-methanol mixtures, determined by emf measurements of solutions of hydrochloric acid:

Pt; H_2, HCl in water or water-methanol, AgCl; Ag.

Values of these standard electromotive forces have been tabulated [7]. Accordingly, the remaining term in eq (12), ${}_m\gamma_{B\cdot HCl}$, the medium effect for the transfer of tris hydrochloride from water to water-methanol mixtures can be calculated and compared with similar free energy changes for other salts.

3. Experimental Procedures

3.1. Dissociation Constants

The dissociation constant of the protonated form of tris was determined in 30, 50, 70, and 90 wt percent methanol at 25 °C by potentiometric titration. The cell:

Glass electrode; HCl (0.01 m) in water-methanol, AgCl; Ag

was set up and its emf (E_1) measured when the silver-silver chloride electrode had come to equilibrium. A solution consisting of (0.01 *m* HCl + 0.1 *m* tris) in the same water-methanol mixture was then added in measured amounts and the emf (E_2) measured after each addition. Under these conditions of constant chloride concentration and constant total ionic strength (but varying ratio of tris to tris hydrochloride), the electrode comes to equilibrium quickly [8, 9]. Then,

$$p_sK = (E_2 - E_1)/k + \log \frac{m_{BH^+}}{0.01\ m_B} + \log \frac{{}_s\gamma_{BH^+} \cdot {}_s\gamma_{Cl^-}}{{}_s\gamma_B \cdot {}_s\gamma'_{H^+} \cdot {}_s\gamma'_{Cl^-}} \qquad (13)$$

where $k = (RT \ln 10)/F$ and the primed quantities refer to the initial solution to which no tris had been added. A number of determinations of p_sK can be made, one corresponding to each addition of the (HCl + tris) solution. The last term of eq (13) should be negligible for solutions of these low ionic strengths and we can write:

$$pK = (E_2 - E_1)/k + \log m_{BH^+}/(0.01\ m_B). \qquad (14)$$

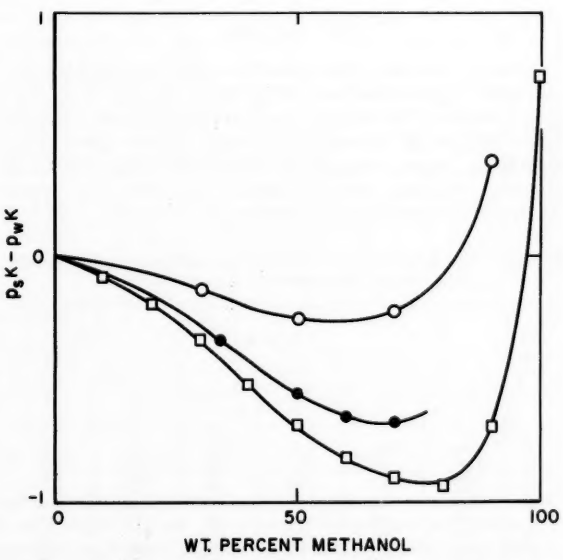

FIGURE 1. *Difference between the* pK *value in water-methanol mixtures and in water* ($p_sK - p_wK$), *for three acids.*
O, Protonated form of tris(hydroxymethyl)aminomethane.
●, Ammonium ion.
□, *o*-Chloroanilinium ion.

This neglect of the activity coefficient term in eq (13) appears justifiable because, omitting this term, we find $p_sK = 7.825$ in 50 percent methanol. This value compares well with $p_sK = 7.818$ obtained earlier [3] using an emf method in which the activity coefficient term was eliminated by extrapolating the data to zero ionic strength.

The results of these potentiometric titrations are given in table 1. They are compared, in figure 1, with similar data for the ammonium ion [10] and the *o*-chloroanilinium ion [11]. It is apparent that the effect of solvent composition on p_sK is specific to each acid, but there is a general resemblance between the three curves insofar as the effect of adding methanol to the solvent medium is concerned. Addition of methanol first reduces the value of p_sK. A minimum is reached between 60 and 80 percent methanol, after which p_sK rises to high values when the methanol content is large. There is evidence, for two of the acids, that the value of p_sK in solvents of high methanol content can exceed the pK value in water; this is probably true also for the ammonium ion.

TABLE 1. *Values of* p_sK *for the dissociation of the protonated form of tris(hydroxymethyl)aminomethane in water-methanol mixtures at 25 °C*

Wt percent methanol	p_sK	$p_sK - p_wK$
0	[a] (8.072)	.....
30	7.940	−0.132
50	7.825	−.247
70	7.855	−.217
90	8.462	+.390

[a] For this value of p_wK, see ref. [1] and [2].

3.2. Solubility

Tris is a very soluble substance which readily supersaturates; moreover, its solubility is highly temperature-sensitive. Solubility measurements were, therefore, made in a constant temperature bath. The solutions were shaken at frequent intervals, but vigorous shaking was avoided. The solutions were analyzed by acidimetric titration at intervals of 24 hr.

TABLE 2. *Solubility of tris(hydroxymethyl)aminomethane in water-methanol mixtures at 15, 25, and 35 °C*

Wt percent methanol	15 °C		25 °C		35 °C	
	S	σ	S	σ	S	σ
0	4.593	0.001	5.780	0.008	7.261	0.004
10	3.940	.001	5.092	.003	6.550	.010
20	3.363	.002	4.450	.010	5.827	.003
30	2.845	.004	3.821	.027	5.087	.003
40	2.382	.004	3.223	.027	4.366	.003
50	1.920	.005	2.622	.002	3.610	.004
60	1.455	.001	2.009	.011	2.813	.001
70	1.022	.001	1.440	.003	2.503	.006
80	0.6727	.0007	0.9359	.0007	1.356	.008
90	.3700	.0003	.5368	.0006	0.8443	.0021
100	.2186	.0001	.2918	.0007	.4266	.0007

S = solubility in moles per kilogram of solvent.
σ = standard deviation.

TABLE 3. *Medium effects and free energy changes in the transfer of tris(hydroxymethyl)aminomethane from water to water-methanol solvents*

Wt percent methanol	15 °C		25 °C		35 °C	
	$\log {}_m\gamma_B$	$\Delta_mG_B^\circ$	$\log {}_m\gamma_B$	$\Delta_mG_B^\circ$	$\log {}_m\gamma_B$	$\Delta_mG_B^\circ$
10	0.066_7	0.36_8	0.055_9	0.31_4	0.044_8	0.26_0
20	.135	$.74_8$	.114	$.65_1$	$.095_8$	$.56_2$
30	.208	1.15	.180	1.03	.154	$.90_4$
40	.285	1.57	.254	1.45	.221	1.30
50	.379	2.09	.343	1.96	.303	1.79
60	.499	2.75	.459	2.62	.412	2.43
70	.653	3.60	.604	3.45	.549	3.24
80	.834	4.60	.791	4.52	.729	4.30
90	1.094	6.04	1.032	5.89	.935	5.52
100	1.322	7.29	1.297	7.40	1.231	7.26

Values of $\Delta_mG_B^\circ$ are expressed in kJ mol^{-1}.

The solutions were assumed to be in equilibrium with the solid phase if no change in concentration was found over a period of 72 hr. The equilibration time was between two and three weeks.

Table 2 gives the solubilities (in moles per kilogram of solvent) at 15, 25, and 35 °C. Table 3 records the medium effect, $\log {}_m\gamma_B$, calculated from these solubility values with the aid of the equation:

$$\log {}_m\gamma_B \approx \log m_w/m_s \qquad (15)$$

and also the corresponding free energy changes, $\Delta_mG_B^\circ = RT \ln {}_m\gamma_B$. From the temperature coefficient of the free energy change, it is possible to calculate the enthalpy and entropy changes accompanying the transfer process. Values of $\Delta_mH_B^\circ$ and $\Delta_mS_B^\circ$ are given in table 4. These were calculated by assuming that over this 20 °C temperature range:

$$\Delta_mG_B^\circ = A + BT + CT^2. \qquad (16)$$

TABLE 4. *Enthalpy and entropy changes in the transfer of tris(hydroxymethyl)aminomethane from water to water-methanol solvents at 25 °C*

Wt percent methanol	$\Delta_mH_B^\circ$	$\Delta_mS_B^\circ$
10	1.9	5
20	3.4	9
30	4.6	12
40	5.5	14
50	6.5	15
60	7.4	16
70	8.8	18
80	9.0	15
90	13.6	26
100	7.9	2

$\Delta_mH_B^\circ$ is given in kJ mol^{-1} and $\Delta_mS_B^\circ$ in J deg^{-1} mol^{-1}.

Then, it can be shown that:

$$\Delta_mH_B^\circ = g_2 - 0.05(g_3 - g_1)T_0 \qquad (17)$$

and

$$\Delta_mS_B^\circ = 0.05(g_1 - g_3), \qquad (18)$$

for the enthalpy and entropy changes at the middle temperature ($T_0 = 298.15$ °K), where g_1, g_2, and g_3 are the values of $\Delta_m G^\circ_B$ at 15, 25, and 35 °C, respectively.

4. Discussion

We now have the three quantities necessary to calculate log $_m\gamma_{B\cdot HCl}$ by means of eq (12). Values of $(p_sK - p_wK)$ are given in table 1, log $_m\gamma_B$ appears in table 3, and 2 log $_m\gamma_{HCl}$ is calculated from the standard potentials of cells containing hydrochloric acid [7, 12]. All of these values are collected in table 5 along with log $_m\gamma_{B\cdot HCl}$ calculated with the aid of eq (12). The latter have also been expressed in terms of the free energy of transfer of tris hydrochloride from water to water-methanol. Table 5 also contains values of log $_m\gamma_{LiCl}$ for the transfer of lithium chloride from water to water-methanol [13]. It can be seen, especially if the data are plotted as in figure 2, that the energies of transfer between water and water-methanol solvents of the same composition are similar for lithium chloride and for tris hydrochloride.

TABLE 5. *Medium effects involved in the dissociation of protonated tris(hydroxymethyl)aminomethane in water-methanol solvents at 25 °C*

Wt percent methanol	30	50	70	90
$p_sK - p_wK$	−0.132	−0.247	−0.217	+0.390
log $_m\gamma_B$	.180	.343	.604	1.032
log $_m\gamma_{HCl}$	.162	.268	.456	0.920
log $_m\gamma_{B\cdot HCl}$	.319	.563	.867	1.240
log $_m\gamma_{LiCl}$	.361	.620	.936	1.369
$\Delta_m G^\circ_{B\cdot HCl}$ (kJ mol^{-1})	3.64	6.43	9.90	14.16

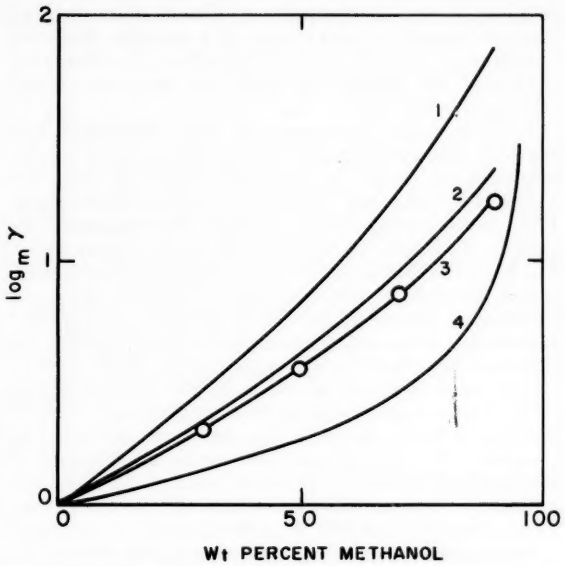

FIGURE 2. *Medium effects for the transfer of electrolytes from water to water-methanol solvents.*
1 NaCl, 2 LiCl, 3 Tris · HCl, 4 HCl.

The present picture of the transfer process is different from that discussed earlier [3], as shown by the following résumé of the free energies of transfer (in kJ mol^{-1}) from water to 50 percent methanol:

The small difference between the two values given for the energy of process (i) arises from the difference between the values of p_sK recorded in table 1 and that given earlier [3]. As already indicated, the calculations of the earlier study gave only the free energy of transfer of the solvated hydrogen ion (1.24 kJ mol^{-1}) and that of the B · H$^+$ ion (0.87 kJ mol^{-1}) for the transfer from water to 50 percent methanol. Therefore, for the comparisons shown above we have also used eq (7) to calculate a value of 1.91 kJ mol^{-1} for the transfer of a mole of chloride ion from water to 50 percent methanol, assuming a radius of 1.81 Å for this ion. The calculated values for the processes (ii) and (iii) accordingly become −2.78 and 3.15 kJ mol^{-1}.

		$\Delta_m G^\circ$	
		Ref 3	This paper
(i)	B · HCl (s) + HCl (w) + B (w) → B · HCl (w) + HCl (s) + B (s)	−1.45	−1.41
(ii)	B · HCl (s) → B · HCl (w)	−2.78	(−6.43)
(iii)	HCl (w) → HCl (s)	3.15	3.06
(iv)	B (w) → B (s)		1.96
(v)	"Basicity effect"	(−1.82)	
		−1.45	−1.41

Although specific interactions and selective solvation might be expected to have a stronger influence in solutions of hydrochloric acid than in solutions of tris hydrochloride, it is interesting to note that the transfer free energy for hydrochloric acid computed from purely electrostatic considerations is close to the experimental value given in the last column, while the differences for tris hydrochloride are considerable. In the earlier work, no attempt was made to estimate the free energy of process (iv). Instead, the discrepancy between the known value for process (i) and the sum of the calculated energies of processes (ii) and (iii) was attributed to a basicity effect (v), considered to be superimposed on the electrostatic energies, calcu-

lated from the Born model, eq (7). A more detailed analysis based on the concept of a variable dielectric constant in the vicinity of the ion affects the numerical values of the transfer energies but does not change the conclusions [3].

In this paper, however, we have described how transfer energies for tris can be determined experimentally by means of solubility measurements. The value of 1.96 kJ mol^{-1} in the above tabulation, therefore, is an experimental quantity. Furthermore, the energy of transfer of hydrochloric acid, 3.06 kJ mol^{-1}, has been derived from emf measurements. The approximate agreement with the value of 3.15 kJ mol^{-1} calculated by means of the Born equation, assuming a reasonable value of the ionic radius, suggests that the electrostatic effect is the main one in this instance.

The value of -6.43 kJ mol^{-1} for the transfer energy of tris hydrochloride has not been derived by independent means but is based on the experimental values for processes (i), (iii), and (iv). The pertinent relationship among these quantities is set forth in eq (12). The discrepancy between the two values for the tris.H$^+$ ion arises from the fact that Woodhead et al. [3], ascribed a reasonable value of 4 Å to the radius of the tris cation and assumed that the electrostatic effect, as calculated by means of eq (7), gives a complete account of the transfer process. It is now found that the energy of transfer of tris hydrochloride from water to 50 percent methanol is 3.7 kJ mol^{-1} larger than that so calculated.

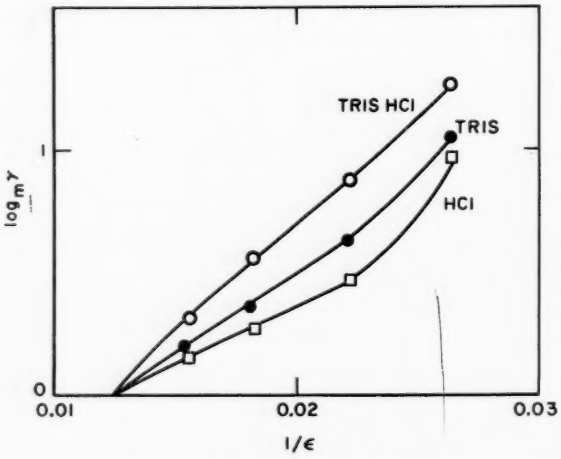

FIGURE 3. *Medium effects for the transfer from water to water-methanol solvents, as a function of the reciprocal of the dielectric constant of the medium.*

O, Tris(hydroxymethyl)aminomethane hydrochloride.
●, Tris(hydroxymethyl)aminomethane.
□, Hydrochloric acid.

Figure 3 is a plot of log $_m\gamma$ for three transfer processes from water to water-methanol against the reciprocal of the dielectric constant of the solvent. According to eq (7), two of these should be straight lines; it is curious that the best approximation to a straight line is found for the nonelectrolyte, tris. Nevertheless, up to a solvent composition of 70 percent methanol, the plots for hydrochloric acid and tris hydrochloride are almost linear and therefore satisfy one requirement of eq (7). According to this equation, however, if we take 1.91 kJ mol^{-1} for the energy of transfer of the chloride ion from water to 50 percent methanol, the radius of the cation is given by the equation:

$$r_+ = \frac{Ne^2}{2\Delta_m G_+^\circ}\left(\frac{1}{\epsilon_s} - \frac{1}{\epsilon_w}\right) \tag{19}$$

or

$$r_+ = 3.466(\Delta_m G_+^\circ)^{-1} \tag{19a}$$

if r_+ is expressed in Å and $\Delta_m G_+^\circ$ in kJ mol^{-1}, and the transfer process occurs between water ($\epsilon_w = 78.3$) and 50 percent methanol ($\epsilon_s = 56.3$).

Åkerlöf [13] has determined log $_m\gamma$ for the transfer of potassium chloride, sodium chloride, and lithium chloride and, if his data for the transfer of these salts from water to 50 percent methanol are used, values of $r_+ = 0.40$, 0.44, and 0.67 Å are obtained for the potassium, sodium, and lithium cations, respectively, assuming a radius of 1.81 Å for the chloride ion. Similarly, from the values of $\Delta_m G^\circ$ for tris hydrochloride and hydrochloric acid, we find $r_+ = 0.77$ and 3.02 Å for protonated tris and hydrogen ions, respectively. Of these five cationic radii, only one, that of the hydrogen ion, is reasonable; the others are much too small. The anomaly is all the more curious because there is every reason to believe that the Debye-Hückel theory gives the correct values of the activity coefficients $_s\gamma$ in 50 percent methanol just as it does for water as solvent, provided that the *macroscopic* dielectric constant is used in the Debye-Hückel equation and a reasonable value of the ion-size parameter is introduced. The use of the macroscopic dielectric constant, therefore, explains the concentration dependence of the activity coefficient in both solvent media but fails to account for the energy of transfer from one solvent to the other.

The standard state used in this discussion is that for the molal scale of concentration, both in water and in water-methanol. It is possible that the standard state on the mole-fraction scale would be a better choice. Equations for the conversion from one scale to the other can be found elsewhere [14]; the energy of transfer of the hydrogen ion from water to 50 percent methanol is lower by 0.61 kJ mol^{-1} on the mole-fraction scale than on the molality scale, and the same is true of the chloride ion. Thus the energy of transfer of hydrochloric acid is 1.84 kJ mol^{-1} on the mole-fraction scale and 3.06 kJ mol^{-1} on the molality scale. Nevertheless, the adoption of the mole-fraction scale does not lead to a more reasonable set of ionic radii.

It is clear that there are difficulties in reconciling the transfer processes with a purely electrostatic theory. Nevertheless, if the experimental finding that the transfer process for tris hydrochloride is about equal in magnitude to that for lithium chloride is accepted, the diminution in the value of *pK* of the tris cation on addition of methanol (except for those solutions very

high in methanol content) is seen to be due to the much higher transfer energy of tris hydrochloride (or lithium chloride) over that of hydrochloric acid. Assuming that the transfer energy of tris hydrochloride is identical with that of lithium chloride and using values of the latter taken from the work of Åkerlöf [13], p_sK values of the protonated form of tris can be calculated. Figure 4 compares such calculated values with the observed.

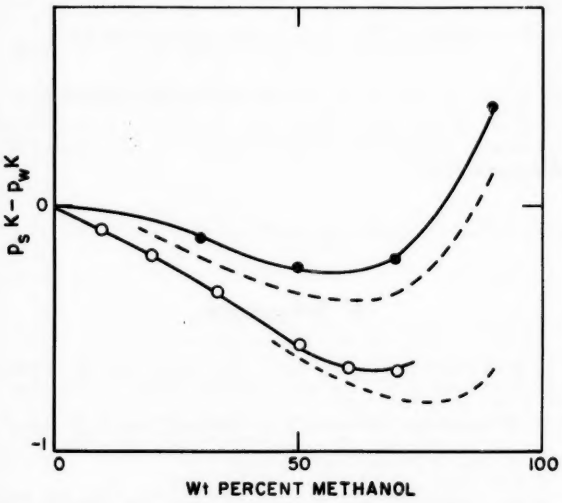

FIGURE 4. *Comparison of experimental and calculated values of* $(p_sK - p_wK)$ *in water-methanol mixtures.*
———, experimental.
- - - -

solvent can be measured relative to the hypothetical standard state in that solvent:

$$G = {}_{s}G^{\circ} + RT \ln {}^{s}_{s}\gamma \cdot m_{s}, \tag{20}$$

where m_s is the molality of the solution, ${}_{s}G^{\circ}$ is the free energy of the solute in the standard state in this solvent mixture, and ${}^{s}_{s}\gamma$ is the activity coefficient of the solute referred to the standard state in this solvent.

The free energy could, however, be referred to the hypothetical standard state in water as solvent:

$$G = {}_{w}G^{\circ} + RT \ln {}^{s}_{w}\gamma \cdot m_{s}, \tag{21}$$

where ${}_{w}G^{\circ}$ is the free energy of the solute in the standard state in water and ${}^{s}_{w}\gamma$ is the activity coefficient of the solute *in the mixed solution* (s) but *referred to the standard state in water* (w).

We now consider the limit when $m_s \rightarrow 0$ and ${}^{s}_{s}\gamma \rightarrow 1$. Under these circumstances,

$${}_{s}G^{\circ} - {}_{w}G^{\circ} = RT \lim_{m_s \rightarrow 0} \ln {}^{s}_{w}\gamma. \tag{22}$$

This is an expression for the free energy change in transferring the solute from water to the mixed solvent in the limit of extreme dilution when the concentration effects on the free energy change are absent. It is, therefore, the free energy change for the transfer from one hypothetical standard state to another, where also concentration effects are absent. Consequently,

$$\lim_{m_s \rightarrow 0} \ln {}^{s}_{w}\gamma = \ln {}_{m}\gamma, \tag{23}$$

from which follows the important relation:

$${}^{s}_{w}\gamma = {}_{m}\gamma \cdot {}^{s}_{s}\gamma \cdot \tag{24}$$

Equation (24) is sometimes abbreviated to:

$${}_{w}\gamma = {}_{m}\gamma \cdot {}_{s}\gamma, \tag{25}$$

but when this is done care should be taken to note that here ${}_{w}\gamma$ is an activity coefficient in the *mixed solvent* relative to the standard state in water, whereas in eq (1) ${}_{w}\gamma$ designates an activity coefficient in aqueous solution relative to the standard state in water.

We next consider the equilibrium between a solid and its saturated solution. The condition for equilibrium between a solid and its saturated solution in a mixed solvent is:

$$G(\text{solid}) = {}_{w}G^{\circ} + RT \ln {}_{m}\gamma \cdot {}^{s}_{s}\gamma \cdot m_{s} \tag{26}$$

and the condition for equilibrium between the solid and its saturated aqueous solution is:

$$G\ (\text{solid}) = {}_{w}G^{\circ} + RT \ln {}^{w}_{w}\gamma \cdot m_{w}. \tag{27}$$

Hence,

$$\ln m_{w}/m_{s} = \ln {}_{m}\gamma + \ln {}^{s}_{s}\gamma/{}^{w}_{w}\gamma, \tag{28}$$

which is sometimes abbreviated to:

$$\ln m_{w}/m_{s} = \ln {}_{m}\gamma + \ln {}_{s}\gamma/{}_{w}\gamma, \tag{29}$$

which is eq (11). It should be noted that ${}_{w}\gamma$ is now used, as in the body of the text, to denote an activity coefficient in *aqueous* solution relative to the standard state in water.

6. References

[1] R. G. Bates and H. B. Hetzer, J. Phys. Chem. **65,** 667 (1961).
[2] S. P. Datta, A. K. Grzybowski, and B. A. Wilson, J. Chem. Soc. (London), 792 (1963).
[3] M. Woodhead, M. Paabo, R. A. Robinson, and R. G. Bates, J. Res. NBS **69A** (Phys. and Chem.) No. 3, 263 (1965).
[4] M. Born, Z. Physik **1,** 45, 221 (1920).
[5] L G. Hepler, Aust. J. Chem. **17,** 587 (1964).
[6] R. A. Robinson and V. E. Bower, J. Chem. Eng. Data **10,** 246 (1965).
[7] R. G. Bates and R. A. Robinson, Acid-base behavior in methanol-water solvents, in Chemical physics of ionic solutions, B. E. Conway and R. G. Barradas, Eds (John Wiley & Sons, Inc., New York, N.Y., 1966).
[8] R. G. Bates, G. L. Siegel, and S. F. Acree, J. Res. NBS **30,** 347 (1943).
[9] J. M. Stokes and R. H. Stokes, J. Phys. Chem. **67,** 2442 (1963).
[10] M. Paabo, R. G. Bates, and R. A. Robinson, J. Phys. Chem. **70,** 247 (1966).
[11] E. E. Sager, R. A. Robinson, and R. G. Bates, J. Res. NBS **68A** (Phys. and Chem.), No. 3, 305 (1964).
[12] I. T. Oiwa, Sci. Rpt. Tohoku Univ., Ser. 1, **41,** 47 (1957).
[13] G. Åkerlöf, J. Am. Chem. Soc. **52,** 2353 (1930).
[14] R. A. Robinson and R. H. Stokes, Electrolyte solutions, pp. 39 and 352, revised edition (Butterworths Scientific Publications, London, 1965).
[15] D. H. Everett and W. F. K. Wynne-Jones, Trans. Faraday Soc. **48,** 531 (1952).
[16] F. E. C. Scheffer and H. J. DeWijs, Rec. Trav. Chim. **44,** 655 (1925).
[17] W. Y. Wen, S. Saito, and C. M. Lee, J. Phys. Chem. **70,** 1244 (1966).
[18] W. Y. Wen and S. Saito, J. Phys. Chem. **69,** 3569 (1965).

(Paper 72A2–489)

JOURNAL OF RESEARCH of the National Bureau of Standards—A. Physics and Chemistry
Vol. 72A, No. 2, March-April 1968

Calibration of the Nickel Dimethylglyoxime Spectral Shift at Pressures to 20 Kilobars for Use in Spectroscopic Pressure Measurement

Helen W. Davies*

Institute for Materials Research, National Bureau of Standards, Washington, D.C. 20234

(October 28, 1967)

A method for incorporating solid nickel dimethylglyoxime in a liquid enclosed by a gasket in the diamond-anvil high pressure cell is described. A calibration curve relating the spectral shift of the nickel dimethylglyoxime visible absorption band to the known freezing pressures of 14 liquids has been obtained. The equation for the calibration line is $\Delta\bar{\nu}=-158.9\,P+1.82\,P^2$ where P is expressed in kilobars. The 90 percent confidence band about the calibration curve has been computed, and the curve has been used to determine the room-temperature freezing pressures of acetone and methylcyclohexane.

Key Words: Absorption spectra, diamond-anvil cell, high pressure measurement, nickel dimethylglyoxime.

1. Introduction

Previous methods for the calibration of high pressure equipment have generally depended upon the use of materials having known pressure-induced transitions, such as bismuth and thallium [1].[1] Observation of their solid-solid transitions (e.g., the Bi I–II transition at 25 kbar) permits the assignment of the corresponding pressure at specific points. This paper describes a method for continuous pressure measurement, based on the change in the spectral properties with pressure of nickel dimethylglyoxime ($Ni(DMG)_2$). Pressure-dependence of the position of the visible absorption band ($\bar{\nu}\approx 18900$ cm^{-1}) of solid $Ni(DMG)_2$ has been reported [2]. In addition to the large red shift in the spectrum with pressure, this material has further advantages for use in pressure measurement in that it is easily prepared, it is insoluble in most liquids, and the spectral band is relatively sharp. A method for incorporating this material in a liquid in a high-pressure vessel is described, and a calibration curve relating the observed spectral shifts to known hydrostatic pressures is given. The pressure data employed are the known freezing pressures of various liquids. The curve is then used to determine the room-temperature freezing pressures of two other liquids. The 90 percent confidence band about the calibration curve has been determined and it will be seen that the principal disadvantage of this method of pressure measurement is the considerably lower precision with which pressures can be assigned as compared with the precision of piston or manganin gages. However, the spectroscopic method is particularly useful for measurements in high pressure optical devices such as the diamond-anvil cell, where other methods are not easily used.

2. Experimental Procedures

$Ni(DMG)_2$ was prepared by the method of Yamada and Tsuchida, by the reaction of nickel sulfate and dimethylglyoxime, followed by recrystallization of the product from chloroform [3]. Liquids used either were from fresh supplies of spectro grade material or were distilled to constant boiling point just prior to use.

The high pressure equipment used for these measurements was the diamond-anvil high pressure cell [4]. Liquids were contained in the cell with metal gaskets. The preparation of these gaskets has been described [5]. The selection of the metal to be used for a measurement depended upon the maximum pressure range to be reached. The spectral data were obtained with a microscope spectrophotometer, an instrument particularly well suited to investigations of the small samples in the diamond cell [6].

*Present address: 8309 Woodhaven Blvd., Bethesda, Md. 20034.
[1] Figures in brackets indicate the literature references at the end of this paper.

The methods used for the preparation of a sample for measurement and for the determination of the spectral shift at the freezing pressure of the liquid are as follows. First, a gasket was prepared and cleaned. Then, with the gasket out of the cell, finely ground $Ni(DMG)_2$ or a mixture of $Ni(DMG)_2$ and an inert solid was placed in the cell and pressure was applied to obtain a thin film of the material between the diamond anvils. The cell was then opened and the large diamond cleaned. With both anvils now out of the cell, viewing through a microscope and using a pointed instrument, a small section of the $Ni(DMG)_2$ film adhering to the small diamond surface was transferred to the center of the large diamond surface. The small diamond was then cleaned, again placed in the cell, and the gasket properly positioned on it. The liquid was added and the cell quickly assembled. In this way the bit of $Ni(DMG)_2$ film on the face of the large diamond was trapped in the liquid enclosed between the diamond anvils by the gasket in the cell.

Alternatively, the small diamond could first be placed in the cell and the gasket positioned on it. The piece of $Ni(DMG)_2$ film could then be placed in the hole in the gasket onto the small diamond surface, the liquid added and the cell assembled, with the same result as above.

When a number of measurements were contemplated, the general practice was to transfer several pieces of $Ni(DMG)_2$ film from a single film preparation to a glass slide where they could be reserved for later use, being transferred to the diamond anvil surfaces as needed. This eliminated the necessity of pressing a new film for each measurement.

The assembled cell was then positioned for viewing the enclosed sample with a microscope. The pressure was increased to completely freeze the liquid and then slowly and carefully decreased to melt most of the crystals. The pressure was then increased sufficiently to grow the remaining crystals slightly in order to ensure that equilibrium between solid and liquid was attained. It was this point of solid-liquid equilibrium that was taken as the freezing point of the liquid, and the spectrum of the $Ni(DMG)_2$ was recorded. It was the general practice then to decrease the pressure to allow the solid to melt completely, to refreeze the liquid, and to obtain the condition of solid-liquid equilibrium a second time. Having thus obtained two (or more) measurements of the position of the $Ni(DMG)_2$ absorption band peak at the liquid freezing pressure, the pressure was released and the position of the absorption band peak at 1 atm pressure recorded. In many instances the cell was disassembled before this final measurement to ensure that no residual pressure was applied to the specimen. The ambient temperature was recorded for each measurement. It was in this way that the data for the calculation of

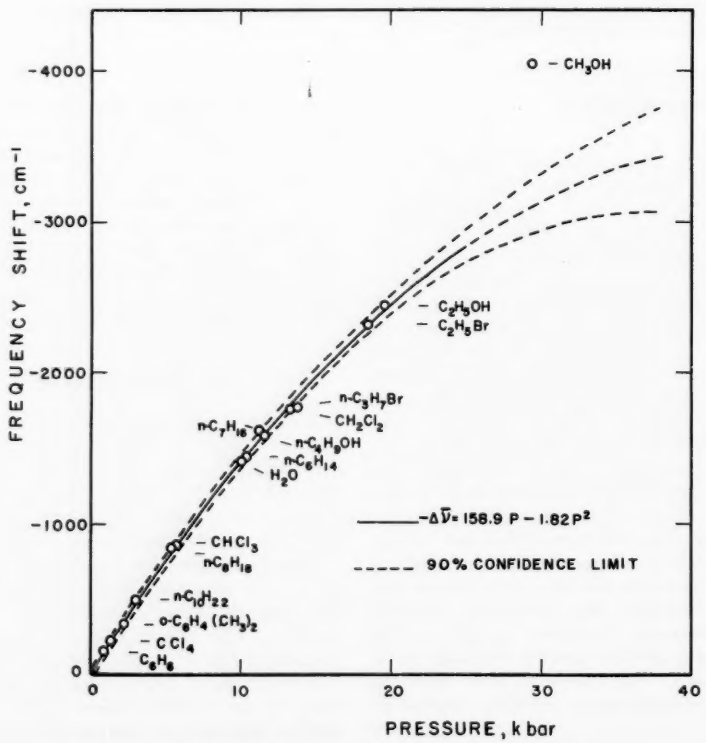

FIGURE 1. *Measured shift of the* $Ni(DMG)_2$ *absorption band at the freezing pressures of various liquids at room temperature.*

the absorption band shift, $\Delta\bar{\nu}$, corresponding to the freezing pressure for each liquid were obtained.

It was found that either finely ground pure $Ni(DMG)_2$ or a finely ground mixture of $Ni(DMG)_2$ and an inert solid such as sodium chloride or silver chloride could be used interchangeably for the determination of spectral shifts. The latter, specifically a mixture with sodium chloride, was preferred because when pressed between the diamond anvils it gave the most-easily-transferred films. Pure $Ni(DMG)_2$ films were somewhat brittle and tended to break up when removal from the diamond surface was attempted. Values of $\Delta\bar{\nu}$ obtained were found to be the same whether pure $Ni(DMG)_2$ or mixtures in sodium chloride or silver chloride were used. For the measurement on water, where because of its solubility sodium chloride could of course not be used, either pure $Ni(DMG)_2$ or $Ni(DMG)_2$ in silver chloride was used. In the course of this work several different batches of $Ni(DMG)_2$, prepared as previously described, were used. $\Delta\bar{\nu}$ values obtained for any liquid were reproducible when a different sample of $Ni(DMG)_2$ was used.

3. Results

The experimental spectral band shift data are given in table 1. It will be noted that each $\Delta\bar{\nu}$ figure is the result of measurements on at least two different samples of liquid. In addition, a number of successive freezing point measurements were made with each sample, to determine the reproducibility for the sample. The freezing pressure data are from Bridgman's work, expressed here in kilobars.[2] As indicated in table 1, where possible, i.e., where sufficient pressure-temperature information was given in the original reference, these freezing pressure data are for the same temperature as that at which the liquid was studied in these experiments.

For all of the liquids except water the $Ni(DMG)_2$ was diluted with sodium chloride (20% $Ni(DMG)_2$ by weight). For the measurements on water $Ni(DMG)_2$ (7%) in silver chloride was used.

In figure 1 are plotted the data given in table 1.

The equation of the best line through the experimental points has been derived by the method of least squares, using the OMNITAB program POLYFIT [12]. It was found that a quadratic equation fitted the data quite well, except for the methanol point ($\Delta\bar{\nu}=-4040$ cm^{-1}, $P=30$ kbar). Bridgman was able to freeze methanol only once and he noted furthermore that on that one occasion the freezing was very sluggish [11]. This point was therefore omitted from the fitting process. When this was done, the least squares values for b and c in the equation $\Delta\bar{\nu}=bP+cP^2$ were:

$$b=-158.9$$
$$c=+1.82,$$

for P expressed in kilobars. (A constant term was first included. As expected it turned out to be nonsignificant.

TABLE 1. *Shift of the $Ni(DMG)_2$ absorption band at known liquid freezing pressures*

Liquid	Temperature of measurement	Freezing pressure	Temperature	Reference	Mean measured $\Delta\bar{\nu}$	Sample standard deviation $\Delta\bar{\nu}$	Number of samples
	°C	kbar	°C		cm^{-1} [a]	cm^{-1}	
1. Benzene	29	0.834	29	(7)	−155	20	7
2. Carbon tetrachloride	28	1.383	28	(7)	−227	20	11
3. *o*-Xylene	28	2.256	25	(8)	−338	8	3
4. *n*-Decane	28	2.991	25	(8)	−490	0	3
5. *n*-Octane	25	5.403	25	(8)	−845	27	6
6. Chloroform	27	5.541	27	(7)	−852	13	5
7. Water	28	10.052	28	(9)	−1417.5	15	4
8. *n*-Hexane	28.5	10.395	30	(10)	−1433	46	3
9. *n*-Heptane	27.5	11.229	25	(8)	−1610	0	2
10. *n*-Butanol	27	11.572	27	(11)	−1580	0	2
11. Methylene chloride	30	13.337	30	(11)	−1750	0	3
12. *n*-Propyl bromide	25	13.729	25	(11)	−1770	0	2
13. Ethyl bromide	27	18.437	27	(11)	−2315	7	2
14. Ethanol	25	19.613	25	(11)	−2450	14	2
15. Methanol	25	[b] 29.420	25	(11)	−4040	14	2

[a] $\bar{\nu}_0 \sim 18900$ cm^{-1}.
[b] This value for the freezing pressure of methanol appears to be considerably too low and was not employed in any calculations.

[2] Recent experiments indicate that the pressures assigned by Bridgman to the mercury freezing point and the bismuth transition and then used by him as fixed points in the calibration of manganin pressure gauges are about 1 percent low (S. E. Babb, Jr., in *High Pressure Measurement*, A. A. Giardini and E. C. Lloyd, Eds. (Butterworths, Washington, D.C., 1963), p. 115). Therefore the liquid freezing pressures determined by Bridgman and used here are likely to be approximately 1 percent low. An increase of 1 percent in the pressures would give the following equation for $\Delta\bar{\nu}$: $\Delta\bar{\nu}=-157.3P+1.78P^2$. The changes in the equation are less than the standard errors of the b and c coefficients given below.

Theoretically for $P=0$, one must have $\Delta\bar{\nu}=0$. The fit was then repeated assuming a zero intercept.) The standard errors of the b and c coefficients were 3.3 and 0.21, respectively. The standard error of scatter about the fitted curve was 36, which was determined with 12 degrees of freedom. This equation ($\Delta\bar{\nu}=-158.9\,P+1.82\,P^2$) was used to obtain the calculated curve of $\Delta\bar{\nu}$ versus P shown in figure 1.

The 90 percent confidence band about the calibration line, also shown in figure 1, was obtained by computing

$$\Delta\bar{\nu}\pm t_{.90}\sqrt{(\text{estimate of }\sigma^2)+(\text{estimate of variance of }\Delta\bar{\nu})}$$

where:

$\Delta\bar{\nu}$ is the value of $\Delta\bar{\nu}$ computed for a P, using the fitted equation; $t_{.90}$ is Student's "t" for a confidence coefficient of 90 percent, for 12 deg of freedom; σ^2 is the variance of the error in measuring the future $\Delta\bar{\nu}$.

Now we have:

$$\text{Variance of }\Delta\hat{\bar{\nu}}=\text{Var}(bP+cP^2)$$
$$=P^2\,\text{Var}(b)+P^4\,\text{Var}(c)+2P^3\,\text{Cov}(b,c)$$
$$=P^2\{\text{Var}(b)+[2\text{Cov}(b,c)]P+\text{Var}(c)P^2\}.$$

In this case the equation for the 90 percent confidence band is

$$\Delta\hat{\bar{\nu}}\pm 1.78\sqrt{1296+P^2\,[10.7076-1.3371\,P+4.513\times10^{-2}\,P^2]}.$$

The σ^2 estimate, 1296, is obtained from the standard error of scatter about the fitted curve, which was 36, and allows for both the experimental error in a measured $\Delta\bar{\nu}$ and the error due to lack of fit.

4. Discussion

The calibration curve for the shift of the $Ni(DMG)_2$ visible absorption band as a function of pressure, based on 14 known pressure points, has been obtained. In addition, the 90 percent confidence band about the calibration line has been computed. Use of this curve permits the assignment of pressures corresponding to measured $\Delta\bar{\nu}$ values. The confidence band indicates the limits within which an assigned pressure is known.

The use of the calibration curve can be illustrated with the determination of the room-temperature freezing pressures of two liquids: acetone and methylcyclohexane. Bridgman noted the freezing of acetone but was unable to obtain a sample of sufficient purity to make an accurate determination of the freezing pressure [7]. He also studied methylcyclohexane and reported the liquid-solid transition not reproducible [8]. No difficulty in freezing methylcyclohexane was encountered here, largely because the design of the diamond cell permits the visual observation of the sample and the investigator can simply continue to increase the pressure until the anticipated phase change has been seen to occur.

The experimental data for the shift of the $Ni(DMG)_2$ absorption band (20% $Ni(DMG)_2$ in NaCl) are given below:

	Mean measured $\Delta\bar{\nu}$	Standard deviation	Number of samples
	(cm^{-1})	(cm^{-1})	
Acetone	−1335	6	4
Methylcyclohexane	−1540	14	4

Using the calibration curve, the following freezing pressure assignments can be made:

Acetone	9.35 kbar ± 0.50 kbar
Methylcyclohexane	11.10 kbar ± 0.55 kbar

The ± values represent the 90 percent confidence intervals.

As was stated earlier, in the determination of the best equation for the calibration curve it was found that a satisfactory fit to the experimental data could be had by excluding the point for methanol. On examining the curve thus obtained (fig. 1), it is readily noted that a spectral band shift of -4040 cm^{-1}, the shift measured for methanol at its freezing point, would correspond to a pressure much greater than the value of 30 kbar reported by Bridgman [11]. It is suggested therefore that the room-temperature freezing pressure of methanol is not 30 kbar, but that on the basis of the experimental data presented here, it is not less than 38 kbars. This estimate is based on linear extrapolation of the curve of figure 1 from the highest experimental points. The maximum in this curve is not meaningful but is a fictitious maximum imposed by the polynomial used to fit the data. In as much as the curvature is positive the linear extrapolation is not expected to overestimate the freezing point.

As mentioned earlier, the shift of the visible absorption band of $Ni(DMG)_2$ with pressure has been reported by Zahner and Drickamer [2]. It should be noted however that, within the range of our experiments, the pressures given by these authors for any

$\Delta\bar{\nu}$ are not in agreement with the results of the measurements made in this laboratory. In fact, up to our highest measured $\Delta\bar{\nu}$ for which the pressure is known (-2450 cm^{-1}), their pressures are about 50 percent greater than our values. The freezing point data from Bridgman on which a number of our pressure points have been based were determined by him under true hydrostatic conditions. The present data also were obtained under purely hydrostatic conditions, while those of Zahner and Drickamer were not. Therefore, it seems that in this range the nonhydrostaticity might contribute to an overestimate of the pressure by about 50 percent.

The author is indebted to J. Mandel for aid in the statistical analysis of the data and to C. E. Weir for many helpful comments and suggestions.

5. References

[1] F. P. Bundy, in Modern Very High Pressure Techniques, p. 18, R. H. Wentorf, Jr., Ed. (Butterworth, Inc., Washington, D.C., 1962).
[2] J. C. Zahner and H. G. Drickamer, J. Chem. Phys. **33,** 1625 (1960).
[3] S. Yamada and R. Tsuchida, Bull. Chem. Soc. Japan **26,** 489 (1953).
[4] C. E. Weir, E. R. Lippincott, A. Van Valkenberg, and E. N. Bunting, J. Res. NBS **63A** (Phys. and Chem.), No. 1, 55 (1959).
[5] C. E. Weir, S. Block, and G. Piermarini, J. Res. NBS **69C** (Engr. and Instr.), 275 (1965).
[6] H. C. Duecker and E. R. Lippincott, Rev. Sci. Instr. **35,** 1108 (1964).
[7] P. W. Bridgman, Phys. Rev. **3,** 153 (1914).
[8] P. W. Bridgman, Proc. Am. Acad. Arts Sci. **77,** 129 (1949).
[9] P. W. Bridgman, Proc. Am. Acad. Arts Sci. **47,** 441 (1911).
[10] P. W. Bridgman, Proc. Am. Acad. Arts Sci. **61,** 57 (1926).
[11] P. W. Bridgman, Proc. Am. Acad. Arts Sci. **74,** 399 (1942).
[12] J. Hilsenrath et al., OMNITAB, A computer program for statistical and numerical analysis, p. 113, NBS Handbook 101 (U.S. Government Printing Office, Washington, D.C. 20402).

(Paper 72A2–490)

JOURNAL OF RESEARCH of the National Bureau of Standards—A. Physics and Chemistry
Vol. 72A, No. 2, March–April 1968

Second Virial Coefficient of He^4 in the Temperature Range from 2 to 20 °K

Marjorie E. Boyd, Sigurd Y. Larsen, and Harmon Plumb

Institute for Basic Standards, National Bureau of Standards, Washington, D.C. 20234

(December 7, 1967)

We present preliminary values for the second virial coefficient of He^4 in the temperature range from 2 to 20 °K. They were derived from recent sound velocity measurements in the gas made by Plumb and Cataland using an ultrasonic interferometer.

Key Words: He^4, low temperature, second virial.

In this communication we present values for the second virial coefficient of He^4 in the temperature range from 2 to 20 °K. They were derived from recent sound velocity measurements in the gas made by Plumb and Cataland using an ultrasonic interferometer [1].[1] Our values for the virials must be considered as preliminary since the method for determining them from sound velocity data places such stringent demands on the numerical accuracy of the latter that it will be necessary to accumulate a much larger body of data than is now available to achieve more exact virials.

However, the problem of discrepancies existing between various provisional temperature scales below 20 °K is currently of strong interest [2] and contributes a note of urgency to the problem of obtaining new measured values of the second virial coefficient in this temperature range. Currently, the only values available are obtained either by extrapolating upward from the *PVT* data of Keller [3] in the 2 to 4 °K region, by relying on a very few points obtained by Keesom and Walstra [4] more than twenty years ago, or by using theoretical calculations based on assumed intermolecular potential functions. We thus believe that our values, although they must be regarded as tentative, are probably the best now available and may therefore prove useful as guides toward resolving the international temperature scale difficulties. Further measurements of sound velocity isotherms which should enable more accurate and reliable values to be determined are now in progress in this laboratory.

Isotherms of the speed of sound as a function of pressure were obtained [1] at pressures low enough that the isotherms could be represented by a linear relationship, $W^2=C(1+\alpha p)$, where W is the sound velocity, $C=\frac{5}{3}RT/M$, and $C\alpha$ is the slope of the isotherm. The coefficient α is related to the second virial coefficient B by [5] the equation

$$\alpha(T)=(RT)^{-1}\left[2B+\frac{4}{3}TB'+\frac{4}{15}T^2B''\right]$$

where the primes denote differentiation with respect to T, the temperature. To obtain the second virial from the α's it is thus necessary to assume a functional form for $B(T)$ with coefficients to be determined, differentiate it twice, and determine the constants by least squares fitting of the data for $\alpha(T)$. This approximation of B by an arbitrarily chosen expression introduces a strong uncertainty in the results in addition to the uncertainties involved in determining the α's from the isotherms.

Many experimentalists have used the form $B=a+b/T$, and recent experience of two of the authors (MEB and SYL) [6] in fitting results of an accurate phase-shift calculation of B for He^4, using a Lennard-Jones potential with deBoer parameters, indicates that this is a reasonable form in the temperature range of this data. However, curvature as a function of $1/T$ does become increasingly apparent for the L-J virials at about 20 °K, as well as at the low T end.

Using, then, $B=a+b/T$ we find the results shown in table 1. An idea of the accuracy may be obtained by both observing the changes in the results when fitting to different temperature ranges separately and by noting the effect of adding additional terms in the functional form for B. Of these two types of changes the first is the least serious in its effects on the results. Comparing the virials obtained when fitting the middle temperature range to those obtained fitting the high and low ranges separately we find them to differ by

[1] Figures in brackets indicate the literature references at the end of this paper.

TABLE 1. *Second virial coefficient of* He^4 *from 2 to 20 °K*

Range fitted	Derived formula for B	σ_α	B calculated from derived formula (cm^3/mol)				
			2 °K	4 °K	10 °K	16 °K	20 °K
2–10 °K	$(21.28\pm0.46)-(449.2\pm3.2)/T$	1.30	−203.3	−91.0	−23.64	.....	.....
	$(19.6\pm1.1)-(422\pm17)/T-\frac{(69\pm42)}{T^2}$	1.19	−209.	−90.0	−23.3	.....	.....
	$(24.4\pm2.3)-(459.9\pm8.3)/T-(0.18\pm0.13)T$	1.23	−205.9	−91.3	−23.4	.....	.....
11–20 °K	$(17.00\pm0.20)-(379.1\pm5.0)/T$	0.25	.....	.....	−20.91	−6.69	−1.96
	$(14.30\pm0.71)-(246\pm34)/T-\frac{(1223\pm314)}{T^2}$	.15	.....	.....	−22.5	−5.8	−1.1
	$(22.6\pm1.3)-(446\pm25)/T-(0.111\pm0.026)T$	.15	.....	.....	−23.1	−7.1	−1.9
4–16 °K	$(19.43\pm0.24)-(430.3\pm3.1)/T$	.73	−195.8	−88.2	−23.60	−7.46	−2.08
	$(17.60\pm0.39)-(378\pm11)/T-\frac{(235\pm47)}{T^2}$	.42	−230.	−91.6	−22.6	−6.9	−1.9
	$(23.40\pm0.73)-(455.1\pm4.8)/T-(0.131\pm0.024)T$	.39	−204.5	−90.9	−23.42	−7.14	−1.98

amounts varying from about 7 cm^3/mol at 2 °K down to about 0.1 at 20 °K.

Introduction of another term in the expression for B, can, depending on the particular form, lead to drastically differing results, even though the standard deviations (σ_α) for the fitting of α are similar. This is illustrated in table 1. Thus it would appear that the fitting of more complicated expressions for B than the simple 2-constant function used here cannot be justified unless either more extensive data are available or a strong theoretical justification of a particular functional form for $B(T)$ can be made.

References

[1] H. Plumb and G. Cataland, Metrologia **2**, 127 (1966).
[2] Meeting of Advisory Committee on Thermometry to International Committee on Weights and Measures, Gaithersburg, Md., and Ottawa, Canada, Sept. 6–14, 1967.
[3] W. E. Keller, Phys. Rev. **97**, 1 (1955).
[4] W. H. Keesom and W. K. Walstra, Physica **13**, 225 (1947).
[5] A. Van Itterbeek and W. H. Keesom, Commun. Kamerlingh Onnes. Lab., Leiden No. 216c; Proc. Koninkl. Ned. Akad. Wetenschap. **34**, 988 (1931).
[6] S. Y. Larsen, M. E. Boyd and J. E. Kilpatrick, to be published.

(Paper 72A2–491)

JOURNAL OF RESEARCH of the National Bureau of Standards—A. Physics and Chemistry
Vol. 72A, No. 2, March–April 1968

Diffusion Rates in Inorganic Nuclear Materials

A. L. Dragoo

Institute for Materials Research, National Bureau of Standards, Washington, D.C. 20234

(December 13, 1967)

The tracer diffusion coefficient, the self-diffusion coefficient, the intrinsic diffusion coefficient and the interdiffusion coefficient are briefly described. Grain boundary and lattice (volume) diffusion are contrasted. The frequency factors (D_0) and activation energies (Q) are tabulated for diffusion in the borides, carbides, and oxides of Be, Hf, Mo, Nb, Ta, Th, Ti, and Zr and for diffusion of C, N, and O in these metals. The purity of the solvent media, the preparation and properties of the samples, the method, the type of diffusion coefficient measured and the temperature range are also specified.

Key Words: Chemical interdiffusion, grain-boundary diffusion, intrinsic diffusion, lattice diffusion, self-diffusion, tracer diffusion.

1. Introduction

Since diffusion is often the rate controlling step in kinetic processes in solids—such as sintering, creep, precipitation, and corrosion—diffusion data have a necessary part in deciding the role of many metals and their compounds in high-temperature nuclear technology. Borides, carbides, nitrides, and oxides of plutonium and uranium, as well as the alloys of Pu and U with refractory metals, are potential high-temperature nuclear fuels. Refractory metals, such as Hf, Mo, Nb, Ta, Ti, and Zr also may be used as structural and cladding materials. Thorium compounds can be transmuted to ^{233}U-fuels in breeder reactors, and BeO can serve as a neutron moderator and reflector.

In this compilation diffusion data are presented for the borides, carbides, and oxides of Be, Hf, Mo, Nb, Ta, Th, Ti, and Zr. No diffusion data are available to date for the nitrides nor for plutonium compounds. A similar compilation of the very extensive data for uranium compounds is now in progress. Since corrosion of the metals by C, N, and O often proceeds by reactive diffusion, diffusion data for C, N, and O diffusion in the eight metals listed above have been included (data for B diffusion in these metals were not available).

2. Diffusion Coefficients

In general, a diffusion coefficient D is defined by Fick's first law as the constant which relates the flux of matter J to the concentration gradient causing the flow. The gradient usually is taken to be only in the x direction, thus

$$J=-D(\partial C/\partial x). \quad (1)$$

In the case of solids, three different diffusion coefficients—tracer diffusion (D_T), intrinsic diffusion (D_i) and chemical interdiffusion ($\tilde{D}$)—can be considered depending on the experimental conditions. The tracer and intrinsic diffusion coefficients apply to the diffusion of a single species; whereas the interdiffusion coefficient applies to the intermingling of species.

In the case of tracer diffusion, only a trace amount of species "i" diffuses into a homogeneous solid from a very thin layer at the surface of the sample. In the absence of any external force field and of the influence of other species, the i-atoms will diffuse in a random manner toward an equilibrium distribution due only to their own concentration gradient ($\partial C_i/\partial x$). If the tracer is the same as one of the elements of the solid matrix, D_T becomes the self-diffusion coefficient, D^*. The tracer and self-diffusion coefficients can be determined by a wide variety of techniques which are noted in the tables.

The intrinsic diffusion coefficient takes into account the atom flux resulting from (1) the redistribution described by D_T, (2) the effect of a nonideal and nonhomogeneous solid solution of "i," and (3) the influence of the driving forces of the other species on the diffusion of "i." When substituted into eq (1), D_i describes the flux of "i" with respect to a local lattice plane in a nonhomogeneous, nonideal, solid solution which is not subject to any external driving force. The driving forces in a nonideal, nonhomogeneous solid solution are the chemical potential gradients ($\partial\mu_i/\partial x$) of the various constituents of the material. The intrinsic diffusion coefficient generally is not measured experimentally, but it can be calculated if tracer diffusion coefficients of the species and the variation of the activity coefficient γ_i with respect to the mole fraction N_i of "i" are known.

If the rates of diffusion of different ionic species are not equalized by an internal potential gradient or by external forces, their interdiffusion will be accompanied by a net flow of imperfections. This flow of imperfections can be observed by inert marker techniques as a net movement of the lattice with respect to some fixed plane (e.g., the end of the sample). Thus, if the net flow of species is measured with respect to a fixed plane outside the diffusion zone, diffusion and the movement of the local lattice planes together will be measured. The chemical interdiffusion coefficient (or merely the "chemical diffusion coefficient") $\tilde{D}$ is obtained from eq (1) if the flux J in this equation is measured with respect to a fixed plane outside the diffusion zone. If it is assumed that $\tilde{D}$ is a function of the ratio $x/\sqrt{t}$, where t is time, $\tilde{D}$ can be determined by the classical method of Boltzmann [1][1] and Matano [2]. If there is no net flow of imperfections during diffusion, $\tilde{D}$ for interdiffusion in a binary system equals the intrinsic diffusion coefficients of the two species (D_{12} will be used in this case).

It should be emphasized that D_T can be determined only in a homogeneous solid. If the solid is nonhomogeneous, then $\tilde{D}$, and in some cases D_i, can be determined if the flux with respect to a fixed plane is known. These three diffusion coefficients apply to diffusion through the lattice.

In addition, diffusion can take place along grain boundaries. Grain-boundary diffusion of a tracer into a solid gives a nearly linear [3–6] decrease of $\ln C_i$ with penetration depth x, whereas $\ln C_i$ varies linearly with x^2 for lattice (volume) diffusion. The grain-boundary diffusion coefficient is represented in the tables by D_{gr}.

Diffusion coefficients for the borides, carbides, and oxides of Be, Ti, Zr, Hf, Nb, Ta, Mo, and Th have been measured generally for the cations and occasionally for the anions. The self-diffusion and tracer diffusion coefficients correspond empirically to the Arrhenius relation

$$D = D_0 \exp(-Q/RT) \qquad (2)$$

where D_0 is the frequency factor, Q is the activation energy, R is the ideal gas constant and T is the absolute temperature. Although the chemical and intrinsic diffusion coefficients may be expressed in terms of eq (2), $\tilde{D}$ and D_i have a more complex temperature dependence.

3. Experimental Methods

In general, there are two modes of determining D. The direct method measures the distribution of concentration through the solid at a time t. The indirect method determines the diffusion coefficient by measuring a diffusion controlled phenomenon: attenuation of radioactivity, exchange of isotopes between a solid and a gas, release of anelastic strain, change of a physical property of the surface or the release of rare gases.

4. Reliability

Most of the diffusion values in the tables are "preliminary." That is, they are the only values presently available, and they will suffice for rough estimates of the behavior of materials in technological applications.

The immediate needs of technology have provided the rationale for including many of the diffusion values in this compilation. Since the ratios of two independent measurements of the diffusion coefficient can be as great as 10^6 (see Be diffusion in BeO, low temperatures) due primarily to differences in materials and experimental methods, caution is required in the use of diffusion values. To this end, diffusion values from more than one source have been tabulated when they have been available and auxiliary information and comments have been included in the tables.

To go beyond the rough estimate to the fundamental understanding of the properties of solids requires that a very exacting set of criteria be placed upon materials and methods. The solvent medium should be a very pure, well-characterized single crystal. In the case of chemical diffusion, the concentration dependence of the diffusion coefficient should be determined or the diffusion coefficient should be determined at given concentrations. Indirect determinations of D should be compared with direct determinations of D from chemical or isotopic concentration profiles. Measurements of a physical property related to the concentration do not establish the concentration profile unless the property's functional dependence on concentration is determined (e.g., the assumption of linearity is not sufficient). Diffusion anneals should be carried out above one-half the melting point temperature so that extrinsic diffusion is avoided, unless impurity effects are to be measured. These anneals must be carried out under thermodynamically specifiable conditions—temperatures and partial pressures must be known.

The scope of this compilation prevented a detailed use of these criteria in establishing the degree of reliability of each diffusion coefficient. Critical evaluations also were limited by the lack of first-hand experience with most of the experimental techniques, and by the absence of experimental details, of tabulated data and of careful error analyses in many of the original works. Nevertheless, some general comments can be made.

Much of the unreliability results from the specimens used, and high impurity concentrations are foremost among the causes. Impurity controlled diffusion rates (extrinsic diffusion) are to be expected when impurities with valences other than that of the diffusing species are present in concentrations greater than 100 ppm and when the annealing temperature is low with respect to the melting point. Diffusion coefficients measured under such conditions are strictly only characteristic of the specimen studied and are not "intrinsic" to the material.

[1] Figures in brackets indicate the literature references at the end of this paper.

Several errors can arise from the use of polycrystalline materials. Grain boundaries and pores provide high diffusivity paths. Experimental observations of these effects and experiments in which these may have been a major factor have been noted in the tables. These high diffusivity paths probably contributed measureably to the observed rates in experiments carried out below 700 to 1000 °C, but it has not been possible to assess the magnitude of these contributions here. Grain orientation is important when the material has less than cubic symmetry because the diffusion coefficient is a second rank tensor and, therefore, depends on crystallographic direction.

Dislocations, subgrain boundaries and microcleavages due to surface damage are other sources of high diffusivity paths which can occur in both single and polycrystalline specimens. These sources of error have been overlooked by most investigators.

Diffusion coefficients from any experiments in which chemical concentration gradients were present, such as oxidation of metals, have been classed as chemical diffusion coefficients. Apparent agreement between such diffusion coefficients and self-diffusion coefficients should be considered fortuitous. Furthermore, when these diffusion coefficients have been obtained by assuming that they are independent of concentration, they are first order approximations for the overall diffusion zone in the specimen studied.

Experimental methods are the second area in which problems arise. Indirect measurements usually depend upon the change of a physical property which is assumed to depend on concentration. In some cases, notably anelastic strain measurements, such methods can be very reliable. However, indirect methods usually do not reveal the concentration dependence of the chemical diffusion coefficient nor the presence of high diffusivity paths.

In regard to both indirect and direct methods, the functional dependence of the measured property on concentration often has not been demonstrated and the influence of other factors has not been determined. Microhardness, for example, depends on microstructure, impurities, and preferred orientation of the grains as well as on chemical composition, and it is not necessarily a linear function of concentration. The absorption of beta radiation by a solid is generally more complex than a mere exponential function of distance. If the functional relationship only has been assumed, the reported diffusion coefficient should be considered a preliminary value.

Some other sources of unreliability which the user of the tables should determine from the original work if accuracy is very important are:

(1) temperature control and measurement;

(2) failure to satisfy the boundary conditions of the diffusion problem;

(3) change in the characteristics of the specimen during the diffusion anneal due to sintering, vaporization, annihilation or production of defects and reaction with components of the furnace; and

(4) hysteresis in the response of the measuring instrument.

5. Key to the Tables

Each table contains data for a metal and its borides, carbides, and oxides. The data in each table is ordered first according to the solvent medium, i.e., the matrix metal or compound. First the matrix metal is presented, followed in turn by the borides, the carbides and the oxides. For example, in the table for thorium, thorium metal occurs first followed by ThO_2 (there is no data for the borides and carbides).

The data for the diffusion in the metallic solvent medium is ordered alphabetically with respect to the diffusing element (C, N, or O). A further ordering with respect to the metallic phase is used if this distinction is important (e.g., C-diffusion in α-Ti precedes C-diffusion in β-Ti).

The compound solvent medium (e.g., oxides) is subdivided first with respect to the number of cations per molecule. For example, the niobium carbides have the following order: $NbC \rightarrow Nb_2C \rightarrow Nb_4C_3 \rightarrow$ mixed carbides. Each compound subdivision next is arranged alphabetically with respect to the diffusing element. The order for BeO is: Be → O → $T(^3H)$ → Xe.

In addition to specifying the solvent medium and diffusing element, each entry gives the purity of the solvent medium, the preparation and properties of the diffusion sample, the method used to measure the diffusion coefficient, the type of diffusion coefficient measured, the temperature range, the frequency factor (D_0) and the activation energy (Q), in cal/mol (1 cal = 4.184 J).

I thank J. R. Manning for the many helpful discussions during the preparation of this compilation. This work was partially supported by the Advanced Research Projects Agency, U.S. Department of Defense.

Solvent medium	Diffusing element	Purity[a]	Preparation and properties	Method	Diffusion coefficient	Temperature range, °C	D_0 cm²/s	Q cal/mol	Comments	Ref.
BeO	Be[b]	Al, 15; Fe, 200; Pb, 20; Si, 500.	Polycrystalline, cold-pressed and sintered, 96–98% of theoretical density.	Determination of the radioisotope distribution by sectioning.	D^* (self-diffusion).	1180–1800	2.49×10^{-3}	62,500	Grain-boundary diffusion was considered insignificant because grain size exceeded diffusion depth; impurity content was probably important.	[1]
BeO	Be	Al, 3000; Ca, 330; Fe < 25; Si < 77; Ti, 61; P < 500.	Polycrystalline, slip cast and sintered 92–93% of theoretical density.	Determination of the radioisotope distribution by sectioning.	D^* D^*	1550–1730 1730–1960	5.56×10^{-3} 6.14×10^{-3}	111,600 66,100	Variation in diffusion coefficient was primarily due to impurity content; scatter in data makes the actual magnitude of curvature uncertain. "Tailing" of concentration distribution curve in single crystal specimens (which is suggestive of grain boundary diffusion in polycrystalline samples) was ascribed to microcleavages due to grinding.	[2]
BeO	Be	Al < 160; Fe, 43; Si, 60; Ti, 33; P < 500.	Polycrystalline, hot-pressed, 99.3% of theoretical density.	Determination of the radioisotope distribution by sectioning.	D^* D^*	1550–1725 1725–2000	1.35 1.07×10^{-6}	92,000 36,000		[2]
BeO	Be	Mo microinclusions; all other impurities under 100.	Single crystal; grown in lithium molybdate flux.	Determination of the radioisotope distribution by sectioning.	D^* D^*	1500–1760 1720–1975	1.27×10^{-3} 1.23×10^{-6}	64,000 36,000		[2, 3]
BeO	O	Al, 3000; Ca, 330; Fe < 25; Si, < 77; Ti, 61; P < 500.	Polycrystalline, slip cast and sintered, 92–93% of theoretical density.	Heterogeneous isotopic exchange between a solid sample and a gas.	D^*	1600–1900	5.2×10^{-7}	42,900	Evidence of significant grain-boundary diffusion; the rates may also be affected by the impurity concentration.	[2, 4, 5]
BeO	O	Fe, 25; Li, 20; Mo, 1200; all others ≦ 10.	Single crystal; grown in a molybdate flux.	Heterogeneous isotopic exchange between a solid sample and a gas.	D^*	1300–1700	2.95×10^{-5}	68,500	Grain boundary effects were removed by use of single crystal.	[6]
BeO	T(^{3}H)	Not stated.	Commerical BeO powder (Brush UOX).	Rate of fission gas release from irradiated powder, spherical particles were assumed.	D_T (tracer diffusion)	673–923	6.6×10^{-13}	24,500	T was assayed as T_2O, recovery as T_2O was quantitative. The very low values for both D_0 and Q are suggestive of significant grain boundary diffusion.	[7]
BeO	T	Not stated.	Commerical BeO powder (Brush Minox).	Rate of fission gas release from irradiated powder, spherical particles were assumed.	D_T	673–873	7.6×10^{-13}	24,000		[7]
BeO	T	Not stated.	Sintered compacts and powders were investigated; powder data was considered more reliable.	Rate of fission gas release from irradiated powder, spherical particles were assumed.	D_T	700–1000	0.131	70,000	Data indicated a lower activation energy below 700 °C; T was assayed as HT, a correction was required for the loss as HTO.	[8]
BeO	Xe	Samples were obtained from S. B. Austerman, Ref. 2, 3.	Pyramidal, single-crystals, were assumed to be spherical for calculation of D.	Hahn emanation technique, Xe recoiled into oxide when oxide was irradiated in contact with UO_2.	D_T	800–1500	3.0×10^{-6}	63,500		[9]

[a] Impurity concentrations are given in ppm unless otherwise stated.

[b] Note added in proof: Condit and Hashimoto [10] reported $D = (1 \times 20\, F_p)N_v[10 \times \exp(-62.0\ \text{Kcal}/RT)]\ \text{cm}^2\,\text{s}^{-1}$ for Be diffusion in polycrystalline BeO in the temperature range between 1330 to 2135 °C. F_p is the fraction of porosity and N_v is the molar fraction of vacancies introduced by impurities.

[1] H. J. DeBruin and G. M. Watson, J. Nucl. Mater. **14,** 239 (1964); U.S. At. Energy Comm. Report ORNL-3526 (1964).
[2] S. B. Austerman, J. Nucl. Mater. **14,** 248 (1964); U.S. At. Energy Comm. Report NAA-SR-5893 (1961).
[3] S. B. Austerman and J. W. Wagner, J. Am. Ceram. Soc. **49,** 94 (1966).
[4] S. B. Austerman, R. A. Meyer, and D. G. Swarthout, U.S. At. Energy Comm. Report NAA-SR-6427 (1961).
[5] S. B. Austerman and R. A. Meyer, U.S. At. Energy Comm. Report NAA-SR-7637 (1962).
[6] J. B. Holt, J. Nucl. Mater. **11,** 107 (1964).
[7] A. R. Palmer, D. Roman, and H. J. Whitfield, J. Nucl. Mater. **14,** 141 (1964).
[8] E. Rothwell and L. L. Wassell, J. Nucl. Mater. **16,** 208 (1965).
[9] D. L. Morrison, T. S. Elleman, and D. N. Sunderman, J. Appl. Phys. **35,** 1616 (1964).
[10] R. H. Condit and Y. Hashimoto, J. Am. Ceram. Soc. **50,** 425 (1967).

Hafnium

Solvent medium	Diffusing element	Purity [a]	Preparation and properties	Method	Diffusion coefficient	Temperature range, °C	D_0 cm²/s	Q cal/mol	Comments	Ref.
Hf.....	O.....	Zr < 100; O, 120; N, 16; C, 37.	Zone-refined; oxide layer formed by anodization.	Time rate of change of interference color (i.e., thickness) of oxide film on metal due to solution of film in metal.	$\tilde{D}$ (chemical diffusion).	500–1050	0.660	50,820	$\tilde{D}$ assumed to be independent of concentration.	[1]
Hf.....	O.....	Zr, 1.0 w/o; Al, 1100; Fe, 450; Cu, 60; Cr, 800; Mg, 50; Ti, 300; Ni, 60; all others < 50.	Hot-rolled and annealed at 800° C; machined and polished; oxidized in air.	Determination of concentration gradient by microhardness measurements.	D	700–1200	1.6	49,300	Assumption of linear relationship between oxygen concentration and hardness probably was not justified, according to [4] the relationship is parabolic; nitrogen gradient was superimposed on oxygen gradient.	[2]
$Hf_{0.86}$—.... $Ca_{0.14}$—.... $O_{1.86}$	O.....	Fe_2O_3, 0.012–0.1%; Al_2O_3, 0.012–0.1%; TiO_2, 0.01-0.2%; ZrO_2, 2.5-3%; Nb_2O_5, 0.05–0.1% (weight percent).	Tube closed at one end; density 9.51 g/cm³; porosity ~ 5%.	Determination of the rate of permeation of O_2 through walls of stabilized hafnia tube.	$\tilde{D}$	1100–1600	22	55,700	A large drop in partial pressure between the inside and outside of the tube caused a large chemical potential gradient.	[3]

[a] Impurity concentrations are given in ppm unless otherwise stated.

[1] J. P. Pemsler, J. Electrochem. Soc. **111**, 1185 (1964); J. Electrochem. Soc. **106**, 1067 (1959).
[2] J. D. Gadd and E. B. Evans, Corrosion **17**, 441t (1961).
[3] A. W. Smith. F. W. Meszaros, and C. D. Amata, J. Am. Ceram. Soc. **49**, 240 (1966).
[4] E. Rudy and P. Stecher, J. Less-Common Metals **5**, 78 (1963).

Molybdenum

Solvent medium	Diffusing element	Purity [a]	Preparation and properties	Method	Diffusion coefficient	Temperature range, °C	D_0 cm²/s	Q cal/mol	Comments	Ref.
Mo_2B.....	B.....	Not stated.	Boride layer was formed on a Mo cylinder by boronizing in boron carbide and borax.	Determination of the concentration gradient by microhardness measurements.	$\tilde{D}$ (chemical diffusion)	1100–1400	0.0696	45,000	$\tilde{D}$ was assumed to be independent of concentration; absence of a homogeneity range [2] was probably a major source of error.	[1]
Mo_2C.....	C.....	Not stated.	Carbide layer was formed on a Mo cylinder by carburizing in graphite.	Determination of the concentration gradient by microhardness measurements.	$\tilde{D}$	1400–1700	1,640	83,000	$\tilde{D}$ was assumed to be independent of concentration; narrow homogeneity range [3].	[1]

[a] Impurity concentrations are given in ppm unless otherwise stated.

[1] G. V. Samsonov and A. P. Epik, Dopovidi Akad. Nauk Ukr. RSR [1], 67 (1964).
[2] M. Hansen and K. Anderko, Constitution of Binary Alloys, p. 253 (McGraw-Hill Book Co., New York, N.Y., 1958).
[3] ibid., p. 370.

Niobium

Solvent medium	Diffusing element	Purity [a]	Preparation and properties	Method	Diffusion coefficient	Temperature range, °C	D_0 cm²/s	Q cal/mol	Comments	Ref.
Nb.....	C.....	Not stated.	Not stated.	Measurement of anelastic strain by elastic aftereffect and by internal friction.	D_T (tracer diffusion)	55–160	0.015	27,000	Effects of possible interstitial impurity (C, N, O) interactions were not ascertained.	[1]
Nb.....	C.....	Nb, 99.4 w/o; C, 1000 (max.); Ta, 5000; Ti, 400; Si, 200; Fe, 100. Degassed to reduce O and N damping peaks.	Carbon introduced by pyrolysis of hydrocarbons, and in a few samples by heating wires coated with graphite-water slurry.	Measurement of anelastic strain by elastic aftereffect and by internal friction.	D_T	140–275	0.004	33,020	Effects of interestitial impurity interactions were determined; carbide precipitation was observed at "high" C concentrations.	[2, 3]

[a] Impurity concentrations are given in ppm unless otherwise stated.

Solvent medium	Diffusing element	Purity [a]	Preparation and properties	Method	Diffusion coefficient	Temperature range, °C	D_0 cm²/s	Q cal/mol	Comments	Ref.
Nb	C	Nb, 99.01 w/o; Ta, 0.94 w/o; O, 400; Ti, Fe, Si and C not detected.	Porosity of metal ~ 13%; ^{14}C labeled emulsion pyrolyzed on specimen, specimens were cleaved and were fastened together in pairs along active faces.	Measurement of attenuation of β-radiation by the method of Gruzin [5] (ratio of activities).	D_T	900–1100	1.09×10^{-5}	32,000	High diffusivity paths probably existed along pores.	[4]
Nb	N	Nb, 99.4 w/o; C, 1000 (max.); Ta, 5000; Ti, 400; Si, 200; Fe, 100. Degassed to remove O and N initially.	N added by absorption of molecular nitrogen or NH_3.	Measurement of anelastic strain by elastic after-effect and by internal friction.	D_T	150–290	8.6×10^{-3}	34,920	Effects of interstitial impurity interactions were determined.	[2, 3]
Nb	N	Not stated.	N introduced by heating a wire in NH_3, followed by a brief vacuum anneal.	Measurement of anelastic strain by elastic after-effect.	D_T	285–310	0.098	38,600	Effects of possible interstitial impurity interactions were not ascertained.	[6]
Nb	N	Nb, 99.9 w/o	Nb foil; N introduced by annealing in air.	Measurement of anelastic strain by internal friction.	D_T	563–644		28,100	Effects of possible interstitial impurity interactions were not ascertained.	[7]
Nb	O	Nb, 99.4 w/o; C, 1000 (max.); Ta, 5000; Ti, 400; Si, 200; Fe, 100. Degassed to remove O and N initially.	O introduced by absorption of molecular oxygen.	Measurement of anelastic strain by elastic after-effect and by internal friction.	D_T	44–150	0.0212	29,910	Effect of interstitial impurity interactions were determined.	[2]
Nb	O	Not stated.	Not stated.	Measurement of anelastic strain by elastic after-effect.	D_T	148–168	0.0147	27,600	Effects of possible interstitial impurity interactions were not ascertained.	[6]
Nb	O	Nb, 99.9 w/o	Nb foil; O introduced by annealing in air.	Measurement of anelastic strain by internal friction.	D_T	377–423		22,000	Effects of possible interstitial impurity interactions were not ascertained.	[7]
Nb	O	O, 1000; N, 500; C, 300.	Nb cylinders machined from arc-melted buttons; reacted with O_2 in modified Sieverts apparatus; O_2 from decomposition of permanganate.	Determination of the concentration gradient by microhardness measurements.	$\tilde{D}$	600–1000	4.07×10^{-3}	24,900	The following were assumed: (a) $\tilde{D}$ independent of concentration, (b) Nb-Nb oxide boundary stationary.	[8]
NbB_2	B	Not stated.	Boride layer was formed on a Nb cylinder by boronizing in boron carbide and borax.	Determination of the concentration gradient by microhardness measurements.	$\tilde{D}$	1100–1400	2.94	59,000	$\tilde{D}$ was assumed to be independent of the B concentration.	[9]
NbC	C	Not stated.	Niobium sheets heated in presence of CH_4-Ar atmosphere.	Rate of carbide layer growth measured with filar micrometer.	$\tilde{D}$	1900–2300	1.2	79,000	The results represent average values for $\tilde{D}$ over the composition range. $\tilde{D}$ was assumed to be independent of concentration. The boundary compositions of the carbide layer were taken from phase equilibrium diagrams [11].	[10]
NbC	C	Nb slab; W, 290; Fe < 100; C, 100; Si, 50; W, 110; Ta, 600; Zr < 100.	Niobium slabs packed in high-purity lampblack and heated.	Rate of carbide layer growth; movement of inert markers (holes) in diffusion regions of bonded graphite and Nb slabs.	$\tilde{D}$	1700–2300	7.6	88,200	Nb was found to be immobile as compared to C. $\tilde{D}$ was assumed to be independent of concentration. X-ray data indicated higher diffusion rates in the more carbon deficient region of the NbC layer.	[12, 13]

[a] Impurity concentrations are given in ppm unless otherwise stated.

Solvent medium	Diffusing element	Purity [a]	Preparation and properties	Method	Diffusion coefficient	Temperature range, °C	D_0 cm²/s	Q cal/mol	Comments	Ref.
$NbC_{0.98}$	C	Not stated.	Nb carbides were synthesized from Nb_2O_5.	Measurement of attenuation of β-radiation by the method of Gruzin [5] (ratio of activities).	D^* (self-diffusion)	1600–2000	1.0×10^{-6}	32,300	High diffusivity paths probably existed along pores.	[4]
$NbC_{0.98}$	Nb	Not stated.	Nb carbides were synthesized from Nb_2O_5.	Measurement of attenuation of β-radiation by the method of Gruzin [5] (ratio of activities).	D^*	1800–2200	5.5×10^{-6}	55,000	High diffusivity paths probably existed along pores.	[4]
Nb_2C	C	Not stated.	Nb carbides were synthesized from Nb_2O_5.	Measurement of attenuation of β-radiation by the method of Gruzin [5] (ratio of activities).	D^*	1600–2000	5.7×10^{-6}	29,800	High diffusivity paths probably existed along pores.	[4]
Nb_4C_3	C	Not stated.	Nb carbides were synthesized from Nb_2O_5.	Measurement of attenuation of β-radiation by the method of Gruzin [5] (ratio of activities).	D^*	1600–2000	8.8×10^{-6}	35,300	High diffusivity paths probably existed along pores.	[4]
NbC:TiC	Nb	Starting materials: TiO_2 99.7 w/o; Nb 98 w/o; lamp black with 4 w/o ash residue.	TiO_2-Nb mixture carbidized with lamp black in graphite furnace, carbide powder pressed and sintered; density 6.55 g/cm³; grain size 20–30 μm.	Measurement of attenuation of β-radiation by the method of Zhukhovitskii and Geodakyan [15] (nonexponential absorption).	D^*	2170–2280	470	120,000		[14]
$Nb_2O_{4.975}$	O	Ta_2O_5, 0.01 w/o; SiO_2, 0.02 w/o; TiO_2, 0.005 w/o; Fe_2O_3, 0.003 w/o.	Hot-pressed anion-deficient oxide slabs, density of 4.55 g/cm³.	Microphotometric determination of the color change associated with the advance of an "oxygen-rich" front into an oxygen deficient oxide slab.	$\bar{D}$	500–900	0.038	28,200	$\bar{D}$ was measured for the particular oxide composition given.	[16]
Nb_2O_5 + 1 m/o ZrO_2.	O	Impurity content of Nb_2O_5 same as given above.	Hot-pressed anion-deficient oxide slabs, densities varied between 4.52 and 4.55 g/cm³.	Microphotometric determination of the color change associated with the advance of an "oxygen-rich" front into an oxygen-deficient oxide slab.	$\bar{D}$	500–900	0.00201	24,000		[16]
Nb_2O_5 + 1 m/o TiO_2.	O	Impurity content of Nb_2O_5 same as given above.	Hot-pressed anion-deficient oxide slabs, densities varied between 4.52 and 4.55 g/cm³.	Microphotometric determination of the color change associated with the advance of an "oxygen-rich" front into an oxygen-deficient oxide slab.	$\bar{D}$	500–900	0.0262	30,700		[16]
Nb_2O_5 + 1 m/o. V_2O_5.	O	Impurity content of Nb_2O_5 same as given above.	Hot-pressed anion-deficient oxide slabs, densities varied between 4.52 and 4.55 g/cm³.	Microphotometric determination of the color change associated with the advance of an "oxygen-rich" front into an oxygen-deficient oxide slab.	$\bar{D}$	500–900	0.0432	32,400		[16]

[a] Impurity concentrations are given in ppm unless otherwise stated.

[1] C. A. Wert, J. Appl. Phys. **21,** 1196 (1950).
[2] R. W. Powers and M. V. Doyle, J. Appl. Phys. **30,** 514 (1959).
[3] ibid. Trans. AIME **209,** 1285 (1957).
[4] P. V. Gel'd and V. D. Lyubimov, Isv. Akad. Nauk SSSR, Otdel. Tekh. Nauk Met. I Toplivo [6], 199 (1961).
[5] P. L. Gruzin, Dokl. Akad. Nauk SSSR **86,** 289 (1952).
[6] C. Y. Ang. Acta Met. **1,** 123 (1953).
[7] J. W. Marx, G. S. Baker and J. M. Silvertsen, Acta Met. **1,** 193 (1953).
[8] W. D. Klopp, C. T. Sims, and R. I. Jaffe, Trans, ASM **51,** 282 (1959).
[9] G. V. Samsonov and A. P. Epik, Dopovidi Akad. Nauk Ukr. RSR [1], 67 (1964).
[10] R. Resnick, R. Steinitz and L. Seigle, Trans. AIME **223,** 1915 (1965).
[11] E. K. Storms and N. H. Krikorian, J. Phys. Chem. **64,** 1471 (1960).
[12] W. F. Brizes, L. H. Cadoff and J. M. Tobin, J. Nucl. Mater. **20,** 57 (1966).
[13] J. M. Tobin, L. M. Adelsberg, L. H. Cadoff and W. F. Brizes, Nuclear applications of nonfissionable ceramics, p. 257, American Nuclear Society and American Ceramic Society (American Nuclear Society, Inc., Hinsdale, Ill., 1966).
[14] M. L. Baskin, V. I. Tret'yakov, and I. N. Chaporova, Fiz. Metal. I Metallovid. **12,** 860 (1961).
[15] A. A. Zhukhovitskii and V. A. Geodakyan, Dokl. Akad. Nauk SSSR **102,** 301 (1955).
[16] D. L. Douglass, Corrosion of Reactor Materials, **2,** p. 233 (International Atomic Energy Agency, Vienna, Austria, 1962).

Solvent medium	Diffusing element	Purity [a]	Preparation and properties	Method	Diffusion coefficient	Temperature range, °C	D_0 cm²/s	Q cal/mol	Comments	Ref.
Ta	C	Not stated.	Not stated.	Measurement of anelastic strain by after-effect and by internal friction.	D_T (tracer diffusion)	55–160	0.015	27,000	Effects of possible interstitial impurity (C, N, O) interactions were not ascertained.	[1]
Ta	C	Metallic contaminants not stated; 99.9 w/o Ta; C, 100–900.	C was added to a degassed wire by pyrolysis of carbonaceous vapor or by heating a wire coated with a carbon black-water slurry.	Measurement of anelastic strain by elastic after-effect and by internal friction.	D_T	193–350	6.1×10^{-3}	38,510	Effects of interstitial impurity interactions were determined; carbide precipitation was observed at "high" C concentrations.	[2]
Ta	C	C, 1000.	^{14}C was introduced into about 10 mm center portion of a 70 mm Ta wire.	Determination of the concentration gradient by radioisotope distribution.	D_T	600–2600	2.78×10^{-3}	24,600	An increase in the activation energy was observed below 800 °C.	[3]
Ta	N	Metallic contaminants not stated; 99.9 w/o Ta; O, 320; N, 50–1000.	Degassed wire was enriched in N by heating in N_2 or NH_3 at low partial pressure.	Measurement of anelastic strain by elastic after-effect and by internal friction.	D_T	187–350	5.6×10^{-3}	37,840	Effects of interstitial impurity were determined.	[2]
Ta	N	Not stated.	N introduced by heating a wire in NH_3, followed by a brief vacuum anneal.	Measurement of anelastic strain by elastic after-effect and by internal friction.	D_T	360–662	0.0123	39,800	Effects of possible interstitial impurity interactions were not ascertained.	[4]
Ta	N	C, 60; N < 20; W, 1000; Cu < 40; Fe < 50; Si < 100; Ti < 50; Mo < 80; Sn < 40; Nb, 500; O, 60; all others < 20.	Cold-rolled specimens were polished, annealed, etched; reacted with N_2 (99.995 v/o).	Determination of the concentration gradient by microhardness measurements.	$\tilde{D}$ (chemical diffusion)	800–1000	0.024	40,900	Linear dependence of hardness on N concentration was demonstrated by Gebhardt et al. [13]; $\tilde{D}$ was assumed to be independent of the N concentration.	[5]
Ta	N	O, 16; N, 10; C, 30; Nb, 100–300; Cu, 30; all others < 10.	Ta plates were used below 1000 °C, cylindrical specimens were used above 1000 °C: vacuum annealed; reacted with prepurified N_2 (99.996 v/o).	Determination of concentration gradient by microhardness measurements.	$\tilde{D}$	800–1300	0.0182	41,100	$\tilde{D}$ was assumed to be independent of the N concentration.	[6]
Ta	O	Metallic contaminants not stated; 99.9 w/o Ta; O, 90–1630; N, 50.	Degassed Ta wire loaded with O by heating in O_2 at low partial pressure.	Measurement of anelastic strain by elastic after-effect and by internal friction.	D_T	38–250	4.4×10^{-3}	25,450	Effects of interstitial impurity interactions were determined.	[2]
Ta	O	Not stated.	Not stated.	Measurement of anelastic strain by elastic after-effect and by internal friction.	D_T	155–355	0.0190	27,300	Effects of possible interstitial impurity interactions were not ascertained.	[4]
Ta	O	Not stated.	Band-shaped specimens with one section enriched in O used.	Determination of the concentration gradient by microhardness measurements.	D	700–1400	0.015	26,700	Linear dependence of hardness on O concentration was demonstrated up to 1.1 at. % O. D was assumed to be independent of the O concentration.	[7]
Ta	O	O, 16; N, 10; C, 30; Nb, 100–300; Cu, 30; all others < 10.	Ta plates were used below 1000 °C, cylindrical specimens were used above 1000 °C; vacuum annealed; reacted with O_2 from decomposition of permanganate.	Determination of the concentration gradient by microhardness measurements.	D	900–1200	2.14×10^{-3}	22,900	Linear dependence of hardness on O concentration was established at low concentrations by [8]. D was assumed to be independent of the O concentration.	[6]
TaB_2	B	Not stated.	Boride layer was formed on a Ta cylinder by boronizing in boron carbide and borax.	Determination of the concentration gradient by microhardness measurements.	D	1100–1400	9.44×10^{-4}	47,000	D was assumed to be independent of the B concentration.	[9]

[a] Impurity concentrations are given in ppm unless otherwise stated.

Tantalum—Continued

Solvent medium	Diffusing element	Purity[a]	Preparation and properties	Method	Diffusion coefficient	Temperature range, °C	D_0 cm²/s	Q cal/mol	Comments	Ref.
TaC.....	C.....	Nb, 40–50; Ti, < 25; Mo, < 40; W < 40; all others < 50; O_2 and N_2 ~ 100 in carbide slab.	Slabs with marker holes near the surface were carburized in high purity graphite powder, for Kirckendall shift measurements. TaC slabs with low carbon content (45 to 46 at pct C) were heated in CH_4-Ar mixture for chemical diffusion measurements.	Determination of carbon concentration profile by x-ray diffraction analysis; A Matano analysis was performed, but values of D_0 and Q were calculated from values of $\bar{D}$ averaged over the slab.	$\bar{D}$	1700–2700	0.18	85,000	The marker movement study indicated that D_C: $D_{Ta} \cong 80{:}1$ in TaC at 2500 °C. The Matano analysis indicated that $\bar{D}$ had a complicated dependence on C concentration. Grain boundary diffusion was not important.	[10]
TaC.....	C.....	Not stated.		Determination of carbon concentration profiles by electron microprobe analysis.	$\bar{D}$	2100–2650	1.8	87,000	The carbon concentration profiles were found to be nonlinear in the TaC layer.	[11]
TaC.....	C.....	Nb, 50; Ti < 25; Fe, 10; Mo < 50; W < 50; all other metals < 50; O, 15–75; N, 10–30; C, 10–30.	Carbide layer was formed by heating Ta sheets in an Ar-methane atmosphere.	Measurement of the rate of movement of the TaC-Ta_2C and Ta_2C-Ta interfaces.	$\bar{D}$	1800–2700	1.04	86,000	Rate of movement of the interfaces was assumed to be controlled by diffusion through the carbide layers. D was assumed to be independent of the C concentration.	[12]
TaC.....	W.....	Free C, 500; Fe, 800.	Carbide was formed by carburization in graphite charge; carbide powder sintered; density 14.2 g/cm³; porosity 3 %; grain size 50–100 μm.	Measurement of the attenuation of the β-radiation by the method of Kryukov and Zhukhovitskii [14].	D^* (self-diffusion)	2130–2300	19.2	142,000	There may be some error in this data due to vaporization of the radioactive layer.	[13]
Ta_2C.....	C.....	Nb, 50; Ti < 25; Fe, 10; Mo < 50; W < 50; all other metals < 50; O, 15–75; N, 10–30; C, 10–30.	Carbide layer was formed by heating Ta sheets in Ar-methane atmosphere.	Measurement of the rate of movement of TaC-Ta_2C and Ta_2C-Ta interfaces.	$\bar{D}$	1800–2700	7.0	89,000	Rate of movement of the interfaces was assumed to be controlled by diffusion through the carbide layers. D was assumed to be independent of C concentration.	[15]

[a] Impurity concentrations are given in ppm unless otherwise stated.

[1] C. A. Wert, J. Appl. Phys. **21**, 1196 (1950).
[2] R. W. Powers and M. V. Doyle, J. Appl. Phys. **28**, 255 (1957); ibid **30**, 514 (1959).
[3] D. F. Kalinovich, I. I. Kovenskiy, and M. D. Smolin, Fiz. Metal. I Metalloved. **18**, 314 (1964).
[4] C. Y. Ang, Acta Met. **1**, 123 (1953).
[5] K. Östhagen and P. Kofstad, J. Less-Common Metals **5**, 7 (1963).
[6] W. M. Albrecht, W. D. Kloop, B. G. Koehl, and R. I. Jaffe, Trans. AIME **221**, 110 (1961).
[7] E. Gebhardt, H. D. Seghezzi, and A. Stegherr, Z. Metallk. **48**, 624 (1957).
[8] R. H. Perkins, U.S. At. Energy Comm. Report LA-2136 (1957).
[9] G. V. Samsonov and A. P. Epik, Dopovidi Akad. Nauk Ukr. RSR [1], 67 (1964).
[10] R. Resnick and L. Seigle, Trans. AIME **236**, 1732 (1966).
[11] J. M. Tobin, L. M. Adelsberg, L. H. Cadoff, and W. F. Brizes, Nuclear applications of non-fissionable ceramics, p. 257, American Nuclear Society and American Ceramic Society (American Nuclear Society, Inc., Hinsdale, Ill., 1966).
[12] R. Resnick, R. Steinitz, and L. Steigle, Trans. AIME **233**, 1915 (1965).
[13] M. S. Baskin, V. I. Tret'yakov, and I. N. Chaporova, Fiz. Metal. I Metalloved. **14**, 422 (1962).
[14] A. A. Zhukhovitskii and S. N. Kryikov, Dokl. Akad. Nauk SSSR **102**, 301 (1955).
[15] E. Gebhardt, H. D. Seghezzi, and W. Dürrschnabel, Plansee Proc. 3rd Plansee Seminar, Reutte, Austria, p. 291 (1958).

Thorium

Solvent medium	Diffusing element	Purity[a]	Preparation and properties	Method	Diffusion coefficient	Temperature range, °C	D_0 cm²/s	Q cal/mol	Comments	Ref.
Th.....	C, 0.4 w/o.	Not stated.	Thorium cylinders were carburized in a graphite charge.	Determination of the concentration gradient by chemical analysis.	$\bar{D}$ (chemical diffusion)	1000–1200	~ 0.03	38,200	The concentration dependence of D was determined by the method of Smith and Danielson [2]; D_0 has a large uncertainty.	[1]
ThO_2.....	Ce.....	Not stated.	Grain size 0.2 μm; irradiated with 3.8×10^{17} fast neutrons/cm².	Determination of the rate of leaching of fission products into molten NaCl.	D_T (tracer diffusion)	910–1010	5.5×10^{-7}	70,000		[3]

[a] Impurity concentrations are given in ppm unless otherwise stated.

Solvent medium	Diffusing element	Purity[a]	Preparation and properties	Method	Diffusion coefficient	Temperature range, °C	D_0 cm²/s	Q cal/mol	Comments	Ref.
ThO_2	I	Not stated.	ThO_2 powder, was irradiated for 32 days at 3×10^{13} n/cm²/s (fast); post-irradiation anneals, I collected on Ag wool at 400 °C.	Measurement of the rate of release of fission gas from irradiated powder.	D_T	800–1220	7×10^{-11}	28,600		[4]
ThO_2	Kr	Not stated.	Sintered ThO_2; Kr was introduced by ion bombardment.	Measurement of the rate of Kr release from ion bombarded sample.	D_T	1100–1350		104,000	D_0 was assumed to be $\sim3\times10^{-1\pm1}$ cm²/s for purposes of calculating D from the release data.	[5]
ThO_2	Kr	Si ~ 3; Mg and Cu ~ 1; all other elements were not detectable.	ThO_2 powder; irradiated with fast neutron, dosage 10^{20} nvt.[b]	Measurement of the rate of Kr release neutron irradiated powder.	D_T	600–1200	2.5×10^{-10}	32,300		[6]
ThO_2	Nb	Not stated.	Grain size 0.2 μm; irradiated with 3.8×10^{17} fast neutrons/cm².	Determination of the rate of leaching of fission products into molten NaCl.	D_T	820–960	8.3×10^{-6}	65,400		[3]
ThO_2	O	Not stated.	Grain size about 10 μm.	Heterogeneous isotopic exchange between a solid sample and a gas.	D^* (self-diffusion)	800–1420	1×10^{-8}	14,700	Low values of D_0 and Q are suggestive of grain-boundary diffusion.	[7]
ThO_2	O	Co, Mg, Fe each < 100.	ThO_2 powder fused into spheres in a plasma torch.	Heterogeneous isotopic exchange between a solid sample and a gas.	D^*	800–1500	4.4	65,800	Finite rate of exchange accounted for in treatment of results.	[8]
ThO_2	Rn	Not stated.	ThO_2 was labeled with Rn by recoil from α-decay of Ra adsorbed on the powder; the Ra was quantitatively removed after labeling.	Measurement of the rate of release of Rn from recoil labeled powder.	D_T	565–1515		59,000		[4]
ThO_2	Rn	Not stated.	Sintered ThO_2; Rn was introduced by recoil from α-decay of Ra on one face of sample; the Ra was quantitatively removed after labeling.	Measurement of the rate of release of Rn from recoil labeled disk.	D_T	1100–1300		93,000	D_0 was assumed to be $\sim3\times10^{-1\pm1}$ cm²/s for purposes of calculating D from the release data.	[5]
ThO_2	Th	Not stated.	ThO_2 pellets; 97.5% of theoretical density.	Determination of isotopic concentration gradient by mass spectrometric analysis of thin sections.	D^*	925–1480	4×10^{-8}	27,000	Data was adjusted to eliminate grain-boundary contribution.	[9]
ThO_2	Xe	Not stated.	ThO_2 powder was irradiated for 32 days at 1.5×10^{14} n/cm² (thermal), post-irradiation anneals.	Measurement of the rate of release of fission gas from irradiated powder.	D_T	700–1220		30,000		[4]
ThO_2	Xe	Not stated.	Single crystal ThO_2; neutron dose $\sim3\times10^{16}$ n/cm² (fast).	Measurement of the rate of release of fission gas from irradiated crystals.	D_T	1200–2000	1×10^{-4} -2×10^{-3}	81,000	Based on preliminary D/a^2 values (a = average particle radius).	[10]
ThO_2	Xe	Not stated.	Polycrystalline ThO_2; neutron dose 7×10^{15} n/cm² (fast).	Measurement of the rate of release of fission gas from irradiated powder.	D_T	500–1100		37,000	Evaluated as D/a^2 values after subtraction of the initial burst.	[10]
ThO_2	Xe	Th, 99.23 m/o; U 0.77 m/o.	ThO_2 powder; neutron dose $\sim2.4\times10^{12}$ nvt (thermal).	Measurement of the rate of release of fission gas from irradiated powder.	D_T	800–1600		50,000		[11]

[a] Impurity concentrations are given in ppm unless otherwise stated.
[b] The notation "nvt" represents a quantity of neutron exposure and has the units neutron–cm^{-2}.

Thorium—Continued

Solvent medium	Diffusing element	Purity [a]	Preparation and properties	Method	Diffusion coefficient	Temperature range, °C	D_0 cm²/s	Q cal/mol	Comments	Ref.
ThO_2.....	Zr.....	Not stated.	Grain size 0.2 μ; irradiated with 3.8×10^{17} fast neutrons/cm².	Determination of the rate of leaching of fission products into molten NaCl.	D_T	840–960	6.9×10^{-7}	62,300		[3]
ThO_2 + 12%UO_2	Kr.....	Not stated.	Sintered ThO_2-UO_2 compact; Kr was introduced by ion bombardment.	Measurement of the rate of Kr release from ion bombarded sample.	D_T	1250–1350		110,000	D_0 was assumed to be $\sim 3 \times 10^{-121}$ cm²/s for purposes of calculating D from the release data.	[5]
ThO_2 + 10%Y_2O_3	Se.....	Th 89.39 m/o; U, 0.70 m/o; Y, 9.91 m/o.	Neutron dose $\sim 2.4 \times 10^{17}$ nvt (thermal)	Measurement of the rate of release of fission gas from irradiated powder.	D_T	1000–1600		75,000		[11]
ThO_2 + 30%Y_2O_3	Se.....	Th 69.48 m/o; U, 0.74 m/o; Y 29.78 m/o.	Neutron dose $\sim 2.4 \times 10^{17}$ nvt (thermal)	Measurement of the rate of release of fission gas from irradiated powder.	D_T	900–1600		90,000		[11]

[a] Impurity concentrations are given in ppm unless otherwise stated.
[b] The notation "nvt" represents a quantity of neutron exposure and has the units neutron-cm^{-2}.

[1] D. T. Peterson, Trans. ASM **53,** 765 (1961).
[2] J. F. Smith and G. C. Danielson, J. Chem. Phys. **22,** 266 (1954).
[3] R. Thomas and R. Lindner, Radiochimica Acta **4,** 170 (1965).
[4] Hj. Matzke and R. Lindner, Z. Naturforsch **15a,** 647 (1960).
[5] R. Kelly and Hj. Matzke, J. Nuclear Mater. **17,** 179 (1965).
[6] Hj. Matzke, Z. Naturforsch. **16a,** 1255 (1961).
[7] C. S. Morgan and C. S. Yust, U. S. At. Energy Comm. Report ORNL–3160, 41 (1961).
[8] H. S. Edwards, A. F. Rosenberg, and J. T. Bittel, Technical Documentary Report ASD–TDR–63–635, 2 (1963).
[9] C. S. Morgan and C. S. Yust, U. S. At. Energy Comm. Report ORNL–3313, 142 (1962).
[10] F. Felix, T. Lagerwall, P. Schmeling, and K. E. Zimen, Third Geneva Conf. A/CONF. 28/P/472, 363 (1964).
[11] G. Long, W. P. Stanaway, and D. Davies, At. Energy Research Establishment Report AERE–M 1251 (1964).

Titanium

Solvent medium	Diffusing element	Purity [a]	Preparation and properties	Method	Diffusion coefficient	Temperature range, °C	D_0 cm²/s	Q cal/mol	Comments	Ref.
α-Ti.....	C.....	Other than C: O, 180–2360 (highest in C-Ti alloy); H, 90–200; N, 110–340; Al, 30; Fe, 10–70; Si, 20–50; Mn, 10–30; all others ≦ 10.	C-Ti alloy (0.4 w/o or higher in C) buttwelded to high purity Ti (0.038 w/o C).	Determination of the concentration gradient by chemical analysis.	$\tilde{D}$ (chemical diffusion coefficient).	736–882	5.06	43,500	$\tilde{D}$ was assumed to be independent of C concentration.	[1]
β-Ti.....	C.....		C-Ti alloy (0.4 w/o or higher in C) buttwelded to high purity Ti (0.038 w/o C).	Determination of the concentration gradient by chemical analysis.	D	920–1150	108	48,400	$\tilde{D}$ was assumed to be independent of concentration.	[1]
β-Ti.....	N.....	Principal impurities: C, 360; Mn, 300; O, 110; Al, 100. Commercial N_2 passed through liquid N_2 trap or tube furnace with Ti turnings.	Argon-arc-melted iodide Ti, hot-forged and rolled, swaged cold to rod-shaped, machined into cylindrical specimens.	Determination of the concentration gradient by chemical analysis (Kjeldahl).	$\tilde{D}$	800–1400	3.5×10^{-2}	33,800	Measurements were complicated by formation of outer nitride layer and α-phase, but less than 3% of cylindrical radius; $\tilde{D}$ was assumed to be independent of concentration.	[2]
α-Ti.....	O.....	Not stated.	VT-1 Ti, samples were polished and then etched for 60 s in 7% Hf in HNO_3.	Determination of the concentration gradient by microhardness measurements.	$\tilde{D}$	800–900	1.80×10^{-3}	35,900	$\tilde{D}$ was assumed to be independent of concentration; hardness was assumed to be linearly dependent on the concentration of O.	[3]
α-Ti.....	O.....	Fe, Mn, Al, Sn, Mg and Cr, each 100; Cu, 10.	Electron-beam-melted titanium.	Determination of the concentration gradient by microhardness measurements.	$\tilde{D}$	800–1000	0.5	51,000	$\tilde{D}$ was assumed to be independent of concentration; hardness was assumed to be linearly dependent on concentration of O.	[4]

[a] Impurity concentrations are given in ppm unless otherwise stated.

Solvent medium	Diffusing element	Purity[a]	Preparation and properties	Method	Diffusion coefficient	Temperature range, °C	D_0 cm²/s	Q cal/mol	Comments	Ref.
α-Ti	O	Si, 600; Fe, 1500; Al, 2000; Mg, 200; Mn, 100–500; W, 300; N, 100; all others ≦ 100.	Ti bars were oxidized by TiO_2 powder.	Determination of the concentration gradient by microhardness measurements.	$\tilde{D}$	700–850	5.08×10^{-3}	33,500	$\tilde{D}$ was assumed to be independent of concentration; hardness was assumed to be linearly dependent on the concentration of O.	[5]
β-Ti	O	Principal impurities: C, 360; Mn, 300; O, 110; Al, 100. Dried commercial O_2 and O_2 from decomposition of permanganate were used.	Argon-arc-melted iodide Ti, hot-forged and rolled, swaged cold to rod-shape, machined into cylindrical specimens.	Determination of the concentration gradient by chemical analysis (vacuum fusion with tin).	$\tilde{D}$	950–1414	1.6	48,200	$\tilde{D}$ was assumed to be independent of concentration.	[2]
β-Ti	O	Si, 600; Fe, 1500; Al, 2000; Mg, 200; Mn, 10–50; W, 300; Ni, 10; all others ≦ 100.	Ti cylinders were oxidized by TiO_2 powder.	Determination of the concentration gradient by microhardness measurements.	$\tilde{D}$	930–1150	3.14×10^{4}	68,700	Measurements were complicated by grain growth and formation of the α-phase. $\tilde{D}$ was assumed to be independent of concentration; hardness was assumed to be linearly dependent on concentration.	[5]
β-Ti	O	Ti, 99.7 w/o, Cu major impurity.	Ti-wire (Ti-75A); initially ~ 1 mm section of wire oxidized in O_2.	Determination of the concentration gradient by change in resistance along the sample.	$\tilde{D}$	1130–1350	0.083	31,200	Results may be complicated by formation of α-phase which would be stabilized by oxygen atoms in the metal; linear dependence of resistance on O concentration up 1% O was verified by [24].	[6]
TiB_2	B	Not stated.	Boronization of surface of Ti-cylinder by heating in a boron carbide-borax charge.	Determination of the concentration gradient by microhardness measurements.	$\tilde{D}$	1100–1400	8.9×10^{-5}	30,600	$\tilde{D}$ was assumed to be independent of B concentration.	[7]
TiC	C	Not stated.	Carburization of the surface of Ti cylinder by heating in a boron carbide-borax charge.	Determination of the concentration gradient by microhardness measurements.	$\tilde{D}$	900–1300	2.04×10^{-3}	33,000	$\tilde{D}$ was assumed to be independent of concentration.	[7]
TiC	Nb	Free C, 4000; Fe, 150; N, 350.	Carburization of $TiO_2 + C$ in vacuum furnace with graphite heater, carbide was crushed, Fe was removed with HCl; density approximated theoretical values.	Method of Zhukhovitskii and Geodakyan [8]; nonexponential attenuation of β-radiation when a radioisotope diffuses into a solid.	D_T (tracer diffusion).	1935–2170	2.4	84,000		[9]
TiC·NbC (1:1)	Nb	Free C, 2600; Fe. 200; N, 700.	Carburization of $TiO_2 + NbC + C$ in vacuum furnace, etc.	Method of Zhukhovitskii and Geodakyan.	D^* (self-diffusion).	2170–2280	470	120,000		[9]
TiC	W	Free C, 1100	Carburization of TiO_2 in vacuum furnace; porosity up to 0.2%; grain size 50–100 μm; density 4.97 g/cm³.	Method of Kryukov and Zhukhovitskii [10]; diffusion of thin radioactive layer into thin sample (30 to 100 μm).	D_T	2130–2300	7.7	115,000	There may be some error in this data due to vaporization of the radioactive layer.	[11]
TiC·WC (77:23)	W	Free C, 1700.	Carburization in vacuum furnace; porosity 0.2%; grain size 50–70 μm; density 7.35 g/cm³.	Method of Kryukov and Zhukhovitskii.	D^*	2130–2300	31.6	138,000	Measurements also were made on other mixed carbides, but these appear to have large errors due to vaporization of the radioactive layer.	[11]

[a] Impurity concentrations are given in ppm unless otherwise stated.

Solvent medium	Diffusing element	Purity[a]	Preparation and properties	Method	Diffusion coefficient	Temperature range, °C	D_0 cm²/s	Q cal/mol	Comments	Ref.
TiO_2	Ba	Rutile: traces of Si and Fe Ba: Ca, 2; Mg, 1; Cu, 1; Na, 1.	^{133}Ba labeled carbonate was decomposed to oxide on TiO_2 single crystal in O_2 atmosphere, second-phase region formed in TiO_2.	Determination of the concentration gradient by radioisotope distribution, Matano analysis [12, 13].	$\tilde{D}$, perpendicular to C axis of crystal.	1100–1200		~59,000		[14]
TiO_2	Ba	Rutile: traces of Si and Fe Ba: Ca, 2; Mg, 1; Cu, 1; Na, 1.	^{133}Ba labeled carbonate was decomposed to oxide on TiO_2 single crystal in O_2 atmosphere, second-phase region formed in TiO_2.	Determination of the concentration gradient by radioisotope distribution, Matano analysis.	$\tilde{D}$, parallel to C axis of crystal.	1100–1200		~43,000		[14]
TiO_2	Fe	Impurities not precipitated with NH_3, 1000; Fe, 100; heavy metals of sulfide type, 500.	TiO_2 powder was compressed into pellets and sintered at 1100 °C; ^{59}Fe was vacuum deposited on pellet face.	Determination of the concentration gradient by radioisotope distribution.	D_T (air)	800–1000	1.98×10^{-2}	55,000		[15]
TiO_2	Fe	Impurities not precipitated with NH_3, 1000; Fe, 100; heavy metals of sulfide type, 500.	TiO_2 powder was compressed into pellets and sintered at 1100 °C; ^{59}Fe was vacuum deposited on pellet face.	Determination of the concentration gradient by radioisotope distribution.	D_T (vacuum).	770–1000	0.192	55,400		[15]
TiO_2	Fe	Impurities not precipitated with NH_3, 1000; Fe, 100; heavy metals of sulfide type, 500.	TiO_2 powder was compressed into pellets and sintered at 1100 °C; ^{59}Fe was vacuum deposited on pellet face.	Determination of the concentration gradient by radioisotope distribution.	D_{gr}, grain-boundary diffusion in the presence of air.	800–1000	1.56×10^{-3}	34,000		[15]
TiO_2	Fe	Impurities not precipitated with NH_3, 1000; Fe, 100; heavy metals of sulfide type, 500.	TiO_2 powder was compressed into pellets and sintered at 1100 °C; ^{59}Fe was vacuum deposited on pellet face.	Determination of the concentration gradient by radioisotope distribution.	D_{gr} (vacuum).	770–1000	1.13×10^{-3}	34,700		[15]
TiO_2	Li	Not stated.	Single crystal TiO_2 doped uniformly with Li.	Measurement of the change in optical absorption due to the diffusion of Li out of the crystal.	$\tilde{D}$, parallel to C axis of crystal.	80–550	0.295	7,610	Impurity concentration and surface damage were observed to affect diffusion rates; impurities were minimized by taking cuts near center of boule; abrasion of surfaces was used to control diffusion direction.	[16]
TiO_2	O	Al_2O_3, 100 to 200; infrared measurements showed that OH-groups were present.	Single crystal TiO_2 pulverized to 10–250 μm.	Heterogeneous isotopic exchange between solid sample and a gas.	D^* (self-diffusion).	700–1300	2.0×10^{-3}	60,000	"High" Al_2O_3 concentration may have caused extrinsic diffusion.	[17, 18]
TiO_2	Rn	Not stated.	TiO_2 powder labeled with Rn by recoil from Ra decay.	Hahn emanation technique, modified by mixing oxide powder with Ra salt allowing Rn to recoil into oxide and then dissolving away the Ra.	D_T	315–1150		22,000		[19]
TiO_2	Sn	Not stated.	TiO_2 single crystal; SnO_2 applied to face of crystal.	Determination of the concentration gradient by x-ray analysis (change in the intensity of x rays reflected as TiK_α and $SnL_{\alpha 1}$).	D_T, parallel to C axis of crystal.	900–1050	0.16	80,000		[20]

[a] Impurity concentrations are given in ppm unless otherwise stated.

Titanium—Continued

Solvent medium	Diffusing element	Purity[a]	Preparation and properties	Method	Diffusion coefficient	Temperature range, °C	D_0 cm²/s	Q cal/mol	Comments	Ref.
$BaTiO_3$	Ba	Not stated.	$BaCO_3$ reacted with TiO_2 to form $BaTiO_3$; compressed and sintered, 80% of theoretical density.	Determination of the concentration gradient by radioisotope distribution.	D^*	884–1180	0.8	89,000		[21]
$SrTiO_3$	O	Mg ≦ 1; Si ~ 100; Al ≦ 10; Au ≦ 1; Pb, 10.	Single crystal; dislocation density of ~ 1.4×10^6/cm².	Heterogeneous isotopic exchange between a solid sample and a gas.	D^*	825–1200	1.6×10^{-7}	15,500	Low frequency factor, D_0, was taken as evidence for extrinsic diffusion; diffusion rate was found to depend on dislocation density.	[22]
$SrTiO_3$	O	Mg ≦ ; Si ~ 10; Al ≦ 10; Au ≦ 1; Pb, 10.	Single crystal; dislocation density ~ 6.6×10^5/cm².	Heterogeneous isotopic exchange between a solid sample and a gas.	D^*	850–1525	1.2×10^{-5}	29,300	Possible extrinsic diffusion; diffusion rate was found to depend on dislocation density.	[22]
$SrTiO_3$	Sr	Not stated.	$SrCO_3$ was reacted with anatase to form $SrTiO_3$; compressed and sintered; 95% theoretical density.	Method of Kryukov and Zhukhovitskii.	D^*	1000–3000	4.0	70,000		[23]

[a] Impurity concentrations are given in ppm unless otherwise stated.

[1] F. C. Wagner, E. J. Bucur and M. A. Steinberg, Trans. ASM **48,** 742 (1956).
[2] R. J. Wasilewski and G. L. Kehl, J. Inst. Metals **83,** 94 (1954).
[3] A. V. Revyakin, Izv. Akad. Nauk SSSR, Otdel, Tekh. Nauk, Met. I Toplivo 113 (1961).
[4] P. Kofstad, P. B. Anderson, and O. J. Krudtaa, J. Less-Common Metals **3,** 89 (1961).
[5] W. P. Roe, H. R. Palmer, and W. R. Opie, Trans. ASM **52,** 191 (1960).
[6] F. Claisse and H. P. Koenig, Acta Met. **4,** 650 (1956).
[7] G. V. Samsonov and A. P. Epik, Dopovidi Akad. Nauk Ukr. RSR [1], 67 (1964).
[8] A. A. Zhukhovitskii and V. A. Geodakyan, Dokl. Akad. Nauk SSSR **102,** 301 (1955).
[9] M. L. Baskin, V. I. Tret'yakov, and I. N. Chaporova, Fiz. Metal. I Metalloved. **12,** 860 (1961).
[10] A. A. Zhukhovitskii and S. N. Kryukov, Dokl. Akad. Nauk SSSR **90,** 379 (1953).
[11] M. L. Baskin, V. I. Tret'yakov, and I. N. Chaporova, Fiz. Metal I Metalloved. **14,** 422 (1962).
[12] J. Boltzmann, Ann. Physik **53,** 959 (1894).
[13] C. Matano, Japan. J. Phys. **8,** 109 (1933).
[14] T. Nakayama and T. Sasaki, Bull. Chem. Soc. Japan **36,** 569 (1963).
[15] V. I. Izvekov and K. M. Gorbunova, Fiz. Metal. I Metalloved. **7,** 713 (1959).
[16] O. W. Johnson, Phys. Rev. **136,** A284 (1964).
[17] R. Haul, D. Just, and G. Dumbgen, Reactivity of Solids, p. 65 (Elsevier Publishing Co., Amsterdam, Netherlands, 1961).
[18] R. Haul and G. Dumbgen, J. Phys. Chem. Solids **26,** 1 (1965).
[19] R. Lindner and Hj. Matzke, Z. Naturforsch. **15a,** 1082 (1960).
[20] W. R. Sinclair and T. C. Loomis, Kinetics of High Temperature Processes, p. 58 (Technology Press, Cambridge, Mass., 1959).
[21] A. G. Verduch and R. Lindner, Arkiv. Kemi **5,** 313 (1953).
[22] A. E. Paladino, L. G. Rubin, and J. S. Waugh, J. Phys. Chem. Solids **26,** 391 (1965).
[23] P. Turlier, P. Bussiere, and M. Preffe, Compt. Rend. **250,** 1649 (1960).
[24] R. I. Jaffe and I. E. Campbell, Trans. AIME **185,** 646 (1949).

Zirconium

Solvent medium	Diffusing element	Purity[a]	Preparation and properties	Method	Diffusion coefficient	Temperature range, °C	D_0 cm²/s	Q cal/mol	Comments	Ref.
β-Zr	C	Hf, 700; N, 140; Fe, 400; Si, 500.	Zr-bars were melted in an electron arc furnace; ^{14}C was added to some specimens which were continually remelted to obtain uniform distribution.	Determination of the concentration gradient by radioisotope distribution.	$\tilde{D}$ (chemical diffusion).	900–1260	0.0048	26,700	$\tilde{D}$ was assumed to be independent of concentration.	[1]
β-Zr	N	Hf, 150; Fe, 250; Si, 100; Sn, 100; all others < 100.	Zr: iodide-crystal bars were produced by deBoer process, double arc melted, cold rolled into rods. Prepurified tank N_2 was passed over heated Zr turnings and then through a cold-trap.	Determination of the concentration gradient by chemical analysis (Kjeldahl).	$\tilde{D}$	920–1640	0.015	30,700	$\tilde{D}$ was assumed to be independent of concentration.	[2]

[a] Impurity concentrations are given in ppm unless otherwise stated.

Zirconium — Continued

Solvent medium	Diffusing element	Purity[a]	Preparation and properties	Method	Diffusion coefficient	Temperature range, °C	D_0 cm²/s	Q cal/mol	Comments	Ref.
β-Zr	N	Hf, 1.8–2.2 w/o; O, N, H, Fe, Si, totaling < 100.	Cylindrical specimens were machined from outgassed iodide Zr bars. Commercial N_2 was dried by Mg perchlorate.	Determination of the concentration gradient by chemical analysis (Kjeldahl).	$\tilde{D}$	900–1600	0.003	33,600	$\tilde{D}$ was assumed to be independent of concentration.	[3]
α-Zr	O	O, 300; C, 150; Fe, 120; Al, 50; P < 75; Cr, 40.	Oxide films grown on Zr plates in the presence of O_2 at one atm pressure.	Determination of the concentration gradient by microhardness measurement and analysis of the reaction rates.	D_{gr} (grain-boundary). $\tilde{D}$	400–650 650–850	4.57×10^{-4} 224	35,000 59,700	Electron microscope studies of fracture surfaces of the metal suggested that grain boundary diffusion was the predominant mode at low temperatures.	[4]
α-Zr	O	High temperature samples: O, 1300; N, 240; Hf, 2.04 w/o; Fe, 190; Al, 95; Ba < 650; Si < 650. Low temperature samples: O, 600; Fe, 170; Al, 290; Cr < 650.	Vacuum annealed Zr plates were oxidized in O_2 at high temperatures plus one sample in O_2-bearing Na. Low temperature oxidations in O_2-bearing Na or CO_2.	Determination of the concentration gradient by microhardness measurements.	$\tilde{D}$ $\tilde{D}$	400–700 700–850	9.13×10^{-5} 69.2	29,800 56,190	Use of O_2-bearing sodium gave diffusion results similar to O_2 oxidations. D-values were calculated only over range where linearity existed between hardness and O concentration.	[5]
α-Zr	O	Low Hf content, concentrations of impurities not stated.	Rolled stock annealed, polished and etched; samples anodized in KOH solution to form the oxide film.	Time rate of change of the interference color (i.e., thickness) of the oxide film due to solution of the film in the metal.	$\tilde{D}$	400–585	9.4	51,780	$\tilde{D}$ was assumed to be independent of concentration.	[6]
α-Zr	O	Al, 45; C, 50; Fe, 218; Hf, 68; Mo, 25; O, 140; Si < 40; Zr < 50; all others < 25.	Iodide-refined Zr, polished. O_2 (99.6 v/o pure) was passed through heated cupric oxide, Ascarite, Linde 5A molecular sieves and cold trap.	Determination of the concentration gradient by microhardness measurements.	$\tilde{D}$	400–850	28.8	53,400	$\tilde{D}$ was assumed to be independent of concentration.	[7]
α-Zr	O	Zr sample: Fe < 100; Hf, 55; C, 80; O, 160; all others < 50. Zr-O alloy: Fe, 510; Al, 200; Hf, < 300; C, 200; H, 57; N, 89; O, 3100; all others < 50.	Oxygen enriched Zr disk was pressure bonded to low oxygen Zr disk at 675 °C to form the diffusion couple.	Determination of the concentration gradient by microhardness measurements.	$\tilde{D}$	622–840	3.3	49,500	Linearity of concentration to hardness was demonstrated for O-Zr alloys with less than 2.4 a/o oxygen; linearity of the probability plot indicated that $\tilde{D}$ was independent of concentration.	[8]
α-Zr	O	Al, 100; Fe, 1000; Si, 425; Ca, 200; Hf, 200; N, 437; O, 800; all others < 50.	Zr bars; annealed, polished and etched; surface oxidized in O_2.	Determination of the concentration gradient by microhardness measurements; gravimetric determinations also were used.	$\tilde{D}$	550–650 650–850	7.9×10^{-5} 0.22	30,500 47,000	$\tilde{D}$ was assumed to be independent of concentration. Grain boundary diffusion probably was important at low temperatures.	[9]
α-Zr	O				$\tilde{D}$	400–850	6.81 ±2.9	51,200 ±800	Combined data; data from only the high temperature ranges of [5] and [9] were used. This agreement is remarkable.	[5–9]
ZrB_2	B	Not stated.	Boride layer was formed on a Zr cylinder by boronizing in boron carbide and borax.	Determination of the concentration gradient by microhardness measurements.	$\tilde{D}$	1100–1400	1.26×10^{-4}	34,500	$\tilde{D}$ was assumed to be independent of concentration; narrow homogeneity range [11] may be a major source of error in the results.	[10]

[a] Impurity concentrations are given in ppm unless otherwise stated.

Solvent medium	Diffusing element	Purity [a]	Preparation and properties	Method	Diffusion coefficient	Temperature range, °C	D_0 cm²/s	Q cal/mol	Comments	Ref.
ZrC	C	Not stated.	Carbide layer was formed on a Zr cylinder by carburizing in graphite.	Determination of the concentration gradient by microhardness	$\tilde{D}$	900–1300	0.0344	41,000	$\tilde{D}$ was assumed to be independent of concentration.	[10]
ZrC	C	Zirconium: Cr, 84; Fe, 570; Hf, 68; O, 375; all others <50. Graphite: Ca, 140; Fe, 73; all others < 50.	ZrC layer formed between liquid Zr and graphite crucible.	Determination of the rate of growth of ZrC layer from photomicrographs of longitudinal sections of the samples.	$\tilde{D}$	2000–2860	0.95	78,700	D was assumed to be independent of concentration. The boundary concentrations were taken from phase diagrams [13, 14].	[12]
ZrO_2	O	Zr substrate: O, 300; C, 150; Fe, 120; Al, 50; P < 75; Cr, 40.	Oxide layers grown on Zr plates in O_2; monoclinic oxide studied.	Determination of rate of oxide layer growth	$\tilde{D}$	400–850	1.05×10^{-3}	29,300		[4]
ZrO_2	O vacancies	Impurities in metal substrate not stated.	Oxide layers formed on crystal bar Zr in O_2, then the anion vacancy concentration in the oxide equilibrated by annealing in vacuum; approximate composition, $ZrO_{1.998}$; monoclinic phase.	Interruption kinetics technique of Rosenburg [16]: rate of oxygen uptake by oxygen deficient ZrO_{2-x}.	$\tilde{D}$	300–386	9.0×10^{-4}	28,700	Comparison of $\tilde{D}$ for vacancy diffusion with O-anion diffusion requires the use of an unknown correlatior factor. The anion vacancy concentration in the deficient oxide was $\sim 7 \times 10^{-3}$ g atom/cm³ (386 °C).	[15]
$ZrO_{1.994}$	O	SiO_2, 0.15 w/o; TiO_2, 50; Fe_2O_3, 30; MgO, 300.	Hot pressed nonstoichiometric oxide compacts; density 5.82 g/cm³; monoclinic phase.	Determination of the rate of migration of stoichiometric oxide front into nonstoichiometric grains.	$\tilde{D}$	700–1000	0.055	33,400	Rapid grain boundary diffusion into the compacts was noted so that the re-oxidation of individual grains was measured. A comparison with [4] and [15] above suggests that (a) grain boundary effects may be small in coherent oxide layers, (b) $\tilde{D}$ does not vary strongly with composition nor with crystallographic direction, and (c) the correlation factor may be near unity.	[17]
$Zr_{0.84}Ca_{0.16}O_{1.84}$	Ca	99.95 w/o ZrO_2 and $CaCO_3$ used in fabrication; W < 100.	Calcined mixture of ZrO_2 and $CaCO_3$ pressed into pellets, fused with plasma torch; grain size 0.2–1.0 mm; porosity 0.0–0.5%; cubic phase.	Determination of the concentration gradient by radioisotope distributions.	D^*	1700–2100	0.444	100,200	The error due to grain boundary diffusion was within the experimental uncertainty of the data.	[18]
$Zr_{0.92}Ca_{0.08}O_{1.92}$	O	HfO_2, 1.5%; SiO_2, 0.5%; MgO, 0.20%; Fe_2O_3, 0.10%; Al_2O_3, 0.17%; TiO_2, 0.11%. (weight percent).	Tube closed at one end; density 5.4 g/cm³; porosity ~ 5%; pores not connected; cubic phase.	Determination of the rate of permeation of O_2 through the walls.	$\tilde{D}$	1100–1600	185	57,600	A large drop in O_2 partial pressure between the inside and outside caused a large chemical potential gradient.	[19]
$Zr_{0.858}Ca_{0.142}O_{1.858}$	O	Not stated.	Polycrystalline samples: porosity 3–6%; grain size 100 μm. Single crystal sample: verneuil method; crack-free specimens used; cubic phase.	Heterogeneous isotopic exchange between solid sample and ^{18}O-enriched O_2.	D^*	780–1100	0.018	31,200	D_0 and Q were determined from the combined data from both types of samples.	[20]
$Zr_{0.85}Ca_{0.15}O_{1.85}$	O	Not stated.	Arc-fused, polycrystalline spheres.	Heterogeneous isotopic exchange.	D^*	700–1100	6.9×10^{-3}	30,400	D_0 and Q are given as recalculated by Simpson and Carter [20].	[21]

[a] Impurity concentrations are given in ppm unless otherwise stated.

Solvent medium	Diffusing element	Purity [a]	Preparation and properties	Method	Diffusion coefficient	Temperature range, °C	D_0 cm²/s	Q cal/mol	Comments	Ref.
$Zr_{0.84}$-$Ca_{0.16}$-$O_{1.84}$; $Zr_{0.88}$-$Ca_{0.12}$-$O_{1.88}$	Zr.....	99.95 w/o ZrO_2 and $CaCO_3$ used in fabrication; W < 100.	Calcined mixture of ZrO_2 and $CaCO_3$ pressed into pellets, fused with plasma torch; grain size 0.2-1.0 mm; porosity 0.0-0.5%; cubic phase.	Determination of the concentration gradient by radioisotope distribution.	D^*	1700–2150	0.035	92,500	D_0 and Q represent the combined results for the two compositions. The error due to grain boundary diffusion was within the experimental error of the data.	[18]

[a] Impurity concentrations are given in ppm unless otherwise stated.

[1] L. V. Pavlinov and V. N. Bykov, Fiz. Metal. I Metalloved. **19,** 397 (1965).
[2] M. W. Mallett, J. Belle, and B. B. Cleland, J. Electrochem. Soc. **101,** 1 (1954); U.S. At. Energy Comm. Report BMI-829 (1953).
[3] M. W. Mallett, E. M. Baroody, H. R. Nelson, and C. A. Papp, J. Electrochem. Soc. **100,** 103 (1953).
[4] J. Debuigne and P. Lehr, Compt. Rend. **256,** 1113 (1963); Conf. Corrosion of Reactor Materials **2,** p. 105 (International Atomic Energy Agency, Vienna, 1962).
[5] M. Davis, K. R. Montgomery, and J. Standring, J. Inst. Metals **89,** 172 (1961).
[6] J. P. Pemsler, J. Electrochem. Soc. **105,** 315 (1958).
[7] R. J. Hussey and W. W. Smeltzer, J. Electrochem. Soc. **111,** 564 (1964); ibid. **111,** 1221 (1964).
[8] J. J. Kearns and J. N. Chirigos, U.S. At. Energy Comm. Report WAPD-TM-306 (1962).
[9] G. Beranger and P. Lacombe, J. Nucl. Mater. **16,** 190 (1965).
[10] G. V. Samsonov and A. P. Epik, Dopovidi Akad. Nauk Ukr. RSR [1] 67 (1964).
[11] M. Hansen and K. Anderko, Constitution of Binary Alloys, p. 265 (McGraw-Hill Book Co., New York, 1958); R. P. Elliott, Constitution of Binary Alloys, First Supplement, p. 145 (McGraw-Hill Book Co., New York, 1965).
[12] L. M. Adelsberg, L. H. Cadoff, and J. M. Tobin, Trans. AIME **236,** 972 (1966).
[13] R. V. Sara, C. E. Lowell, and R. T. Dolloff, U.S. At. Energy Comm. Report WADD-TR-143, p. 8-19 (1963); R. V. Sara, J. Am. Ceram. Soc. **48,** 243 (1965).
[14] R. Rudy and D. P. Harmon, AFML-TR-65-2, part I, **11** (April 1965).
[15] T. Smith, J. Electrochem. Soc. **112,** 560 (1965).
[16] A. J. Rosenburg, J. Electrochem. Soc. **107,** 795 (1960).
[17] D. L. Douglass, Conf. Corrosion of Reactor Materials, **2,** p. 224 (International Atomic Energy Agency, Vienna, 1962).
[18] W. H. Rhodes and R. E. Carter, J. Am. Ceram. Soc. **49,** 244 (1966).
[19] A. W. Smith, F. W. Meszaros, and C. D. Amata, J. Am. Ceram. Soc. **49,** 240 (1966).
[20] L. A. Simpson and R. E. Carter, J. Am. Ceram. Soc. **49,** 139 (1966).
[21] W. D. Kingery, J. Pappis, M. E. Doty, and D. C. Hill, J. Am. Ceram. Soc. **42,** 393 (1959).

6. References

[1] J. Boltzmann, Ann. Physik. **53,** 959 (1894).
[2] C. Matano, Japan. J. Phys. **8,** 109 (1933).
[3] J. C. Fisher, J. Appl. Phys. **22,** 74 (1951).
[4] R. T. P. Whipple, Phil. Mag. **45,** 1225 (1954).
[5] H. S. Levine and C. J. MacCallum, J. Appl. Phys. **31,** 595 (1960).
[6] T. Suzuoka, Trans. Japan. Inst. Metals **2,** 25 (1961).

(Paper 72A2-492)

JOURNAL OF RESEARCH of the National Bureau of Standards—A. Physics and Chemistry
Vol. 72A, No. 2, March–April 1968

Effect of Oxide Additions on the Polymorphism of Tantalum Pentoxide (System Ta_2O_5-TiO_2)

J. L. Waring and R. S. Roth

Institute for Materials Research, National Bureau of Standards, Washington, D.C. 20234

(December 8, 1967)

The phase equilibrium relationships of the TiO_2-Ta_2O_5 system were determined in air. An equimolar compound, $TiTa_2O_7$, was found to melt congruently at about 1662 °C and have a monoclinic unit cell $a=20.297$ Å, $b=3.804$ Å, $c=11.831$ Å, $\beta=120°14'$, apparently isostructural with $TiNb_2O_7$. In addition, two other compounds are postulated to occur at about TiO_2:$49Ta_2O_5$ and TiO_2:$7Ta_2O_5$ and to dissociate at about 1230 and 1190 °C, respectively. TiO_2 apparently accepts a maximum of 9 mole percent Ta_2O_5 in solid solution at 1630 °C. Two eutectics occur in the system at 54 mole percent Ta_2O_5 and 1650 °C and 31 mole percent Ta_2O_5 and 1630 °C.

The high temperature form of Ta_2O_5 is apparently triclinic at room temperature with $a=3.801$ Å, $b=3.785$ Å, $c=35.74$ Å, $\alpha=90°54.4'$, $\beta=90°11.5'$, and $\gamma=89°59.9'$. A metastable transition occurs at 320 °C to a monoclinic form which inverts to tetragonal at 920 °C with $a=3.81$ Å, $c=36.09$ Å. Several intermediate morphotropic phases are found with up to 9 mole percent TiO_2 in solid solution.

Key Words: Phase equilibria, polymorphism, tantalum pentoxide, titanium dioxide.

1. Introduction

The increased commerical importance of tantalum oxide together with the apparent ambiguity of its phase relationships have served as an impetus to investigate both the pure oxide and the interaction of Ta_2O_5 with other oxides. As part of a continuing program of phase equilibria studies, it was decided to investigate the effect of various impurities and environments on Ta_2O_5. Titanium dioxide was selected to be studied in air because the cation has a radius similar in size to Ta^{+5} but differing in oxidation state. Investigations of other tantalate systems are in progress and the results will be reported subsequently.

No systematic attempt to study the phase equilibrium relationships in the system Ta_2O_5-TiO_2 has been previously reported. However, some attempts to investigate the polymorphs of Ta_2O_5 have been described in the literature [1–12].[1] The exact relationships of the various polymorphs are still in doubt because of the lack of suitable single crystals needed to properly characterize the phases. However, it has been concluded by various workers [10, 11] that Ta_2O_5 has at least two structurally different polymorphs, with a reversible phase transition occurring at about 1360 ± 10 °C [11].

[1] Figures in brackets indicate the literature references at the end of this paper.

2. Materials

The starting materials used in this study were found by general quantitative spectrochemical analyses to have the following impurities:

TiO_2—Si present in amounts less than 0.01 percent, Cu present in amounts less than 0.001 percent, Ca present in amounts less than 0.0001 percent.

Ta_2O_5—Al and Si present in amounts less than 1.0 percent; Cu and Mg present in amounts less than 0.1 percent; Ag, Ca, and Mn each present in amounts less than 0.0001 percent.

3. Specimen Preparation and Test Methods

Three-gram batches of various proportions of Ta_2O_5 and TiO_2 were weighed, mixed in a mechanical shaker for approximately 10 min, and pressed into disks at about 10^4 psi. The disks were placed on platinum setters and calcined in air at 1000 °C for 16 hr. Following this preliminary heat treatment portions of the ground specimen were placed in platinum alloy tubes and heated in the quenching furnace at various temperatures for different periods of time.

The tubes containing the specimens were quenched into ice water and examined by x-ray diffraction techniques. A high-angle recording Geiger counter-

diffractometer and Ni-filtered Cu radiation was used in the study. The Geiger counter traversed the specimen at 1/4 deg/min. and radiation was recorded on the chart at 1 deg-2θ/in. The unit cell dimensions reported can be considered accurate to about ± 2 in the last decimal place listed. Equilibrium was considered to have been achieved when x-ray patterns showed no change after successive heat treatments of a specimen or when the data were consistent with the results from a previous set of experiments. Solidus and liquidus temperatures were obtained by using both a quenching furnace and an induction furnace. Because of the temperature limitation of the quenching furnace, melting points above 1800 °C were determined with an induction furnace. Some duplicate determinations below 1800 °C were made using both furnace types.

The quenching furnace consisted of two concentric ceramic tubes wound with platinum-rhodium alloy wire. The inner tube served as the primary winding and the outer one as the booster. Separate power sources were used with each winding.

The power for the outer winding (booster) was supplied from a variable autotransformer. An a-c bridge type controller in which the furnace winding was one arm of the bridge was used to control the temperature of the inner winding.

The induction furnace consisted of an iridium crucible and cover which acted as the susceptor and specimen container. A small fragment of the calcined material was placed in the iridium crucible on an iridium setter or button and heated to the desired temperature for about 2 min to achieve thermal equilibrium. Apparent temperatures were measured with a calibrated, disappearing filament-type optical pyrometer which was sighted through a 45 deg calibrated prism into a viewing hole at the center of the crucible cover. The temperature measuring system of both the quenching furnace and the induction furnace were calibrated frequently against the melting point of Au (1063 °C), Pd (1552 °C), and Pt (1769 °C). In addition, the measuring system of the induction furnace was calibrated against the melting point of Rh (1960 °C). Temperatures reported in the present study are considered accurate to within ± 10 °C below 1650 °C and to within ± 20 °C above. The measurements were reproducible to within ± 5 °C, or better. The degree of melting was determined by the physical appearance of quenched or cooled specimens. The first adherence of the specimen to the platinum container or iridium setter generally established the beginning of melting. In quenched specimens, complete melting was established by the formation of a meniscus. Similarly, the slumping or loss of shape of the inductively heated specimens established complete melting.

4. Results and Discussion

The phase diagram, figure 1, for the system Ta_2O_5-TiO_2 in air was constructed from data in table 1 (part A, B and C). Circles represent composition and temperature of experiments conducted in the quenching furnace; triangles represent those conducted with a high temperature x-ray furnace. A triangle with an arc under the base represents experiments conducted in both types of furnaces at the same temperature and a square represents those conducted in an induction furnace. Heavy dashed lines delineate regions of the phase diagram where equilibrium could not be unequivocally established by the experimental methods employed in this study.

Alternate dotted and dashed lines represent metastable equilibrium relationships on the phase diagram.

Several melting points of Ta_2O_5 have been reported [11, 13] previously. The melting point of Ta_2O_5 determined in this investigation was 1887 ± 20 °C which is in reasonable agreement with the previously reported value of Reisman et al., [11]. The numerous reported melting points of TiO_2 have been tabulated by Schneider [14]. A redetermination of the melting point of TiO_2 was not attempted because of the inherent problems associated with the determination.

4.1. L-Ta_2O_5 and Related Phases [2]

Brauer [1] reported a structural modification of Ta_2O_5 which was isostructural with the low temperature form of Nb_2O_5. Hahn [2] listed x-ray diffraction powder data for a similar form of Ta_2O_5.

The x-ray diffraction pattern of L-Ta_2O_5 is characterized by strong subcell lines and numerous weak superstructure lines. Lehovec [3] indicated that the major lines of the x-ray powder pattern for Ta_2O_5 could be accounted for on the basis of an orthorhombic subcell $a' = 6.20$ Å, $b' = 3.66$ Å, and $c' = 3.89$ Å. The powder pattern given in reference 4 failed to account for the superstructure lines on the basis of a similar size subcell. Zaslavskii [5] and Harvey and Wilman [6] on the basis of single crystal data, accounted for the superstructure lines in *their* respective patterns by increasing the b axis to $b = 44.02$ Å ($12b'$) and $b = 69.6$ Å ($19b'$), respectively. Frevel and Rinn [7] attempted to account for the superstructure lines of their powder pattern by selecting a monoclinic cell $a = 7.32$ Å ($2b'$), $b = 15.55$ Å ($4c'$), $c = 10.79$ Å, $\beta = 120°36'$. However, Terao [8] found that his powder pattern could be indexed only by utilizing approximately twice the previous monoclinic c axis ($c = 21.549$ Å).

The subcell of the low temperature form of Ta_2O_5 used for this study can be indexed on the basis of an orthorhombic cell $a' = 6.19$ Å, $b' = 3.67$ Å, $c' = 3.89$ Å. The various published unit cell constants [4–9], including those employed by the present authors as well as those derived by others from single crystal and electron diffraction data, failed to provide suitable *hkl* values to account for the superstructure reflections in the Ta_2O_5 used in this study. Therefore, no x-ray diffraction pattern for low Ta_2O_5 is given. Although the published d-spacings derived from the subcell of the various patterns of Ta_2O_5 agree with those found to occur in the present work, some reflections resulting from the superstructure have not been reported previously. The variance of superstructure reflections

[2] L-Ta_2O_5 represents the low temperature polymorph of Ta_2O_5.

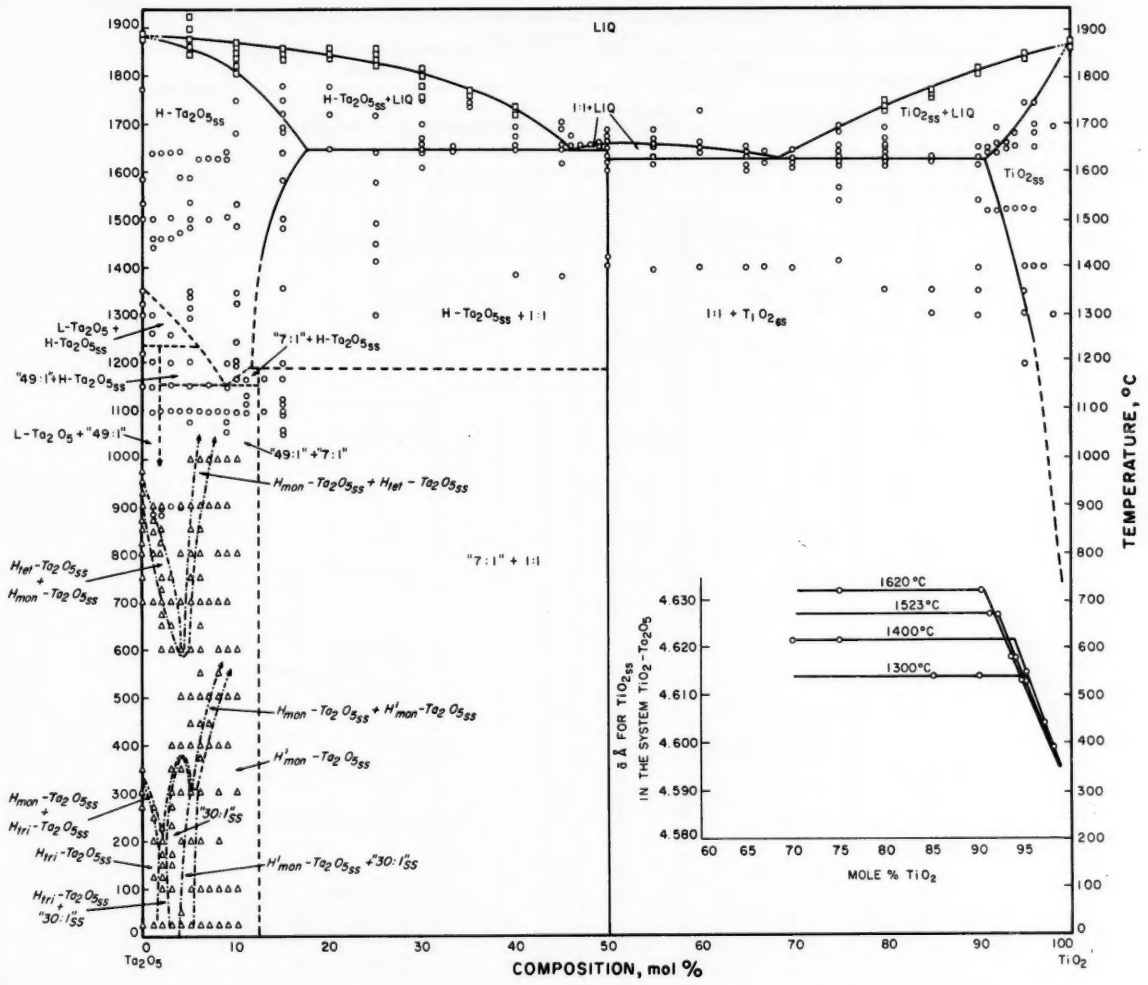

FIGURE 1. *Phase equilibrium diagram for the system* TiO_2-Ta_2O_5.

H-Ta_2O_5 – High temperature form of Ta_2O_5.
H_{tet}-Ta_2O_5 – Tetragonal form.
H_{mon}-Ta_2O_5 – Monoclinic metastable form.
H_{tri}-Ta_2O_5 – Triclinic metastable form.
"3o:1" – A metastable monoclinic solid solution phase occurring at about 30Ta_2O_5:TiO_2.
H'_{mon}-Ta_2O_5 – A morphotropic modification of H_{mon}-Ta_2O_5.
L-Ta_2O_5 – Low temperature form of Ta_2O_5.
"49:1" – A L-Ta_2O_5 type compound postulated to occur at about 49Ta_2O_5:TiO_2.
"7:1" – A L-Ta_2O_5 type compound postulated to occur at about 7Ta_2O_5:TiO_2.
1:1 – $TiTa_2O_7$.
Liq. – Liquid.
ss – Solid solution

O – Compositions and temperatures of experiments conducted in quench furnace.
△ – Compositions and temperatures of experiments conducted in high temperature x-ray furnace.
□ – Compositions and temperatures of experiments conducted in an iridium crucible induction furnace.
⌀ – Compositions and temperatures of experiments conducted in both the quenching and high temperature x-ray furnaces.

For clarity not all experimental data appearing in table 1 are plotted on this diagram.
Heavy dashed lines represent regions where equilibrium was not unequivocally established.
Alternate dot-dash lines represent metastable equilibrium.
Quotation marks around a composition indicate that the exact stoichiometry is not known.

may be due, among other things, to a nonequilibrium low-temperature poorly crystallized material lacking sufficient energy for proper ordering of the superstructure. Similarly the influence of anion and cation impurities on phase formation has essentially not been reported. In fact, most of the materials used for the previously reported Ta_2O_5 x-ray diffraction patterns apparently were not characterized by spectrographic analyses.

In the present work, TiO_2 additions were found to have a significant effect on the nature of the L-Ta_2O_5 type x-ray diffraction powder patterns. Specimens were prepared at close intervals, up to 13 mole percent TiO_2. Since equilibrium was difficult to achieve on heating, these specimens were equilibrated at 1500 °C and reheated at about 1100 °C in excess of 200 hr. A cursory examination of the x-ray data derived from these quenched specimens would suggest a solid solution between L-Ta_2O_5 and TiO_2 up to about 13 percent. However, these x-ray patterns show additional reflections derived from a superstructure. Moreover, the superstructure reflections shift significantly with the

TABLE 1. *Experimental data for compositions in the system* TiO_2-Ta_2O_5

Part A. Quenching data

Composition		Heat treatments				Results	
		Initial[a]		Final[b]		Physical observation	X-ray diffraction analyses[c]
TiO_2	Ta_2O_5	Temp	Time	Temp	Time		
Mole %	*Mole %*	*°C*	*Hour*	*°C*	*Hour*		
0	100			1220	264	Not melted.	L-Ta_2O_5.
				1306	16	....do....	Do.
				1350	65	....do....	H-Ta_2O_5 + L-Ta_2O_5.
				1506	24	....do....	H-Ta_2O_5.
				1535	4.5	....do....	Do.
				1775	6	....do....	Do.
		1220	264	1329	336	....do....	L-Ta_2O_5.
		1506	24	1299	90	....do....	Do.
1	99			1204	72	....do....	Do.
				1462	19	....do....	H_{trt}-Ta_2O_{5ss}.
				1506	24	....do....	Do.
				1640	4.5	....do....	Do.
				1641	16	....do....	Do.
		1506	24	1100	432	....do....	L-Ta_2O_5 phase(s).
				1155	66	....do....	Do.
				1204	72	....do....	H_{trt}-Ta_2O_{5ss}.
				1260	112	....do....	L-Ta_2O_5 phase(s) + H_{trt}-Ta_2O_{5ss}.
				1299	90	....do....	Do.
		1640	4.5	887	65	....do....	H_{trt}-Ta_2O_{5ss}.
2	98			1461	19	....do....	H_{trt}-Ta_2O_{5ss} + "30:1"$_{ss}$.
				1640	4.5	....do....	Do.
				1641	19	....do....	Do.
		1640	4.5	887	65	....do....	Do.
		1461	19	901	67	....do....	Do.
				1100	432	....do....	L-Ta_2O_5 phase(s).
				1200	64	....do....	"30:1"$_{ss}$.
3	97			1461	16	....do....	Do.
				1506	24	....do....	
				1641	16	....do....	Do.
		1461	16	901	67	....do....	Do.
		1506	24	1100	432	....do....	L-Ta_2O_5 phase(s).
				1155	66	....do....	"30:1"$_{ss}$ + L-Ta_2O_5 phase(s).
				1260	112	....do....	Do.
4	96			1471	16	....do....	"30:1"$_{ss}$.
				1590	20	....do....	Do.
				1641	16	....do....	Do.
		1471	16	901	67	....do....	Do.
				1100	432	....do....	L-Ta_2O_5 phase(s).
5	95			1297	20	....do....	H'_{mon}-Ta_2O_{5ss} + L-Ta_2O_5 phase(s).
				1316	65	....do....	Do.
				1345	65	....do....	Do.
				1486	16	....do....	H'_{mon}-Ta_2O_{5ss} + "30:1"$_{ss}$.
				1506	72	....do....	Do.
				1535	4.5	....do....	Do.
				1588	64	....do....	Do.
		1486	16	924	89	....do....	Do.
		1506	72	1078	72	....do....	L-Ta_2O_5 phase(s).
				1104	65	....do....	Do.
				1150	16	....do....	H'_{mon}-Ta_2O_{5ss} + L-Ta_2O_5 phase(s).
				1155	64	....do....	L-Ta_2O_5 phase(s) + H_{mon}"Ta_2O_{5ss}.
				1201	16	....do....	H'_{mon}-Ta_2O_{5ss}.
		1535	4.5	876	16	....do....	H'_{mon}-Ta_2O_{5ss} + "30:1"$_{ss}$.
				950	19	....do....	Do.
				1297	20	....do....	Do.
				1351	2	....do....	Do.
		1588	64	800	2.5	....do....	Do.
6	94			1628	16	....do....	
		1628	16	1097	336	....do....	L-Ta_2O_5 phase(s).
7	93			1506	72	....do....	H'_{mon}-Ta_2O_{5ss}.
				1628	16	....do....	Do.
		1506	72	1097	336	....do....	L-Ta_2O_5 phase(s).
				1155	60	....do....	H'_{mon}-Ta_2O_{5ss} + L-Ta_2O_5 phase(s).
8	92			1628	16	....do....	H'_{mon}-Ta_2O_{5ss}.
		1628	16	1097	336	....do....	L-Ta_2O_5 phase(s).
9	91			1628	16	....do....	H'_{mon}-Ta_2O_{5ss}.
				1643	24	....do....	Do.
				1506	24	....do....	Do.
		1506	24	1055	112	....do....	L-Ta_2O_5 phase(s) + H'_{mon}-Ta_2O_{5ss}.
				1078	72	....do....	Do.
				1097	336	....do....	L-Ta_2O_5 phase(s).
				1104	72	....do....	L-Ta_2O_5 phase(s) + H'_{mon}-Ta_2O_{5ss}.
				1150	16	....do....	H'_{mon}-Ta_2O_{5ss} + L-Ta_2O_5 phase(s).
				1155	64	....do....	Do.
				1201	16	....do....	H'_{mon}-Ta_2O_{5ss}.
10	90			1345	65	....do....	Do.
				1486	16	....do....	Do.
				1504	24	....do....	Do.
				1535	4.5	....do....	Do.
				1560	168	....do....	Do.
				1580	2	....do....	
				1640	16	....do....	Do.
				1684	16	....do....	Do.
		1400	6			....do....	
		1486	16			....do....	
				924	89	....do....	H'_{mon}-Ta_2O_{5ss}.
				1124	65	....do....	Do.
				1247	48	....do....	Do.
		1400	6			....do....	

See footnotes at end of table, p. 181.

TABLE 1. *Experimental data for compositions in the system* TiO_2-Ta_2O_5—Continued

Part A. Quenching data

Composition		Heat treatments				Results	
		Initial [a]		Final [b]		Physical observation	X-ray diffraction analyses [c]
TiO_2	Ta_2O_5	Temp	Time	Temp	Time		
Mole %	*Mole %*	*°C*	*Hour*	*°C*	*Hour*		
		1486	16			do	
		1535	4.5	1351	16	do	H'_{mon}-Ta_2O_{5ss}.
		1580	2	1097	192	do	L-Ta_2O_5 phase(s).
				1203	312	do	H'_{mon}-Ta_2O_{5ss} + L-Ta_2O_5 phase(s).
11	89	1580	2			do	H'_{mon}-Ta_2O_{5ss}.
		1580	2	1097	192	do	L-Ta_2O_5 phase(s).
				1132	64	do	L-Ta_2O_5 phase(s) + H'_{mon}-Ta_2O_{5ss}.
				1167	168	do	Do.
				1197	168	do	L-Ta_2O_5 phase(s).
13	89	1580	2			do	H'_{mon}-Ta_2O_{5ss}.
				1097	168	do	L-Ta_2O_5 phase(s) + 1:1.
				1167	168	do	L-Ta_2O_5 phase(s) + H'_{mon}-Ta_2O_{5ss} + 1:1.
15	85	1400	6			do	
				1358	7	do	H'_{mon}-Ta_2O_{5ss}.
				1470	16	do	
				1480	16	do	
				1486	16	do	H'_{mon}-Ta_2O_{5ss} + 1:1.
				1508	16	do	Do.
				1580	16	do	
				1640	16	do	H'_{mon}-Ta_2O_{5ss}.
				1687	16	do	Do.
				1695	.5	do	Do.
				1721	.16	Partially melted.	
				1750	.16	do	H'_{mon}-Ta_2O_{5ss} + Liq.
				1781	.16	do	Do.
		1400	6			Not melted.	
		1470	16	1127	192	do	H'_{mon}-Ta_2O_{5ss} + L-Ta_2O_5 phase(s) + 1:1.
		1406	6			do	
		1480	16	1167	168	do	H'_{mon}-Ta_2O_{5ss} + L-Ta_2O_5 phase(s) + 1:1.
		1406	6			do	
		1486	16	924	89	do	H'_{mon}-Ta_2O_{5ss} + 1:1.
				1097	168	do	L-Ta_2O_5 phase(s) + 1:1.
		1406	6			do	
		1508	16	1055	112	do	H'_{mon}-Ta_2O_{5ss} + L-Ta_2O_5 phase(s) + 1:1.
				1060	19	do	Do.
				1091	120	do	L-Ta_2O_5 phase(s) + H'_{mon}-Ta_2O_{5ss} + 1:1.
20	80	1406	6			do	
				1640	20	do	H'_{mon}-Ta_2O_{5ss} + 1:1.
				1651	.16	Partially melted.	H_{mon}-Ta_2O_{5ss} + 1:1 Liq.
				1687	.16	do	
				1721	.16	do	H'_{mon}-Ta_2O_{5ss} + 1:1 Liq.
				1780	.16	do	Do.
25	75	1406	6			Not melted.	
				1413	17	do	H'_{mon}-Ta_2O_{5ss} + 1:1.
				1450	3	do	Do.
				1576	16	do	Do.
				1646	16	do	Do.
				1722	1	Partially melted.	Do.
		1400	6			Not melted.	
		1646	16	1300	16	do	H'_{mon}-Ta_2O_{5ss} + 1:1.
30	70	1400	6			do	
				1612	2	do	H'_{mon}-Ta_2O_{5ss} + 1:1.
				1642	0.16	do	Do.
				1646	1	do	Do.
				1652	1	Partially melted.	Do.
				1656	0.16	do	
				1662	.16	do	
				1671	.16	do	
				1704	.33	do	
				1726	.16	do	
				1753	.16	do	
				1759	.16	do	
33.33	66.67	1400	6			Not melted.	
				1649	.16	do	1:1 + H'_{mon}-Ta_2O_{5ss}.
				1656	.16	Partially melted.	
35	65	1400	6			Not melted.	
				1735	.08	Partially melted.	
				1745	.08	do	
40	60	1400	6			Not melted.	
				1388	113	do	1:1 + H'_{mon}-Ta_2O_{5ss}.
				1650	1	do	Do.
				1660	0.08	Partially melted.	
				1679	.16	do	1:1-Liq. + H'_{mon}-Ta_2O_{5ss}.
				1698	.16	do	Do.
				1722	.16	do	
				1741	.16	Completely melted.	
45	55	1400	6			Not melted.	
				1388	113	do	1:1 + H'_{mon}-Ta_2O_{5ss}.
				1621	0.16	do	
				1651	.16	do	
				1653	.16	Partially melted.	
				1660	.16	do	
				1666	.16	do	
				1698	.16	Completely melted.	
				1708	.16	do	
46	54	1400	6			Not melted.	
				1652	.16	do	
				1662	.16	Partially melted.	
				1680	.16	Completely melted.	

See footnotes at end of table, p. 181.

TABLE 1. *Experimental data for compositions in the system* TiO_2-Ta_2O_5—Continued

Part A. Quenching data

Composition		Heat treatments				Results	
		Initial [a]		Final [b]		Physical observation	X-ray diffraction analyses [c]
TiO_2	Ta_2O_5	Temp	Time	Temp	Time		
Mole %	*Mole %*	*°C*	*Hour*	*°C*	*Hour*		
47	53	1400	6			Not melted.	
				1662	.16	Completely melted.	
48	52	1400	6			Not melted.	
				1662	.16	Completely melted.	
49	51	1400	6			Not melted.	
				1662	.16	Partially melted.	
				1669	.16	Completely melted.	
50	50	1406	6			Not melted.	
(1:1)				1402	18	.....do.....	1:1 + TiO_{2ss} + H'_{mon}-Ta_6O_{15ss}.
		1400	6	1428	19	.....do.....	1:1.
				1607	19	.....do.....	Do.
				1626	16	.....do.....	Do.
				1639	0.08	.....do.....	Do.
				1656	.16	.....do.....	Do.
				1663	19	.....do.....	Do.
				1664	0.16	Completely melted.	1:1 + Liq.
				1678	1	.....do.....	
				1690	3	.....do.....	1:1 + Liq.
55	45			1400	22	Not melted.	1:1 + TiO_{2ss} + H'_{mon}-Ta_6O_{15ss} (nonequilibrium).
				1621	0.16	Partially melted [d]	1:1 + TiO_{2ss}.
				1636	.16	Partially melted.	1:1 + TiO_{2ss}.
				1653	.08	.....do.....	Do.
				1661	.16	.....do.....	
				1672	.16	Completely melted.	
60	40			1403	16		
				1645	0.16	Partially melted.	
				1648	.16	.....do.....	
				1654	.16	Completely melted.	
				1662	.16	.....do.....	
				1730	.16	.....do.....	
65	35			1403	16	Not melted.	1:1 + TiO_{2ss}.
				1606	0.16	.....do.....	Do.
				1619	.16	Partially melted [d]	Do.
				1636	.16	.....do.....	1:1 + Liq.
				1641	.16	.....do.....	
				1647	.16	Completely melted.	
				1656	.16	.....do.....	
66.67	33.33			1405	16	Not melted.	1:1 + TiO_{2ss}.
				1628	0.16	Partially melted. [d]	
				1645	.16	Completely melted.	
70	30			1405	16	Not melted.	1:1 + TiO_{2ss}.
				1611	0.16	.....do.....	
				1620	.16	Partially melted. [d]	
				1624	.16	.....do.....	
				1629	.16	.....do.....	
				1631	.16	Completely melted.	
				1649	.16	.....do.....	
75	25			1413	19	Not melted.	TiO_{2ss} + 1:1.
				1420	4	.....do.....	
				1542	19	.....do.....	TiO_{2ss} + 1:1.
				1569	2	.....do.....	Do.
				1611	0.16	.....do.....	
				1612	1	.....do.....	TiO_{2ss} + 1:1.
				1619	0.16	.....do.....	
				1625	1	Partially melted. [d]	TiO_{2ss} + 1:1.
				1626	0.16	.....do.....	Do.
				1633	1	Partially melted.	
				1638	0.16	.....do.....	TiO_{2ss} + Liq.
				1643	.16	.....do.....	Do.
				1644	.16	.....do.....	
				1658	1	.....do.....	
				1689	0.16	.....do.....	
				1700	.16	Completely melted.	
80	20			1357	16		
				1617	0.25	Partially melted. [d]	
				1620	.25	.....do.....	
				1623	.25	.....do.....	
				1626	.25	.....do.....	
				1627	.25	.....do.....	
				1631	.25	Partially melted.	TiO_{2ss} + Liq.
				1642	.08	.....do.....	Do.
				1649	.25	.....do.....	
				1674	.08	.....do.....	
				1694	.16	.....do.....	
				1725	.16	.....do.....	
				1742	.08	.....do.....	
85	15			1303	16	Not melted.	TiO_{2ss} + 1:1.
				1357	16	.....do.....	
				1627	0.16	Partially melted. [d]	TiO_{2ss} + 1:1.
				1630	.16	Partially melted.	TiO_{2ss} + Liq.
90	10			1303	16	Not melted.	TiO_{2ss} + 1:1.
				1357	16	.....do.....	
				1406	16	.....do.....	TiO_{2ss} + 1:1.
				1620	0.25	.....do.....	Do.
				1624	1	.....do.....	
				1628	0.16	.....do.....	TiO_{2ss} + 1:1.
				1632	1	Partially melted.	TiO_{2ss} + Liq.
				1659	1	.....do.....	
		1542	19	900	19		TiO_{2ss} + 1:1.

See footnotes at end of table, p. 181.

TABLE 1. *Experimental data for compositions in the system* TiO_2-Ta_2O_5—Continued

Part A. Quenching data

Composition		Heat treatments				Results	
		Initial [a]		Final [b]		Physical observation	X-ray diffraction analyses [c]
TiO_2	Ta_2O_5	Temp	Time	Temp	Time		
Mole %	*Mole %*	*°C*	*Hour*	*°C*	*Hour*		
91	9			1523	19	Not melted.	Do.
				1637	1	Partially melted.	TiO_{2ss} + Liq.
				1643	0.25	....do....	
				1653	.16	....do....	
92	8			1523	19	Not melted.	TiO_{2ss} + 1:1.
				1647	0.16	....do....	Do.
				1660	.16	Partially melted.	TiO_{2ss} + Liq.
93	7			1523	19	Not melted.	TiO_{2ss}.
				1651	19	....do....	Do.
				1666	19	Partially melted.	TiO_{2ss} + Liq.
94	6			1396	1.5	Not melted.	
				1528	65	....do....	TiO_{2ss}.
				1659	0.16	....do....	
				1694	.16	Partially melted.	TiO_{2ss} + Liq.
95	5			1197	113	Not melted.	TiO_{2ss} + 1:1.
				1303	16	....do....	TiO_{2ss}.
				1357	16	....do....	Do.
				1406	16	....do....	Do.
				1528	65	....do....	Do.
				1623	2	....do....	Do.
				1749	0.16	Partially melted.	TiO_{2ss} + Liq.
		1357	16	1197	113	Not melted.	TiO_{2ss} + 1:1.
96	4			1528	65	....do....	TiO_{2ss}.
				1657	19	....do....	Do.
				1659	0.16	....do....	Do.
				1684	.16	....do....	Do.
				1700	.16	....do....	Do.
				1750	.16	....do....	Do.
		1657	19	1000	.16	....do....	Do.
97	3			1406	16	....do....	Do.
98	2			1303	16	....do....	Do.

[a] All specimens were initially calcined at 1000 °C for 10 hr with heating and cooling rates of approximately 4 °C/min. Small portions of this calcine were then reheated for the designated time of one or more designated higher temperatures and generally quenched in Pt tubes.

[b] After the initial heat treatment(s) all specimens were reheated in Pt tubes to the indicated temperature.

[c] The phases identified are given greatest amount first in the order of amount present at room temperature. The phases are not necessarily those present at the temperature to which the specimen was heated.

H_{mon}-Ta_2O_5—Monoclinic metastable form.

H_{tet}-Ta_2O_5—Triclinic metastable form.

"30:1"—Metastable monoclinic solid solution phase occurring at about $30Ta_2O_5$:TiO_2.

H'_{mon}—A morphotropic modification of H_{mon}-Ta_2O_5.

L-Ta_2O_5 phase(s)—One or more phases with an x-ray powder diffraction pattern similar to low temp. form of Ta_2O_5.

1:1—$TiTa_2O_7$.

Liq.—Metastable phase which forms only from the quenched liquid and gives a characteristic but very poorly defined x-ray pattern.

ss—Solid solution.

" "—Indicate that the exact stoichiometry is not known.

[d] Specimens appeared partially melted below the solidus and were interpolated to provide the best approach to binary equilibrium.

TABLE 1.

Part B: Induction furnace data

Composition [a]		Temp.	Observation	Composition [a]		Temp.	Observation
TiO_2	Ta_2O_5			TiO_2	Ta_2O_5		
	100	1872	Not melted.			1861	Completely melted.
		1882	Do.	30	70	1757	Not melted.
		1891	Melted.			1766	Do.
5	95	1850	Not melted.			1781	Do.
		1861	Partially melted.			1801	Do.
		1868	Do.			1810	Partially melted.
		1882	Completely melted.			1819	Completely melted.
		1903	Do.	35	65	1762	Partially melted.
		1924	Do.			1776	Completely melted.
10	90	1809	Not melted.	40	60	1726	Partially melted.
		1821	Partially melted.			1744	Completely melted.
		1840	Do.	80	20	1735	Partially melted.
		1855	Do.			1742	Do.
		1865	Completely melted.			1757	Completely melted.
		1872	Do.	85	15	1762	Partially melted.
15	85	1840	Partially melted.			1770	Do.
		1852	Do.			1778	Do.
		1864	Completely melted.	90	10	1810	Do.
20	80	1840	Partially melted.			1820	Completely melted.
		1850	Completely melted.	95	5	1840	Partially melted.
		1860	Do.			1845	Completely melted.
25	75	1829	Partially melted.	100		1860	Not melted.
		1840	Completely melted.			1875	Completely melted.
		1850	Do.				

[a] All specimens were initially calcined at 1000 °C for 10 hr with heating and cooling rates of approximately 4 °C/min.

TABLE 1.

Part C: High temperature x-ray diffraction experimental data for selected compositions in the system TiO_2-Ta_2O_5

Composition		Previous heat treatment		Temp.	Results [a]
TiO_2	Ta_2O_5	Temp.	Time		
Mole %	*Mole %*	*°C*	*hr*	*°C*	
0	100	1000	10		
		1220	264		L-Ta_2O_5.
				25	Do.
				500	Do.
				1000	Do.
		1000	10		
		1640	16		H_{tet}-Ta_2O_5.
				25	Do.
				270	Do.
				300	Do.
				350	H_{mon}-Ta_2O_5.
				700	Do.
				750	Do.
				800	Do.
				825	Do.
				850	Do.
				875	Do.
				900	Do.
				925	Do.
				950	H_{mon}-Ta_2O_5 + H_{tet}-Ta_2O_5.
				975	H_{tet}-Ta_2O_5.
1	99	1000	10		
		1640	4.5		H_{tet}-Ta_2O_{5ss}.
				25	Do.
				125	Do.
				200	Do.

See footnotes at end of table, p. 182.

TABLE 1.—Continued

Part C: High temperature x-ray diffraction experimental data for selected compositions in the system TiO_2-Ta_2O_5

Composition		Previous heat treatment		Temp.	Results [a]
TiO_2	Ta_2O_5	Temp.	Time		
Mole %	*Mole %*	*°C*	*hr*	*°C*	
				250	Do.
				275	H_{mon}-Ta_2O_{5ss}.
				700	Do.
				800	Do.
				825	Do.
				850	H_{tet}-Ta_2O_{5ss} + H_{mon}-Ta_2O_{5ss}.
				875	Do.
				900	H_{tet}-Ta_2O_{5ss}.
2	98	1000	10		
		1640	16		H_{trt}-Ta_2O_{5ss} + "30:1"$_{ss}$.
				25	Do.
				100	Do.
				125	Do.
				150	Do.
				175	Do.
				200	H_{trt}-Ta_2O_{5ss} + H_{mon}-Ta_2O_{5ss}.
				225	H_{mon}-Ta_2O_{5ss}.
				600	Do.
				650	Do.
				675	Do.
				700	Do.
				725	Do.
				750	H_{mon}-Ta_2O_{5ss} + H_{tet}-Ta_2O_{5ss}.
				775	Do.
				800	Do.
				825	Do.
				850	H_{tet}-Ta_2O_{5ss}.
				900	Do.
3	97	1000	10		
		1640	40		"30:1"$_{ss}$.
				25	Do.
				150	Do.
				175	Do.
				200	Do.
				235	Do.
				275	Do.
				300	Do.
				350	H_{mon}-Ta_2O_{5ss}.
				400	Do.
				600	Do.
				650	H_{mon}-Ta_2O_{5ss} + H_{tet}-Ta_2O_{5ss}.
				700	H_{tet}-Ta_2O_{5ss} + H_{mon}-Ta_2O_{5ss}.
				750	Do.
				775	Do.
				800	H_{tet}-Ta_2O_{5ss}.
4	96	1000	10		
		1590	20		
				25	"30:1"$_{ss}$ + H'_{mon}-Ta_2O_{5ss}.
				50	Do.
				200	"30:1"$_{ss}$.
				300	Do.
				350	Do.
				400	H_{mon}-Ta_2O_{5ss}.
				500	Do.
				600	H_{mon}-Ta_2O_{5ss} + H_{tet}-Ta_2O_{5ss}.
				700	H_{tet}-Ta_2O_{5ss}.
				800	Do.
				900	Do.
5	95	1000	10		
		1486	16		H'_{mon}-Ta_2O_{5ss} + "30:1"$_{ss}$.
				25	Do.
				200	Do.
				100	Do.
				300	Do.
				400	H_{mon}-Ta_2O_{5ss}.
				450	Do.
				500	Do.
				600	Do.
				700	H_{tet}-Ta_2O_{5ss} + H_{mon}-Ta_2O_{5ss}.
				750	Do.
				800	H_{tet}-Ta_2O_{5ss}.
				850	Do.
				900	Do.
				1000	Do.
6	94	1000	10		
		1628	16		H'_{mon}-Ta_2O_{5ss}.
				25	Do.
				100	Do.
				200	Do.
				300	Do.
				325	H_{mon}-Ta_2O_{5ss} + H'_{mon}-Ta_2O_{5ss}.
				375	Do.
				400	Do.
				450	H_{mon}-Ta_2O_{5ss}.
				500	Do.
				550	Do.
				600	Do.
				650	Do.
				700	Do.
				750	Do.
				800	Do.

TABLE 1.—Continued

Part C: High temperature x-ray diffraction experimental data for selected compositions in the system TiO_2-Ta_2O_5

Composition		Previous heat treatment		Temp.	Results [a]
TiO_2	Ta_2O_5	Temp.	Time		
Mole %	*Mole %*	*°C*	*hr*	*°C*	
				850	Do.
				900	H_{mon}-Ta_2O_{5ss} + H_{trt}-Ta_2O_{5ss}.
				930	Do.
				1000	H_{tet}-Ta_2O_5.
7	93	1000	10		
		1563	230		
				25	H'_{mon}-Ta_2O_{5ss}.
				100	Do.
				200	Do.
				300	Do.
				400	Do.
				450	Ta_2O_{5ss} [b]
				500	Do.
				700	Do.
				900	Do.
				1000	Do.
				1100	H_{tet}-Ta_2O_{5ss}.
8	92	1000	10		
		1628	16		
				25	H'_{mon}-Ta_2O_{5ss}.
				100	Do.
				200	Do.
				300	Do.
				400	Do.
				450	H'_{mon}-Ta_2O_5. [b]
				500	H_{mon}-Ta_2O_{5ss}. [b]
				550	Do.
				600	H_{mon}-Ta_2O_{5ss}.
				700	Do.
				800	Do.
				900	Do.
				1000	Do.
				1100	H_{tet}-Ta_2O_{5ss}.
9	91	1000	10		
		1628	16		
				25	H'_{mon}-Ta_2O_{5ss}.
				100	Do.
				300	Do.
				400	Do.
				500	Do.
				600	H_{mon}-Ta_2O_{5ss}. [b]
				700	Do.
				800	Do.
				900	Do.
				1000	Do.
				1100	Do.
10	90	1000	10		
		1560	168		
				25	H'_{mon}-Ta_2O_{5ss}.
				100	Do.
				300	Do.
				400	Do.
				500	Do.
				600	H'_{mon}-Ta_2O_{5ss}. [b]
				800	Do.
				1000	Do.
				1100	Do.

[a] L-Ta_2O_5 —low temperature stable form of Ta_2O_5.
H_{trt}-Ta_2O_5 —a metastable triclinic form of Ta_2O_5 with $a \approx 3.8$ Å, $b \approx 3.8$ Å, and $c \approx 3.5$ Å.
H_{mon}-Ta_2O_5 —a metastable monoclinic form of Ta_2O_5 related to H_{trt}-Ta_2O_5 by $a \approx \sqrt{2} \times 3.8$, $b \approx \sqrt{2} \times 3.8$.
H_{tet}-Ta_2O_5 —a high temperature tetragonal modification of Ta_2O_5.
H'_{mon}-Ta_2O_{5ss} —a monoclinic phase related to H_{trt}-Ta_2O_5 by having a significant smaller β angle than H_{mon}-Ta_2O_5.
"30:1" —a metastable monoclinic solid solution phase occurring at about $30Ta_2O_5$:TiO_2.
ss —solid solution.
[b] H_{mon}-Ta_2O_{5ss} could not be detected in the presence of H'_{mon}-Ta_2O_5 because of β angle similarity.

addition of TiO_2 whereas those derived from the subcell appear to have essentially the same spacings.

A typical example would be a diffraction line occurring at 26.53° 2θ in Ta_2O_5 which was found to occur at 26.24° with 10 percent TiO_2 addition. Conversely, a reflection positioned at 63.60° 2θ in Ta_2O_5 appeared to move less than 0.1° 2θ over the same compositional range. Some of the low angle x-ray diffraction lines, which, for a solid solution, should exhibit the least 2θ shift, actually shift more than many of the high angle lines.

The relative peak intensity of the x-ray powder patterns of specimens in this compositional range seem to show maximum intensity at 2 percent TiO_2, diminishing while becoming more diffuse with increasing TiO_2 and sharpen up with a maximum of intensity at about 12 mole percent TiO_2. These fine line differences, abnormal shifts in *d*-spacings, and intensity difference, are more characteristic of compounds than of solid solution phenomena. For these reasons, phases occurring at the approximate compositions $98Ta_2O_5$:$2TiO_2$ ("49:1") and[3] $88Ta_2O_5$:$12TiO_2$ ("7:1") are postulated in the system. Although the exact compositions of the postulated "nonstoichiometric" compounds cannot be established by x-ray powder diffraction this method is sufficient to indicate that the solid solution interpretation is unlikely. Since the stoichiometries of the compounds are not known exactly, the compounds are dashed on figure 1.

A similar phenomenon has been found to occur in other tantalate systems. For example, in the system Ta_2O_5-TaO_2F, Jahnberg and Andersson [15] obtained single crystal data on samples of different compositions within a field which might have been interpreted as a continuous solid solution series of the L-Ta_2O_5 type. From the single crystal data they concluded that a series of discrete compounds exist within this composition region.

Lehovec [3] described the structure of the tantalum oxide subcell with the tantalum atoms near positions (000), (1/2,1/2,0), two oxygen atoms at about (0,0,1/2) (1/2,1/2,1/2) and the other three oxygen atoms in the same plane as the tantalum atoms. He concluded that the loose packing of oxygen atoms in the plane $z=1/2$ could easily permit the diffusion of interstitial oxygen ions and/or the incorporation of interstitial cations and therefore the existence of oxides with cation/anion ratios differing from that of Ta_2O_5.

From x-ray powder diffraction data Moser [9] suggested that the low temperature form of Ta_2O_5 may occur in several states. On the basis of change in *d*-values of some weak powder lines, especially the one occurring between 3.6 and 3.3 Å, he arbitrarily divided low Ta_2O_5 into four "states" γ_1, γ_2, γ_3, and γ_4.

4.2. H-Ta_2O_5 and Related Metastable Phases[4]

Lagergren and Magneli [10] reported the existence of a high temperature polymorph occurring above 1320 °C and indexed the x-ray pattern on the basis of an orthorhombic unit cell with $a=35.6$ Å, $b=3.79$ Å, $c=3.735$ Å. Zaslavskii et al. [5], concluded from powder data that the high temperature form was tetragonal with $a=3.801$ Å, $c=35.67$ Å.

Reisman et al. [11], postulated from fine line splits in the x-ray powder diffraction pattern that the high temperature modification had a symmetry lower than orthorhombic. They further concluded that the phase transition occurred at 1360 °C, and was sluggish but conpletely reversible.

Laves and Petter [12] reported three polymorphic forms of high Ta_2O_5 from x-ray and optical data. At room temperature a monoclinic form (α'') was found to occur, with $a=3.784$ Å, $b=3.802$ Å, $c=35.82$ Å, and $\beta=91.00°$. This polymorph was reported to undergo a phase transition at 320 °C (to α') with $a=b=5.365$ Å, $c=35.85$ Å, $\beta=91.00°$ at 400 °C. A tetragonal modification was apparently obtained with long time heating at 1450 °C which, when examined at 20 °C, was found to have $a=3.795$ Å, $c=35.54$ Å.

Franklin and Wu [16] have suggested that, from room temperature single crystal data, the high temperature form of Ta_2O_5 can be interpreted as triclinic with $a=7.58$ Å, $b=7.59$ Å, $c=35.71$ Å, $\alpha=90.23°$, $\beta=91.14°$, and $\gamma=90.12°$.

4.2.1. H-Ta_2O_5

In the present investigation Ta_2O_5 was found to exhibit an enantiotropic phase transition at about 1360 ± 10 °C. The addition of TiO_2 lowers the phase transition from about 1360 to about 1150 °C at 9 mole percent TiO_2. By extrapolation from high temperature x-ray data the high temperature form is postulated to be tetragonal in its stability field rather than the monoclinic or triclinic symmetry generally observed at room temperature. The symmetry of H-Ta_2O_5 cannot be proven conclusively since the phase transition temperature is above the upper temperature limitation of the high temperature x-ray furnace used for this study.

4.2.2. Metastable Phases of Ta_2O_5

From high temperature data, Ta_2O_5 can be shown to have a number of metastable phases occurring in the stability field of the low temperature polymorph. They are indicated on figure 1 as H_{tri}-Ta_2O_5,

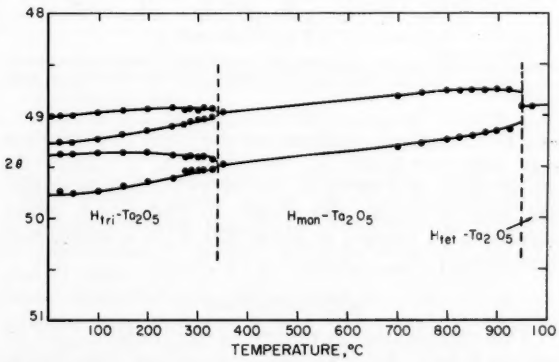

FIGURE 2. *Metastable phase transitions in the high temperature form of* Ta_2O_5 *(from high temperature x-ray data)* (CuK_α).

H_{mon}-Ta_2O_5, and H_{tet}-Ta_2O_5. A plot of temperature versus 2θ is shown in figure 2 for the family of peaks generated by symmetry changes for the tetragonal (1,0,17). The metastable phase assemblage of the high temperature form of Ta_2O_5 is significantly changed by the addition of TiO_2 and the existence of several solid solution phases was established. They are indicated on figure 1 as $30{:}1_{ss}$, H_{mon}-Ta_2O_{5ss}, and H'_{mon}-Ta_2O_{5ss}.

[3] Quotation marks around a compound indicate uncertainty in the exact composition.

[4] H-Ta_2O_5 represents the high temperature polymorph of Ta_2O_5 and phases structurally related to it.

4.2.2.1. H_{tri}-Ta_2O_5: Room Temperature Form

Ta_2O_5 when quenched from above the stable 1360 °C phase transition has undergone at least two metastable phase transitions (tetragonal → monoclinic → triclinic). "Single crystal" precession patterns show a multiplicity of crystallites partially ordered with respect to each other. If a quenched specimen is ground lightly in a mortar and pestle the x-ray powder diffraction pattern shows diffuse peaks. However, if the specimen is carefully prepared for diffraction, with a minimum of mechanical deformation, then the diffuse peaks are resolved into fine line splittings, as previously described by Reisman et al. [11]. This room temperature x-ray diffraction powder pattern (table 2)

TABLE 2. *X-ray diffraction powder data for* H_{tri}-Ta_2O_5 [a]
(CuK$_\alpha$ radiation)

d_{obs}	d_{calc}	hkl [b]	I/I_0 [c]	d_{obs}	d_{calc}	hkl [b]	I/I_0 [c]
8.93	8.93	004	6				
4.47	4.47	008	7	2.485	2.485	$0,\bar{1},11$	12
3.776	3.781	101	58	2.474	2.474	$1,0,11$	17
3.773	3.778	$\bar{1}01$	70	2.466	2.465	$\bar{1},0,11$	26
3.768	3.770	$0\bar{1}1$	55	2.457	2.458	$1\bar{1}6$	64
3.759	3.758	$01\bar{1}$	51	2.454	2.453	$\bar{1}16$	73
	3.624	$\bar{1}03$		2.445	2.446	$0,1,11$	16
3.620			30	2.436	2.437	$\bar{1}16$	61
	3.624	$0\bar{1}3$		2.433	2.433	$1\bar{1}6$	58
3.617	3.617	103	30	2.239	2.241	$0,1,13$	4
3.590	3.591	$01\bar{3}$	3	2.232	2.234	$0,0,16$	12
3.363	3.367	$0\bar{1}5$	68	2.230	2.231	$1,0,13$	9
3.357	3.360	$\bar{1}05$	77	2.224	2.224	$1,0,13$	8
3.354	3.351	105	68	2.207	2.208	$0,\bar{1},13$	4
3.321	3.323	$01\bar{5}$	20	2.031	2.031	$0,\bar{1},15$	7
3.060	3.064	$0\bar{1}7$	25	2.022	2.022	$1,0,15$	7
3.052	3.054	$\bar{1}07$	26	2.015	2.016	$1,0,15$	7
3.044	3.044	107	25	1.8997	1.9004	200	27
3.015	3.018	017	16	1.8915	1.8924	020	27
2.979	2.978	0,0,12	100	1.8492	1.8502	$0,\bar{1},17$	8
2.763	2.762	$01\bar{9}$	3	1.8417	1.8422	$1,0,17$	14
2.751	2.750	$\bar{1}09$	3	1.8360	1.8369	$1,0,17$	15
2.739	2.741	109	5	1.8257	1.8255	$0,1,17$	9
2.717	2.718	$01\bar{9}$	5	1.7861	1.7869	$0,0,20$	3
	2.578	$\bar{1}14$			1.7525	$02\bar{8}$	
	2.575	114		1.7517			1
2.586			3		1.7508	$\bar{2}08$	
	2.562	$\bar{1}14$		1.7461	1.7466	208	1
	2.559	114					

[a] Specimen of Ta_2O_5 heated to 1775 °C for 6 hr and quenched.
[b] Relative intensity.
[c] Based on triclinic cell $a=3.801$ Å, $b=3.785$ Å, $c=35.74$ Å, $\alpha=90°54.5'$, $\beta=90°11.5'$, and $\gamma=89°59.9'$. (The last decimal point of the angles is given for the purpose of recalculation.)

can be completely indexed on the basis of a triclinic cell with $a=3.801$ Å, $b=3.785$ Å, $c=35.74$ Å, $\alpha=90°54.4'$, $\beta=90°11.5'$, $\gamma=89°59.9'$. In this study, the triclinic form was found to undergo a phase transition on heating at about 320 °C to a monoclinic modification (H_{mon}-Ta_2O_5).

4.2.2.2. H_{mon}-Ta_2O_5

This modification is related to the triclinic form by $a_{mon} \approx \sqrt{2}a_{tri}$, $b_{mon} \approx \sqrt{2}b_{tri}$, $c_{mon} \approx c_{tri}$. This monoclinic polymorph is apparently the α' phase reported by Laves and Petter [12]. At about 950 °C on heating in the high temperature x-ray furnace, H_{mon}-Ta_2O_5 inverts to a tetragonal modification (H_{tet}-Ta_2O_5).

4.2.2.3. H_{tet}-Ta_2O_5

This tetragonal modification of Ta_2O_5 may be related to the tetragonal phase (α) reported by Laves and Petter [12]. According to Laves and Petter [12] a tetragonal form was obtained at room temperature by heating Ta_2O_5 for extended periods of time at 1450 °C. The high temperature (950 °C) indexed powder pattern for the tetragonal modification of Ta_2O_5 is given in table 3. The pattern was indexed on the basis of a tetragonal cell $a=3.81$ Å, $c=36.09$ Å. In this study, pure Ta_2O_5 could not be stabilized to room temperature. However, the stabilization could be achieved by the addition of certain impurities [17].

TABLE 3. *High temperature x-ray diffraction powder data for* H_{tet}-Ta_2O_5 [a]
(CuK$_\alpha$ radiation)

d_{obs}	d_{calc}	hkl [b]	I/I_0 [c]
4.55	4.51	008	7
3.80	3.79	101	93
3.65	3.64	103	37
3.37	3.37	105	80
3.07	3.07	107	54
3.02	3.01	0,0,12	80
2.76	2.76	109	10
2.491	2.487	1,0,11	53
2.461	2.461	116	100
2.256	2.256	0,0,16	10
2.247	2.245	1,0,13	17
2.039	2.035	105	7
1.907	1.907	200	43
1.900	1.897	202	47
1.855	1.855	1,0,17	37
1.702	1.704	211	23
	1.700	1,0,19	
1.687			7
	1.690	213	

[a] X-ray taken at 950 °C.
[b] Based on tetragonal cell $a=b=3.81$ Å, $c=36.09$ Å.
[c] Relative intensity.

4.2.3. Metastable Solid Solutions

4.2.3.1. H_{mon}-Ta_2O_{5ss}

The effect of TiO_2 additions was investigated by both high temperature x-ray and conventional quenching techniques. From high temperature x-ray data, Ta_2O_5 accepts in excess of 7 mole percent TiO_2 at 470 °C to form a metastable solid solution phase (H_{mon}-Ta_2O_{5ss}, fig. 1).

The metastable tetragonal ⇄ monoclinic transition indicated in figure 1 as continuing to temperatures above 1000 °C may possibly be stable in the field labeled H-Ta_2O_{5ss}. An ultra-high temperature x-ray study would be needed to establish the equilibrium conditions in this region.

4.2.3.2. H'_{mon}-Ta_2O_{5ss}

The H_{mon}-Ta_2O_{5ss} phase has an apparent morphotropic phase transition to another metastable monoclinic form (H'_{mon}-Ta_2O_{5ss}, fig. 1). The monoclinic angle of H'_{mon}-Ta_2O_{5ss} apparently changes with composition and temperature, and grades into that of the other monoclinic form at about 550 °C and 9 mole percent TiO_2. The x-ray diffraction pattern for H'_{mon}-Ta_2O_{5ss} from the 9:1 composition at room temperature is given in table 4. The specimen was indexed from powder data on the basis of a monoclinic cell with $a=5.367$ Å, $b=5.368$ Å, $c=35.70$ Å, and

TABLE 4. *X-ray diffraction powder data for the phase* H'_{mon}-Ta_2O_5 ($10TiO_2$:$90Ta_2O_5$) [a]

(CuK$_\alpha$ radiation)

d_{obs}	d_{calc}	hkl [b]	I/I_0 [c]
4.469	4.461	008	8
3.771	3.781	111	100
	3.765	$\bar{1}11$	
3.638	3.637	$\bar{1}13$	38
3.596	3.593	$\bar{1}13$	8
3.380	3.379	$\bar{1}15$	65
3.321	3.322	$\bar{1}15$	50
3.076	3.075	$\bar{1}17$	20
3.014	3.014	$\bar{1}17$	25
2.973	2.973	0,0,12	95
2.714	2.713	$\bar{1}19$	15
2.492	2.492	1,1,11	28
2.472	2.472	$\bar{2}06$	38
2.444	2.441	$\bar{1}$,1,11	63
2.418	2.418	$\bar{2}06$	43
2.247	2.247	1,1,13	3
2.232	2.231	0,0,16	8
2.203	2.202	$\bar{1}$,1,13	5
2.036	2.035	1,1,15	5
1.897	1.897	220	63

[a] Specimen heated to 1640 °C for 16 hr and quenched.

[b] Based on monoclinic cell $a=5.367$ Å, $b=5.368$ Å, $c=35.707$ Å and $\beta=91°42'$.

[c] Relative intensity.

$\beta=91°42'$. This phase is apparently related to H_{tri}-Ta_2O_5 in the following manner:

$$a_{mon} \approx \sqrt{2}a_{tri},\ b_{mon} \approx \sqrt{2}b_{tri},\ c_{mon} \approx c_{tri}.$$

4.2.3.3. "30:1$_{ss}$"

From high temperature x-ray data, another phase was found to occur from about 2.5 to 4.5 mole percent TiO_2 and to have a maximum dissociation temperature of about 375 °C. This metastable solid solution phase is apparently related to H_{tri}-Ta_2O_5 and can be indexed on the basis of a monoclinic cell $a=3.794$ Å, $b=3.807$ Å, $c=35.70$ Å, $\beta=90°51'$. This phase corresponds closely to the α'' form of Laves and Petter [12]. The indexed x-ray powder pattern for the 3 mole percent TiO_2 specimen is given in table 5. It should be emphasized again that the high temperature tetragonal form of Ta_2O_5 is not quenched-in and that it is the various metastable phases which are detected when specimens are quenched from elevated temperatures and examined at room temperature by x-ray diffraction.

4.3. $TiO_2 \cdot Ta_2O_5$($TiTa_2O_7$)

The intermediate compound $TiO_2 \cdot Ta_2O_5$ was found to occur in the system and to melt congruently at about 1662 °C. From x-ray diffraction data, table 6, the compound can be indexed on a monoclinic basis $a=20.397$ Å, $b=3.804$ Å, $c=11.831$ Å, $\beta=120°14'$ and is apparently isostructural to the compound $TiNb_2O_7$ reported previously by Roth and Coughanhour [18] and by Wadsley [19]. It is interesting to note that phases analogous to those compounds richer in Nb_2O_5 than $TiNb_2O_7$ [20, 21] were not found to occur in the $TiO_2-Ta_2O_5$ system under the conditions studied. Two eutectics were found to occur in the system (fig. 1) at approximately 54 mole percent Ta_2O_5 and 1650 °C and 31 mole percent Ta_2O_5 and 1630 °C, respectively. Some difficulty was encountered in establishing the solidus curve near the higher TiO_2 eutectic composition since the surface of specimens quenched in this compositional region appeared glazed or partially melted below the solidus. For this reason these data were interpolated to provide the best approach to binary equilibrium. This phenomena is probably due to partial reduction in the subsolidus near the melting point of the phase assemblage. The possible deviations in stoichiometry should be investigated at higher oxygen pressures and temperatures.

TABLE 5. *X-ray diffraction powder data for the phase* "30:1$_{ss}$" ($3TiO_2$:$97Ta_2O_5$) [a]

(CuK$_\alpha$ radiation)

d_{obs}	d_{calc}	hkl [b]	I/I_0 [c]
4.46	4.46	008	3
3.78	3.79	011	80
	3.78	$\bar{1}01$	
	3.78	101	
3.63	3.63	$\bar{1}03$	15
	3.63	013	
3.373	3.371	$\bar{1}05$	13
3.361	3.359	015	60
3.330	3.329	$\bar{1}05$	11
3.066	3.066	$\bar{1}07$	5
3.050	3.051	017	13
3.022	3.022	107	6
2.974	2.975	0,0,12	100
2.761	2.762	$\bar{1}09$	1
2.747	2.746	019	3
2.722	2.721	$\bar{1}09$	3
2.484	2.484	$\bar{1}$,0,11	6
2.469	2.470	0,1,11	15
2.451	2.459	$\bar{1}16$	50
	2.448	1,0,11	
	2.439	116	
2.313	2.313	$\bar{1}18$	2
2.241	2.240	$\bar{1}$,0,13	2
2.231	2.231	0,0,16	6
2.227	2.227	0,1,13	4
2.210	2.209	$\bar{1}$,0,13	2
2.030	2.030	$\bar{1}$,0,15	2
2.018	2.018	0,1,15	2
1.9034	1.9034	020	11
1.8964	1.8967	200	13
1.8926	1.8927	022	7
1.8885	1.8891	$\bar{2}02$	3
1.8486	1.8488	$\bar{1}$,0,17	5
1.8394	1.8386	0,1,17	8
1.8257	1.8256	1,0,17	4
1.7846	1.7848	0,0,20	2

[a] Specimen of $3TiO_2$:$97Ta_2O_5$ heated to 1640 °C for 40 hr and quenched.

[b] Relative intensity.

[c] Based on monoclinic cell $a=3.794$ Å, $b=3.307$ Å, $c=35.70$ Å, and $\beta=90°51'$.

4.4. TiO_2 Solid Solutions

Titanium dioxide was found to exhibit maximum solubility of 10 mole percent Ta_2O_5 at 1625 °C. The

TABLE 6. *X-ray diffraction powder data for* $TiO_2 \cdot Ta_2O_5$ ($TiTa_2O_7$) [a]
(CuK$_\alpha$ radiation)

d_{obs}	d_{calc}	hkl [b]	I/I_0 [c]
10.24	10.22	$00\bar{1}$	2
9.42	9.42	$20\bar{1}$	5
5.11	5.11	$00\bar{2}$	55
5.07	5.08	$40\bar{1}$	24
4.70	4.71	$40\bar{2}$	7
4.41	4.41	400	2
3.714	3.718	110	83
	3.689	$20\bar{2}$	
3.619	3.620	$11\bar{1}$	12
3.461	3.462	401	12
3.398	3.407	$00\bar{3}$	100
	3.388	$60\bar{2}$	
	3.381	$11\bar{1}$	
3.317	3.317	$31\bar{1}$	12
3.297	3.298	$60\bar{1}$	12
2.949	2.946	$40\bar{4}$	12
2.866	2.865	$11\bar{2}$	38
2.754	2.760	$51\bar{1}$	48
	2.753	$51\bar{2}$	
2.725	2.723	$60\bar{4}$	14
2.658	2.657	$11\bar{3}$	38
2.560	2.556	$00\bar{4}$	7
2.540	2.541	$80\bar{2}$	5
2.507	2.508	601	23
2.427	2.426	312	5
2.390	2.389	113	7
2.312	2.312	511	51
	2.310	$60\bar{5}$	
2.290	2.289	$51\bar{4}$	19
2.047	2.044	$00\bar{5}$	38
2.039	2.039	$10,0,\bar{3}$	25
2.006	2.006	$10,0,\bar{2}$	5
	2.004	$51\bar{5}$	
1.9019	1.9020	$02\bar{0}$	29
1.8797	1.8822	$80\bar{6}$	7
	1.8777	$11\bar{5}$	
1.8447	1.8440	404	5
1.8185	1.8177	603	5
1.7825	1.7825	022	7
1.7621	1.7623	10,0,0	7
1.7403	1.7410	910	7
1.7178	1.7162	115	14
1.7066	1.7064	$71\bar{2}$	8
1.6939	1.6940	$12,0,\bar{4}$	19
	1.6938	$12,0,\bar{3}$	
1.6653	1.6658	$11,1,\bar{3}$	29
1.6620	1.6621	$80\bar{7}$	36

[a] Specimen heated to 1620 °C for 16 hr and quenched.
[b] Based on monoclinic cell $a = 20.397$ Å, $b = 3.804$ Å, $c = 11.831$ Å and $\beta = 120°14'$.
[c] Relative intensity.

amount of titanium dioxide solid solution (TiO_{2ss}, fig. 1) at the solidus of 1630 °C decreases with both increasing and decreasing temperatures. The extent of solid solution was delineated by both the disappearing phase and parametric surface methods. The a parameters in Å for the various selected compositions used in the study are shown in figure 1.

Any discussion of the nature of the solid solution would be pure speculation; however, an investigation of the physical properties might prove enlightening in characterizing this solid solution.

5. Future Study

This study has established that although ions of a size similar to Ta^{+5} but with different valence apparently enter into solid solution with H-Ta_2O_5 they form discrete phases with L-Ta_2O_5. However, the reasons for this type of interaction cannot be determined without a knowledge of the crystal structures of both forms. The crystal structures cannot be determined without single crystals. *Single* crystals of pure Ta_2O_5 apparently cannot be grown in either of the two main polymorphic forms. We, therefore, propose that a study of other systems will be of help in determining proper compositions to be used in the growth of single crystals of phases having structures similar to the polymorphs of Ta_2O_5. Such studies are in progress and will be reported at a future date.

The authors wish to thank Mrs. E. K. Hubbard of the National Bureau of Standards for the spectrochemical analysis.

6. References

[1] G. Brauer, Z. Anorg. Allgem. Chem. **82,** 373 (1913).
[2] R. Hahn, J. Am. Chem. Soc. **73,** 5091 (1951).
[3] K. Lehovec, J. Less-Common Met. **7,** 397 (1964).
[4] X-ray Powder File Card 8–255, ASTM.
[5] A. Zaslavskii, Dokl. Akad. Nauk SSSR, 104 (1955).
[6] J. Harvey and H. Wilman, Acta Cryst. **14,** 1278 (1961).
[7] L. Frevel and H. Rinn, Analyt. Chem. **27,** 1329 (1955).
[8] N. Terao, Japan, J. Appl. Phys. **6,** 21 (1967).
[9] R. Moser, Schweiz. Mineral. Petrog. Mitt. **45,** [1], 35 (1965).
[10] S. Lagergren and A. Magneli, Acta Chem. Scand **6,** 444 (1952); and ASTM Card 5–0258.
[11] A. Reisman, F. Holtzberg, M. Berkenblit, and M. Berry, J. Am. Chem. Soc. **78,** 4514 (1956).
[12] F. Laves and W. Petter, Naturw. **51,** 633 (1964).
[13] O. Ruff, Z. Anorg. Allgem. Chem. **82,** 373 (1913).
[14] S. J. Schneider, NBS Monograph 68 (1963).
[15] L. Jahnberg and S. Andersson, Acta Chem. Scand. 21, 615 (1967).
[16] E. Franklin and V. Wu, Owens-Illinois Technical Center, personal communication.
[17] To be published.
[18] R. S. Roth and L. Coughanhour, J. Res. NBS **55,** No. 4, 209–211 (1955) (RP2621).
[19] A. D. Wadsley, Acta Cryst. **14,** 660 (1961).
[20] A. D. Wadsley, Acta Cryst. **14,** 664 (1961).
[21] R. S. Roth and A. D. Wadsley, Acta Cryst. **18,** 724 (1965).

(Paper 72A2–493)

JOURNAL OF RESEARCH of the National Bureau of Standards—A. Physics and Chemistry
Vol. 72A, No. 2, March–April 1968

Effect of Statistical Counting Errors on Wavelength Criteria for X-Ray Spectra*

John S. Thomsen[1] and F. Y. Yap[2]

(June 29, 1967)

Various features of the spectral profile of an x-ray line can be measured with an uncertainty which is only a small fraction of the observed line width. With recent improvements in measurement techniques, statistical errors due to the random fluctuations of the intensities in counter recordings may become significant. The present study considers the effect of such errors on several features of the line profile which could be used for definition of its wavelength. These may be broadly classified into three groups, viz, the peak, the centroid, and the median. In the present analysis the statistical errors associated with these features are compared theoretically, with the assumption of negligible error in angular measurement. Certain systematic errors are also briefly examined. The effects of truncation range, asymmetry, and background intensity are considered, as well as possible optimization of the data-taking procedure.

In general, σ, the standard deviation of the wavelength, is given by $\sigma/W = F/(I_p T)^{1/2}$, where W is the full width at half-maximum intensity, I_p the peak intensity, T the total counting time, and F a dimensionless factor of the order of unity. Thus F may be regarded as a factor of merit for comparing the various cases, a low value of F being desirable. When the form of the line profile is known a priori, it is usually best to make use of this knowledge; e.g., a Lorentzian can be thus fitted with $F \approx 0.8$ for any of the three wavelength features. Using optimized truncation ranges and including the error in locating end points, one obtains approximately this same F for the centroid or median even without prior knowledge of the profile. In the latter case the value of F for the peak usually ranges from about 1.6 to 2.1. However, the peak is less subject to certain systematic errors and is preferable from the viewpoint of simplicity and historical precedent. It is recommended that use of the peak be continued at present; further study of the problem from the viewpoint of atomic energy level interpretation would be desirable.

Key Words: Lattice constants, peak intensity, physical constants, spectral line profiles, statistical error analysis, x-ray line shapes, x-ray spectra, x-ray wavelength criteria.

Contents

	Page
1. Introduction	188
1.1. Problem of wavelength criterion	188
1.2. Previous investigations	188
1.3. Profile features for wavelength criteria	189
2. Preliminary considerations	189
2.1. Experimental assumptions	189
2.2. Lorentzian line profile	190
2.3. Asymmetric lines	190
2.4. Gaussian profile	191
2.5. Variance of data points	191
3. Centroid	191
3.1. Truncation procedure	191
3.2. Idealized statistical error	192
3.3. Optimization of statistical error	192
3.4. Truncation mislocation factor	192
3.5. Application to quasi-Lorentzian profile	193
3.6. Application to quasi-Gaussian profile	194
3.7. Systematic errors	194
3.8. Effect of asymmetry	194
4. Median	195
4.1. Computation and truncation procedure	195
4.2. Idealized statistical error	195
4.3. Optimization of statistical error	195
4.4. Truncation mislocation factor	195
4.5. Application to quasi-Lorentzian profile	196
4.6. Application to quasi-Guassian profile	196
4.7. Systematic errors	196
4.8. Effect of asymmetry	197
5. Geometrical peak	197
5.1 Orthogonal polynomial technique	197
5.2. Statistical error	197
5.3. Goodness of fit	198
5.4. Application to quasi-Lorentzian profile	198
5.5. Optimization of statistical error	199
5.6. Application to quasi-Gaussian profiles	199
5.7. Systematic errors	199
5.8. Effect of asymmetry	200
5.9. Parabolic fit	200
5.10. Optimization of parabolic fit	200
5.11. Profile known a priori	201
5.12. Optimization of Lorentzian	201
6. Extrapolated peak	202
6.1. Midpoint of single chord	202
6.2. Use of fitted curve	202
6.3. Use of raw data	203
7. Conclusions	203
8. References	204

*An invited paper. This work supported in part by the National Bureau of Standards.
[1] Department of Physics, Johns Hopkins University, Baltimore, Md. 21218.
[2] Physics Department, Wilson College, Chambersburg, Pa. 17201.

1. Introduction

1.1. Problem of Wavelength Criterion

X-ray emission lines have natural widths of the order of 0.1 percent of their wavelengths and in many cases show considerable asymmetry in their line profiles [1].[3] Precision wavelength measurements [2,3] have frequently claimed accuracies of a few parts per million; in a recent paper by Bearden and coworkers [4] probable errors of approximately one part per million were reported for five standard reference lines. Since the error estimate is thus only a fraction of 1 percent of the line width, it is clearly necessary to use some specific feature of the line profile in defining the wavelength. For symmetric lines all criteria which are likely to be regarded as reasonable definitions will reduce to the same value; in the more general case of asymmetric lines, the resulting values may differ appreciably.

These wavelengths are vitally important both in determining atomic energy levels and in providing standards for crystallography and γ-ray spectroscopy. Hence at least four factors should be considered in formulating a wavelength criterion, viz:

1. Consistency of the resulting energy level scheme with the Ritz combination principle, i.e., the atomic interpretation.
2. Simplicity of the definition.
3. Historical precedents and current usage.
4. Attainable accuracy as limited by the effects of both systematic and statistical errors.

While the first factor is clearly the one of most fundamental physical significance, presently available experimental data and theoretical knowledge of x-ray line shapes do not appear to provide a clear answer to this point. From the standpoint of simplicity and intuitive appeal the peak of the line profile is probably the most acceptable criterion. This is also generally supported by current usage in x-ray spectroscopy, as well as considerable historical precedent.

The majority of tabulated x-ray emission wavelengths were recorded with photographic plates. Usually it was not stated just what point on the profile defined wavelength, although this probably corresponded, at least approximately, to the position of maximum blackening. In some cases a microdensitometer trace of the plates was made and the maximum used to specify wavelength.

Most recent high precision determinations measure the peak of a line by rotating a crystal through small angular increments and recording the intensity at each step by means of a photon counter (gas or scintillation counter), yielding a step-by-step scan of the line profile. This basic method has been used with single-crystal [4], double-crystal [4], and curved-crystal [5] spectrometers. High angular accuracy has long been attainable; the recent development of an angular interferometer [6] has furnished a new precise and convenient technique to facilitate the required angular measurements.

The accuracy of a wavelength measurement is limited by both systematic and statistical errors. Systematic errors may arise from numerous causes, e.g., drift in x-ray tube voltage, presence of satellites, and distortion due to the instrumental "window." While this window may be the predominant factor in crystallography and γ-ray spectroscopy, it is much less serious in x-ray spectroscopic work.

With good crystals and proper geometry, such distortion of the true line profile may be held to a minimum. For example, using two good quartz crystals with the Mo $K\alpha_1$ line in second order, Bearden [4] obtained a window curve which was only about 3 percent of the natural line width. Brogren [7] reported a comparably narrow window with the Cu $K\alpha_1$ line. Moreover, Bonse and Hart [8] recently reported almost tailless x-ray rocking curves obtained by multiple Bragg reflections between the walls of grooves cut into large perfect crystals of silicon and germanium. Furthermore, one may remove much of the residual instrumental distortion by "unfolding techniques" [9]; Sauder [10] has given a somewhat simplified method of correcting selected features of the line profile.

The statistical error is largely due to random intensity fluctuations, caused by the inherent nature of the photon emission from the x-ray target and by the properties of the counter. The present paper is principally concerned with this factor as it affects the various features used to define wavelength. It also treats briefly certain sources of systematic error which are sensitive to the choice of wavelength criterion.

Thomsen [11] has given a preliminary analysis of the problem and indicated how the errors may often be reduced by varying the counting times for different points on the line profile. Subsequently Wilson, Thomsen, and Yap [12] generalized this optimization procedure. The overall problem has been comprehensively treated in a thesis by Yap [13], which forms the basis for the present paper.

This treatment will consider at length three features of the line profile, viz, the centroid, the median, and the peak. To date the peak has been used almost exclusively in x-ray spectroscopy whenever a defining feature was explicitly specified. Some crystallographers [14] and γ-ray spectroscopists [15] have employed the centroid and the median in a limited number of cases.

The greater mathematical simplicity of the centroid and median facilitates a more straightforward and complete analysis; hence we will treat them first. Both offer the possibility of a limited improvement in the statistical error. However, we finally recommend continued use of the peak, primarily because of its simplicity and its current acceptance. The statistical error of the peak is treated at length in section 5, which is independent of the analysis of the centroid and median in sections 3 and 4.

1.2. Previous Investigations

Other investigators have studied various aspects of the problem. Pike and Wilson [16] derived the statis-

[3] Figures in brackets indicate the literature references at the end of this paper.

tical error of the centroid; Parrish [14] and his coworkers studied, both theoretically and experimentally, the use of the centroid for lattice parameter measurements, including the effect of truncation error. Merrill and DuMond [17] analyzed the problem of fitting a Lorentzian to the data points by least squares and outlined a method for obtaining the resulting statistical error of the peak. Previously Muller, Hoyt, Klein, and DuMond [18] had derived an expression for the statistical error that arises in fitting any assumed profile to the data and applied this result to the case of an isosceles triangle. Knowles [19] obtained an approximate expression for the statistical error of the median.

Several workers have made comparative studies of various features. Cohen and DuMond [20] discussed the relative merits of the centroid and the peak, and recommended the use of the latter. The same conclusion was reached earlier by Porteus and Parratt [21] in an unpublished investigation. Wilson [22] analyzed both the statistical and the systematic errors that result from locating the peak by a least-squares parabolic fit to the data and by finding the midpoint of a horizontal chord. Beu and Scott [23] discussed reasons for preferring the peak to the centroid for lattice parameter measurements. Recently Bačkovsky [24] compared several features, including the peak and the midpoint of a horizontal chord, and suggested using the latter, with the chord drawn near the inflection point of the line profile.

1.3. Profile Features for Wavelength Criteria

a. *The Centroid.* In the present analysis we will define the *centroid* x_c as the center of mass of some specified truncated portion of the line profile, i.e.,

$$x_c = \int_{X_1}^{X_2} xI(x)dx \Big/ \int_{X_1}^{X_2} I(x)dx, \tag{1.1}$$

where $I(x)$ represents the true intensity and X_1 and X_2 the selected truncation limits. In principle, the abscissa variable x should represent wavelength; however, x-ray lines are sufficiently narrow so that an angle or an energy scale may be employed with negligible error.

It should be noted that crystallographers [14] who have employed the centroid have always assumed an infinite range in the above *definition* (which is essential in order to apply the convolution theorem for addition of centroids). Experimentally it was, of course, necessary to infer the centroid value by extrapolation from a finite truncated portion of the curve. By contrast the present paper considers the possibility of *defining* the centroid with *finite truncation limits*, which represents a generalized concept.

b. *The Median.* Similarly we will define the *median* as that value x_m which equally divides some specified portion of the line profile, i.e.,

$$\int_{X_1}^{x_m} I(x)dx = \int_{x_m}^{X_2} I(x)dx. \tag{1.2}$$

c. *The Peak.* Finally we will define the *peak* simply as the abscissa x_p corresponding to the maximum intensity. (In this connection we will disregard the possibility of multiple peaks.) In practice two primary techniques have been used to locate this feature; the results so obtained will be termed (i) the geometrical peak and (ii) the extrapolated peak.

(i) *The Geometrical Peak.* A smooth curve may be fitted to the raw data points by a computer (using either a theoretical line profile or an empirical function with undetermined parameters) or drawn in graphically. The *geometrical peak* x_p is then defined as the abscissa value for which the maximum occurs, i.e.,

$$[dI(x)/dx]_{x=x_p} = 0. \tag{1.3}$$

(ii) *The Extrapolated Peak.* When graphical methods are used, statistical fluctuations make it difficult to determine the exact maximum of a smooth curve. Hence spectroscopists developed the technique of drawing several horizontal chords across the upper portion of the profile, determining their midpoints, and drawing a smooth "bisector curve" (often simply a straight line) through these midpoints; the bisector was then extrapolated to intersect the line profile to obtain the peak [25]. This method is illustrated in figure 1. With the advent of computers various analytical modifications of this technique are now feasible; these are described more fully in section 6. We will denote the peak found by any of these methods as the *extrapolated peak.*

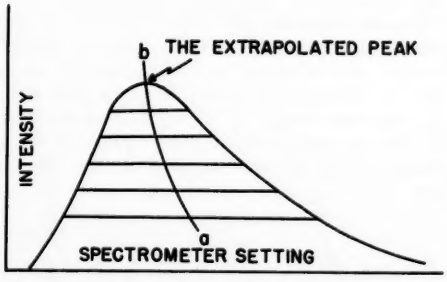

FIGURE 1. *Extrapolation technique of locating peak by means of a smooth bisector curve through chord midpoints.*

For symmetric lines it is also possible to use the average of the midpoints of several chords [26] or even the midpoint of a single chord [27] as a means of determining the peak. (Since the lines are assumed symmetric, this technique might equally well be said to determine the centroid or the median.) For reasons of mathematical similarity, this approach is considered along with the extrapolated peak.

2. Preliminary Considerations

2.1. Experimental Assumptions

Our present analysis is primarily from the viewpoint of the spectroscopist rather than the crystallographer.

The spectroscopist is chiefly interested in a simple, accurate, reproducible criterion for measuring wavelengths; he normally employs a device with a relatively narrow instrumental window (e.g., a double-crystal spectrometer), which does not greatly distort the natural line profile. The crystallographer uses x rays as a tool to study crystal structure and frequently employs a powder diffractometer, which greatly broadens the natural line.

These differences may lead to the choice of different wavelength criteria. For example, the crystallographer may employ the centroid and the spectroscopist use the peak. No fundamental difficulty should result, provided that these two features can be related with high accuracy for the rather limited number of intense lines commonly used by crystallographers.

We will adopt the following assumptions as to experimental conditions:

(A) There is no drift in x-ray intensity incident on the spectrometer.

(B) Both counting time intervals and angular positions (and hence the corresponding wavelength or energy scales) on the spectrometer can be measured with negligible error.

(C) The instrumental window causes a negligible shift in the selected feature for the wavelength criterion, or the necessary correction may be made with negligible error.

(D) Measurements are recorded at a finite number of closely spaced points (usually at equal abscissa intervals). Consequently *it will always be assumed possible to replace an integral by the corresponding sum, and vice versa, whenever convenient.*

(E) *Photon counts at the individual data points are statistically independent of one another and follow the Poisson distribution*, and the number of counts recorded is always sufficiently large so that *the latter may be approximated by a normal distribution.* It follows that the variance (i.e., the square of the standard deviation) for a total count N at the ith point is given by

$$\sigma_N^2 = N. \tag{2.1}$$

Experimental tests [13] are in good accord with these assumptions.

(F) Background is relatively small compared to the peak intensity and is free from drift. In most of the analysis we will also assume that the background is independent of wavelength over the relevant portion of the profile; however, the effect of a linear variation will also be briefly discussed.

Background intensity B may be determined experimentally by preliminary measurements at points well removed from the peak on either side. This is then subtracted from the experimentally observed value, I_{obs}, for each point to give the computed intensity, i.e.,

$$I = I_{obs} - B. \tag{2.2}$$

An error in the background *correction* B may produce a systematic effect throughout a given run, but will not affect the statistical error discussed under assumption (E) above. Hence the effective variance of I is

$$\sigma^2(I) = \sigma^2(I_{obs}). \tag{2.3}$$

Thus it is governed by the total intensity, both line and background.

2.2. Lorentzian Line Profile

There is both theoretical [28] and experimental [29] evidence to indicate that many x-ray emission line profiles are closely approximated by a Lorentzian curve (often referred to as a witch), which is given by

$$I(x) = I_p \left[1 + \frac{4(x - x_p)^2}{W^2}\right]^{-1}, \tag{2.4}$$

where I and x represent intensity and wavelength respectively, I_p and x_p denote the respective coordinates of the peak, and W represents the *full width* of the curve at *half maximum intensity.*

Frequently the Lorentzian curve may be a fair approximation to the true line profile, but *not* sufficiently good to be assumed a priori. In such cases, after the standard deviation has been calculated in generalized form, we may then insert the Lorentzian expression, eq (2.4), *only for the purpose of obtaining an error estimate.* We will term such a line profile a *quasi-Lorentzian.*

It is convenient to normalize I and x in the above expression by defining

$$g = I/I_p, \tag{2.5}$$

$$v = 2(x - x_p)/W. \tag{2.6}$$

Except where otherwise indicated, all equations will be expressed in terms of these normalized coordinates.

The Lorentzian equation then becomes

$$g(v) = (1 + v^2)^{-1}. \tag{2.7}$$

2.3. Asymmetric Lines

Many prominent x-ray emission lines are asymmetric; this property has usually been described by an index of asymmetry given by $(v_+ - v_p)/(v_p - v_-)$, where v_p is the wavelength of the peak while v_+ and v_- represent the wavelengths of the half intensity points (*i.e.*, $g_\pm = g_p/2$) on the long and short wavelength sides respectively. Under this definition asymmetries ranged from zero to infinity with a symmetric line having a value of unity.

More recently Sauder [10] proposed the definition

$$s = \frac{(v_+ - v_p) - (v_p - v_-)}{(v_+ - v_p) + (v_p - v_-)} = \frac{v_+ + v_- - 2v_p}{v_+ - v_-}. \tag{2.8}$$

With this convention we have $-1 \leq s \leq 1$, with $s = 0$ corresponding to a symmetric line. We will employ this definition throughout the present paper.

Asymmetric line profiles may be represented by a simple modification of eq (2.7), viz,

$$g(v)=\begin{cases}\{1+[v/(1-s)]^2\}^{-1} & v\leq 0\\ \{1+[v/(1+s)]^2\}^{-1} & v>0.\end{cases} \tag{2.9}$$

Figure 2 shows typical examples of one symmetric and one asymmetric line fitted by eqs (2.7) and (2.9) respectively.

While eq (2.9) furnishes a reasonably good model function, it has at its peak a discontinuity in the second derivative, which seems physically unrealistic. Hence, in some calculations which are sensitive to behavior at this point, it is preferable to employ the alternative model function

$$g(v)=(1+\zeta v)/(1+v^2), \tag{2.10}$$

which has a qualitatively similar behavior for $\zeta \ll 1$, provided we set $\zeta=2s$ and translate the origin by $\zeta/2$.

2.4. Gaussian Profile

While a Gaussian profile is not representative of most lines encountered in x-ray spectroscopy, it does furnish another example which is straightforward to compute mathematically. Hence it is of some interest to consider this case in order to see how far the results for a quasi-Lorentzian can be qualitatively applied to other profiles. The Gaussian case is represented by

$$g(v)=\exp[-(\ln 2)v^2] \tag{2.11}$$

in place of eq (2.7). We may then define a quasi-Gaussian profile analogously to the quasi-Lorentzian one.

2.5. Variance of Data Points

To express the variances of the individual data points in terms of the new normalized variables, we note that the intensity I is defined as $I=N/\Delta t$, where N counts have been recorded in an interval Δt. The corresponding variance of the intensity thus becomes $\sigma_N^2/(\Delta t)^2$ or, by eq (2.1), simply $I/\Delta t$. Employing eq (2.5) to compute the variance of g, we find

$$\sigma_g^2=\sigma^2(I)/I_p^2=g/I_p\Delta t. \tag{2.12}$$

In the case of background the calculation is similar except that, in accordance with eq (2.3), we must replace I by I_{obs}, which is given by eq (2.2). For constant background B, the result may be expressed as

$$\sigma_g^2=(g+\eta)/I_p\Delta t, \tag{2.13}$$

where

$$\eta=B/I_p. \tag{2.14}$$

3. Centroid

3.1. Truncation Procedure

To complete the definition of the centroid given by eq (1.1) we must specify the truncation limits. Taylor, Mack, and Parrish [14] have discussed at length several alternative definitions from the viewpoint of crystallographers. They recommended using a specified

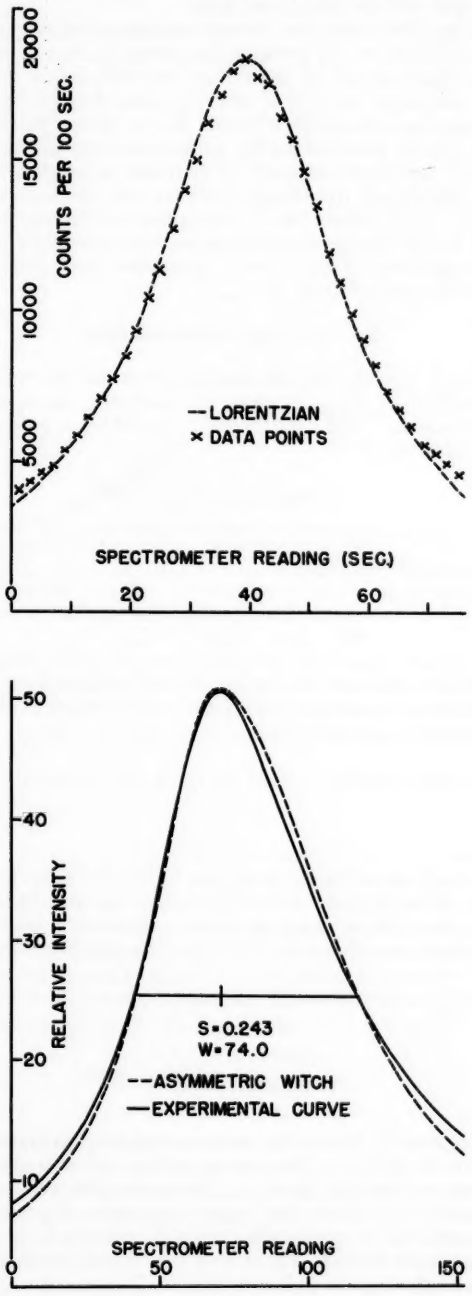

FIGURE 2. (a) *Lorentzian curve fitted to experimental data for* W $K\alpha_1$ *line obtained with a double-crystal spectrometer in* $(1,+3)$ *position.* (b) *Model function of eq* (2.9) *compared with experimental curve for the highly asymmetric* Fe $K\alpha_1$ *line.*

interval symmetric about the centroid; this interval may be located by successive approximations. This definition permits a rather straightforward error analysis and will be employed here.

Even if we knew the correct truncation limits exactly, there would be an error in the centroid due to statistical fluctuations in intensities; we will define this as the *idealized statistical error*, ϵ_c, and denote the corresponding standard deviation by σ_c. Since the limits are in fact determined by successive approximations which are in turn influenced by these statistical errors, an additional uncertainty occurs. As demonstrated below, this introduces a multiplicative factor, which will be denoted as the *truncation mislocation factor*, f_c. The product of these two quantities then gives the *total statistical error*, $(\sigma_c)_{tot}$.

3.2. Idealized Statistical Error

For N equally spaced abscissa intervals the centroid definition in eq (1.1) may be rewritten in terms of summations and normalized variables, given by eqs (2.5–6), as

$$v_c = \Sigma_i v_i g_i / \Sigma_i g_i. \tag{3.1}$$

($1 \leq i \leq N$ in all summations, unless otherwise specified.) It follows that

$$\frac{\partial v_c}{\partial g_j} = \frac{v_j}{\Sigma_i g_i} - \frac{\Sigma_i v_i g_i}{(\Sigma_i g_i)^2} = \frac{v_j - v_c}{\Sigma_i g_i}. \tag{3.2}$$

Since the g_j's are statistically independent with variances given by eq (2.13), the variance of the centroid is now given by

$$\sigma_c^2 = \Sigma_j (\partial v_c / \partial g_j)^2 \sigma_j^2 = (\Sigma_i g_i)^{-2} \Sigma_j (v_j - v_c)^2 (g_j + \eta) / I_p \Delta t_j. \tag{3.3}$$

We may immediately write this in integral form for the case of equal time intervals, noting the $\Delta v = 2V/N$ for the normalized abscissa range $-V \leq v \leq V$ and that the total counting time $T = N\Delta t$. The result is

$$(\sigma_c)_{\text{eq } \Delta t} = (2V/I_p T)^{1/2} \left[\int_{-V}^{V} g(v)\,dv\right]^{-1} \left\{\int_{-V}^{V} (v - v_c)^2 [g(v) + \eta]\,dv\right\}^{1/2}. \tag{3.4}$$

In general, it may be necessary to employ fractional intervals for Δv at the end points in order to obtain a range symmetric about v_c. However, this refinement should not affect the error estimate appreciably, provided N is reasonably large. Furthermore we may frequently bypass the use of fractional intervals by the method given below in section 3.4.

3.3. Optimization of Statistical Error

The idealized statistical error may be reduced by proper choice of the time intervals Δt_j. Let us fix the total time T, which is given by

$$\Sigma_j \Delta t_j = T. \tag{3.5}$$

We may then use the method of Lagrangian multipliers to minimize the j summation in eq (3.3) subject to the constraint of eq (3.5) with the result

$$-[(v_j - v_c)^2 (g_j + \eta)/(\Delta t_j)^2] + \lambda^2 = 0. \tag{3.6}$$

Solving for Δt_j and employing eq (3.5) to evaluate λ yields

$$\Delta t_j = T|v_j - v_c|\,(g_j + \eta)^{1/2} \Big/ \Sigma_i |v_i - v_c|\,(g_i + \eta)^{1/2}, \tag{3.7}$$

where the absolute value sign is used to assure that all time intervals are positive. This equation indicates that, for optimum error, more time should be spent at points on the sides than those at the center; a large background tends to equalize the optimized intervals, as might be expected.

Inserting these values in eq (3.3) and expressing the result in integral form, as done with eq (3.4), we find for the optimized error

$$(\sigma_c)_{\text{opt}} = \int_{-V}^{V} |v - v_c|[g(v) + \eta]^{1/2} dv \Big/ (I_p T)^{1/2} \int_{-V}^{V} g(v)\,dv. \tag{3.8}$$

This result is a special case of that given by Wilson, Thomsen and Yap [12]. From eqs (3.4) and (3.8) we may form the optimization ratio

$$\frac{(\sigma_c)_{\text{opt}}}{(\sigma_c)_{\text{eq } \Delta t}} = \frac{\int_{-V}^{V} |v - v_c|[g(v) + \eta]^{1/2} dv}{\left\{2V \int_{-V}^{V} (v - v_c)^2 [g(v) + \eta]\,dv\right\}^{1/2}}. \tag{3.9}$$

The above expression is simply the ratio of the mean value of the function $|v - v_c|[g(v) + \eta]^{1/2}$ to its root-mean-square value. Hence its qualitative behavior can readily be visualized by plotting this function for any specific case.

3.4. Truncation Mislocation Factor

Let us define our coordinate system with origin at the true centroid. If the desired truncation limits were known exactly, there would be only the idealized statistical error ϵ_c as discussed in section 3.1. Actually the limits are never exactly known; we may begin with a trial value of $v_c^{(0)}$ for the centroid and use this to compute a first approximation $v_c^{(1)}$. Similarly successive approximations may be computed, the kth approximation being denoted by $v_c^{(k)}$.

In eq (3.1), the denominator is proportional to the area under the profile in the range $-V \leq v \leq V$; this is insensitive to small location errors for a curve of moderate asymmetry. The numerator represents a first moment and is sensitive to such errors. For the $(k+1)$th approximation the range is

$$-V + v_c^{(k)} \leq v \leq V + v_c^{(k)};$$

if $v_c^{(k)}$ should vanish, we would obtain the idealized statistical error, ϵ_c, for the particular curve. Hence eq (3.1) may be rewritten as

$$v_c^{(k+1)} \approx \int_{-V+v_c^{(k)}}^{V+v_c^{(k)}} vg(v)dv \Big/ \int_{-V}^{V} g(v)dv \approx \epsilon_c + r_c v_c^{(k)}, \quad (3.10)$$

where

$$r_c \equiv V[g(V)+g(-V)] \Big/ \int_{-V}^{V} g(v)dv. \quad (3.11)$$

Now r_c is simply the ratio of the average height of of the profile at the end points to the average height over the entire range; hence $r_c < 1$. The recursion relation, eq (3.10), and the initial condition are satisfied by

$$v_c^{(k)} = \epsilon_c \sum_{m=0}^{k-1} r_c^m + r_c^k v_c^{(0)}, \quad (3.12)$$

which converges to the value v_c given by

$$v_c = \epsilon_c/(1-r_c). \quad (3.13)$$

The denominator on the right is independent of the particular curve. Hence the standard deviations given by eqs (3.4) and (3.8) (which represent averages over several curves) must be multiplied by a *truncation mislocation factor* f_c, i.e.,

$$f_c \equiv (\sigma_c)_{tot}/\sigma_c = 1/(1-r_c). \quad (3.14)$$

The above results also suggest a means of bypassing the successive iterations. For $k=1$, eq (3.12) becomes simply $v_c^{(1)} = \epsilon_c + r_c v_c^{(0)}$. Solving for ϵ_c and substituting in eq (3.13) yields

$$v_c - v_c^{(0)} = (v_c^{(1)} - v_c^{(0)})/(1-r_c). \quad (3.15)$$

Thus, if the trial value $v_c^{(0)}$ is a reasonably good guess, the value of r_c may be approximated and v_c then computed from the above expression without further iterations.

3.5. Application to Quasi-Lorentzian Profile

If the line profile is quasi-Lorentzian (see sec. 2.2), we may substitute eq (2.7) in the various expressions for the centroid to obtain more explicit results. Since $v_c = 0$ for this model, eq (3.4), for equal time intervals, yields

$$(\sigma_c)_{eq\ \Delta t} = (V/I_p T)^{1/2}(\tan^{-1} V)^{-1}[V - \tan^{-1} V + (\eta V^3/3)]^{1/2}. \quad (3.16)$$

This result is essentially the same as that obtained by Pike and Wilson [16]. In figure 3 it has been transformed to the wavelength variable x by means of eq (2.6) and is plotted for various values of range and background.

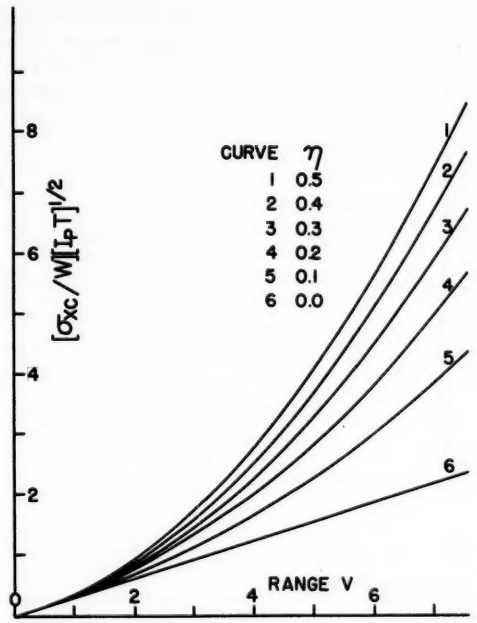

FIGURE 3. *Idealized statistical error of centroid of a quasi-Lorentzian profile as function of truncation range for various values of background parameter* η.

Similarly we may integrate eq (3.9) explicitly for the quasi-Lorentzian case; however, the resulting expression is rather complicated and not particularly informative. For the special case of zero background, the result in simply

$$(\sigma_c)_{opt}/(\sigma_c)_{eq\ \Delta t} = [(1+V^2)^{1/2} - 1][V(V - \tan^{-1} V)]^{-1/2}. \quad (3.17)$$

This ratio varies from 0.86 at $V=0$ to 1.00 as $V \to \infty$. (Detailed calculations indicate that it is insensitive to background.) Hence only a limited improvement can be achieved by optimizing the data-taking procedure.

The *truncation mislocation factor* is found by combining eqs (2.7), (3.11), and (3.14), with the result

$$f_c = \frac{(1+V^2)\tan^{-1} V}{(1+V^2)\tan^{-1} V - V}. \quad (3.18)$$

This factor is unity for infinite V, attains a value of 2.75 for $V=1.0$, and approaches infinity as $V \to 0$.

Idealized statistical errors for the case of zero background and equal time intervals have been calculated from eq (3.16), multiplied by the above factor to obtain the total error, and plotted in figure 4 (after conversion to the wavelength variable x). This curve reaches a minimum for $V \approx 1$, in which case the *total statistical error* is given by

$$(\sigma_{xc}/W)_{tot} = \sigma_c/2 = 0.81/(I_p T)^{1/2}, \quad (V=1). \quad (3.19)$$

289-015 O-68—6

(Note that $V=1$ implies the centroid of a relatively narrow truncated portion of the profile, rather than the centroid definition as used by some crystallographers.) Optimization can reduce this error by only 11 percent, as shown by eq (3.17) and by figure 4.

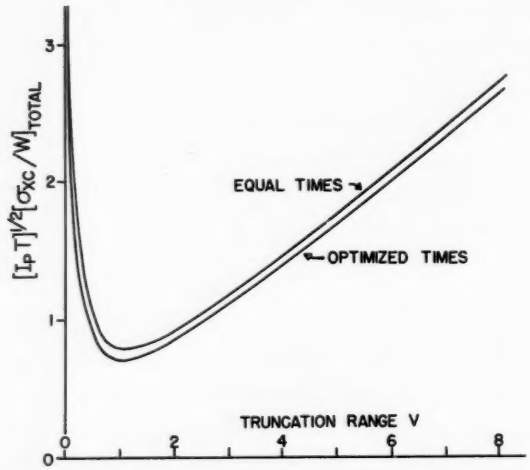

FIGURE 4. *Total statistical error of centroid of a quasi-Lorentzian profile as a function of truncation range for equal and for optimized counting time intervals (zero background).*

3.6. Application to Quasi-Gaussian Profile

We may carry out similar calculations for the quasi-Gaussian profile defined by eq (2.11). The minimum error occurs at $V \approx 1.8$, for which the numerical factor in eq (3.19) is reduced to 0.62. In contrast to the Lorentzian case, this range includes over 90 percent of the area under the profile; this is due to the rapid decay of the tails of a Gaussian.

Optimization of time intervals can reduce the above figure by about 8 percent. For large truncation ranges and zero background, optimization could be of crucial importance; the numerical factor would then asymptotically approach 0.68 in sharp contrast with the case of equal intervals, where the error approaches infinity. However, any appreciable background will cause an increase in the error at large ranges and greatly reduce the advantage of optimization.

3.7. Systematic Errors

There are at least two sources of systematic error whose effects may depend upon the choice of wavelength criterion adopted; these are *undetected* background and the presence of unresolved satellites. Since we consider only the case where truncation limits are taken symmetrically about the centroid, the resulting centroid position must be unaffected by a *constant* background, even if no correction is made for it. However, if there is an undetected linearly varying background, i.e., if the observed intensity (after the experimental background correction) is given by

$$g_{obs}(v) = g(v) + \eta + \mu v, \tag{3.20}$$

the linear term will cause a systematic error. Assuming that the curve is almost symmetrical, we may as a first approximation calculate the centroid for a symmetric range about the origin and then apply eq (3.15) to find the centroid of the observed curve. The result may be expressed as

$$v_c + \delta v_c = \frac{v_c^{(1)} + \delta v_c^{(1)}}{1 - r_c} = \frac{\int_{-V}^{V} v g(v) dv + (2\mu V^3/3)}{\int_{-V}^{V} g(v) dv - V[g(V) + g(-V)]}, \tag{3.21}$$

where δv_c represents the systematic error due to the background term in μ. For a quasi-Lorentzian profile this term becomes

$$\delta v_c = \frac{\mu V^3 (1 + V^2)}{3[(1 + V^2) \tan^{-1} V - V]}. \tag{3.22}$$

This error is roughly equal to μ for $V=1$ and to $0.2\mu V^3$ for $V \gg 1$. Thus for $V=1$ and $I_p T \sim 10^6$, we must have $\mu \sim 10^{-3}$ to keep this systematic error of the same order as the statistical one; for $V \gg 1$, the requirement is clearly far more stringent. It should be reemphasized that μ refers only to the undetected portion of the background, i.e., it is an error term in the background correction.

A satellite, whose amplitude is likely to be voltage dependent, may be strong enough to cause an appreciable systematic error in the centroid and yet not be resolved. For large truncation ranges, the worst situation occurs with the satellite just short of the truncation limit; its moment arm is then almost equal to V. If W_s denotes the satellite width and α_s the ratio of its amplitude to that of the main peak, the systematic error is roughly $V\alpha_s W_s/W$. For $V \sim 1$, the worst situation occurs when the satellite peak is appreciably inside the truncation limit; the error is then of the order of 0.5 α_s and is less sensitive to W_s.

3.8. Effect of Asymmetry

The form of eqs (3.4) and (3.9) indicates that the centroid statistical errors should be insensitive to moderate asymmetries since they depend on the shape only through integral expressions involving the normalized profile. Furthermore it seems clear that the error should not depend on the sign of s (the index of asymmetry defined by eq (2.8)); hence we might expect that the relative change in the standard deviation is of the order of s^2. This expectation was verified [13] by taking the model function of eq (2.9) with asymmetry $s=0.24$ (corresponding to the Fe $K\alpha_1$ line) and inserting it in eq (3.4). The resulting error was about 1 percent greater than that for the symmetric quasi-Lorentzian.

The actual displacement of the centroid from the peak will depend both on the range and on the model function employed. For $V=1$ the displacement $v_c - v_p$ is approximately 0.67 s with eq (2.9) and 0.50 s with eq (2.10). In terms of wavelength these expressions become 0.34 sW and 0.25 sW, respectively.

4. Median

4.1. Computation and Truncation Procedure

As in the case of the centroid, we must employ a truncated portion of the line profile for a practical determination of the median. For simplicity, we will adopt the same convention, viz, a specified range which is symmetric about the median and which may be determined by successive approximations. The *total statistical error* will again be given by an *idealized statistical error*, ϵ_m, with corresponding standard deviation σ_m, multiplied by a *truncation mislocation factor*, f_m.

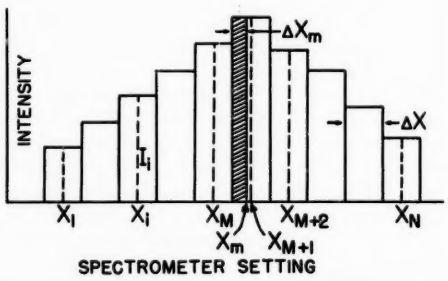

FIGURE 5. *Illustration of median located in the* (M + 1)*th interval, as used in derivation of eq (4.3).*

In order to calculate the median error it is helpful to derive a more explicit expression for the median than that given by eq (1.2). Let us pass from the continuous to the discrete case and represent the data by the histogram of figure 5, where each abscissa value corresponds to the *midpoint* of the base of the corresponding rectangle. If the median is located in the $(M+1)$th interval, its position x_m is defined by

$$_m = x_M + (\Delta x/2) + \Delta x_m. \tag{4.1}$$

Equation (1.2) now becomes

$$\sum_{i=1}^{M} I_i \Delta x + I_{M+1}\Delta x_m = \sum_{i=M+1}^{N} I_i \Delta x - I_{M+1}\Delta x_m. \tag{4.2}$$

Rearranging and inserting the normalized variables defined by eqs (2.5–6) yields

$$\Delta v_m = (\Delta v/2g_{M+1})\left[\sum_{i=M+1}^{N} g_i - \sum_{i=1}^{M} g_i\right]. \tag{4.3}$$

4.2. Idealized Statistical Error

The statistical error in v_m is just that in Δv_m. The calculation is similar to that for the centroid in section 3.2, except that two cases must be considered for the required partial derivatives. For $i \neq M+1$, eq (4.3) yields

$$[\partial(\Delta v_m)/\partial g_i]^2 = (\Delta v/2g_{M+1})^2. \tag{4.4}$$

For the special case in which $i = M+1$, we obtain

$$[\partial(\Delta v_m)/\partial g_{M+1}] = -(\Delta v/2g_{M+1}^2)\left[\sum_{i=M+2}^{N} g_i - \sum_{i=1}^{M} g_i\right]. \tag{4.5}$$

The summations may now be eliminated through the help of eq (4.3); it follows that

$$[\partial(\Delta v_m)/\partial g_{M+1}] = (\Delta v - 2\Delta v_m)/2g_{M+1}. \tag{4.6}$$

By figure 5, $0 \leq \Delta v_m \leq \Delta v$. Hence it is clear that the right side of eq (4.4) represents an upper limit for $i = M+1$; if $N \gg 1$ we may employ this equation for all i without serious error.

The calculation then proceeds as for the centroid, with the result

$$(\sigma_m)_{\text{eq }\Delta t} = (V/2g_m^2 I_p T)^{1/2}\left\{\int_{-V}^{V}[g(v)+\eta]dv\right\}^{1/2}, \tag{4.7}$$

where we have set $g_{M+1} \approx g_m$, the ordinate at the median.

4.3. Optimization of Statistical Error

The optimization procedure may again be carried out by the method of Lagrangian multipliers. The optimum time intervals are

$$\Delta t_j = T(g_j+\eta)^{1/2} \Big/ \sum_i (g_j+\eta)^{1/2}, \tag{4.8}$$

which yield for the optimization ratio

$$\frac{(\sigma_m)_{\text{opt}}}{(\sigma_m)_{\text{eq }\Delta t}} = \frac{\int_{-V}^{V}[g(v)+\eta]^{1/2}dv}{\left\{2V\int_{-V}^{V}[g(v)+\eta]dv\right\}^{1/2}}. \tag{4.9}$$

4.4. Truncation Mislocation Factor

Calculation of the truncation mislocation factor is also similar to that for the centroid case. Let the origin be located at the true median position and the idealized statistical error be ϵ_m. Then, if the range for the $(k+1)th$ approximation is $-V + v_m^{(k)} \leq v \leq V + v_m^{(k)}$, eq (1.2) is approximated by

$$v_m^{(k+1)} \approx (1/2g_m)\left[\int_0^{V+v_m^{(k)}} g(v)dv - \int_{-V+v_m^{(k)}}^{0} g(v)dv\right]$$

$$\approx \epsilon_m + r_m v_m^{(k)}, \tag{4.10}$$

where

$$r_m \equiv (1/2g_m)[g(V)+g(-V)]. \qquad (4.11)$$

The factor r_m represents the ratio between the average ordinate at the end points and the ordinate at the median position; it will normally be substantially less than unity. Hence the same analysis as for the centroid follows and the truncation mislocation factor has the same form as eq (3.14), i.e., $f_m = 1/(1-r_m)$. Equation (3.15) is also applicable to bypass the need for successive approximations, with v_m and r_m replacing v_c and r_c.

4.5. Application to Quasi-Lorentzian Profile

For the case of a quasi-Lorentzian line (which implies that $g_m \approx 1$), eqs (2.7) and (4.7) give

$$(\sigma_m)_{\text{eq }\Delta t} = \{V(\tan^{-1} V + \eta V)/I_p T\}^{1/2}. \qquad (4.12)$$

This equation is illustrated in figure 6. If this result is reexpressed in terms of the total number of counts for the case of zero background, it agrees with the calculation of Knowles [19] within the approximation of the latter.

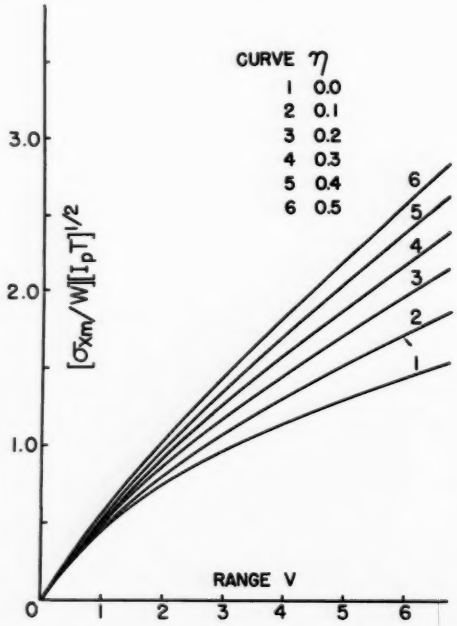

FIGURE 6. *Idealized statistical error of median of a quasi-Lorentzian profile as function of truncation range for various values of background parameter η.*

Equation (4.9) may easily be integrated for the case of zero background to yield

$$\frac{(\sigma_m)_{\text{opt}}}{(\sigma_m)_{\text{eq }\Delta t}} = \frac{\ln [V+(1+V^2)^{1/2}]}{[V \tan^{-1} V]^{1/2}}. \qquad (4.13)$$

The factor r_m defined by eq (4.11) is simply $(1+V^2)^{-1}$; the truncation mislocation factor then becomes

$$f_m = 1/(1-r_m) = (1+V^2)/V^2. \qquad (4.14)$$

Assuming zero background, we may calculate the total statistical error for the case of equal time intervals by combining eqs (4.12) and (4.14); the optimized case is obtained through multiplication by the ratio given in eq (4.13). The results are plotted in figure 7. For equal time intervals we find that the minimum error occurs for $V \approx 1.2$ and is

$$(\sigma_{xm}/W)_{\text{tot}} = \sigma_m/2 = 0.88/(I_p T)^{1/2}, \qquad (V=1.2). \qquad (4.15)$$

Optimized time intervals reduce this figure by only about 1 percent.

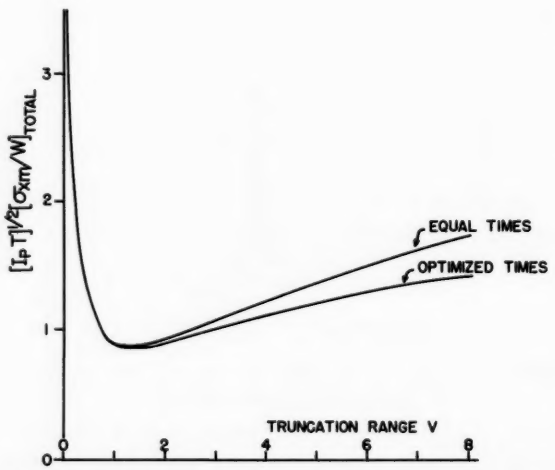

FIGURE 7. *Total statistical error of median of a quasi-Lorentzian profile as a function of truncation range for equal and for optimized counting time intervals (zero background).*

4.6. Application to Quasi-Gaussian Profile

When the results for the median are applied to a quasi-Gaussian profile, the minimum error occurs for $V \approx 1.7$, with the numerical factor in eq (4.15) becoming 0.76. Optimized time intervals can reduce this figure by about 5 percent. As in the case of the centroid, optimization appears to be of great significance for large truncation ranges and zero background; the numerical factor then approaches asymptotically a value of 0.75. However, this advantage would be greatly reduced by the presence of any appreciable background.

4.7. Systematic Errors

Like the centroid, the median is immune to any systematic error from a constant background, pro-

vided that the truncation limits are defined as in sec. 4.1. A linearly varying background $\eta+\mu v$ may be shown to produce a systematic error δv_m equal to μ for $V=1$ and approaching $\mu V^2/2$ for $V \gg 1$.

For a large truncation range and a satellite with a width comparable to that of the main line the worst systematic error occurs when the satellite is centered at $\pm V/2$. In this case substantially all its area lies to one side of the true median and is included in the integration. This area is $\pi\alpha_s W_s/W$; inspection of eq (4.3) shows that this will cause a systematic error, δv_m, equal to $\pi\alpha_s W_s/2W$. For smaller ranges the error will be magnified by the truncation mislocation factor; on the other hand it will be reduced by the fact that not all of the satellite area is included within the limits of integration and the included part has significant portions on both sides of the true median. The net result will usually be to reduce the above estimate quite substantially.

4.8. Effect of Asymmetry

As in the case of the centroid, we might expect that the statistical error is insensitive to asymmetry and that the relative change in the standard deviation is of the order of s^2. This prediction has been tested [13] by a calculation with the Fe $K\alpha_1$ line, for which $s=0.24$. The standard deviation is within roughly 1 percent of the value for a symmetric line.

For the truncation range $V=1$, the displacement of the median from the peak, i.e., v_m-v_p, is 0.57 s for eq (2.9) and 0.39 s for eq (2.10). For infinite range, the former gives a well-defined median with a displacement of 1.57 s; the latter model then becomes physically absurd, since it implies negative values of $g(v)$.

5. Geometrical Peak

5.1. Orthogonal Polynomial Technique

In order to determine the geometrical peak of a line profile we must adopt some method of drawing a smooth curve through the data points. When the form of the profile is not known a priori, it seems reasonable to fit the data with an empirical polynomial by the method of least squares, preferably through the use of a computer.

Forsythe [30] has discussed the difficulties which arise with higher degree polynomials, due primarily to roundoff errors, when this method is applied directly. Hence in such cases he has recommended least squares adjustments by means of the orthogonal polynomial technique, which alleviates the roundoff problem. We will adopt this approach and employ a weighting function for the jth point which is inversely proportional to its variance, i.e.,

$$w_j=K/\sigma_j^2. \tag{5.1}$$

With a slight modification of Forsythe's presentation, a series of orthogonal polynomials may then be defined by

$$\sum_j w_j\varphi_m(z_j)\varphi_n(z_j)\Delta z=\delta_{mn}, \tag{5.2}$$

where m and n denote the degrees of the respective polynomials and z represents a new abscissa variable normalized such that $-1 \leqslant z \leqslant 1$ for the desired range. If the points are closely spaced and of equal weight, then under this definition the φ_n's reduce to the Legendre polynomials. These polynomials may be generated by a variety of techniques, e.g., the Schmidt orthogonalization process or a set of recursion relations given by Forsythe [30].

Let us assume that the *true profile* $\tilde{g}(z)$ is an Mth degree polynomial, which may be expressed in the form

$$\tilde{g}(z)=\sum_{n=0}^{M} a_n\varphi_n(z). \tag{5.3}$$

The true values of the coefficients (the a_n's) are, of course, unknown. However, if we denote the (normalized) observed intensity at the jth point by g_j and compute the coefficients by the relation

$$a_n=\sum_j w_j\varphi_n(z_j)g_j\Delta z, \tag{5.4}$$

we can show [13] that the resulting polynomial is a least squares fit to the data.

We may now show that the coefficients are statistically independent quantities with equal variances. Since the δg_j's, i.e., the errors in g at the various points, are statistically independent, it follows immediately that the average $\langle\delta g_i\delta g_j\rangle=\delta_{ij}\sigma_j^2$. Combining this with eq (5.4) yields

$$\langle\delta a_m\delta a_n\rangle=(\Delta z)^2\sum_i\sum_j w_i w_j\phi_m(z_i)\phi_n(z_j)\langle\delta g_i\delta g_j\rangle$$

$$=(\Delta z)^2\sum_j w_j^2\phi_m(z_j)\phi_n(z_j)\sigma_j^2. \tag{5.5}$$

Eliminating σ_j^2 by eq (5.1) and applying eq (5.2) then shows

$$\langle\delta a_m\delta a_n\rangle=K\Delta z\delta_{mn}, \tag{5.6}$$

which proves the above statement and gives explicitly the variance of a_m.

5.2. Statistical Error

Let us now express the physical problem in terms of the normalized variable z, which was defined such that $-1 \leqslant z \leqslant 1$, i.e.,

$$z=v/V, \tag{5.7}$$

and set $g(v)=\tilde{g}(z)$. If we assume equal counting times Δt and put $K=1/I_p\Delta t$ in eq (5.1), it follows with the help of eq (2.13) that

$$w_j=1/(g_j+\eta). \tag{5.8}$$

By this choice the orthogonal polynomials defined by eq (5.2) depend only on the *shape* of the observed profile and are independent of I_p and Δt. (Note that, in principle, the g_j's in the above expression should be the true values rather than the experimentally observed ones. However, it may be shown [13] that the experimental ones may be used with negligible error under normal conditions.) When the above value of K is substituted in eq (5.6), the result is

$$\langle \delta a_m \delta a_n \rangle = (\Delta z/I_p\Delta t)\delta_{mn} = (2/I_pT)\delta_{mn} \tag{5.9}$$

since $\Delta z = 2/N = 2\Delta t/T$.

To calculate the peak shift due to statistical error we first denote the fitted polynomial by $\hat{\tilde{g}}(z)$. This may be expressed as the sum of the true profile $\tilde{g}(z)$ and an error term $\delta\tilde{g}(z)$, caused by the δa_n's, i.e.,

$$\hat{\tilde{g}}(z) \equiv \tilde{g}(z) + \delta\tilde{g}(z) = \tilde{g}(z) + \sum_{n=0}^{M} \delta a_n \varphi_n(z). \tag{5.10}$$

If the true peak is at z_p, for which $\tilde{g}'(z_p)$ vanishes, the observed peak will be at a point $z_p+\delta z_p$ such that

$$\tilde{g}'(z_p+\delta z_p) + \delta\tilde{g}'(z_p+\delta z_p) \approx \tilde{g}''(z_p)\delta z_p + \sum_{n=0}^{M} \delta a_n \phi_n'(z_p) \approx 0 \tag{5.11}$$

with the neglect of second-order terms. By eqs (5.7) and (5.11) it follows that

$$\frac{\partial v_p}{\partial a_n} = V\left(\frac{\partial z_p}{\partial a_n}\right) \approx -\frac{V\phi_n'(z_p)}{\tilde{g}''(z_p)} = -\frac{\phi_n'(z_p)}{Vg''(v_p)}. \tag{5.12}$$

With the help of eqs (5.12) and (5.9) the standard deviation of the peak becomes

$$(\sigma_p)_{\text{eq }\Delta t} = \left\{\sum_{n=0}^{M}\left(\frac{\partial v_p}{\partial a_n}\right)^2 \langle(\delta a_n)^2\rangle\right\}^{1/2} \approx \frac{1}{V}\left\{\frac{2\sum_{n=0}^{M}[\phi_n'(z_p)]^2}{I_pT\,[g''(v_p)]^2}\right\}^{1/2}. \tag{5.13}$$

(In this expression the quantity $g''(v_p)$ in the denominator may be adequately approximated by using the second derivative of the fitted curve, rather than that of the true one.) The φ_n's have a rather insensitive dependence on range through the weighting function w_j in eq (5.2). Hence the error depends on range chiefly through the explicit factor V in the denominator and through the indirect effect on M; the larger the range, the higher will in general be the degree of the polynomial necessary to fit the data.

5.3. Goodness of Fit

Since in practice the proper value of M is not known a priori, we must determine this by some empirical test on the fitted curve. One such criterion is the χ^2 test (see, for example, Bearden and Thomsen [32]). The residuals for the individual points are $g_j-\hat{\tilde{g}}(z_j)$, where g_j is the experimental value and $\hat{\tilde{g}}(z_j)$ the value of the smoothed fitted curve at the jth point; the variances are given by eq (2.13).

Thus the expression for χ^2 becomes

$$\chi^2 = I_p\Delta t \sum_j [g_j - \hat{\tilde{g}}(z_j)]^2/(g_j+\eta). \tag{5.14}$$

When averaged over several runs, the average value $\langle\chi^2\rangle$ should approximate the number of degrees of freedom, which is simply $N-(M+1)$, where N is the number of data points and $(M+1)$ the number of coefficients required for an Mth degree polynomial.

While the χ^2 test is an excellent criterion for a generally reasonable fit, we may often obtain a more sensitive indication of the best value for M by examining values of the $\langle a_n\rangle$'s, i.e., the polynomial coefficients in eq (5.3) averaged over several curves, say N_0 runs. The variance of $\langle a_n\rangle$ is found immediately by dividing eq (5.9) by N_0. When the magnitude of the average value of a particular coefficient is less than its standard deviation, i.e.,

$$|\langle a_m\rangle| < (2/N_0I_pT)^{1/2}, \tag{5.15}$$

it evidently contributes more error than useful information. If this inequality holds for all $m>M$, it will confirm the choice of an Mth degree polynomial.

For lines of high symmetry it is usually best to use an even degree polynomial, since the last term improves the fit without appreciably contributing to the error given by eq (5.13). It has been found empirically [13] that for a range $V\approx 1$ and $I_pT\sim 10^6$ a 6th degree polynomial is usually adequate to represent the data. This holds for most of the strong K and L lines of medium and short wavelength. The highly asymmetric Fe Kα_1 line is somewhat of a borderline case between a 6th and 8th degree fit, with the 8th apparently preferable.

5.4. Application to Quasi-Lorentzian Profile

If the line profile is quasi-Lorentzian with a range $V=1$ and $I_pT\sim 10^6$, theoretical calculations show that a 6th degree polynomial will satisfy the condition given by eq (5.15). The orthogonal polynomials have been evaluated for this case, with zero background, and substituted in eq (5.13) with the result [13]

$$\sigma_{xp}/W = \sigma_p/2 = 1.67/(I_pT)^{1/2}, \qquad (V=1,\ M=6). \tag{5.16a}$$

for the standard deviation in terms of x. It may be shown that the numerical factor is roughly proportional to $M^{3/2}$.

We have checked this equation experimentally with six sets of data on the W $K\alpha_1$ line, comprising a total of 35 curves. The results, as shown in table 1, indicate rather good agreement.

TABLE 1. *Comparison of theoretical (eq (5.16a)) and experimental standard deviations of the geometrical peak of the* W $K\alpha_1$ *line for a 6th degree polynomial fit with range* $V=1$.

Crystal settings	No. of curves	$\langle\chi^2/\text{D.F.}\rangle$	σ_{exp}	σ_{theor}
(2, −3)	7	1.1	0.0046W	0.0033W
(2, −3)	5	1.3	.0035W	.0036W
(2, −3)	6	0.9	.0042W	.0037W
(2, 3)	7	1.1	.0038W	.0030W
(2, 3)	4	1.0	.0032W	.0033W
(2, 3)	6	1.0	.0032W	.0033W

Since the geometrical peak is usually determined with a range $V \sim 1$, background will normally be a rather minor factor. We may obtain an estimate of the background effect as follows: The average value of $g(v)$ over the range $V=1$ is easily computed from eq (2.7) and found to be $\pi/4$. If we assume equal weights and employ this average value of g in eq (5.8), it follows that for zero background $\varphi_n(v)=(\pi/4)^{1/2}\pi_n(v)$, where the π_n's are the orthonormal forms of the Legendre polynomials. If these are used in eq (5.13), the numerical factor in the above expression becomes 1.68, a change of less than 1 percent. Hence it seems reasonable to adopt this same approximation for a nonzero background. Thus for a range $V=1$, the average value of the observed profile is $(\pi/4)+\eta$ and eq (5.16a) becomes

$$\sigma_{xp}/W \approx [1+(4\eta/\pi)]^{1/2}[1.67/(I_pT)^{1/2}], \quad (V=1). \tag{5.16b}$$

5.5. Optimization of Statistical Error

The time intervals, i.e., the Δt's, enter eq (5.13) only implicitly through the definition of the orthogonal polynomials in eq (5.2). Because of this indirect relationship it does not seem feasible to optimize the time intervals for minimum statistical error by the same straightforward method used for the centroid and median. Hence a somewhat less satisfactory alternative approach has been adopted for the peak.

After passing from the sum to the integral in eq (5.2), we may arbitrarily assign a weighting function $w(z)$ to obtain one of the standard sets of orthogonal polynomials. (For a concise summary of several well known examples, see Abramowitz and Stegun [31].) Thus, for example, assigning $w(z)=1$ generates the Legendre polynomials.

Equations (5.1) and (2.13) then fix the relative values of the time intervals required to produce the desired weight. Summing these and equating to the total time T gives the constant K in eq (5.1), which may next be substituted in eq (5.6). It is then straightforward to obtain an error expression analogous to eq (5.13).

We have applied this procedure to a quasi-Lorentzian profile with zero background for three cases, viz, Legendre polynomials and Chebyshev polynomials of the first and second kind. Table 2 shows the results for a 6th degree polynomial fitted over a range $V=1$, with the previously treated case of equal time intervals listed for comparison. In this instance the latter turns out to give the lowest error.

TABLE 2. *Comparison of standard deviations obtained for the geometrical peak with a 6th degree polynomial fit and a range* $V=1$.

z represents the abscissa variable normalized such that the range becomes $-1 \leq z \leq 1$.

Weighting function	Polynomials	$(\sigma_{xp}/W)(I_pT)^{1/2}$
$1+z^2$	(Equal times—see sec. 5.4)	1.67
1	Legendre	1.68
$(1-z^2)^{1/2}$	Chebyshev (first kind)	1.76
$(1-z^2)^{-1/2}$	Chebyshev (second kind)	1.70

Various other ranges and degrees of polynomials were analyzed. In most cases varying the weighting function did not affect the error by more than a few percent. Hence it seems that no significant improvement in the peak error can be obtained by optimizing time intervals.

The calculations described above show that, for the case of Legendre polynomials, we may replace eq (5.16a) by the approximate expression

$$\sigma_{xp}/W \approx 0.13(M/V)^{3/2}\,(\tan^{-1} V)^{1/2}/(I_pT)^{1/2}, \quad (\eta=0), \tag{5.16c}$$

where M is the degree of the polynomial. For the range $0.5 \leq V \leq 1$ and $M=4, 6, 8$, this approximation is good to within 5 percent; it may also be used for other weighting functions, but will be a somewhat cruder estimate. It is important to note that M itself is implicitly a function of V, as discussed in section 5.2.

5.6. Application to Quasi-Gaussian Profile

The peak error was also computed for the quasi-Gaussian profile as given by eq (2.11). For simplicity, we employed Legendre polynomials according to the procedure outlined in the previous section. With $I_pT \sim 10^6$ a 4th degree polynomial gave an adequate fit, as judged by the criterion of eq (5.15). For the range $V=1$ the numerical factor in eq (5.16a) was then reduced to 1.40.

5.7. Systematic Errors

Systematic errors in the geometrical peak due to background and unresolved satellites are easily treated. A linear background, as given by eq (3.20), will have a slope μ; the resulting slope of the observed profile near the origin is approximately $g''(v_p)\delta v+\mu$, which vanishes when $\delta v_p=-\mu/g''(v_p)$ or, in the case of a quasi-Lorentzian, $\delta v_p=\mu/2$.

The maximum slope of a quasi-Lorentzian satellite with amplitude α_s and width W_s is $3\sqrt{3}\,\alpha_s W/8W_s$. This plays the same role as μ in the above expression, giving a systematic error $\delta v_p = 3\sqrt{3}\,\alpha_s W/16W_s$ for the worst case of an unresolved satellite.

There is an additional systematic error in the geometrical peak due to the degree of the polynomial used to approximate the profile. If the test of eq (5.15) controls the fit, there might conceivably be any number of omitted orthogonal polynomials whose coefficients (i.e., the a_n's) are just under $(2/N_0 I_p T)^{1/2}$. It seems reasonable to estimate the error on the basis of the first neglected orthogonal polynomial with an appreciable derivative at the origin; for the quasi-Lorentzian case, this means the first neglected odd coefficient. Comparing the systematic error caused by a neglected coefficient $a_7 = (2/N_0 I_p T)^{1/2}$ with the statistical error of the mean of N_0 runs in which a 6th degree polynomial was used, we find that they are roughly equal. For a 2d or 4th degree fit, the systematic error can be still more serious.

However, if both the profile and the range of observation are nearly symmetric, the odd coefficients tend to be much smaller than the preceding even ones. Thus, if a_6 is barely significant statistically, it is likely that a_7 is substantially smaller. Hence the above estimate of systematic error is probably overly pessimistic, except perhaps in cases of high asymmetry, e.g., Fe Kα_1.

5.8. Effect of Asymmetry

The error quoted in sec. 5.4 is not particularly sensitive to moderate values of asymmetry. To check this point the Cu Kα_1 line ($s \approx 0.06$) and the Fe Kα_1 line ($s \approx 0.24$) were chosen as typical examples of low and high asymmetries. The required orthogonal polynomials were then generated by computer from the original experimental data of Bearden and Shaw [1] and substituted in eq (5.13). As a result, the factor of 1.67 in eq (5.16) was changed to 1.52 and 1.93 in the two respective cases.

5.9. Parabolic Fit

If the profile is fitted only in a relatively small region near the peak, a parabolic fit may be sufficient. In this case the weighting factor in eq (5.8) is substantially constant with the value $(1+\eta)^{-1}$. Thus, in analogy to sec. 5.4, it follows from the integral form of eq (5.2) that the orthogonal polynomials are simply $(1+\eta)^{1/2}\pi_n(z)$, where the π_n's are the normalized Legendre polynomials. The only one presently required is $\pi_1(z) = (3/2)^{1/2} z$. If we assume the line is quasi-Lorentzian and compute $g''(0) = -2$ from eq (2.7), eq (5.13) then yields

$$\sigma_{xp}/W = \sigma_p/2 = 0.433(1+\eta)^{1/2}/V(I_p T)^{1/2}. \quad (5.17)$$

The calculation suggests the possibility of a significant reduction in error. Hence a rather detailed study [13] has been made on the range of validity of a parabolic fit. This showed that, on the assumption of a quasi-Lorentzian line with $I_p T \approx 10^6$, a parabolic fit will be satisfactory up to $V = 0.32$; the right-hand side of eq (5.17) then becomes $1.35/(I_p T)^{1/2}$, an appreciable improvement over the 6th degree polynomial for $V = 1$.

Furthermore, if the true curve is symmetric and if the range of observation is almost symmetric about the true peak, a parabola will locate the peak quite accurately even though it fails to satisfy the χ^2 test for goodness of fit. In this case the resulting systematic error is found to be proportional to ϵV^2, where V defines the observed range and ϵ represents the displacement of the origin from the peak (in units of v). If, for example, we choose $V = 0.5$ and keep $\epsilon \leq 0.02$, the systematic error in the computed peak will be about 0.1 percent of the line width.

For an asymmetric line there will be a systematic error even if the range is fortuitously centered about the true peak. Based on the model of eq (2.10), this turns out to be $0.6\,sV^2$ (in units of v). Thus for $V = 0.5$ and $s = 0.05$, the systematic error is about 0.4 percent of the line width. Thus an appreciable asymmetry can preclude use of a parabola over an extended range, as might be expected. This result and eq (5.18) as well are in essential agreement with the calculations of Wilson [22].

5.10. Optimization of Parabolic Fit

An effort to optimize the time intervals at each data point for a parabolic fit yields the result [13] that virtually all the time should be divided equally between the two end points. While the proof is somewhat lengthy, the resulting error is easily computed. Let the fitted curve be represented by

$$\hat{g}(v) = 1 - A(v - v_p)^2, \quad (5.18)$$

where an approximate value of A has been determined in a preliminary scan. If now readings g_2 and g_1 are recorded at $\pm V$, with a time interval $T/2$ at each, it follows that

$$g_2 - g_1 = 4AVv_p. \quad (5.19)$$

It is clear that the primary factor determining the error in v_p is the small difference $g_2 - g_1$, whose variance is found with the help of eq (2.13) as $2[g(V)+\eta]/I_p \Delta t$. It follows that

$$\sigma_p^2 = \frac{2}{(4AV)^2}\left[\frac{g(V)+\eta}{I_p(T/2)}\right]. \quad (5.20)$$

For a quasi-Lorentzian line with $V \ll 1$, we have $g(V) \approx 1$ and $A \approx 1$; hence for this case

$$\sigma_{xp}/W = \sigma_p/2 \approx (1+\eta)^{1/2}/4V(I_p T)^{1/2}. \quad (V \ll 1). \quad (5.21)$$

This is a distinct improvement over eq (5.17), which represents the case of equal counting times at many points. However, as V is increased, the coefficient A in eq (5.18) will be decreased, and the possible improve-

ment in accuracy correspondingly diminished. Furthermore, this two-point method assumes the line is exactly symmetrical and provides no internal check on this assumption; this fact would seem to limit its practical application.

5.11. Profile Known a Priori

We now turn to the case where the *exact* form of the profile is known or assumed a priori. The problem then reduces to determining the amplitude, width, and peak position, which may be done by a least squares adjustment.

The present analysis will be restricted to a symmetric line profile, e.g., a Lorentzian; in this case a determination of the peak is, of course, also a determination of the centroid and the median.

Let the given functional *form* be denoted by $f(v)$. We will assume that the approximate parameters for the line are known from a preliminary scan and that the approximate peak location is used to define the origin of the v-coordinate. In forming the dimensionless variables g and v, let these approximate values I_{p0} and W_0 be employed. The corresponding true values, I_p and W, may be expressed as $I_{p0}(1+\gamma)$ and $W_0(1+\mu)$ respectively. The true line profile will then become

$$g(v)=(1+\gamma)f\left(\frac{v-v_p}{1+\mu}\right), \tag{5.22}$$

where γ, μ, and v_p are all small compared with unity.

The above equation may be linearized by expanding in a Taylor series and neglecting higher order terms with the result

$$\Delta g=g(v)-f(v)\approx f(v)\gamma-vf'(v)\mu-f'(v)v_p. \tag{5.23}$$

The experimental value of Δg_j at the jth point is simply the difference between g_j, the observed value, and $f(v_j)$, the quantity obtained by substituting v_j in the given functional form. If the number of points $N>3$, there will now be an overdetermined set of linear equations with unknowns γ, μ, and v_p. This set may be solved by the method of least squares (see, for example, Bearden and Thomsen [32]).

The equation thus obtained by differentiation with respect to v_p is

$$-\Sigma_i[f_if_i'/\sigma_i^2]\gamma+\Sigma_i[v_i(f_i')^2/\sigma_i^2]\mu$$
$$+\Sigma_i[(f_i')^2/\sigma_i^2]v_p=-\Sigma_if_i'\Delta g_i/\sigma_i^2, \tag{5.24}$$

where $f_i=f(v_i)$ and $f_i'=f'(v_i)$. For a symmetric function $f(v)$ with a range of observation almost symmetric about the peak, the first two sums are negligible, at least for the purpose of an error estimate. In this case eq (5.24) reduces to

$$v_p=-[\Sigma_if_i'\Delta g_i/\sigma_i^2][\Sigma_i(f_i')^2/\sigma_i^2]^{-1}. \tag{5.25}$$

Since the variance of Δg_i is simply that of g_i, i.e., $\langle\Delta g_i\Delta g_j\rangle=\sigma_i^2\delta_{ij}$, it follows that

$$\sigma_p^2=\frac{\Sigma_i\Sigma_j[f_i'f_j'/\sigma_i^2\sigma_j^2]\sigma_i^2\delta_{ij}}{[\Sigma_i(f_i')^2/\sigma_i^2]^2}=[\Sigma_i(f_i')^2/\sigma_i^2]^{-1}. \tag{5.26}$$

This is essentially the same result as obtained by Muller, Hoyt, Klein, and DuMond [18] for a *known* profile (a "composite line profile") with specified amplitude and width; under the symmetry condition assumed here, the same error is obtained with only approximate values for these two parameters.

The variance, σ_i^2, is obtained from eq (2.13); with the restriction that $\eta\ll g_i$ throughout the range of observation, we may approximate this as

$$1/\sigma_i^2\approx(I_p\Delta t_i/g_i)[1-(\eta/g_i)]. \tag{5.27}$$

Since $f(v)\approx g(v)$, the distinction may now be dropped for the error calculation. Equations (5.26) and (5.27) then give

$$\frac{1}{\sigma_p^2}=I_p\Sigma_i\left[\frac{(g_i')^2}{g_i}-\frac{\eta(g_i')^2}{g_i^2}\right]\Delta t_i. \tag{5.28}$$

For equal time intervals $\Delta t_i=T/N=T\Delta v/2V$; passing from the sum to the integral thus yields

$$\frac{1}{\sigma_p^2}=\frac{I_pT}{2V}\int_{-V}^{V}\left\{\frac{[g'(v)]^2}{g(v)}-\eta\left[\frac{g'(v)}{g(v)}\right]^2\right\}dv. \tag{5.29}$$

We may now evaluate this integral for the case of a Lorentzian profile, given by eq (2.7), and obtain finally

$$\left(\frac{\sigma_{xp}}{W}\right)_{\text{eq }\Delta t}=\frac{\sigma_p}{2}=\left(\frac{V}{2I_pT}\right)^{1/2}\left[\frac{V(V^2-1)}{(1+V^2)^2}+\frac{4\eta V}{1+V^2}\right.$$
$$\left.+(1-4\eta)\tan^{-1}V\right]^{-1/2}. \tag{5.30}$$

Figure 8 shows the resulting errors, plotted as a function of V for various values of η. In all cases the error is large for small values of V, decreases to a minimum near $V=1$, and rises slowly thereafter. For the range $V=1$, the error is

$$\sigma_{xp}/W=0.80\ (1+0.73\eta)/(I_pT)^{1/2}, \qquad (V=1), \tag{5.31}$$

which is obviously competitive with the optimum values for the centroid and the median.

A similar analysis may be applied to any known symmetric profile. If the profile is qualitatively similar to a Lorentzian, the error should be comparable to the above result. For a Gaussian profile the numerical factor 0.80 is reduced to 0.76. Moderate asymmetry will complicate computation in the least squares adjustment, since it will then usually be necessary to solve three simultaneous equations in γ, μ, and v_p; however, it should not greatly change the resulting error.

5.12. Optimization of Lorentzian

The sum in eq (5.28) is a linear function of the Δt_i's; it will obviously be maximized (and the error

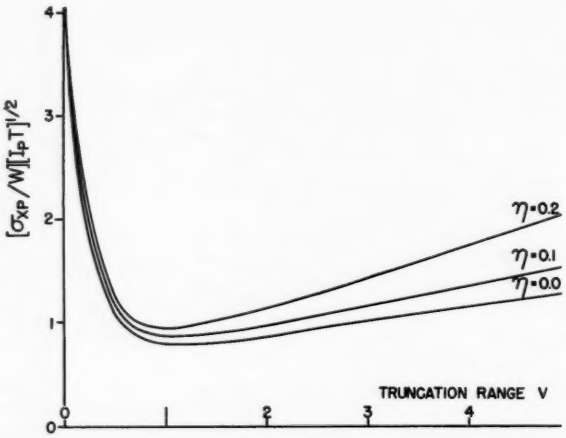

FIGURE 8. *Statistical error of peak of a Lorentzian profile (form known a priori) as a function of range for various values of background parameter* η.
Since the profile is symmetric, this also represents the error of the centroid or median.

correspondingly minimized) by dividing substantially all the time between those points for which the coefficient is a maximum. Substitution of the Lorentzian profile function, eq (2.7), and differentiation with respect to v^2 yields

$$\frac{d}{d(v^2)}\left[\frac{4v^2}{(1+v^2)^3}-\frac{4\eta v^2}{(1+v^2)^2}\right]=0. \tag{5.32}$$

With the neglect of second-order terms in η the optimized value for v^2 becomes $(1/2)[1-(3\eta/4)]$ and it follows that

$$x_{\text{opt}}=v_{\text{opt}}W/2=\pm(0.71W/2)[1-(3\eta/8)], \tag{5.33}$$

in agreement with the result of Merrill and DuMond [17].

If time $T/2$ is spent at each of these two optimized points, the resulting error obtained from eq (5.28) becomes

$$\sigma_{xp}/W=[0.65/(I_pT)^{1/2}][1+(3\eta/4)], \tag{5.34}$$

again with the neglect of second-order terms in η. The above result represents the lowest statistical error obtained for any case treated in the present paper; however, this method can introduce a serious undetected systematic error if the line profile is slightly asymmetric.

6. Extrapolated Peak

6.1. Midpoint of Single Chord

The error in the midpoint of a single chord is of interest in itself as well as being a starting point for analysis of the extrapolated peak technique. Suppose a smooth curve $\hat{g}(z)$ has been fitted to the data by the orthogonal polynomial technique described in secs. 5.1 and 5.2. Assume a specified value G and let this be the *true* value of the curve at z_{k1}, i.e., $\tilde{g}(z_{k1})=G$; let the fitted curve attain this value at $z_{k1}+\delta z_{k1}$, i.e., $\hat{g}(z_{k1}+\delta z_{k1})=G$. Then it follows from eq (5.10) that

$$\tilde{g}'(z_{k1})\delta z_{k1}+\sum_{n=0}^{M}\delta a_n\phi_n(z_{k1})\approx 0, \tag{6.1}$$

which yields immediately the value of $\partial z_{k1}/\partial a_n$.

Now let $\bar{z}_k$ be the midpoint of a chord drawn at height G, intersecting the fitted curve at $z_1+\delta z_{k1}$ on the left side of the profile and at $z_2+\delta z_{k2}$ on the right. Employing eq (6.1) and setting $\tilde{g}'\approx\hat{g}'$ now yields

$$\frac{\partial\bar{z}_k}{\partial a_n}=\frac{\partial}{\partial a_n}\left(\frac{z_{k1}+z_{k2}}{2}\right)=-\frac{1}{2}\left[\frac{\phi_n(z_{k1})}{\hat{g}'(z_{k1})}+\frac{\phi_n(z_{k2})}{\hat{g}'(z_{k2})}\right]. \tag{6.2}$$

For symmetric curves the two terms in the bracket cancel for even n (since the even order orthogonal polynomials then contain *only* even terms) and are equal for odd n. Thus for this case the above result becomes

$$(\partial\bar{z}_k/\partial a_n)=\begin{cases}0 & (n\text{ even})\\ -\phi_n(z_k)/\hat{g}'(z_k) & (n\text{ odd})\end{cases}, \tag{6.3}$$

where z_k denotes *either* end point of the chord.

Combining this with eqs (5.7) and (5.9) now gives

$$\sigma_k^2=\sum_{n=0}^{M}(\partial v_k/\partial a_n)^2\langle(\delta a_n)^2\rangle$$

$$=(2/I_pT)\sum_{n\text{ odd}}^{M}V^2[\phi_n(z_k)/\hat{g}'(z_k)]^2, \tag{6.4}$$

or

$$\sigma_{xk}/W=\sigma_k/2=V/(2I_pT)^{1/2}\left\{\sum_{n\text{ odd}}^{M}[\phi_n(z_k)]^2\right\}^{1/2}\Big/|\hat{g}'(z_k)| \tag{6.5}$$

for symmetric line profiles.

This expression was evaluated [13] for a quasi-Lorentzian line with a 6th degree polynomial and a range $V=1$. It is found to give a minimum for $g(z_k)\approx 0.75$, in reasonable agreement with the result of Bačkovský [24], who used uniform weighting. In this case we have

$$\sigma_{xk}/W=0.95/(I_pT)^{1/2}, \qquad (g=0.75). \tag{6.6}$$

This accuracy is obviously competitive with the centroid or median under optimum conditions. However, unless the true line profile is *exactly* symmetric, it will define an entirely new feature and will introduce a systematic error if used to approximate the peak.

6.2. Use of Fitted Curve

If we draw a number of chords as described in the above section, it is possible to fit a smooth "bisector

curve" through their midpoints with the use of Legendre polynomials and extrapolate this curve to the top of the profile to obtain the peak. This follows a commonly used graphical technique and is shown in figure 1. With the aid of eq (6.3) we may compute the resulting statistical errors.

Such calculations [13], which are somewhat lengthy, show only minor differences when compared with the result of sec. 5.2 for the geometric peak. For chords equally spaced along the ordinate the error seems to be slightly higher. With chords drawn at equally spaced v_k's along the abscissa, experimental results indicate a slight reduction in statistical error. However, additional sources of systematic error may be introduced by the choice of range in which the chords are constructed, as well as by the polynomial degree of the bisector curve. Hence, while this extrapolation technique is a valuable tool for graphical work, it seems to offer little advantage for computer calculations.

6.3. Use of Raw Data

It is possible to bypass the fitted curve and construct the bisector curve directly from the data points on either side of the line profile. The error analysis [13] of this method is somewhat simpler mathematically than the preceding case and hence permitted a more comprehensive study. With a straight line as the bisector curve, the resulting statistical error is competitive with the geometrical peak. In the case of a parabola, this error is increased by roughly 50 percent. Actually it is very doubtful that even a parabola is of sufficiently high degree to represent the bisector curve of a line profile with moderate asymmetry. Thus, except as a possible alternative technique for almost symmetric lines, this approach appears to offer little advantage.

7. Conclusions

In general our results are in good agreement with prior workers for cases which have been treated previously. The only possible exception seems to be the suggestion of Porteus and Parratt [21] that the use of the centroid involves an unduly large error; their conclusion appears based on consideration of an infinite truncation range rather than the truncated portions which must be used in practice.

While our experimental results on the peak, as reported in sec. 5.4, are in good agreement with theory, further experiments to verify other predictions would be desirable. In this connection it might be helpful to compare the reproducibility of the difference between two wavelengths (e.g., the $K\alpha_{1,2}$ doublet) as determined by different criteria.

Our analysis is not, of course, restricted to x-ray line profiles, but applies to any similar problem where the errors in the ordinates are primarily due to counting statistics (e.g., nuclear spectroscopy and Mössbauer studies). Furthermore, even when a different error law holds, the basic method of optimizing counting times, as developed in sec. 3.3, may be of value in suggesting a more efficient data-taking technique. In fact, the possible gain may be greater in other fields than in the x-ray problems which we have analyzed.

All of our results may be expressed in the form

$$\sigma_x/W = F/(I_p T)^{1/2}, \tag{7.1}$$

where F is a dimensionless factor of the order of unity. Values for a few representative cases are listed in table 3. (While standard deviations are tabulated, error distributions are normal; hence probable errors can be immediately obtained by multiplying by 0.67.)

TABLE 3. *Statistical errors of wavelength features determined by various methods (zero background).*

σ represents standard deviation, W the full width of the profile at half intensity, I_p the peak intensity, and T the total counting time. The range is specified by the dimensionless parameter $V = 2X/W$, where $-X \leqslant x \leqslant X$.

Case	Truncation range V	$F = (\sigma/W)(I_p T)^{1/2}$	
		Equal times	*Opt. times*
a. *Lorentzian Profile known a priori*	0.71		0.65
Peak, centroid, and median	*1.00	0.81	
b. *Quasi-Lorentzian profile not known a priori.*			
Centroid	*1.0	0.81	0.73
	6.0	2.11	2.05
Median	*1.2	0.88	0.88
	6.0	1.49	1.28
Peak—6th degree polynomial fit	1.0	1.67	≈ 1.67
Peak—parabolic fit	0.32	1.35	0.82

*Optimized range for equal counting times.

Obviously it will require the order of 10^6 counts to define a wavelength to within 0.1 percent of the line width. It is also clear that optimization of time intervals can produce only a rather limited improvement in accuracy.

If the line profile is known a priori, it is usually advantageous to make use of this knowledge in calculating the wavelength; e.g., a Lorentzian can be fitted by this method with $F \approx 0.8$. For the Lorentzian or any other symmetric profile known a priori, all three wavelength criteria coincide and any method of locating one locates all. Hence their errors must, of course, be identical. For any known profile of moderate asymmetry the errors should be identical if the width is specified a priori and roughly equal when the width is an adjustable parameter.

In the general case, where the profile form is not known a priori, we may fit a smooth curve to the data by the orthogonal polynomial technique and compute the peak from the fitted curve. (The extrapolation or chord method is a useful graphical technique, but offers no particular advantage in numerical computation, where it can indeed introduce additional systematic error.) With the total counts of the order of 10^6, a 6th degree polynomial is often satisfactory for the range between the half intensity points (i.e., $V = 1$); resulting values of F range from about 1.6 to 2.1.

We may obtain somewhat lower errors, with a minimum of computational effort, by fitting a parabola over a limited range near the peak. However, extreme caution is necessary when even small asymmetries

are involved. If the number of counts is substantially lower ($\sim 10^4$), or if the curve is more nearly Gaussian in shape, a 4th degree polynomial may be satisfactory over the range $V=1$, which will give $F \approx 0.9$.

In many cases, adoption of the centroid or median would promise a reduction in statistical error; these criteria can, in fact, be determined to almost the same precision for a quasi-Lorentzian profile as for a true Lorentzian, known a priori. The reduced error is obtained only for a truncated portion with a range $V \sim 1$. Of course, adoption of either criterion would result in new wavelengths, which would frequently differ significantly from the peak values now in general use.

Definition of wavelength in terms of an arbitrarily defined truncation interval appears lacking in fundamental physical significance. Hence it may seem preferable to attempt to approximate the "true centroid" of the entire profile ($V=\infty$), as done by some crystallographers, or the true median. In this connection, the median has one obvious advantage, viz, it is well defined mathematically. By contrast the centroid of a quasi-Lorentzian curve involves a logarithmically divergent integral. If the tails are sufficiently symmetric, it may be defined by using symmetric truncation limits in the limiting process; otherwise the true centroid simply does not exist mathematically. In any case, when large truncation limits are used, the statistical error may equal or exceed that for the peak of a 6th degree polynomial.

A linear variation in background will cause a systematic error, about twice as great for the centroid and median as for the peak. (Constant background merely produces an increase in statistical error, which is roughly comparable for all three criteria.) An unresolved satellite may also cause a systematic error. With the range $V \sim 1$, the maximum errors from this source for the centroid or median are again about twice that of the peak. On the other hand, the peak is uniquely subject to an additional systematic error due to the degree of the polynomial used to approximate the observed profile; in some cases this may be of the same order as the statistical error.

We wish to reemphasize that the present study has ignored any errors in correcting for instrumental effects, as stated in Assumption *C* of section 2.1. In γ-ray spectroscopy and in x-ray crystallography these corrections may be much greater than the natural line widths. In such cases the statistical error calculations will still give the errors for the respective features of the *observed* experimental profiles, but these may be completely overshadowed by systematic errors in instrumental corrections. Under these circumstances, statistical counting errors are not particularly relevant in the choice of a wavelength criterion.

Even where instrumental corrections are small, as in the case of x-ray spectroscopy, the present error analysis is somewhat inconclusive in indicating a clear choice among the three wavelength criteria considered. Simplicity and historical precedent clearly favor retention of the peak. It seems doubtful that the limited statistical error reduction attainable in some cases by abandoning the peak, seldom greater than a factor of two, is sufficient incentive to warrant a new wavelength definition which would alter many presently tabulated values.

Before reaching a final decision, it would be highly desirable to know how closely each criterion is associated with the term values for the various energy levels. This problem might be attacked by either a theoretical or an experimental approach.

In our present state of knowledge, we recommend that the use of the peak to define x-ray wavelength be continued. We further recommend that the geometric peak method be used in preference to extrapolation techniques.

The authors express their thanks to J. A. Bearden for his continuing interest in this work and for numerous helpful discussions. They are grateful to R. T. Cox and Richard D. Deslattes for reading the manuscript and offering suggestions. They are much indebted to William C. Sauder, who began the study of this problem, for his cooperation and for his unpublished calculations. J. W. Knowles, J. O. Porteus, and Lyman G. Parratt were also most helpful in sharing their unpublished work. The National Bureau of Standards has provided much of the necessary support for the project. One of the authors (F. Y. Y.) also gratefully acknowledges support from the Chinese-American Fund of the Johns Hopkins University. Finally thanks are due to Mrs. Mary B. Rowe for typing the manuscript and to Frank Nemec for preparing the figures.

8. References

[1] J. A. Bearden and C. H. Shaw, Phys. Rev. **48,** 18 (1935).
[2] A. E. Sandström, Handbuch der Physik, **30,** Ed. by S. Flügge (Springer-Verlag, Berlin, 1957).
[3] J. A. Bearden, Rev. Mod. Phys. **39,** 78 (1967).
[4] J. A. Bearden, A. Henins, J. G. Marzolf, W. C. Sauder, and J. S. Thomsen, Phys. Rev. **135,** A899 (1964).
[5] O. Beckman, P. Bergvall, and B. Axelsson, Arkiv Fysik **14,** 419 (1958).
[6] J. G. Marzolf, Rev. Sci. Instr. **35,** 1212 (1964).
[7] G. Brogren, Arkiv Fysik **8,** 391 (1954).
[8] U. Bonse and M. Hart, Appl. Phys. Letters **7,** 238 (1965).
[9] J. O. Porteus, J. Appl. Phys. **33,** 700 (1962).
[10] W. C. Sauder, J. Appl. Phys. **37,** 1495 (1966).
[11] J. S. Thomsen, Bull. Am. Phys. Soc. **10,** 1219 (1965).
[12] A. J. C. Wilson, J. S. Thomsen, and F. Y. Yap, Appl. Phys. Letters **7,** 163 (1965).
[13] F. Y. Yap, Dissertation (The Johns Hopkins University, Baltimore, Maryland, 1967).
[14] J. Taylor, M. Mack, and W. Parrish, Acta Cryst. **17,** 1229 (1964).
[15] J. W. Knowles, α, β, and γ Ray Spectroscopy, **I,** 203, Ed. by Siegbahn (North Holland Publishing Co., 1965).
[16] E. R. Pike and A. J. C. Wilson, Brit. J. Appl. Phys. **10,** 57 (1959).
[17] J. J. Merrill and J. W. M. DuMond, Ann. Phys. (N.Y.) **14,** 166 (1961).
[18] D. E. Muller, H. C. Hoyt, D. J. Klein, and J. W. M. DuMond, Phys. Rev. **88,** 775 (1952).
[19] J. W. Knowles (private communication).
[20] E. R. Cohen and J. W. M. DuMond, Rev. Mod. Phys. **37,** 537 (1965),

[21] J. O. Porteus and L. G. Parratt (private communication).
[22] A. J. C. Wilson, Brit. J. Appl. Phys. **16,** 665 (1965).
[23] K. Beu and D. L. Scott, US AEC Report GAT-T-1374 (1960) (unpublished).
[24] J. Bačkovský, Czech J. Phys. **B15,** 753 (1965).
[25] J. A. Bearden, Phys. Rev. **43,** 92 (1933).
[26] J. J. Merrill and J. W. M. DuMond, Phys. Rev. **110,** 79 (1958).
[27] G. Donnay and J. D. H. Donnay, Am. J. Sci. Bowen Vol. (Pt. 1), 115 (1952).
[28] V. Weisskopf and E. Wigner, Z. Physik **63,** 54 (1930).
[29] A. Hoyt, Phys. Rev. **40,** 477 (1932).
[30] G. E. Forsythe, J. Soc. Indust. Appl. Math. **5,** 74 (1957).
[31] M. Abramowitz and I. Stegun, Handbook of Mathematical Functions, ch. 22 (Dover Publications, Inc., New York, 1965).
[32] J. A. Bearden and J. S. Thomsen, Nuovo Cimento **5,** Suppl., 267 (1957).

(Paper 72A2-494)

JOURNAL OF RESEARCH of the National Bureau of Standards—A. Physics and Chemistry
Vol. 72A, No. 2, March–April 1968

Thermodynamic Properties of Ammonia as an Ideal Gas*

Lester Haar

Institute for Basic Standards, National Bureau of Standards, Washington, D.C. 20234

(December 15, 1967)

Thermodynamic functions for ammonia as an ideal gas at one atmosphere pressure have been evaluated. The contribution of the highly anharmonic out-of-plane vibrational mode, including its large coupling with rotation and its coupling with the other vibrational modes, is considered in detail. Tables of C_P°/R, $(H^\circ - E_0^\circ)/RT$, $(E_0^\circ - G^\circ)/RT$, and S°/R have been calculated at closely spaced intervals from 50 to 5000 °K within an overall uncertainty of less than 0.1 percent at 1000 °K.

Key Words: Ammonia, ideal gas, thermodynamic functions.

1. Introduction

This paper is part of a program originating with the Office of Standard Reference Data of the National Bureau of Standards to obtain accurate thermodynamic properties for ammonia. Subsequent papers of this program will include real-gas corrections to the ideal-gas properties contained herein.

In this paper the ideal-gas thermodynamic properties of ammonia in the ground electronic state are calculated at closely spaced temperature intervals from 50 to 5000 °K. The calculations include the contributions of ordinary vibrational anharmonicity and vibrational-rotational coupling together with rotational stretching and rotational quantum effects. Particular attention is given to the treatment of the rotational and vibrational anharmonic effects due to the molecular inversion. To this end a method is developed for calculating this contribution such that an overall accuracy for the thermodynamic properties of ammonia approaching that of the simplest diatomic molecules is obtained.

In the vibrational ground state ammonia is a pyramidal molecule with the nitrogen atom approximately 0.38 Å above the plane of the three hydrogen atoms. The distance between the nitrogen atom and each of the hydrogen atoms is approximately 1.0 Å. Thus the pyramid is relatively flat and the potential barrier to vibration of the nitrogen atom through the plane of the hydrogen atoms so as to invert the pyramid is low (approximately 2000 cm^{-1} [1]).[1]

Ammonia has six vibrational degrees of freedom. However, owing to symmetry there are only four normal vibrational modes, two of which have double degeneracies. The vibrational structure may thus be characterized by the six quantum numbers $(v_1 v_2 v_3^l v_4^l)$, where the v_i are the principal vibrational quantum numbers associated with the vibrational modes ν_i and the l characterize the small coupling of the degenerate ν_3 and ν_4 asymmetric vibrational modes with the angular momentum of the molecule. The ν_1 and ν_2 modes are symmetric, nondegenerate vibrations corresponding to stretching the N-H bond and spreading the pyramid, respectively. (The ν_2 mode is also referred to as the out-of-plane vibration.) The rotational structure for the ground state is that of a symmetric top, so that the rotational energy levels are characterized by the two quantum numbers J and K.

The ν_2 mode is the vibration associated with the inversion of the pyramid. Each vibrational state of this mode is split into two components, corresponding respectively to symmetric and antisymmetric eigenfunctions. (In the nomenclature these are identified by the superscript "s" or "a" to the quantum number v_2.) The spacing of these levels is highly anharmonic except for vibrational energies sufficiently higher or lower than the potential barrier to inversion. Thus the vibrational levels for the ground state of the ν_2 mode are only slightly split, of the order of a fraction of a wavenumber, but the splitting increases rapidly with increasing vibrational quantum number. At energy levels sufficiently elevated above the barrier (greater than about 3000 cm^{-1}) the levels become uniformly spaced with a spacing of approximately half that of the ν_2 fundamental. Similarly, due to inversion the rotational structure undergoes a transition from that of a pyramid for the low values of the v_2 quantum number to that of a planar molecule for the higher values, so that the rotational motion is also strongly coupled to the ν_2 mode. For a more detailed discussion of these effects, see the review by Herzberg [2] of the pyramidal XY_3 molecule and Nielsen [3]. The energy structure

*This work was supported in part by the Office of Standard Reference Data, NBS.
[1] Figures in brackets indicate the literature references at the end of this paper.

of the other vibrational modes is similar to that of typical, slightly anharmonic rotating vibrators.

In section 2 the equations for the calculations are developed. This is followed in section 3 by a discussion of the molecular data, and in section 4 by a discussion of the calculated properties and an evaluation of their accuracy. Finally, a discussion is given in section 5 of some of the earlier work.

2. Partition Function

It is convenient to represent the rotational and vibrational structure by an expression for which the energy levels of the ν_2 mode and its coupling with the other degrees of freedom are written explicitly. Thus the energy levels in wavenumbers are written

$$T(v, J, K) = G'(v) + F'(v, J, K) + G_2(v, J, K), \quad (1)$$

where the primes denote that dependence on v_2 is omitted. The first term in eq (1) describes the vibrational energy characterized by $(v_1 0 v_3^{l_3} v_4^{l_4})$ and in notation similar to that in Herzberg [2] is approximated by

$$G'(v) = \sum_i{}' \omega_i v_i + \sum_{i \geq j}{}' x_{ij} v_i v_j + \sum_i{}' x_{ii}(v_i - 1) v_i + \ldots$$

$$+ g_{34} l_3 l_4 + g_{33}(l_3^2 - v_3) + g_{44}(l_4^2 - v_4) + \ldots, \quad (2)$$

$$i, j \neq 2,$$

where the ν_i are fundamentals and the x and g are relatively small anharmonicities. The second term in eq (1) is approximated by

$$F'(v, J, K) = B_v' J(J+1) + (C_v' - B_v') K^2 \quad (3)$$

$$- D_v^{J\prime} J^2 (J+1)^2 - D_v^{JK\prime} J(J+1) K^2 - D_v^{K\prime} K^4 + \ldots,$$

where C_v is the rotational constant corresponding to rotation about the symmetry axis and B_v is the constant for axes perpendicular to the symmetry axis. The quantities D_v^J, D_v^{JK}, and D_v^K are small coefficients associated with centrifugal distortion of the molecule. The subscript v to each of the coefficients of eq (3) indicate dependence or coupling with the vibrational motion. The primes indicate that dependence on v_2 is omitted; that is, the rotational constants of eq (3) are evaluated for v_2 equal to zero. The coupling of the rotational motion to vibrations other than the ν_2 mode is relatively small and is included here only to first order in the fundamentals.

$$B_v' = B_0 - \sum_i{}' \alpha_i^B v_i +$$

$$C_v' = C_0 - \sum_i{}' \alpha_i^C v_i +, \qquad i \neq 2$$

where B_0 and C_0 are rotational constants, and the α are small corrections. All coordinates involving the ν_2 mode, including its coupling with the other degrees of freedom are included in G_2. Thus G_2 includes those effects characterized by

$$(v_1 v_2 v_3^{l_3} v_4^{l_4} JK) - (v_1 0 v_3^{l_3} v_4^{l_4} JK).$$

The partition function for the rotational and vibrational structure may be written

$$Q = \sum_{v,J,K} \exp\{-T(v, J, K) c_2/T\}, \quad (4)$$

where $T(v, J, K)$ is discussed in eqs (1), (2), and (3). c_2 is the second radiation constant and T is the absolute temperature. The sum extends over all rotational and vibrational degrees of freedom including all values of the v, J, K quantum numbers. In the evaluation of eq (4) the contributions of the vibrational anharmonicity and vibration-rotation coupling effects contained in eqs (2) and (3) are all to be accounted for to first order; that is, only terms linear in x, g, and α are retained. Though G_2 is not conveniently described by the usual power series in the vibrational quantum numbers, its contribution, including coupling effects with the other degrees of freedom, is also to be included to this order.

The contribution of the G_2 term is obtained by expanding the partition function about the term-by-term sum of the observed $(0v_200)$ energy levels. This summation incorporates the major effect of the highly anharmonic ν_2 mode, which is the coupling between the symmetric and antisymmetric states, but it does not include the contribution of the ν_2 coupling with the other vibrational modes. From an examination of the spectroscopic vibrational data (see Benedict et al. [4]), it can be seen that this cross coupling produces a shifting of energy levels of about the same magnitude as that of the other vibrational couplings (those represented by the x and g terms in eq (2)). Thus the contribution to the partition function of this cross coupling should be of the same order as that from the other anharmonicities, and a first order approximation for this contribution should be adequate.

In the expansion that follows expressions for the cross coupling are developed and their contribution for each individual $(0v_200)$ state obtained explicitly. The cross coupling between a pair of vibrational states, e.g., states corresponding to the particular quantum numbers v_1 and v_2, is defined as

$$G_{v_1 v_2} \equiv G(v_1 v_2 00) - G(v_1 000) - G(0 v_2 00), \quad (5)$$

where $G(v_1 v_2 v_3^{l_3} v_4^{l_4})$ is the vibrational energy. A useful representation for the coupling involving the highly anharmonic ν_2 mode is the development of $G_{v_1 v_2}$ as a power series of products of the observed energies, that is

$$G_{v_1 v_2} = k_{12} G(v_1 000) \cdot G(0 v_2 00) + \ldots. \quad (6)$$

The constant k_{12} is readily determined in terms of the observed coupling. Thus for coupling between the fundamentals the observed coupling x_{12} is given by

$$x_{12} = k_{12}G(1000) \cdot G(0100) \quad + \ . \ . \ .$$

$$= k_{12}\nu_1\nu_2 + \ . \ . \ . \ .$$

Note that eq (6) reduces identically to the power series of eq (2) when the cross coupling is between nearly harmonic modes.

Consider the energy of the nearly harmonic oscillator ν_m, neglecting all anharmonicities but the cross coupling with ν_2. The energy levels for such an oscillator are given by

$$G_m = \nu_m v_m + G_{v_m v_2}.$$

Substituting from eq (6) and defining $E_2 \equiv G(0v_200)$, this becomes

$$G_m \cong \nu_m v_m + k_{2m}\nu_m v_m \cdot E_2. \tag{7}$$

The contribution of G_m to the partition function is the factor

$$Q_m = \left\{\sum_{v_m} \exp - \left[(c_2/T)(\nu_m v_m + k_{2m}E_2\nu_m v_m)\right]\right\}^{d_m}, \tag{8}$$

where d_m is the degeneracy of the mth mode. The anharmonicity term in the exponential of eq (8) is now expanded and only the linear term retained to yield

$$Q_m = \left\{\sum_{v_m}\left\{\exp\left[-\frac{c_2}{T}\nu_m v_m\right]\right\}\left\{1 - \frac{c_2}{T}k_{2m}\nu_m v_m E_2\right\}\right\}^{d_m}. \tag{9}$$

Using the identity

$$-\frac{d}{d\alpha}\sum_v e^{-\alpha v} = \sum_v v e^{-\alpha v},$$

the contribution of Q_m becomes

$$Q_m = \left(1 - e^{-\frac{c_2}{T}\nu_m}\right)^{-d_m}\left(1 - f_{2m}\right), \tag{10}$$

where

$$f_{2m} = d_m \frac{c_2}{T}k_{2m}E_2\nu_m/(e^{c_2\nu_m/T} - 1). \tag{11}$$

The factor $(1 - f_{2m})$ is the contribution of the interaction of a particular $(0v_200)$ energy state with the mth vibrational mode, and it depends explicitly on E_2. It is clear then that the effect of this coupling is to modify each of the terms in the term-by-term sum over the $(0v_200)$ energy levels by the factor $(1 - f_{2m})$. The term-by-term sum including cross coupling with the other vibrational modes is thus given by

$$Q_{v_2}\,(\text{vib}) = \sum_{E_2}\prod_m{}' (1 - f_{2m}) \exp(-c_2E_2/T). \tag{12}$$

The prime indicates that the $m = 2$ factor in the product corresponding to self coupling of the ν_2 mode is omitted.

The coupling of rotation with the ν_2 mode is included by evaluating the classical rotational partition function for each of the $(0v_200)$ energy levels and employing these as separate weighting factors to each of the terms in eq (12). These factors are the usual expression for a classical nonrigid rotator,

$$Q_R(v_2) = \pi^{1/2}(\sigma_B^2\sigma_C)^{-1/2}(1 + \rho^{(1)}T + \rho^{(2)}T^2). \tag{13}$$

The quantities σ_B and σ_C are given by,

$$\sigma_B = \frac{c_2}{T}B_{v_2},$$

$$\sigma_C = \frac{c_2}{T}C_{v_2},$$

where B_{v_2} and C_{v_2} are the observed rotational constants for the particular $(0v_200)$ energy level. The factor $1 + \rho^{(1)}T + \rho^{(2)}T^2$ is the contribution of rotational stretching (see, for example (5 and 14)), where the ρ are calculated from the rotational stretching coefficients that apply to the particular $(0v_200)$ level.

One further simplification is required in order to evaluate the out-of-plane contribution. This is to obtain an approximation for the contribution of the energy levels corresponding to high values of the v_2 quantum number. Note that the ν_2 mode is nearly harmonic for energies corresponding to the fourth quantum number and higher, so that the contribution of these levels may be replaced by the well-known expression for a slightly anharmonic rotating vibrator. Combining eqs (12) and (13) and including the closed form approximation for the contribution of the states corresponding to quantum numbers given by $v_2 > 3$ yields the expression for $G_2(v, J, K)$ used in this calculation.

$$Q_{v_2} = \left\{\sum_{v_2<4}\frac{B_0}{B_E}\left(\frac{C_0}{C_E}\right)^{1/2}(1 + \rho^{(1)}T + \rho^{(2)}T^2) \cdot \prod_j{}' (1 - f_{2j})e^{-\frac{c_2}{T}E}\right\}$$

$$+ \frac{\exp(-c_2E_{4s}/T)}{1 - \exp(-c_2\nu_2'/T)} \cdot \frac{B_0}{B_4}\left(\frac{C_0}{C_4}\right)^{1/2} \cdot \prod_j (1 - \theta_{2j})(1 + \phi_2)(1 + \rho^{(1)}T), \tag{14}$$

where $E \equiv E_2$ and the subscript to E now refers to the particular v_2 quantum number. The quantity in the braces in eq (14) includes levels only up to $v_2 = 3^a$. Note that the rigid rotational contribution for the ground state has been factored from eq (14). In the second term the factor $\dfrac{\exp(-c_2E_{4s}/T)}{1 - \exp(-c_2\nu_2'/T)}$ is the harmonic oscillator contribution with E_{4s} as the first level

289-015 O-68—7

and ν_2' the fundamental. The factor $1-\theta_{2j}$ is the ordinary anharmonicity coupling with the jth vibrational mode, where

$$\theta_{ij}=\frac{\frac{c_2}{T}x_{ij}d_id_j}{(\exp(c_2\nu_i/T)-1)(\exp(c_2\nu_j/T)-1)},$$

$$\theta_{ii}=\frac{\frac{c_2}{T}(x_{ii}-g_{ii}/3)d_i(d_i+1)}{(\exp(c_2\nu_i/T)-1)^2}. \tag{15a}$$

The factor $1+\phi_2$ is the well-known contribution of rotation-vibration coupling, where

$$\phi_i=d_i\left(\frac{\alpha_I^B}{B}+\frac{1}{2}\frac{\alpha_I^C}{C}\right). \tag{15b}$$

Details concerning the derivation of quantities in eqs (15) may be found in Friedman and Haar [6], Woolley [7], and Pennington and Kobe [8], for example.

The contributions to the partition function of the two remaining terms $G'(v, J, K)$ and $F'(v, J, K)$ are quite straightforward (see [6, 7, 8]). With these the complete partition function is finally obtained.

$$Q=\frac{1}{S}\prod_{m=1}^{4}{}'(1-e^{-\frac{c_2}{T}\nu_m})^{-d_m}\prod_{i\leq j}^{4}{}'(1-\theta_{ij})\prod_{k=1}^{4}{}'(1+\phi_k)$$
$$\left(\frac{\Pi}{\sigma_{B_0}^2\sigma_{C_0}}\right)^{1/2}\cdot Q_{v_2}\cdot Q_{\mathrm{tr}}\cdot Q_{qr}. \tag{16}$$

As noted earlier the primes on the product summations indicate that factors containing the vibrational coordinate v_2 are omitted. The quantity S is the symmetry number. For the usual symmetric top molecule this has the value three. However, each of the components of the nondegenerate but split $(0v_200)$ levels have been counted with a statistical weight of unity, so that the factor Q_{v_2} is larger by a factor of two. This error is corrected by setting $S=6$. (Incidentally $S=6$ corresponds to the symmetry for a planar configuration for NH_3, and eq (16) might be thought of as an expansion about this planar configuration.) The product over m is the harmonic oscillator contribution for the modes other than ν_2; the products over ij and over k are the corresponding anharmonicity and rotation-vibration coupling contributions, respectively. The degeneracy coefficients d are unity for $m=1, 2$, and two for $m=3, 4$. The θ_{ij} and ϕ_k are given by eq (15). Q_{tr} is the usual contribution of translation. Lastly, the factor Q_{qr} is a correction for rotational quantum effects. It is very small at temperatures for which the vibrations are appreciably excited, so that it is not coupled to the ν_2 mode. The contribution Q_{qr} is given by Stripp and Kirkwood [9] for an asymmetric rotator, which for a symmetric top rotator reduces to

$$Q_{qr}=1+\frac{\sigma_B}{3}\left(1-\frac{1}{4}\frac{\sigma_B}{\sigma_C}\right)+\frac{\sigma_B^2}{15}\left(1-\frac{3}{4}\frac{\sigma_B}{\sigma_C}+\frac{7}{32}\frac{\sigma_B^2}{\sigma_C^2}\right).$$

3. Molecular Data

The molecular data upon which the calculations are based are listed in tables 1 and 2. Table 1 lists the data sensitive to the inversion coordinates and utilized in the term-by-term sum (the quantity in braces in eq (14)). The vibrational energies corresponding to $v_2=0, 3$ are from [4]. The energies corresponding to $v_2=1, 2$ are from Garing et al. [10]. The values listed for the rotational constants B_v and C_v corresponding to the $v_2=0$ states are from [4]; those corresponding to the $v_2=1, 2$ states from [10]; and to the $v_2=3$ states from Benedict et al. [11]. The rotational stretching constants D_v^J, D_v^{JK}, D_v^K are the average of the symmetric and antisymmetric values. The values for $v_2=0$ are from [4]; for $v_2=1$, from [10]; for $v_2=3$, from [11]; finally, data for $v_2=2$ were taken equal to the $v_2=1$ values.

TABLE 1. *The out-of-plane molecular constants in* cm^{-1}, $v_2\leq 3$, $(0v_200)$

State	0^s	0^a	1^s	1^a	2^s	2^a	3^s	3^a
ν_{v_2}	0.0	0.793	932.41	968.04	1597.42	1882.16	2383.46	2895.48
B_{v_2}	9.9443	9.939	10.07	9.89	10.26	9.73	9.50	9.20
C_{v_2}	6.196	6.198	6.05	6.13	5.90	6.13	6.16	6.26
$D_{v_2}^J$	8.1×10^{-4}		8.9×10^{-4}		8.9×10^{-4}		-3.3×10^{-4}	
$D_{v_2}^{JK}$	-14.5×10^{-4}		-17.5×10^{-4}		-17.5×10^{-4}		15.0×10^{-4}	
$D_{v_2}^K$	7.5×10^{-4}		10.5×10^{-4}		10.5×10^{-4}		-11.3×10^{-4}	

TABLE 2. *Vibrational, rotational and coupling constants in* cm^{-1}; *see eqs (2), (3)*

$\nu_1(1\ 0\ 0\ 0)$	$\nu_2'=E_{4s}-E_{4a}$	$\nu_3(0\ 0\ 1\ 0)$	$\nu_4(0\ 0\ 0\ 1)$
3323.06	475	3443.381	1627.77
$x_{11}=-30$	$x_{22}=+9$	$x_{33}=-18.5$	$x_{44}=-8.8$
$x_{12}=+20.6$	$x_{23}=+32.36$	$x_{34}=-17.3$	$g_{44}=+2.65$
$x_{13}=-92$	$x_{24}=-10.7$		
$x_{14}=-6.7$	$B_4=9.35,\ C_4=6.21$		
$\alpha_1^B=0.135$	$\alpha_2^B=+0.015$	$\alpha_3^B=+0.176$	$\alpha_4^B=-0.230$
$\alpha_1^C=.078$	$\alpha_2^C=+0.098$	$\alpha_3^C=-0.009$	$\alpha_4^C=+0.066$

The remaining molecular data are given in table 2. The vibrational fundamental ν_1 is from Benedict et al. [12]; ν_3 is from [11]; ν_4 is from [10]. The constants $\nu_2'$and x_{22} which correspond to the high energy, nearly-harmonic region of the ν_2 mode are derived from the reported values for the (04^s00) and (05^s00) levels at 3330 cm^{-1} and 4315 cm^{-1} given by Walsh and Warsop [13] and from theoretical considerations that at high energies the spacing between the levels should become nearly equal to one-half the (0100) value. Also pertaining to this region are the rotational constants B_4 and C_4 which are taken equal to the averages of the values for $v_2=3^s$ and 3^a. The anharmonicity coefficients x_{12}, x_{13}, x_{14}, x_{23}, x_{24}, x_{33}, and x_{34} are from [4], and the coefficients x_{44} and g_{44} are from [10]. The anharmonicity coefficient x_{11} is estimated from data for similar

stretching vibrations. The coupling constants α_T^N are from [4]. The small coefficient g_{33} is taken as zero.

The values used for the atomic masses are from Cameron and Wichers [35]. The values used for the other physical constants are given in [36].

4. Thermodynamic Functions

The thermodynamic properties of ammonia as an ideal gas at a pressure of one atmosphere are listed in table 3. These include the Gibbs (free) energy function, enthalpy function, heat capacity at constant pressure, and entropy tabulated in dimensionless units at closely spaced temperature intervals from 50 to 5000 °K. Should it be desired to obtain the properties for a pressure of 1 bar (10^6 dynes cm^{-2} or 10^5 Nm^{-2}) the magnitude of the tabulated free energy and entropy values should be increased by 0.0132. Conversion factors to other units in frequent use are given in table 4. The entries in table 3 are truncated at four decimals (except for C_p°/R above 2500 °K which is truncated at three) but at best they are accurate to three decimals. It is felt that the additional significance could be useful in applications involving differences between the entries. The density of entries permits use of linear interpolation throughout the table with a resulting interpolation error smaller than the uncertainty in the tabulated values.

As indicated by the earlier discussion the present calculation, except for the out-of-plane vibrations, is based on an expansion about the harmonic oscillator-rigid rotator model. In this expansion only first order (linear) terms in the coupling between the various degrees of freedom are retained. In addition to the errors inherent in the derivation of the partition function, eq (16), there are also errors due to uncertainties in the molecular constants, errors which arise from certain resonances between several of the low-lying vibrational states, the effects of which are omitted, and lastly errors arising from omission of excited electronic states.

TABLE 3. *Thermodynamic functions for ammonia*

The tabulated values are spaced sufficiently close to permit linear interpolation between the entries with a resulting error less than their overall uncertainty. For convenience the values at 273.15 and 298.15 °K have also been included.

T	$(E_0^\circ - G)/RT$	$(H^\circ - E_0^\circ)/RT$	C_p°/R	S°/R
50.	12.0017	3.9539	4.0029	15.9555
60.	12.7234	3.9620	4.0026	16.6854
70.	13.3346	3.9678	4.0026	17.3024
80.	13.8648	3.9721	4.0027	17.8369
90.	14.3328	3.9756	4.0029	18.3084
100.	14.7519	3.9783	4.0033	18.7302
110.	15.1311	3.9806	4.0039	19.1117
120.	15.4776	3.9826	4.0051	19.4602
130.	15.7964	3.9844	4.0069	19.7808
140.	16.0918	3.9861	4.0097	20.0779
150.	16.3668	3.9878	4.0138	20.3546
160.	16.6243	3.9896	4.0194	20.6138
170.	16.8662	3.9915	4.0267	20.8577
180.	17.0944	3.9937	4.0358	21.0881
190.	17.3104	3.9962	4.0468	21.3066
200.	17.5154	3.9991	4.0599	21.5145
210.	17.7106	4.0023	4.0749	21.7129
220.	17.8969	4.0060	4.0920	21.9029
230.	18.0751	4.0101	4.1110	22.0852
240.	18.2458	4.0147	4.1319	22.2606
250.	18.4098	4.0199	4.1548	22.4297
260.	18.5676	4.0255	4.1794	22.5931
270.	18.7196	4.0317	4.2057	22.7513
273.15	18.7663	4.0338	4.2143	22.8001
280.	18.8664	4.0384	4.2336	22.9048
290.	19.0082	4.0456	4.2630	23.0539
298.15	19.1204	4.0520	4.2882	23.1724
300.	19.1455	4.0534	4.2939	23.1989
310.	19.2785	4.0617	4.3260	23.3402
320.	19.4076	4.0704	4.3593	23.4781
330.	19.5330	4.0797	4.3937	23.6127
340.	19.6550	4.0895	4.4291	23.7444
350.	19.7737	4.0997	4.4654	23.8733
360.	19.8893	4.1104	4.5025	23.9997
370.	20.0021	4.1215	4.5402	24.1235

TABLE 3. *Thermodynamic functions for ammonia*—Continued

T	$(E_0^\circ - G)/RT$	$(H^\circ - E_0^\circ)/RT$	C_p°/R	S°/R
380.	20.1121	4.1330	4.5785	24.2451
390.	20.2196	4.1449	4.6173	24.3646
400.	20.3247	4.1572	4.6565	24.4819
410.	20.4275	4.1699	4.6961	24.5974
420.	20.5282	4.1829	4.7359	24.7111
430.	20.6268	4.1962	4.7759	24.8230
440.	20.7234	4.2098	4.8161	24.9332
450.	20.8181	4.2237	4.8563	25.0419
460.	20.9111	4.2379	4.8966	25.1491
470.	21.0024	4.2524	4.9368	25.2548
480.	21.0921	4.2671	4.9771	25.3592
490.	21.1802	4.2820	5.0172	25.4622
500.	21.2669	4.2971	5.0572	25.5640
520.	21.4360	4.3278	5.1368	25.7639
540.	21.6000	4.3593	5.2158	25.9592
560.	21.7591	4.3912	5.2939	26.1503
580.	21.9137	4.4237	5.3712	26.3374
600.	22.0643	4.4566	5.4475	26.5208
620.	22.2109	4.4898	5.5230	26.7007
640.	22.3540	4.5232	5.5975	26.8772
660.	22.4937	4.5569	5.6711	27.0506
680.	22.6302	4.5907	5.7438	27.2210
700.	22.7638	4.6247	5.8157	27.3885
720.	22.8946	4.6588	5.8867	27.5533
740.	23.0227	4.6929	5.9568	27.7156
760.	23.1483	4.7271	6.0261	27.8754
780.	23.2715	4.7613	6.0946	28.0328
800.	23.3925	4.7954	6.1622	28.1879
820.	23.5113	4.8296	6.2291	28.3409
840.	23.6281	4.8637	6.2952	28.4918
860.	23.7430	4.8978	6.3604	28.6407
880.	23.8559	4.9317	6.4249	28.7877
900.	23.9672	4.9656	6.4885	28.9328
920.	24.0767	4.9994	6.5513	29.0761
940.	24.1845	5.0331	6.6133	29.2176
960.	24.2909	5.0667	6.6745	29.3575
980.	24.3957	5.1001	6.7348	29.4958
1000.	24.4990	5.1334	6.7943	29.6324
1020.	24.6010	5.1665	6.8530	29.7676
1040.	24.7017	5.1995	6.9108	29.9012
1060.	24.8010	5.2323	6.9678	30.0334
1080.	24.8991	5.2650	7.0239	30.1641
1100.	24.9960	5.2975	7.0792	30.2935
1120.	25.0918	5.3298	7.1335	30.4216
1140.	25.1864	5.3619	7.1870	30.5483
1160.	25.2799	5.3938	7.2397	30.6738
1180.	25.3724	5.4256	7.2914	30.7980
1200.	25.4639	5.4571	7.3424	30.9209
1220.	25.5543	5.4884	7.3924	31.0427
1240.	25.6438	5.5195	7.4416	31.1633
1260.	25.7324	5.5504	7.4900	31.2828
1280.	25.8200	5.5811	7.5375	31.4011
1300.	25.9068	5.6115	7.5841	31.5183
1320.	25.9927	5.6418	7.6299	31.6345
1340.	26.0778	5.6718	7.6749	31.7495
1360.	26.1620	5.7016	7.7190	31.8636
1380.	26.2455	5.7311	7.7624	31.9766
1400.	26.3281	5.7604	7.8049	32.0886
1420.	26.4101	5.7895	7.8466	32.1996
1440.	26.4912	5.8184	7.8875	32.3096

TABLE 3. *Thermodynamic functions for ammonia*—Continued

T	$(E_0^\circ - G)/RT$	$(H^\circ - E_0^\circ)/RT$	C_p°/R	S°/R
1460.	26.5717	5.8470	7.9277	32.4187
1480.	26.6514	5.8754	7.9671	32.5268
1500.	26.7305	5.9035	8.0058	32.6340
1550.	26.9252	5.9729	8.0992	32.8981
1600.	27.1159	6.0407	8.1881	33.1566
1650.	27.3028	6.1071	8.2728	33.4099
1700.	27.4861	6.1720	8.3532	33.6581
1750.	27.6659	6.2354	8.4298	33.9013
1800.	27.8424	6.2974	8.5027	34.1398
1850.	28.0158	6.3579	8.5719	34.3737
1900.	28.1862	6.4171	8.6378	34.6032
1950.	28.3536	6.4748	8.7004	34.8284
2000.	28.5182	6.5312	8.7599	35.0494
2050.	28.6802	6.5863	8.8164	35.2664
2100.	28.8395	6.6400	8.8702	35.4795
2150.	28.9964	6.6925	8.9214	35.6889
2200.	29.1508	6.7437	8.9701	35.8945
2250.	29.3030	6.7937	9.0162	36.0966
2300.	29.4528	6.8425	9.0602	36.2953
2350.	29.6005	6.8901	9.1021	36.4906
2400.	29.7460	6.9366	9.1418	36.6826
2450.	29.8895	6.9820	9.1797	36.8715
2500.	30.0310	7.0263	9.216	37.0573
2550.	30.1706	7.0696	9.250	37.2402
2600.	30.3083	7.1118	9.282	37.4201
2650.	30.4441	7.1531	9.313	37.5972
2700.	30.5782	7.1933	9.342	37.7716
2750.	30.7106	7.2327	9.370	37.9432
2800.	30.8413	7.2711	9.397	38.1123
2850.	30.9703	7.3086	9.422	38.2789
2900.	31.0977	7.3452	9.445	38.4429
2950.	31.2236	7.3810	9.468	38.6046
3000.	31.3479	7.4160	9.490	38.7639
3100.	31.5922	7.4835	9.529	39.0757
3200.	31.8308	7.5480	9.564	39.3788
3300.	32.0640	7.6096	9.596	39.6736
3400.	32.2921	7.6684	9.623	39.9605
3500.	32.5152	7.7246	9.648	40.2398
3600.	32.7336	7.7783	9.670	40.5119
3700.	32.9474	7.8297	9.688	40.7771
3800.	33.1568	7.8788	9.704	41.0357
3900.	33.3621	7.9258	9.717	41.2879
4000.	33.5633	7.9707	9.728	41.5341
4100.	33.7607	8.0137	9.737	41.7744
4200.	33.9543	8.0548	9.743	42.0091
4300.	34.1443	8.0941	9.748	42.2384
4400.	34.3308	8.1317	9.750	42.4626
4500.	34.5140	8.1677	9.751	42.6817
4600.	34.6939	8.2021	9.749	42.8960
4700.	34.8706	8.2350	9.746	43.1056
4800.	35.0443	8.2664	9.741	43.3107
4900.	35.2151	8.2964	9.734	43.5115
5000.	35.3833	8.3253	9.725	43.7086

The expansion about the harmonic oscillator limit is essentially a low temperature expansion, and the errors resulting therefrom for a particular vibrational mode are small provided $\frac{\nu}{T}$ is large, and are of the order of about the square of the linear term. The

TABLE 4

Conversion factors to convert tabulated value to quantity having dimensions indicated below	Multiply by
Cal $mole^{-1}$ $°K^{-1}$	1.98717
Cal g^{-1} $°K^{-1}$	0.116682
Joules $mole^{-1}$ $°K^{-1}$	8.3143
Joules g^{-1} $°K^{-1}$	0.488197

largest error of this type occurs for the ν_4 mode. Thus for the most sensitive function, the heat capacity, the uncertainty at 2000 °K is less than 10^{-2} dimensionless units, but increases to the order of 0.1 at 5000 °K. The higher order anharmonicities would contribute an uncertainty perhaps as large. Though the anharmonicity coefficients x_{11} and x_{13} have large uncertainties, the errors introduced by these are mitigated by the fact that the fundamentals ν_1 and ν_3 are large. A 50 percent uncertainty in x_{11} and x_{13} results in an error of about 0.05 dimensionless units in C_p°/R at 5000 °K. Setting g_{33} equal to zero introduces negligible error since this coefficient introduces a small correction to an already small anharmonic contribution (owing to the large value of the ν_3 fundamental). The remaining anharmonicities (other than the x_{22} value in table 2) are probably accurate to better than several percent, and the uncertainties resulting from these are comparatively small. Uncertainties arising from errors in the rotational fundamentals are also comparatively small, as are uncertainties resulting from the use of estimates for some of the rotational stretching constants. The uncertainties that arise from errors in the rotation-vibration coupling constants are perhaps half as large as those arising from errors in the anharmonicity coefficients.

The uncertainties in the values used for the fundamental frequencies are less than several tenths of a wavenumber, and the uncertainty from this source is negligible. Also negligible are the uncertainties due to errors in the observed overtones of the ν_2 fundamental.

It is somewhat more difficult to determine the uncertainty resulting from estimates used for the molecular constants in the second term in eq (14). The largest uncertainty here arises from possible errors in ν_2' and $E_{\nu'}$. An uncertainty of several percent in these results in an uncertainty in C_P°/R of less than 0.002 dimensionless units at 1000 °K, which increases to a maximum near 2000 °K of less than 0.01 dimensionless units. The errors from estimates of the vibrational coupling constants used in this term are completely negligible below 2000 °K. Even if a 100 percent uncertainty in their contribution is assumed, the resulting uncertainty at 5000 °K still would be less than 0.1 dimensionless units in C_p°/R.

The spectrum of ammonia is further complicated by several large resonances that occur between some of the low lying vibrational bands, such as the resonance between the combination bands $(2\nu_4+\nu_3)$ and $(\nu_1+\nu_3)$ and between the bands $2\nu_4$ and ν_1 as discussed in [4]. Since the resonances tend to displace the respective bands symmetrically about their unperturbed values, it can be shown that the errors are less than the neglected higher order anharmonicities. A similar type of error occurs in the treatment of the coupling of the ν_2 mode with the other modes. The coupling constants as reported are the average of the symmetric and antisymmetric values. Thus the effect of this approximation is to introduce errors similar to those arising from neglect of the resonances discussed above. The treatment of centrifugal distortion, which includes a quadratic term in the temperature, is consistent with the other approximations and the error from this source at 5000 °K is probably less than 0.05 in C_P°/R. At the low temperature end there is a small error arising from the rotational quantum approximation Q_{qr} (eq (17)). At 100 °K this error is less than 10^{-3} in C_P°/R, but is appreciably larger at 50 °K.

Finally, the U.V. absorption spectrum indicates bands extending from ~ 46,000 cm^{-1} to over 100,000 cm^{-1}, as discussed, for example, in [13]. The error from omission of these even at the very highest temperatures considered here is completely negligible. It is felt, therefore, that the uncertainty in the tables in the temperature region 100 to 1000 °K is probably less than 0.003 dimensionless units in C_P°/R. This uncertainty increases to 0.02 at 2000 °K and then increases very rapidly to perhaps 0.3 at 5000 °K. A more complete list of the uncertainty estimates, including those for the enthalpy and entropy, are given in table 5.

TABLE 5. *Estimates of uncertainty in dimensionless units*

T	$\Delta C_p^\circ/R$	$\Delta(H^\circ-E_0^\circ)/RT$	$\Delta S^\circ/R$
100	0.003	0.002	0.003
1000	.003	.002	.003
2000	.02	.01	.02
3000	.05	.02	.03
4000	.1	.05	.07
5000	.3	.1	.2

5. Discussion

Ideal-gas calculations for NH_3 have been reported in the literature since the early thirties, but many of these calculations were based on relatively incomplete and inaccurate molecular data and on simplified structural models. Also, for the most part, the temperature ranges were somewhat limited. The references [17–27] are representative of these early efforts.

Some of the more recent calculations which have been widely used include those of Harrison and Kobe [28] who calculated the heat capacity, enthalpy, and entropy from 273.16 to 1500 °K. They included the major effects associated with the molecular inversion by summing the lower states of the ν_2 mode term by term, but omitted all vibration and rotational coupling effects other than rotational stretching. The review by Davies reported in the monograph edited by Din [29]

includes the specific heat, entropy, and enthalpy from 200 to 1000 °K. The calculation follows essentially the procedure in [28], except that centrifugal stretching is omitted. Also it appears that the contribution of the states in the term-by-term sum of the ν_2 mode was omitted above the level 3^a. The most detailed of the previous calculations is that reported by Yungman et al. [30], (which also appears in [16]), in which the free energy, entropy, and enthalpy are tabulated at 100 °K intervals from 298.15 to 6000 °K. In addition to the term-by-term sum for the ν_2 mode, this work also includes several of the first order vibrational and rotational coupling contributions. It omits, however, the contributions due to coupling of the ν_2 mode with the other vibrational modes, and includes a somewhat simplified coupling of the ν_2 mode with rotation. These calculations are based on essentially the same molecular data as those reported here, except that the values used for the vibrational coupling constants x_{13} and x_{44} are about twice as large. One of the most widely used set of tables is that of JANAF [31]. The reference refers to the latest revision for ammonia, September 30, 1965. This calculation follows the procedures of [28] and [30], though the specific details are not given in the text. Finally, there are several recent calculations based on somewhat simplified molecular models, which are included in references [32–34].

The figures 1 and 2 include a comparison of some of the previous calculations with those made here. The ordinates are the deviations from the present calculations, that is the present calculation minus the others. Figure 1 is a plot of entropy differences, and figure 2 is a plot of heat capacity differences. It is most interesting to compare the data of Yungman et al. [30], curve #5 in figure 1. At the low temperatures the agreement is quite good, but as the temperature is increased, a positive deviation occurs until about 3000 °K, when the deviation becomes strongly negative. The difference at the lower temperatures is probably due to their simplified treatment of the coupling of the ν_2 mode with rotation. At temperatures above 1000 °K, the dominant contribution to the difference is from the x_{24} term omitted in [30] which yields a positive contribution. At temperatures above 3000 °K, the dominant contribution is from the omitted x_{12} and x_{23} terms which yield large negative contributions. In addition to these, the high value they used for x_{44} (larger by a factor of two) tends to reduce the differences at temperatures below 3000 °K, but magnifies them above. The same general comments apply to the JANAF [31] comparison as seen in curve #1, except that the difference goes negative at somewhat higher temperatures and the positive deviations are considerably larger. Incidentally, the JANAF and Harrison and Kobe [28] (curve #4) calculations are nearly identical for temperatures up to 1000 °K. Curve #3 applies to a modified rigid rotator harmonic oscillator calculation as given in an older (now superseded) JANAF table. The comparison for curve #2 [29] illustrates the sensitivity to the omission of the hierarchy of states corresponding to large v_2 quantum numbers ($v_2 > 3$). The differences plotted in figure 2 exhibit essentially the same behavior as those in figure 1 except that they are somewhat larger.

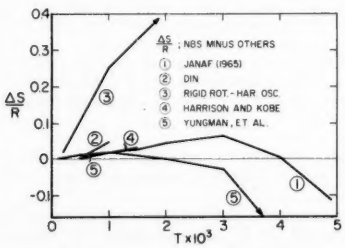

FIGURE 1. *Dimensionless entropy differences.*

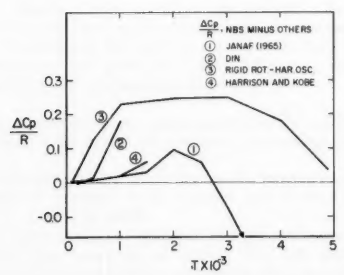

FIGURE 2. *Dimensionless heat capacity differences.*

It is a pleasure to thank Joseph Hilsenrath for many helpful technical discussions, particularly relating to the use of OMNITAB to program the calculation. In this latter connection, I also wish to thank Robert C. Thompson.

6. References

[1] J. D. Swalen and J. A. Ibers, J. Chem. Phys. **36,** 1914 (1962).
[2] G. Herzberg, Infrared and Raman Spectra of Polyatomic Molecules, D. Van Nostrand & Co., New York (1945).
[3] H. H. Nielsen, Revs. Modern Phys. **23,** 90 (1951).
[4] W. S. Benedict and E. K. Plyler, Can. J. Phys. **35,** 1235 (1957).
[5] R. S. McDowell, J. Chem. Phys. **39,** 526 (1963).
[6] A. S. Friedman and L. Haar, J. Chem. Phys. **22,** 2051 (1954).
[7] H. W. Woolley, J. Res. NBS **56,** 105 (1956).
[8] R. E. Pennington and K. A. Kobe, J. Chem. Phys. **22,** 1442 (1954).
[9] K. F. Stripp and J. G. Kirkwood, J. Chem. Phys. **19,** 1131 (1951).
[10] J. S. Garing, H. H. Nielsen, and K. N. Rao, J. Mol. Spect. **3,** 496 (1959).
[11] W. S. Benedict, E. K. Plyler, and E. D. Tidwell, J. Chem. Phys. **29,** 829 (1958).
[12] W. S. Benedict, E. K. Plyler, and E. D. Tidwell, J. Chem. Phys. **32,** 32 (1960).
[13] A. D. Walsh and P. A. Warsop, Trans. Faraday Soc. **57,** 345 (1961).
[14] Y. S. Yungman, Zhur. Fiz. Khim. **35,** 319 (1961).
[15] I. N. Godnev, Zhur. Fiz. Khim. **27,** 1702 (1953).
[16] V. P. Glushko, Ed., Termodinamicheskie Svoistva Individual'nykh Vestchestv, **II,** Acad. Sci., USSR, Inst. of Applied Chemistry, Moscow (1962).
[17] D. S. Villars, Phys. Rev. **38,** 1552 (1931); J. Am. Chem. Soc. **53,** 2006 (1931).
[18] M. Trautz, Ann. Physik **9,** 465 (1931).

[19] F. A. F. Schmidt, Forsch. Arb. Ing. Wes. **8,** 91 (1937).
[20] R. Overstreet and W. F. Giauque, J. Am. Chem. Soc. **59,** 254 (1937).
[21] K. K. Kelley, U.S. Bur. Mines, Bull. **407** (1937).
[22] E. Justi, Spez-Wärme, Enthalpie und Dissociation Technischer Gase, J. Springer, Berlin (1938).
[23] C. C. Stephenson and H. O. McMahan, J. Am. Chem. Soc. **61,** 437 (1939).
[24] K. S. Pitzer, J. Chem. Phys. **7,** 251 (1939).
[25] R. F. Haupt and E. Teller, J. Chem. Phys. **7,** 925 (1939).
[26] H. Zeise, Z. Elektrochem. **47,** 380 (1941).
[27] H. W. Thomson, Trans. Faraday Soc. **37,** 344 (1941).
[28] R. H. Harrison and K. A. Kobe, Chem. Eng. Progress **49,** 351 (1953).
[29] F. Din, Thermodynamic Functions of Gases **1** (Butterworths, London, 1956).
[30] Y. S. Yungman, L. V. Gurvich, and N. P. Rtischeva, Tr. Gos. Inst. Prikl. Khim. **49,** 26 (1962).
[31] JANAF Thermochemical Tables, Distrib. by Clearinghouse for Federal Scientific Information, PB168370–1, Sept. 30, 1965.
[32] C. L. Mader, Ideal Gas Thermodynamics of Detonation Products, U.S. A.E.C., AECU–4508 (1959).
[33] V. N. Khlebnikova and V. P. Morozov, Ukrain. Khim. Zhur. **24,** 3 (1958).
[34] S. Sundaram, F. Suszek, and F. F. Cleveland, J. Chem. Phys. **32,** 251 (1960).
[35] A. E. Cameron and E. Wichers, J. Am. Chem. Soc. **84,** 4192 (1962).
[36] NBS Tech. News Bull. **47,** No. 10 (Oct. 1963).

(Paper 72A2–495).

JOURNAL OF RESEARCH of the National Bureau of Standards—A. Physics and Chemistry
Vol. 72A, No. 2, March–April 1968

Publications of the National Bureau of Standards*

Selected Abstracts

Analytical Mass Spectrometry Section: Summary of activities July 1966 to June 1967, Ed. W. R. Shields, *Tech. Note 426 (Sept. 15, 1967), 40 cents.*
This report describes the advances in instrumentation and the research activities of the Analytical Mass Spectrometry Section during the period July 1966 to June 1967.
Advances in instrumentation include the construction of a multistage mass spectrometer, a high vacuum beam valve, a Z focusing lens, a redesigned collector, a filament degas chamber, and new equipment for sample drying. The new facilities at Gaithersburg are described.
Elements studied during this period include: B, Cr, Pb, Rb, U, and Pu. Chemical procedures are given for B, Cr, Pb, and Pu; mass spectrometric procedures are given for B, Cr, Pb, Pu, Rb, and U.

Key Words: Mass spectrometry, instrumentation, procedures, isotopic analyses.

Comparison of incompressible flow and isothermal compressible flow formulae, J. Hord, *Tech. Note 356 (Aug. 17, 1967), 25 cents.*
Mass flow formulae for incompressible and "modified-incompressible" flow are compared with the isothermal compressible flow relation under the following conditions: The gas flow is steady, isothermal, and fully developed in a horizontal pipe of constant cross section with a prescribed static pressure drop $(P_1 - P_2)$. The comparative data are limited to static pressure ratios $(P_2/P_1) > 1/2$, and subsonic isothermal flow. Laminar and turbulent flows are treated. Under the limitations of the comparison, modified-incompressible flow and isothermal gas flow relations are identical when $fL/2D \gg \ln (P_1/P_2)$. Graphical plots indicate the degree of approximation or error involved in using incompressible relations to solve compressible flow problems. Pressure losses due to end effects are briefly discussed.

Key Words: Compressible flow, flow comparison, fluid flow, incompressible flow, mass flow, pressure drop.

Designs for surveillance of the volt maintained by a small group of saturated standard cells, W. G. Eicke and J. M. Cameron, *Tech. Note 430 (Oct. 9, 1967), 20 cents.*
This technical note describes a procedure for maintaining surveillance over a small group of saturated standard cells. The measurement process is briefly discussed and the principle of left-right balance as a means of eliminating certain systematic errors is developed. Specific designs and their analysis for intercomparing 3, 4, 5 and 6 cells in a single temperature controlled environment are given. Procedures for setting up control charts on the appropriate parameters are given, and a technique is described for detecting certain types of systematic errors.

Key Words: Control charts, experiment design, saturated standard cells, standard cells calibration, statistics, voltage standard.

Realistic uncertainties and the mass measurement process. An illustrated review, P. E. Pontius and J. M. Cameron, *Mono. 103 (Aug. 15, 1967), 20 cents.*
This paper gives a review of the concepts and operations involved in measuring the mass of an object. The importance of viewing measurement as a production process is emphasized and methods of evaluating process parameters are presented. The use of one of the laboratory's standards as an additional unknown in routine calibration provides an accuracy check and, as time goes on, the basis for precision and accuracy statements.

Key Words: Measurement, measurement process, uncertainty, mass measurement, precision, accuracy, statistical control.

Selected values of electric dipole moments for molecules in the gas phase, R. D. Nelson, Jr., D. R. Lide, Jr., and A. A. Maryott, *NSRDS–NBS10 (Sept. 1, 1967), 40 cents. (Supersedes the data on dipole moments included in NBS Circ. 537).*
This table revises, brings up to date, and extends the coverage on numerical values for dipole moments which was included in NBS Circular 537, Tables of Dielectric Constants and Electric Dipole Moments of Substances in the Gaseous State, prepared by Maryott and Buckley in 1953. A recommended value with an estimate of accuracy is presented for more than five hundred organic and inorganic compounds. Extensive comments are given on the definition of dipole moment and principal methods of dipole moment measurement, as well as an exposition of the criteria employed in selecting the tabulated data.

Key Words: Dielectric constant, electric dipole moments, gas phase, microwave, microwave absorption, molecular beam, permittivity, refractive index, spectroscopy.

Standard Reference Materials: Catalog and price list of standard materials issued by the National Bureau of Standards, Misc. Publ. 260, 1967 Edition, Ed. *(Sept. 15, 1967), 45 cents. (Supersedes NBS Misc. Publ. 260, 1965 Edition).*
This catalog describes the various Standard Reference Materials issued by the National Bureau of Standards. These materials are used to calibrate measurement systems and provide scientific information that can be referred to a common base. A schedule of prices and quantities is included for each material, as well as directions for ordering. Listed are the types and compositions of those chemical standards that are presently available. Announcements of new standard reference materials are made in the Federal Register, in scientific and trade journals, and in the Technical News Bulletin of the National Bureau of Standards. Changes affecting the current status of the various standards will be indicated by an insert sheet available quarterly from the Bureau.

Key Words: Analysis, catalog, certificate, characterization, composition, price list, property of material, purity of material, standard reference materials, standards.

Standard x-ray diffraction powder patterns, H. E. Swanson, H. F. McMurdie, M. C. Morris, and E. H. Evans, *Mono. 25, Sect. 5 (Aug. 31, 1967), 55 cents.*
Standard x-ray diffraction powder patterns are presented for 80 substances. Thirty-nine of these patterns represent experimental data and 41 are calculated. The experimental x-ray powder diffraction patterns are made with a Geiger counter x-ray diffractometer, using samples of high purity. All d-values were assigned Miller indices determined by comparison with theoretical interplanar spacings and from consideration of space group extinctions. The densities and lattice constants were calculated, and the refractive indices were measured whenever possible. The calculated x-ray powder diffraction patterns were obtained from published crystal structure data. The reported peak height intensities for calculated patterns were converted from integrated intensities. Reference intensity values based upon the strongest line of corundum (113) in a 50 percent weight mixture are given for 73 materials.

Key Words: Standard, x-ray diffraction, powder-patterns, crystal, structure, measurements, lattice, constants, reference-intensities.

X-ray wavelength conversion tables and graphs for qualitative electron probe microanalysis, K. F. J. Heinrich and M. A. M. Giles, *Tech. Note 406 (Sept. 25, 1967), 70 cents.*
Tables and graphs have been constructed for electron probe x-ray spectrometers equipped with crystal changers and calibrated for LiF crystals in angstroms. These tables indicate the equivalent reading for the lines which can be normally expected to appear in wavelength scans using the following crystals: LiF, EDDT, ADP, KAP, and Pb stearate (LSD). The readings were extracted from the tables of E. W. White, et al. The tables are arranged by the atomic numbers of the emitting elements; the graphs show the readings for observable lines as a function of atomic number for each of the aforementioned crystals. A suggested method for using the tables and graphs is included.

Key Words: X-ray spectrometers, wavelengths, electron probe microanalyzer, x-ray emission.

Electrochemical Analysis Section: Summary of activities July 1966 to June 1967, Ed. R. G. Bates, *Tech. Note 423 (Oct. 1967), 50 cents.*
This survey of the activities of the Electrochemical Analysis Section, Analytical Chemistry Division, covers the period July 1966 to June 1967. An attempt is made to summarize a year's progress on the technical projects of the Section in such a way as to stress the program and capabilities of the organizational unit as a whole. A description of facilities and equipment is presented, and the directions of the programs are indicated. Brief summaries of several lines of work now under way are given. The main areas include the measurement of acidity, with progress toward the establishment of standards for *pH*, *pH**, and *p*D being reported. Studies of the behavior of glass electrodes in deuterium oxide are described and solvent effects on ionic processes are discussed. Equilibrium data for certain ionic systems have been obtained, modifications of a precision conductance bridge are described, and a method for titrating hydrogen fluoride in dimethylformamide is outlined. The survey concludes with lists of the members of the Section staff, publications and manuscripts produced during the year, talks given by the staff, and committee assignments.

Key Words: Electrochemical analysis, analysis, acidity, glass electrodes, *p*H measurements, medium effects, conductance measurements, electrochemistry of solutions.

Field burnout tests of apartment dwelling units, D. Gross, *Bldg. Sci. Series 10 (Sept. 29, 1967), 25 cents.*
Results are reported of three burnout tests in an experimental test building, using a wood crib fuel load of 6 lb/ft², representing combustible contents, and a structural design load of 40 lb/ft² applied to the floor or roof above the test room. Measurements were made of temperature, radiation, smoke, gas composition, and structural deflection. A discussion of the fire performance of materials and methods of construction, and conclusions with regard to specific fire-protective objectives are presented.

Key Words: Burnout test, fire performance, apartment dwelling, smoke, flame penetration, structural load, potential heat, fire load.

"Life cycling" test on several strain gage pressure transducers, P. S. Lederer, *Tech. Note 434 (Oct. 1967), 20 cents.*
This publication reports the effects of many thousands of pressure cycles on the performance characteristic of several types of strain gage pressure transducers. The results obtained indicate permanent changes in zero pressure output and sensitivity. Most of these changes tend to occur during the first few thousands of cycles. The equipment and procedures used to obtain the data are described.

Key Words: Life cycling, pressure cycling, life testing, pressure transducer, strain gage.

Microchemical Analysis Section: Summary of activities July 1966 to June 1967, Ed. J. K. Taylor, *Tech. Note 425 (Oct. 1967), 50 cents.*
This report describes the research activities and scientific programs of the Microchemical Analysis Section of the Analytical Chemistry Divison of the NBS Institute for Materials Research during the period July 1966 to June 1967. General activities are reported in the areas of gas analysis, polarography, potentiometry, coulometry, chemical microscopy, and classical microchemical analysis. Research accomplishments described in some detail include the following: high pressure mass spectrometry; high precision differential polarography; an improved coulometric technique for titration of halides; developments in micro null-point potentiometry; techniques for the accurate weighing of small liquid samples. A number of microchemical procedures which have been developed for the analysis of a variety of materials are also included.

Key Words: Chemical analysis, coulometry, gas analysis, microchemical analysis, potentiometry.

Organic Chemistry; Air pollution studies characterization of chemical structures; synthesis of research materials; novel research materials; isotopic methods for analysis of carbohydrates; occurrence, preparation, and properties of naturally occurring monosaccharides (including 6-deoxy sugars); standard reference materials (organic) July 1966 through June 1967, Ed. R. Schaffer, *Tech. Note 427 (Oct. 1967), 45 cents.*
This report describes work in progress in the Organic Chemistry Section of the Analytical Chemistry Division of the NBS Institute for Materials Research. The following research areas are discussed:
Air Pollution Studies. Information has been obtained on the detection of impurities in, and the purification of, commercial samples of certain polycyclic, aromatic hydrocarbons that are known to occur in polluted air. The oxidation of these hydrocarbons under conditions resembling those encountered in polluted areas has been studied, and some of the products have been identified.
Characterization of Chemical Structures. The infrared absorption spectra of a group of 2-*oxo*-1,3-*bis*(phenylhydrazono) derivatives have been studied, and compared with the spectra of four tris(phenylhydrazones) and six related mono- and bis-(phenylhydrazono) derivatives, in order to identify the important features of the bands arising from N = N, N-H (bending), and Ph-N groups. In addition, the phenylhydrazono–phenylazo tautomerism of 2-*oxo*-1,3-*bis*(phenylhydrazono) compounds has been elucidated. A novel aromatization of inositols in methyl sulfoxide–acetic anhydride has been discovered.
Synthesis of Research Materials: A Disaccharide of D-*Lyxofuranose.* A compound formed in the high-vacuum distillation of 2,3-*O*-isopropylidene-α-D-lyxofurnanose has been obtained crystalline by acetylation, crystallization of the diacetate, and saponification of the latter. From the results of oxidation, reduction, hydrolysis, and nuclear magnetic resonance studies, the compound is believed to be the di-*O*-isopropylidene acetal of 5-*O*-α-D-lyxofurnanosyl-α-D-lyxofurnose. This is the first known example of a thermal condensation providing a reducing disaccharide in which both sugar moieties are furanoid.
Novel Research Materials. The reaction of sulfonic esters of alditols with methoxide has been examined, and a new dianhydrohexitol has been isolated. The literature on the infrared spectroscopy of carbohydrates has been critically evaluated and systematized.
Isotopic Methods for Analysis of Carbohydrates. The various methods of isotope-dilution analysis, the isotope effects that may accompany studies with labeled molecules, and the methods for determining isotopic distribution have been assessed and assembled.
Occurrence, Preparation, and Properties of Naturally Occurring Monosaccharides, Including 6-Deoxy Sugars. A survey has been made of all of the monosaccharides and 6-deoxy sugars that are known to occur naturally, and their preparation has been reviewed In addition, their chemical and physical properties have been collated.
Standard Reference Materials. The preparation of highly pure samples of quebrachital, *levo*-inositol, 1,2-*O*-isopropylidene-β-L-idofuranose, and 2,3-*O*-isopropylidene-β-D-*threo*-pentulofuranose has been achieved, and the compounds have been characterized by melting point, specific optical rotation, and infrared absorption spectrum. These compounds are now available to the public as standard reference materials.
In order to describe experimental procedures adequately, it has occasionally been necessary to identify commercial materials and equipment in this report. In no case does such identification imply recommendation or endorsement by the National Bureau of Standards, nor does it imply that the material or equipment identified is necessarily the best available for the purpose.

Key Words: Air pollution studies, oxidation of polycyclic aromatic hydrocarbons, characterization of chemical structures, phenylhydrazono–phenylazo tautomerism, disaccharide of D-lyxofuranose, infrared absorption methods for analysis of carbohydrates, naturally occurring monosaccharides and 6-deoxy sugars, standard reference materials, quebrachitol, *levo*-inositol, 1,2-*O*-isopropylidene-β-L-idofuranose, 2,3-*O*-isopropylidene-β-D-*threo*-pentulofuranose.

Photonuclear data index, January 1965 through April 1967, *Misc. Publ. 277, Suppl. 1,* T. M. Collins, E. G. Fuller, J. D. Murphy, and J. S. O'Connel *(Oct. 1967), 45 cents.*
This index, a supplement to NBS Miscellaneous Publication 277, primarily covers data published in the period dated January 1, 1965 through the middle of April 1967. Organized by element and isotope, each entry in the index supplies quantitative information for a specific reaction on the ranges of excitation energy, source energy, detected particle energy, and emission angles for reaction produced covered in each reference. Information is also given on the type of measurement and detector used.

Key Words: Bibliography, data index, elements, isotopes, nuclear physics, photonuclear reactions.

Radiometric methods for measuring laser output, D. A. McSparron, C. A. Douglas, and H. L. Badger, *Tech. Note 418 (Nov. 1967), 15 cents.*
The output of pulsed lasers may be measured with reasonable accuracy by modifications of established radiometric methods. The receiver, thermopile or phototube, is used ballistically. It is calibrated by an incandescent-lamp standard of spectral irradiance. The laser beam is attenuated to make its irradiation on the receiver comparable to that from the calibrating source. Attenuation is accomplished by intercepting the entire laser beam on a diffusely reflecting surface. The attenuation factor is determined from direct measurement of the reflectance of this diffusing surface and the geometric constants of the system. The accuracy of the measurement of laser output is dependent upon the accuracy of calibration of the standard of spectral irradiance and the accuracy with which the spectral sensitivity of the receiver, the spectral transmittance of the band-pass filters, and the reflectance of the diffuser can be determined. Measurements made with different photoelectric receivers agree to about 1.5% using a ¼-joule pulsed ruby laser as a source. Total uncertainty is estimated to be about 5%. Measurements made using these radiometric methods have been compared with calorimetric measurements and a discrepancy of 9% was observed.

Key Words: Laser, radiometry, laser energy measurement, radiometric calibration, photoelectric photometry, optical attenuator.

Tables of molecular vibrational frequencies Part 2, T. Shimanouchi, *NSRDS–NBS 11 (Oct. 1967), 30 cents.*
A compilation of vibrational frequency data for selected molecules is being conducted at the University of Tokyo in cooperation with the National Standard Reference Data Program of the National Bureau of Standards as a part of an international effort to compile and evaluate physical and chemical data. This report, as a continuation of Part I published as NSRDS–NBS–6, contains fundamental vibrational frequencies of 54 molecules together with vibrational assignments, sources of data, brief comments, and citations of references. The procedures used for the preparation of tables are the same as given in Part I. The fundamental frequencies are obtained mainly from the infrared and Raman spectra. When these are not available, other experimental data such as microwave results are taken into account. The selection of vibrational fundamentals from observed data is based upon careful studies of the spectral data and comprehensive mathematical analyses. These tables were designed to provide a concise summary needed for the computation of ideal gas thermodynamic properties. They may also provide a convenient source of information to those who require vibrational energy levels and related properties in molecular spectroscopy, analytical chemistry, and other fields of physics and chemistry.

Key Words: Data, force constants, infrared spectra, modes of vibration, molecular vibrational frequencies, molecular spectra, Raman spectra.

X-ray wavelengths and x-ray atomic energy levels, J. A. Bearden, *NSRDS–NBS 14 (Sept. 25, 1967), 40 cents.*
Inconsistencies in accepted values (in x units) of x-ray reference lines have recently been demonstrated, although all are supposedly based on "good" calcite crystals. Factors supporting the selection of the W $K\alpha_1$ line as *the X-Ray Wavelength Standard* are critically discussed. A review is given of the experimental measurements which are used to establish the wavelength of this line on an absolute angstrom basis. Its value is λ W $K\alpha_1 = (0.2090100 \pm 5$ ppm) Å. This may be used to define a new unit, denoted by Å*, such that the W $K\alpha_1$ wavelength is exactly 0.2090100 Å*; hence $1\text{Å}^* = 1\text{Å} \pm 5$ ppm. The wavelengths of the Ag $K\alpha_1$, Mo $K\alpha_1$, Cu $K\alpha_1$, and the Cr $K\alpha_2$ have been established as secondary standards with probable error of approximately one part per million. Sixty-one additional x-ray lines have been used as reference values in a comprehensive review and reevaluation of more than 2700 emission and absorption wavelengths. The recommended wavelength values are listed in Å* units together with probable errors; corresponding energies are given in keV. A second table lists the wavelengths in numerical order, and likewise includes their energies in keV.

Key Words: Crystallographic dimension, x-ray atomic energy levels, x-ray wavelength, x-ray wavelength standards.

Aromatic fluorocarbon polymers, W. J. Pummer and J. M. Antonucci *(Proc. 152d American Chemical Society Meeting, New York, N.Y., Sept. 13, 1966), Polymer Preprint 7, No. 2, 1071–1076 (Sept. 1966).*
Recent synthetic work has led to the preparation of a variety of fluoroaryl polymers. Most of the polymers synthesized are similar in structure to the hydrocarbon analogs except for the fluorine atoms. On this basis, the fluorinated polymers, presented in this paper, will be classified and discussed according to structural features. The first class of polymers contains the polyperfluorophenylenes which will include both the para and meta linked polymers. In the second class, the polymers contain an atom or group of atoms between the fluorinated rings, such as oxygen, sulfur and oxydifluoromethylene groups. Some polymers in this category are the polyperfluorophenylene ethers and sulfides. The final group of polymers contains a pendant pentafluorophenyl ring attached to the main polymer chain such as the various fluorinated styrenes and vinyl ethers.
In all cases, the method of polymerization, physical properties and thermal stability of the polymers will be discussed and whenever possible, comparisons will be made between the fluorinated and hydrocarbon polymers.

Key Words: Fluorinated styrenes; fluoroaryl polymers; para, meta linked polymers; pendant pentafluorophenyl ring; polyperfluorophenylenes; polyperfluorophenylene ethers, sulfides; vinyl ethers.

Calculation of currents of local galvanic cells, J. A. Simmons, S. R. Coriell, and F. Ogburn, *J. Electrochem. Soc.* **114,** *No. 8, 782–787 (Aug. 1967).*
The current flow for a local electrolyte cell with rectangular anode and cathode is calculated as a function of polarization parameter, electrolyte thickness and conductivity, anode and cathode size, and zero current potential difference. The total current is obtained from the numerical computation (with error analysis) of a series solution of Laplace's equation assuming a linear polarization relation at the electrode-electrolyte interface. For high values of the polarization parameter and sufficiently thick electrolytes an asymptotic formula obtains for the current approximately proportional to the anodic fraction—as was found by Waber et al. However, in general the cell geometry greatly influences the amount of current flow, especially for anode shapes near to linear rather than square. This effect can be greater than an order of magnitude. The calculated results are compared with experimental data obtained by Ogburn and Schlissel and are shown to be in good agreement. Corrosion currents in randomly pitted surfaces may be estimated from the above results.

Key Words: Corrosion currents, galvanic cells, galvanic currents, Laplace's equation, pitting corrosion.

Conformation of polystyrene adsorbed on liquid mercury, R. R. Stromberg and L. E. Smith, *J. Phys. Chem.* **71,** *No. 8, 2470–2474 (July 1967).*

Measurement of the extension of polystyrene adsorbed on liquid mercury from cyclohexane near the theta temperature indicate that the molecule is attached at a relatively large number of sites and that the conformation remains constant during most of the adsorption period. In addition, the extension is approximately independent of molecular weight for the range studied (537,000 to 3,300,000). These results are in contrast to previous measurements on polycrystalline metallic surfaces. The behavior may be attributed in part to the large value of the contribution of the London dispersion forces to the surface free energy of mercury as compared to other metals. Other possibilities are also discussed.

Key Words: Polymer adsorption, ellipsometry, adsorption of polymers, mercury, polystyrene, adsorption, conformation of adsorbed polymers.

Determination of bound styrene in insoluble emulsion polymerised styrene-butadiene copolymers, M. A. Post, *J. Appl. Chem.* **17,** *203–208 (July 1967).*
Bound styrene is determined in insoluble emulsion polymerized styrene-butadiene copolymers by measurement of the 10.3 μm/13.2 μm absorbance ratio using the baseline method. This ratio is obtained from the infrared spectrogram of the copolymer and the percent styrene is determined from a standard curve. The standard curve is constructed from absorbance ratios of 10.3 μm/13.2 μm derived from the infrared spectrograms of cast films of styrene-butadiene latexes over a range of percentage compositions. Bound styrene is determined in these latexes by nitration of the isolated and extracted copolymers. Styrene content based on nitration is determined from standard curves relating styrene concentration to spectrophotometric absorbance measurements at wavelengths of 285.0 nm, 273.8 nm and 265.0 nm. The source of the styrene for these curves is NBS standard rubber #1500.

Key Words: Absorbance ratio method, bound styrene, infrared, insoluble styrene-butadiene copolymers, masonry paints.

Effects of impurities on the production of oxygen atoms by a microwave discharge, R. L. Brown, *J. Phys. Chem.* **71,** *No. 8, 2492–2495 (1967).*
The catalytic effects of impurities on the production of O-atoms in microwave discharges have been studied in a flow system by measuring with EPR methods the concentrations of $O_2(^3\Sigma_g^-)$, $O_2(^1\Delta_g)$, O, and H-atoms as a function of the amounts of H_2O, D_2O and N_2 added to the O_2 upstream from the discharge. The effects of varying the microwave power to the discharge, the O_2 flow rate, and the total pressure were also examined.

Key Words: Atomic oxygen, microwave discharges, kinetic EPR spectroscopy, catalysis, reactions of oxygen atoms, flow system reactions.

Electrical conductivity of high purity copper, J. J. Gniewek, J. C. Moulder, and R. H. Kropschot, *Proc. LT-10 Conf., Moscow, USSR, Aug. 31–Sept. 9, 1966.*
The low temperature electrical conductivity of copper single crystals ($R_{273}/R_4 > 30{,}000$) and polycrystalline wire ($R_{273}/R_4 > 10{,}000$) has been measured between 4 °K and 77 °K.
Between 14 and 30 °K the resistance is proportional to T^n where $n = 4.8 \pm 0.1$. Size effects are observed using both eddy current and direct current techniques in samples as large as 2 mm in diameter. Assuming diffuse reflection of the electrons from the surface, direct current size effect measurements give a $\rho_b l_b = 0.53 \times 10^{-11}$ Ωcm^2 which is less than the free electron value of 0.66×10^{-11} Ωcm^2.

Key Words: Copper, electrical conductivity, low temperature, size effect.

Epitaxial growth of iron on tungsten field emission points, A. J. Melmed, *Surface Sci.* **7,** *No. 3, 478–481 (July 1967).*
Iron crystals can be grown from the vapor phase on tungsten field emission points. The crystals tend to nucleate at edges of W (011) planes and grow in the same orientation as the substrate, sometimes with an apparent small parallel displacement. Interdiffusion of W into the growing Fe crystals can occur and evidence for this is presented.

Key Words: Epitaxy, field emission microscopy, crystal growth, vapor deposition, Fe-W alloying.

Growth of large sodium chloride crystals from solution for color center studies, P. M. Gruzensky, *J. Chem. Phys.* **43,** *No. 11, 3807 (Dec. 1, 1965).*
Sodium chloride single crystals with edge dimensions as large as 2.5 cm were grown from aqueous solutions. Solutions were purified by chemical precipitation of trace contaminants and filtration through membrane filters. Crystal defects were apparent in the initial stages of growth, but the outer portions of crystals were free of dislocations. F-band coloration by x rays at room temperature was not linear and the "first stage" was either absent or nearly so. Transition from extrinsic to intrinsic dc conductivity occurred at 350 °C with the extrinsic conductivity two orders of magnitude lower than the "pure" melt-grown crystals.

Key Words: alkali halides, aqueous, color centers, chloride, conductivity, crystal growth, and sodium.

Helium field-ion microscopy of hexagonal close-packed metals, A. J. Melmed, *(Proc. Symp. The Structure of Surfaces, Durham, N.C., Nov. 1966), Surface Sci.* **8,** *No. 12, 191–205 (July–Aug. 1967).*
The atomic structure of curved hexagonal close-packed metal surfaces is complicated compared to curved surfaces of body-centered cubic metals. He field-ion microscopy of Ru and Re field-evaporated surfaces discloses apparent differences in the surface structures developed under similar experimental conditions. The effect of temperature and field strength on the structure developed by field-evaporation is analyzed, and the structures of the (100) and (001) plane regions in particular are discussed in relation to their respective field-ion images.

Key Words: Field-ion microscopy, field evaporation, surface structure and hexagonal close-packed metals.

High pressure adsorption isotherms of neon, hydrogen, and helium at 76 °K, A. J. Kidnay and M. J. Hiza, *(Proc. 1966 Conf., Boulder, Colo., June 13–15, 1966), Book, Advances in Cryogenic Engineering* **12,** *730–740 (Plenum Press Inc., New York, N.Y., 1967).*
A desorption technique was used to measure the physical adsorption isotherms of hydrogen and helium on a synthetic zeolite and of hydrogen, helium, and neon on an activated cocoanut shell charcoal at 76 °K in the pressure range of 1 to 95 atmospheres.
The Polanyi adsorption potential theory, as modified by Dubinin, was used in an attempt to obtain a general correlation of these isotherms. The results, while not completely general, should allow the prediction of the high pressure isotherms of neon, hydrogen, and helium at any temperature with an accuracy sufficient for most engineering calculations.

Key Words: Adsorption potential, charcoal, helium, highpressure physical adsorption, hydrogen, low temperature, neon, zeolite.

History of the National Standard of electromotive force, W. J. Hamer, *(Proc. 22d ISA Conf. and Exhibit, Chicago, Ill., Sept. 11–14, 1967), ISA Preprint No. M2-1-MESTIND-67, pp. 1–10 (1967).*
The history of the National Standard of electromotive force is traced from the meeting of the International Electrical Congress in Chicago in 1893 to the present time. Included are discussions of the transfer of the "volt standard" from its old location in Washington, D.C. to its new location near Gaithersburg, Maryland, of the stability of standard cells, of the application of Gibb's Phase Rule to standard cells, and the relation between the legal and absolute volts.

Key Words: Volt standards, legal volt, absolute volt, Gibb's phase rule, history of volt.

Identation hardness of the fingernail, S. B. Newman and R. W. Young, *J. Invest. Dermatol.* **49,** *No. 1, 103–105 (Mar. 17, 1967).*
Indentation hardness using the Knoop indenter has been used as a quantitative criterion in physiological studies of the human nail plate. Data were collected and are presented to show that values reported in the literature are in serious error. A number of parameters affecting Knoop numbers are examined in an effort to determine the source of error.

Key Words: Fingernail, Knoop indenter, hardness.

Insertion of methylene into alkanes, M. L. Halberstadt and J. R. McNesby, *J. Am. Chem. Soc.* **89,** *No. 14, 3417–3420 (1967).* Ketene was photolyzed in the presence of mixtures of pairs of hydrocarbons with NO added to scavenge alkyl radicals. The relative rates of insertion for methane: primary propane: secondary propane are 0.43:1.0:0.43 and for ethane: primary n-butane: secondary n-butane they are 1.0:1.0:0.88. In the case of isobutane, the relative rates of insertion into primary and tertiary bonds are 1.0:0.13. When effects of recombination of alkyl radicals formed by abstraction of H by CH_3 are eliminated by the NO scavenger, insertion is seen to be essentially indiscriminate. It is suggested that the singlet CH_2 lies not more than about 2.5 kcal above the ground state triplet.

Key Words: Methylene, insertion, ketene, methane, propane, *n*-butane, *i*-butane, photolysis.

Liquid-vapor equilibrium in the system helium-methane, C. K. Heck and M. J. Hiza, *AIChE. J.* **13,** *No. 3, 593–599 (May 1967).* Liquid and gas phase compositions for the system helium-methane have been measured at 15° intervals from 95 to 185 °K up to 200 atmospheres pressure. Data for these seven isotherms were taken in a gas phase recirculation apparatus using chromatographic analysis. In most regions the phase compositions obtained are thought to be within ±3% of the mole fraction of the minor component. The maximum deviation from the enhancement factor curve at the lowest concentration levels was 16%. These data are in excellent agreement with most of the very recent data but are in poor agreement with the older data for this system.

Key Words: Helium, helium-methane binary system, liquid-vapor equilibrium, low-temperature phase-equilibrium, methane, solubility of helium in liquid methane.

Polymerization of fluoroolefins and related monomers, L. A. Wall (*Proc. 152d American Chemical Society Meeting, New York, N.Y., Sept. 13, 1966), Polymer Preprint 7, No. 2, 1112–1115 (Sept. 1966).*
Although some fluorine-containing monomers polymerize readily, there are many which have not as yet been polymerized either by free radical or ionic catalysts. In order to investigate the reasons for the somewhat general tendency of these monomers to resist polymerization, we have initiated a systematic study using high pressures and γ-rays to induce polymer formation.
The technique has been successful for many fluoro monomers, fluoropropylenes, fluorodienes, perfluorostyrene and some fluorovinyl phenyl ethers. In a general way, the results suggest in many cases that slow propagation steps, easy transfer processes with monomer or impurities, and in some cases a tendency to thermally dimerize, interfer with the formation of high polymer.

Key Words: Fluorine-containing monomers, fluorodienes, fluoro monomers, fluoropropylenes, fluorovinyl, free radical, gamma-rays, high pressures, ionic catalysts, perfluorostyrene, phenyl ethers.

The system $Y_2O_3-V_2O_5$, E. M. Levin, *J. Am. Ceram. Soc.* **50,** *No. 7, 381–382 (July 1967).*
The phase diagram of the system $Y_2O_3-V_2O_5$ has been determined experimentally, by the "quenching" method. The subsystem $YVO_4-V_2O_5$ is a simple eutectic one, with a solidus temperature of 672±3 °C. Yttrium vanadate, of industrial importance, melts congruently at 1810±25 °C. The subsystem $YVO_4-Y_2O_3$ is probably pseudobinary because of oxygen losses from the phases of composition $4Y_2O_3:V_2O_5$ and $5Y_2O_3:V_2O_5$. The composition $4Y_2O_3:V_2O_5$ exists in at least three different phases.

Key Words: Phase diagram, V_2O_5, Y_2O_3, yttrium vanadate.

The thermal decomposition of poly-3,3,3-tri-fluoropropene made at high pressure, S. Straus and D. W. Brown (*Proc. 152nd American Chemical Society Meeting, New York, N.Y., Sept. 13, 1966), Polymer Preprint 7, No. 2, 1128–1132 (Sept. 1966).*
Poly-3,3,3-trifluoropropene prepared by irradiating the monomer at various temperatures and pressure has been pyrolyzed in vacuo in the temperature range 397–342 °C. At 402 °C the pyrolysis rates at 20% volatilization vary by a factor of 20 depending on the polymerization conditions. The rate of volatilization decreases smoothly with the fraction volatilized except with the most stable polymer, with which the rate is constant over a considerable portion of the pyrolysis. Molecular weight drops are extremely rapid and the monomer yield is only about 0.3%. Dimer and trimer are thought to be formed in yields of 5 and 15%, respectively. The overall behavior probably results from a mechanism with a large random component but with an initiation rate that depends on the polymerization conditions and extent of pyrolysis.

Key Words: High pressure; initiation rate; poly-3,3,3-trifluoropene; pyrolysis; random component; thermal decomposition; volatilization.

The unperturbed dimension temperature coefficients of some fluorine-containing polymers, H. Yu (*Proc. 152nd American Chemical Society Meeting, New York, N.Y., Sept. 13, 1966), Polymer Preprint 7, No. 2, 1143–1145 (Sept. 1966).*
Thermoelastic measurements on amorphous networks of some fluorine-containing polymers were performed. The corresponding unperturbed dimension temperature coefficients were found to be positive and of the order of 10^{-3} deg^{-1}. The variation of the energy component of tensile stress with the extension ratio was negligibly small for the range of α investigated, whereas the tensile force was linearly proportional to the extension parameter $(\alpha-\alpha^{-2})$. It appears that the effect of fluorine-containing substituents on the hydrocarbon chain backbone can be appreciable in the conformation of the polymer chains.

Key Words: Energy component; fluorine-containing polymers; hydrocarbon chain backbone; unperturbed dimension temperature coefficients; variation.

Microwave standards and measurements in the USA, R. W. Beatty (*Proc. XV General Assembly of URSI, Munich, Germany, Sept. 5–15, 1966), Book, Progress in Radio Science 1963–1966, Part 1, pp. 194–260 (International Scientific Radio Union, Munich, Germany, 1966).*
A report is given on progress within the U.S.A. in the development of radio standards and measurement methods at frequencies from 1 to 300 GHz (GHz = 10^9 cycles per second). The period covered is the three years 1963–1966. The following topics are included within the scope of this report: power; noise; reflection coefficient and impedance; phase shift; attenuation and loss; and field strength and antenna gain.

Key Words: Antenna gain, attenuation, field strength, impedance, measurement, microwave, noise, phase shift, power, progress, reflection coefficient, review, standards, survey.

Proposed recommended practice for description and selection of conditions for photographing specimens, C. S. McCamy, *Photo. Sci. Eng.* **10,** *No. 4, 185–191 (July–Aug. 1966).*
A "Proposed Recommended Practice for Description and Selection of Conditions for Photographing Specimens" has been prepared for the American Society for Testing and Materials so that the photographic method of recording appearance can be made more reproducible from one laboratory to another, for various specimens, and for a given specimen at different times. The proposal defines terms and symbols and provides a systematic method of describing the arrangement of lights, camera, and subject; the characteristics of the illumination; the nature of the photographic process, and the viewing system. Conditions for photographing certain common forms of specimens are recommended. Conventions for exhibiting and publishing photographs of specimens include an orientation mark and a coordinate system for pictures.

Key Words: Specimen photography, camera description, lighting description, appearance.

Protection circuit insulated for high voltage, E. Niesen, *Rev. Sci. Instr.* **38,** *No. 5, 689 (May 1967).*
A circuit using standard components for floating an optical meter relay at high voltage is presented. By plugging in available optical meter relays, sensitivities in microamperes to amperes, millivolts to kilovolts can be controlled for a high or low limit.

Key Words: High voltage insulation, optical meter relay, protection circuit.

Size and power requirements of 4.2 °K refrigerators, T. R. Strowbridge and D. E. Chelton (*Proc. 1966 Conf., Cryogenic Engi-*

neering, Boulder, Colo., June 13–15, 1966), Book, Advances in Cryogenic Engineering **12,** *576–584 (Plenum Press Inc., New York, N.Y., 1967).*
A survey to determine the physical characteristics of 4.2 °K cyclic refrigerators is presented. Although the data acquired through the survey show considerable scatter, the expected trends can be detected and attempts have been to establish guides by which the weight, volume, and power requirements for various capacity refrigerators may be estimated. No attempt is made to assess the reliability, the interval of maintenance free operation, or the capital costs.

Key Words: Cyclic refrigerators, power, volume, weight.

Slush hydrogen characteristics, D. B. Mann, C. F. Sindt, P. R. Ludtke, and D. B. Chelton, *Proc. Conf. Long-Term Cryo-Propellant Storage in Space, National Aeronautics and Space Administration, Huntsville, Ala., Oct. 12–13, 1966.*
The utilization of slush hydrogen as an upgraded fuel is dependent upon knowledge of its physical and transport properties and characteristics. A NASA-sponsored program designed to acquire this information is in progress.
Experimental measurements of solid particle size distribution, aging effects and terminal velocities of the solid particles in the liquid melt have been completed. Transport characteristics have been predicted using these measured parameters. These predictions are currently being submitted to experimental verification.
Two 100 gallon dewars connected by 75 feet of vacuum-insulated transfer line comprise the experimental flow loop. Pressure sensing transducers and visual observation through glass ports allow acquisition of transport data over a broad range of flow rates.
Handling and investigative techniques such as a dewar-to-dewar transfer, straining of the solids through wire mesh screen, and vertical temperature profiles of the settled mixture are presented in the context of a continuing experimental and analytical research program.

Key Words: Cryogenic, fluid transport, freezing, hydrogen-liquid solid, production.

Aggregation in matrix models of resource flows. II. Boolean relation matrix methods, D. R. Rosenblatt, *Am. Stat.* **21,** *No. 3, 32–37 (June 1967).*
A Boolean relation matrix approach is taken to issues of aggregation in matrix models of resource flows involving substochastic matrices A, B. The following results are shown: (i) an aggregation matrix is many-one and onto: (ii) If B is a consolidation of A with weight matrix regular, then if A is indecomposable (primitive), B is indecomposable (primitive): but, if the weight matrix is singular the preceding conclusions fail; if B is a consolidation of A. $(I-B)^{-1}$ exists if, and only if, for every indecomposable stochastic submatrix A_k of A, the image under the consolidation of every row index of A_k is connected in the associated graph of B to the image of a 'nonstochastic row' index of A.

Key Words: Mathematical logic; relation calculus; DeMorgan-Peirce-Schroder relation algebra; Boolean matrices; mathematical economics; statistical economics; input-output models; Markov chains; aggregation; consolidation; indecomposability; primitivity & Automata Theory.

Current distribution and impedance of lossless conductor systems, R. L. Brooke and J. E. Cruz, *IEEE Trans. Microwave Theory Tech.* **MTT-15,** *No. 6, 358–364 (June 1967).*
A general method for determining the characteristic impedance of lossless, uniform, go and return systems is developed. The current distribution within the system is determined by means of a matrix equation programmed for computer solution. Knowing the current distribution, the inductance per unit length and characteristic impedance are obtained. The results obtained by applying this method to several rectangular coaxial systems are compared with the predictions of an approximate analytic expression. The reflection coefficient of a variable characteristic impedance coaxial line is measured on a "Time Domain Reflectometer" (TDR) and the results are compared with both the matrix method and the approximate analytic expression.

Key Words: Characteristic impedance, current distribution, general method, matrix solution, rectangular transmission line, time-domain reflectometer, variable impedance.

A systems concept of electromagnetic measurements in the U.S.A., G. E. Schafer, *Proc. IEEE* **55,** *No. 6, 775–778 (June 1967).*
A brief description of a systems concept of the National Measurement System proposed by Dr. R. D. Huntoon, Director, Institute for Basic Standards, is given first. Activities of the Radio Standards Laboratory as a functional element of this system are then described. Some benefits of looking at RSL as an element of this system are given.

Key Words: National Measurement System, radio standards, electromagnetic measurement.

Liquid hydrogen engineering instrumentation, T. M. Flynn *(Proc. Intern. Inst. Refrigeration, June 9–11, 1965), Book, Liquid Hydrogen, pp. 295–338 (Paris, France, 1965).*
Prudent liquid hydrogen engineering requires the measurement of both extensive and intensive properties of the cryogenic liquid. Transducers are required for liquid level (quantity), both point and continuous systems, and mass rate systems. In addition, there must be transducers of pressure, temperature, density, and occasionally, quality. This paper discusses some of the devices and practices currently used for the measurement of pressure, temperature, flow rate, and liquid level in liquid hydrogen systems.

Key Words: Flow rate, liquid hydrogen, liquid level, measurement of pressure.

Progress in the distribution of standard time and frequency, 1963 through 1965, J. M. Richardson *(Proc. XV General Assembly of URSI, Munich, Germany, Sept. 5–15, 1966), Book, Progress in Radio Science 1963–1966, Part 1, pp. 40–62 (International Scientific Radio Union, Munich, Germany, 1966).*
Progress in accurate long distance distribution of standard time and frequency, as reported in the literature from 1963 through 1965, is summarized. Techniques are by VLF, LF, and HF radio propagation, by satellite relay, and by portable clocks. Effects on standard frequency transmissions of variations in VLF propagation with geophysical phenomena are quantitatively understood. VLF and LF transmissions have provided careful, long-term, statistical comparison of remotely located atomic frequency standards. Precision of at least 2 parts in 10^{11} for a 24-hour observation period is possible at 5000 km. The phase of some standard frequency transmitters is routinely steered by VLF from distances up to 5300 km. Global distribution of standard time by VLF to microsecond resolution has been shown feasible. The null beat between two neighboring VLF carriers propagates stably enough to mark a particular VLF cycle, and the beat period can be long enough to enable ordinary time signals to mark a particular null beat. Intercontinental time synchronization by microwave pulses has been accomplished via Telstar and Relay II satellites. Accuracy is observed to be several microseconds. Portable cesium clocks have served as global transfer standards with degradation of timing accuracy of only about a microsecond per trip. Results by all the above methods are consistent with each other and with stated accuracies of atomic standards involved.

Key Words: Time, frequency, time signals, standard frequency broadcasts, VLF propagation, portable clocks.

Progress in the U.S. on electromagnetic standards and measurements at 30 kHz to 1 GHz, 1963 through 1965, M. C. Selby, *IEEE Trans. Instr. Meas.* **IM-16,** *No. 2, 172–178 (June 1967).*
A digest of highlights is presented on the most significant U.S. contributions to the measurement of attenuation, impedance, voltage, current, field strength, thermal noise, and phase at 30 kHz to 1 GHz. A total of approximately 30 contributions are digested in this section of the report. The following accomplishments are among them: a supersensitive detector for a complex-insertion-ratio measurement system having accuracies of about 0.0005 dB/10 dB at 30 MHz; exact equations for mutual and self-inductance of various combinations of filaments, tapes, and bars; a modified Twin-T-Bridge for measuring resistances of 100 to 10,000 ohms to 15 MHz; a set of Q-factor standards for frequencies to 45 MHz based on accumulated data and experience over 5 years; a unique adjustable characteristic-impedance coaxial line; measurement of Q's greater than 100,000 of cryogenic circuits at frequencies to 300 MHz; a novel Tee-junction to enable calibrations of voltmeters of

any practicable input impedances with VSWR's ranging from 1 to 200, to 1 GHz and higher; a miniaturized dipole-antenna field strength meter, employing a semiconducting plastic transmission line, to measure complex near-zone fields of 0.1 to 1000 volts per meter, from 150 kHz to 30 MHz; a prototype 3-MHz model of precision thermal noise-power comparators for an equivalent noise-temperature range of 75 to 30,000 °K at accuracies of 0.2 to 1%.

Key Words: High frequency measurements, progress in radio measurements, attenuation measurements, impedance measurements, voltage measurements, field strength measurements, thermal noise measurements, phase measurements.

The conference on precision electromagnetic measurements, H. M. Altschuler, *Proc. IEEE* **55,** *No. 6, 782 (June 1967).*
The character of the biennial Conference on Precision Electromagnetic Measurements (CPEM) is described. The scope of the Conference is compared with that of the special issue of the Proceedings of the IEEE on Measurements. Some of CPEM's history is recounted and its increasing international coverage is noted. It is concluded that the challenge to CPEM grows with the expansion of the fields it covers.

Key Words: Conference, precision measurements, measurements, electromagnetic measurements, Conference on Precision Electromagnetic Measurements.

The nature of measurement, A. G. McNish, *Book, Handbook of Industrial Metrology, Chapt. 1, pp. 2–12 (Prentice-Hall, Inc., Englewood Cliffs, N.J., 1967).*
General principles for measurement. Accuracy and precision are discussed.

Key Words: Accuracy, measurement, precision.

U.S.A. National Committee Report, Fifteenth URSI General Assembly, Munich, September 1966: Commission 1, Radio Measurement Methods and Standards, Progress in Radio Measurement Methods and Standards, J. M. Richardson, Editor, *Radio Science* **1,** *No. 11, 1333–1342 (Nov. 1966).*
Progress in radio measurement methods and standards within the United States during the Triennium 1963 through 1965 is reviewed for inclusion in the report of the U.S. National Committee of URSI to the 1966 General Assembly. Topics surveyed are high precision atomic frequency standards, high precision quartz frequency standards, scientific aspects of Universal and/or Atomic time and frequency transmissions, standards and measurements at 30 kc/s to 1 Gc/s, standards and measurements at 1 to 300 Gc/s, precision coaxial connectors, swept-frequency techniques, measurements of electromagnetic properties of materials, and laser standards and measurements. The topics are treated within the length limitation imposed by USNC/URSI.

Key Words: Radio measurement standards, Radio measurement methods, frequency standards, time standards, electromagnetic properties of materials, coaxial connectors, microwaves, lasers.

Dissociative ionization of H_2 and D_2, L. J. Kieffer and G. H. Dunn, *Phys. Rev.* **158,** *No. 1, 61–65 (June 5, 1967).*
Energy distributions of $H^+(D^+)$ from dissociative ionization of $H_2(D_2)$ are reported. Evidence of the $2p\sigma u$ states being the major source of energetic ions is presented. Calculated and measured energy distributions do not agree well. Possible explanations are suggested.

Key Words: Dissociative ionization, H_2, D_2, Franck-Condon principle, energy distributions.

Laser measurements of long distances, P. L. Bender, *Proc. IEEE* **55,** *No. 6, 1039–1045 (June 1967).*
The extension of radio frequency techniques to the optical region of the spectrum has made possible many types of measurements which were not feasible before. One area in which important scientific contributions can be expected during the next few years is the use of lasers to measure long distances with high accuracy. Three types of distance measurements which have been discussed in the literature and which are now being investigated actively are: a) interferometric measurements over distances of up to hundreds of meters through evacuated or sealed-off tubes; b) measurements with modulated laser beams over distances of perhaps one to fifty kilometers with corrections made for the atmospheric index of refraction along the path; and c) range measurements to artificial satellites and to the moon using laser radar. Some of the possible geophysical and geodetic applications of such measurements will also be discussed.

Key Words: Laser measurements, modulated laser beams, radio frequency techniques, range measurements, interferometric measurements.

Low temperature (295–4 K) mechanical properties of selected copper alloys, R. P. Reed and R. Mikesell, *J. Materials* **2,** *No. 2, 370–392 (June 1967).*
Fifteen copper alloys, including brasses, bronzes, and commercially pure coppers were tested to determine their tensile, notch tensile, Youngs modulus, and impact properties. Tests were performed at 295, 195, 76, 20, and 4 °K. It was found that copper alloys, in general, have improved room low temperature properties as compared to room temperature properties. The exception to this result is a cast Ni-Al bronze alloy, which is brittle at low temperatures. In 9 alloys the yield and tensile strengths at 4 °K were less than at 20 °K. A discussion of this strength reduction at low temperatures is presented.

Key Words: Mechanical properties, low temperatures, copper, copper alloys.

Non-linear diffusion with recombination in electron beam excited plasma, E. R. Mosberg, Jr., and M. S. Lojko, *Phys. Fluid Res. Notes* **9,** *No. 4, 824–826 (Apr. 1966).*
The non-linear diffusion equations for an isothermal plasma with a recombination term added are treated for the case of cylindrical geometry and no magnetic field. The radial electron density and light intensity distributions are given for various values of the ratio of the recombination loss rate to diffusion loss rate. The light intensities are computed on the basis of two-body and three-body recombination as well as the intermediate case of collisional-radiative recombination.

Key Words: Diffusion, radial distribution, recombination-electron ion, plasma.

Optical properties of germanium in the far ultraviolet, L. Marton and J. Toots, *Phys. Rev.* **160,** *No. 3, 602–606 (Aug. 15, 1967).*
Reflectance measurements for in-situ-evaporated Ge films are reported for 16 wavelengths between 490 and 1610 Å, corresponding to photon energies of 25.2 and 7.7 eV. Measurements were taken after 3 minute exposures to ambient pressures of 5×10^{-7} Torr. Reflectance values at a number of angles of incidence were used to compute the optical constants: the refraction index n, the extinction coefficient k, the real and imaginary parts of the frequency-dependent dielectric constant $\epsilon(\omega)=\epsilon_1+i\epsilon_2$. Values for the characteristic electron energy loss functions, for $-\mathrm{Im}\ 1/\epsilon$ the volume loss and for $-\mathrm{Im}\ 1/(\epsilon+1)$ the surface loss, are also presented. $-\mathrm{Im}\ 1/\epsilon$ peaked at 16.1 eV and had a half-width of 3.9 eV. Electron oscillator strengths, summed between 8 and 25 eV gave $\hbar\omega_p$ value of 13.7 eV. Some changes of optical characteristics caused by exposure to ambient pressures and air are presented.

Key Words: Characteristic electron energy loss, dielectric constant, far ultraviolet, germanium, optical constants, reflectance.

Positive and negative self-surface ionization of tungsten and rhenium, M. D. Scheer and J. Fine, *J. Chem. Phys.* **46,** *No. 10, 3998–4003 (May 15, 1967).*
The self-surface ionization of tungsten and rhenium has been investigated with a specially designed mass spectrometer. It has been found that both positive and negative singly charged atomic ions sublime from these metal surfaces in the 1900–2600 °K temperature range. The assumption that these processes can be described by a generalized Saha-Langmuir equation has been shown to be valid. The energies required for positive ion sublimation were found to be 12.1 ± 0.2 and 10.7 ± 0.1 eV for tungsten and rhenium, respectively. The negative ion sublimation energy for rhenium was determined as 12.6 ± 0.2 eV and that for tungsten is given by approximately the same value. At 2300 °K, the ratio of positive to negative

ions evaporating from these surfaces was found to be about 40 for tungsten and about 20,000 for rhenium. These results are consistent with the following estimates for the electron affinities: $A(W) = 0.5 \pm 0.3$ eV and $A(Re) = 0.3 \pm 0.2$ eV.

Key Words: Self-surface ionization, mass spectrometry, tungsten, rhenium, positive and negative atomic ions, ion sublimation energy, electron affinity.

Properties of liquid hydrogen, R. J. Corruccini, (*Proc. Intern. Inst. Refrigeration, June 9–11, 1965*), *Book, Liquid Hydrogen, pp. 65–106, (Paris, France, 1965).*
A review is presented of the physics of liquid hydrogen, and extensive extracts are provided of the available data on those of its physical properties that are important in technology.

Key Words: Cryogenic, hydrogen, liquid, low-temperature, properties.

Surface self-diffusion of nickel and platinum, A. J. Melmed, *J. Appl. Phys.* **38,** *No. 4, 1885–1892 (Mar. 1967).*
The surface rearrangement of nickel and platinum due to 1) an electric field (build-up), and (2) surface tension (annealing) as the net driving force, has been studied by field-electron emission microscopy over the temperature range 510–750 °K for Ni and 550–850 °K for Pt. An Arrhenius-type relationship between temperature and time was found in both cases, so that an activation energy could be associated with each process. It is assumed that this is an average activation energy for surface diffusion.
The results of the field build-up experiments gave an activation energy of $Q_f = 18.9 \pm 1.9$ kcal/mole for Ni over the negative field range $(28–38) \times 10^6$ V/cm, and $Q_f = 26.3 \pm 2.6$ kcal/mole for Pt over the negative field range $(27–39) \times 10^6$ V/cm. It was possible to measure the effect of the electric field using a method devised earlier by P. C. Bettler and F. M. Charbonnier. This gave calculated zero-field activation energies of 20.6 ± 2.1 kcal/mole for Ni and 29.8 ± 3.0 kcal/mole for Pt. The results of the annealing experiments (no electric field) gave an activation energy of $Q_0 = 21.4 \pm 2.1$ kcal/mole for Ni and 29.5 ± 3.0 kcal/mole for Pt. (The foregoing indicated uncertainties are estimated over all limits of errors.) It is concluded, from the good agreement between the results of the two different types of measurement, that both types of measurement (for Ni and Pt) determine the same quantity.

Key Words: Activation energy, field emission microscopy, nickel, platinum, surface diffusion, surface properties.

U.S. Department of Commerce and the flammability of clothing fabric, A. F. Robertson, *Bull, N.Y. Acad. Med. Second Series* **43,** *No. 8, 706–710 (Aug. 1967).*
The National Bureau of Standards has conducted studies of existing and modified test methods for measurement of flammable hazards associated with clothing fabrics. Recently, a cooperative program has been initiated with the Public Health Service to secure burn accident experience records which should yield information on the type of fabrics currently associated with clothing burn injuries. This program is just starting and it will be some years before valid information of the national picture becomes available. To date, however, there appears to be no technical evidence to show that a significant modification of the burn accident experience can be achieved without major changes in the flammable behavior of clothing fabrics. Thus, we hope industry will continue research on and development of permanently-retardant-treated fabrics which will be economically, esthetically, and usefully acceptable to the public. It appears, in spite of the lack of direct evidence, that such fabrics will significantly reduce, but not eliminate, clothing fire injuries.

Key Words: Clothing fire injuries, fabrics, permanently-retardant-treated fabrics.

Progress in measurement of electromagnetic properties of material, 1963 to mid-1966, H. E. Bussey, (*Proc. XV General Assembly of URSI, Munich, Germany, Sept. 5–15, 1966*) *Book, Progress in Radio Science 1963–1966, Part 1, pp. 265–289 (International Scientific Radio Union, Munich, Germany, 1966).*
Progress on radio and microwave measurements of dielectric and magnetic properties of materials is reviewed mainly for the period 1963 to mid-1966. Important materials properties, theoretical analysis of circuits containing materials, and representative measurement methods are reviewed. In addition, some earlier basic work is referenced.

Key Words: Review, permittivity, dielectric constant, permeability, ferromagnetic resonance, bibliography.

Excited species and their contribution to NO (β, γ) fluorescence in the photodissociation of N_2O, H. Okabe, *J. Chem. Phys.* **47,** *No. 1, 101–109 (July 1, 1967).*
The fluorescence yield of the NO β bands, originating from photodissociation of N_2O, was measured as a function of wavelength of incident light in the vacuum ultraviolet region. When NO was added to N_2O, the yield increased considerably and the emission changed from β to γ bands. A mechanism of fluorescence was derived from the correlation between the threshold energy at which a specific photochemical process was possible and that at which the fluorescence started to appear. A reaction responsible for the major NO β emission in the region 1150 to 1400 Å from N_2O most likely is the production of $N(^2P)$

$$N_2O \xrightarrow{h\nu} NO(X^2\Pi) + N(^2P)$$

followed by $N(^2P) + N_2O \rightarrow N_2 + NO(B^2\Pi_r)$. A reaction for the minor NO β emission in the region 1400 to 1550 Å is production of either $N(^2D)$ or $O(^1S)$ followed by

$$N(^2D) + N_2O \rightarrow N_2 + NO(B^2\Pi_r)$$

or

$$O(^1S) + N_2O \rightarrow NO + NO(B^2\Pi_r).$$

No appreciable reaction for form $NO(B^2\Pi_r)$ directly from N_2O was observed. Reactions, which produce the γ emission when NO is introduced, are

$$N_2O \xrightarrow{h\nu} N_2(A^3\Sigma_u^+) + O(^3P)$$

$$\xrightarrow{h\nu} N_2(B^3\Pi_g) + O(^3P)$$

$$\xrightarrow{h\nu} N_2(B'^3\Sigma_u^-) + O(^3P)$$

followed by

$$N_2(A^3\Sigma_u^+) + NO \rightarrow N_2 + NO(A^2\Sigma^+)$$

$$N_2(B^3\Pi_g) + NO \rightarrow N_2 + NO(A^2\Sigma^+)$$

$$N_2(B'^3\Sigma_u^-) + NO \rightarrow N_2 + NO(A^2\Sigma^+).$$

Various other possible mechanisms are discussed.

Key Words: Photolysis, vacuum ultraviolet, fluorescence, excited species, N_2O, gas phase, energy transfer.

Interpretation of cyclotron resonance line shapes in slightly ionized gases, F. C. Fehsenfeld, L. R. Megill, and L. K. Dropplemann, *J. Chem. Phys.* **43,** *No. 10, 3618–3624 (Nov. 1965).*
The dependence of cylotron resonance line shape on the velocity dependence of the collision frequency for three different distribution functions is calculated. Several sets of data for various collision frequency dependency upon energy are calculated. These include, in addition to simple one term power laws, results for four gases using measured collision frequencies. Because the line shape is strongly influenced by the energy dependency of the collision frequency, the calculation of collision frequencies from line width data requires an accurate knowledge of the variation of collision frequency with energy. Moreover, with previously used analyses, large errors in the deduced collision frequency may be caused, for some gases, by the presence of small admixtures of other gases, or ions. The examples which are given to illustrate the above statements indicate that extreme care must be exercised if reliable experimental data are to be obtained.

Key Words: Cyclotron resonance line shapes, ionized gases, line shapes, resonance line shapes.

Matrix-isolation study of the reaction of carbon atoms with chlorine. The electronic and vibrational spectra of the free radical CCl_2, D. E. Milligan and M. E. Jacox, *J. Chem. Phys.* **47,** *No. 2, 703–707 (July 15, 1967).*
Studies of the photolysis of N_3CN in the presence of Cl_2 in Ar and N_2 matrices at 14 °K provide evidence for the formation of the free radical CCl_2 by the reaction of photolytically produced C atoms with Cl_2. The two stretching fundamentals of CCl_2 appear at 721 and 748 cm^{-1}. The corresponding fundamentals of $^{13}CCl_2$ have also been observed. When the sample is warmed above about 30 °K, these features disappear, and CCl_4 features grow in intensity, indicating that CCl_2 can react with Cl_2 with little or no activation energy. The valence angle of CCl_2 probably lies between 90° and 110°. A weak band system appearing between 4400 and 5600 Å, with an average band separation of 305 cm^{-1}, may also be attributed to CCl_2. Analogy with the electronic absorption spectrum of CF_2 suggests that CCl_2 possesses a ground singlet state and that this band system arises from a transition between the ground state electronic configuration and the first excited electronic configuration of CCl_2, involving an extensive progression in the upper state bending vibration.

Key Words: Carbon atoms; CCl_2 radical, electronic spectrum, infrared spectrum, matrix isolation, CF_2 radical, cyanogen azide, chlorine.

Modification of the fluoride activity electrode for microchemical analysis, R. A. Durst and J. K. Taylor, *Anal. Chem.* **39,** *No. 12, 1483–1485 (Oct. 1967).*
A fluoride activity electrode has been modified for operation in the inverted position by converting the inner reference solution to a gel. Operation in this position makes possible the use of the single-crystal fluoride-sensitive membrane as the sample "container" and permits the measurement of sample volumes as small as one drop (50 μl). A calibration curve is obtained for solutions containing 10^{-1} *M* to 10^{-6} *M* NaF in 0.1 *M* KNO_3. The precision to which the fluoride concentration can be read from this calibration curve is calculated from the slope of the curve at the various concentrations and the standard deviation of the e.m.f. measurements. In the concentration range from 10^{-1} *M* to 10^{-3} *M* NaF, the calculated error is about 2%. At the 10^{-5} *M* NaF level, 10 nanograms of fluoride can be determined with an error of approximately 0.7 nanogram. For sample volumes of 50 μl, the modified fluoride electrode was found to exhibit a usable response in the range from 10^{-1} *M* to 5×10^{-6} *M* fluoride.

Key Words: Microchemical analysis, potentiometry, fluoride, analysis for, specific ion electrode, fluoride electrode, electrochemical analysis.

Modified linear null-point potentiometry, R. A. Durst and J. K. Taylor, *J. Chem. Educ.* **39,** *No. 12, 1374–1379 (Oct. 1967).*
A modification of the technique of precision null-point potentiometry has been developed in which a linear titration curve is obtained when the logarithm of the amount of coulometrically generated titrant is plotted against the concentration cell potential. The equivalence point is evaluated graphically and by computer techniques. The analyses of standard 0.1 ml samples containing 0 to 13 μg of silver are discussed in detail. This technique was found to be applicable down to one nanoequivalent (0.1 μg) of silver with an error of less than 5%. Below this value, a positive deviation occurs due to the spontaneous dissolution of the silver indicator electrodes. The interference effects of several cations are also discussed.

Key Words: Null-point potentiometry, silver, microtitration, linear potentiometry, electroanalysis, potentiometry.

Optical and magnetic measurements on single crystals of copper(II)-doped *tris*(phenanthroline) zinc(II) nitrate dihydrate, G. F. Kokoszka, C. W. Reimann, H. C. Allen, Jr., and G. Gordon, *Inorg. Chem.* **6,** *No. 9, 1657–1661 (1967).*
The electron paramagnetic resonance spectrum in single crystals ov copper(II)-doped trisphenanthrolinezinc(II) nitrate dihydrate has been observed between 4 °K and 350 °K. The results have been interpreted in terms of a pseudo-Jahn-Teller effect for the copper(II) ion. At 350 °K the spectrum is nearly isotropic with $g = 2.13$ and no observed hyperfine splitting. At 77 °K anisotropy of the g-tensor is observed with $g_{||} = 2.273$, $g_{\perp} = 2.064$, $A_{||} = 160 \times 10^{-4}$ cm^{-1}, $A_{\perp} > 7 \times 10^{-4}$ cm^{-1}, $A'_{||} = 12.5 \times 10^{-4}$ cm^{-1} and $A'_{\perp} = 10.5 \times 10^{-4}$ cm^{-1}. No significant change in the spectrum was observed at temperatures below 77 °K. The optical d–d transitions and their polarization properties are reported. Two bands are observed at 7,000 cm^{-1} and 14,900 cm^{-1}. The 14,900 cm^{-1} band is split at 77 °K into components at 14,700 cm^{-1} and 15,200 cm^{-1}. Bonding parameters are calculated from the data obtained at 77 °K in the usual ligand-field approximation and compared to those previously reported for similar Cu(II) complexes.

Key Words: Trisphenanthroline copper(II) nitrate dihydrate, trisphenanthroline zinc(II) nitrate dihydrate, Jahn-Teller effect, EPR spectrum, polarized optical spectrum, d–d transitions.

Polymerization and pyrolysis of poly-1,2-dihydronaphthalene, L. A. Wall, L. J. Fetters, and S. Straus, *Polymer Letters* **5,** *No. 8, 721–733 (Aug. 1967).*
Polymerization of 1,2-dihydronaphthalene, using anionic catalysts, gave intractable white powders insoluble in all solvents studied, with the exception of bis(phenoxyphenyl)ether at 290 °C. When dissolved, no appreciable viscosity increments could be detected suggesting either low molecular weights or degradation. In thermal volatilization studies, the polymer yields about 35% monomer and vaporizes at rates near those for polystyrene. Single compacted pellets volatilized faster, however. Unlike the initial powders, pellets had detectable electron spins which could be enhanced by partial pyrolysis. It is concluded that compacting the polymer enhances an exothermic decomposition mechanism.

Key Words: polymerization, 1,2-dihydronaphthalene, thermal volatilization, thermal decomposition, degradation, pyrolysis.

Spectroscopic study of the vacuum-ultraviolet photolysis of matrix-isolated HCN and halogen cyanides. Infrared spectra of the species CN and XNC, D. E. Milligan and M. E. Jacox, *J. Chem. Phys.* **47,** *No. 1, 278–285 (July 1, 1967).*
Vacuum ultraviolet photolysis of HCN isolated in Ar and N_2 matrices at 14 °K is found to lead to the production of HNC in concentration sufficient for direct infrared observation of all three vibrational fundamentals. The spectrum of this species is found to be appreciably perturbed by the presence of N_2. The force constants and thermodynamic properties of HNC have been revised to the values appropriate to this species in an environment free of perturbation by an adjacent N_2 molecule. The free radical CN is also produced in these systems in concentration sufficient for direct observation not only of the B $(^2\Sigma^+) - X\ (^2\Sigma^+)$ transition but also of the ground state vibrational fundamental. Isotopic data supporting this identification are presented. Upon vacuum ultraviolet photolysis of matrix-isolated FCN, two infrared absorptions appear which can be identified with the stretching fundamentals of the species FNC. In analogous experiments on the species ClCN and BrCN, infrared absorptions tentatively assigned to ClNC and BrNC have been observed.

Key Words: CN free radical cyanogen, cyanogen bromide, cyanogen chloride, cyanogen fluoride, halogen isocyanides, hydrogen cyanide, hydrogen isocyanide, infrared spectrum, matrix isolation technique, ultraviolet spectrum, vacuum ultraviolet photolysis.

The crystal and molecular structure of tetrakis-pyrazole-nickel chloride, $NI(C_3H_4N_2)_4Cl_2$, C. W. Reimann, A. D. Mighell, and F. A. Mauer, *Acta Cryst.* **23,** *Part 1, 135–141 (July 1967).*
The crystal and molecular structure of tetrakis-pyrazole-nickel chloride $Ni(C_3H_4N_2)_4Cl_2$ was determined by single crystal X-ray diffraction techniques. $Ni(C_3H_4N_2)_4Cl_2$ crystallizes in the monoclinic system with $a = 13.876 \pm 0.001$, $b = 9.263 \pm 0.006$,

$$c = 14.451 \pm 0.003\text{Å}, \quad \beta = 116.83 \pm 0.01°,$$

space group $C2/c$, $\rho_0 = 1.61$ gm cm^{-3} and $Z = 4$. Three-dimensional data (2401 reflections) were used and the structure solved by an analysis of the Patterson. The $Ni(C_3H_4N_2)_4\ Cl_2$ molecule is centric with the nickel atom at the center of an octahedron formed by two chlorine atoms and a nitrogen atom from each of the four pyrazole molecules. One pair of coordinated nitrogen atoms lies 2.097Å and the other pair 2.087Å from the nickel atom. The nickel-chlorine vector makes an angle of 0.4° with the normal to the plane of the coordinating

nitrogen atoms and the chlorine atom lies 2.507Å from the nickel atom. The pyrazole rings were found to be planar within experimental error. Final refinement by a three-dimensional anisotropic least-squares analysis resulted in an R value of 5.4%.

Key Words: Structure, X-ray, tetrakis-pyrazole-nickel chloride, single crystal, octahedral complex.

Dead weight piston gauge for pressures to 26 kilobars, D. P. Johnson and P. L. M. Heydemann, *Rev. Sci. Instr.* **38,** *No. 9, 1294–1300 (Sept. 1967).*
The design and operation of a dead-weight piston gage for pressures to 26 kbar is described. The gage is of the controlled clearance type. The diameter of the gage piston is 0.2 cm. It is loaded directly with up to 840 kg of weights. A volume of about 1 cm^3 is provided inside the gage for the material under test. The use of this gage for transition pressure determinations is briefly discussed.

Key Words: High pressure, piston gage, transition pressure, pressure measurement.

Coping with multiple reflections in precise measurement of the speed of light with a microwave Michelson interferometer, D. M. Kerns (*Proc. URSI Symp. Electromagnetic Wave Theory, Delft, The Netherlands, September 1965), Book, Electromagnetic Wave Theory, pp. 245–249 (Pergamon Press Inc., New York, N.Y., 1967).*
A microwave version of the Michelson interferometer is currently being used for a precise determination of the speed of light c. In preliminary experiments, multiple reflections between the antenna and the movable mirror of the system have been found to produce apparent variations in c, which, if uncorrected, would be an order of magnitude greater than tolerable. This paper establishes a theorem that should enable substantial elimination of errors due to multiple reflections. It is also shown that the four-arm junction in the arrangement—usually visualized as an ideal magic T—need have no special properties and in particular need have none of the ideal properties that distinguish an ideal magic T.

Key Words: Magic T, Michelson interferometer, multiple reflection, speed of light.

Low-frequency electrical calibrations at the National Bureau of Standards, F. L. Hermach, *(Proc. 22nd Annual ISA Conf. and Exhibit, Chicago, Ill., Sept. 11–14, 1967), ISA Preprint M5–1–MESTIND–67 (May 1967).*
Charts are presented to show the present range and accuracy of NBS calibrations of standards of resistance, capacitance, inductance, voltage, and current, from direct current through 50 kHz. The chains of measurements by which these and other calibrations are related to the basic NBS standards of voltage and resistance are also shown.

Key Words: Electrical calibrations, electrical standards, low-frequency calibrations, low-frequency standards.

Measurement standards, A. G. McNish, *IEEE Student J.* **4,** *No. 2, 24–31 (Mar. 1966).*
All units of measurement, including the ampere of current and candela of light intensity—two base units included in the new International System of Units, are ultimately derived from four original prototype units—the meter of length, kilogram of mass, degree Kelvin of temperature, and second of time. To make all measurement units more effective tools, the standards that physically embody or define three of the prototypes—length, time, and temperature—have been changed in recent years.

Key Words: Length, mass, temperature, time, units of measurements.

Application of the Fock expansion to doubly excited states of the helium atom, J. H. Macek, *Phys. Rev.* **160,** *No. 1, 170–174 (Aug. 5, 1967).*
A method of integrating the Schrödinger equation developed by Fock for S states of the helium atom is extended to all angular momentum states. The method makes use of an expansion in powers of R and logR, where $R = (r_1^2 + r_2^2)^{1/2}$. Some applications and generalizations are explored. The convergence of the series is investigated.

Key Words: Solution, Schrödinger equation, helium, power series, hyperspherical coordinates, applications, generalizations.

Characteristic energy losses of 8 KeV electrons in liquid In-Al and In-Bi alloys, C. J. Powell, *Advan. Phys.* **16,** *203 (1967).*
Measurements have been made of the characteristic energy losses of 8 KeV electrons in a series of Liquid In-Al and In-Bi alloys in order to avoid the confusing effects of phase mixtures present in most similar studies of solid alloy systems. Loss spectra were measured in a reflection-type scattering geometry with total electron scattering angles of 15° and 70°. Two principal energy loss peaks, identified as being due to surface plasmon and to volume plasmon excitation, were found to vary as a function of alloy composition in each system. Deviations from the variation expected from a simple free-electron model could be interpreted in some cases in terms of an interband electronic transition occurring near the measured volume and surface energy-loss peaks. For bismuth-rich In-Bi alloys and for indium-rich In-Al alloys the transition energy and oscillator strength could be estimated and shown as a function of composition.

Key Words: Characteristic-electron-energy-losses, electronic excitations, In-Al alloys, In-Bi alloys, liquid alloys.

Cross section for Na($^2P_{1/2}$, $^2P_{3/2}$) intramultiplet transactions induced by collisions with the hydrogen atoms, R. N. Zare and P. L. Bender, *Proc. Am. Phys. Soc. Meeting, Los Angeles, Calif.,* **10,** *1183 (American Physical Society, New York, N.Y., 1965).*
The cross sections for the transfer of excitation between the $3^2P_{1/2}$ and $3^2P_{3/2}$ states of sodium induced by inelastic collisions with hydrogen atoms have been calculated using the impact parameter approximation. When two atoms approach each other a quasimolecule is formed which may be characterized by its spin and projection of its total angular momentum on the molecular axis. For the Na*-H system the electronic wavefunctions are taken to be the antisymmetrized products of the separated atom wavefunctions, from which the $^1\Sigma$, $^3\Sigma$, $^1\Pi$ and $^3\Pi$ energy splittings are determined as a function of internuclear distance. The transition probability for each velocity and impact parameter is found by integrating along the collision trajectory the coupled differential equations arising from the time-dependent Schrödinger equation. Upon averaging over all impact parameters and the distribution in velocities we obtain for the total cross section $\bar{\sigma}$ (Na $^2P_{1/2} \rightarrow$ Na $^2P_{3/2}$) 61.8, 58.0, and 55.2 πa_0^2 at $T = 5000$, 7500 *and* 10,000 °K. Corrections to these values still have to be made for deviations from straight-line paths and for the neglect of van der Waals forces, although these are anticipated to be small.

Key Words: Atom wavefront, hydrogen atoms, inelastic collisions.

Equations of motion in nonequilibrium statistical mechanics. II. Energy transport, B. Robertson, *Phys. Rev.* **160,** *No. 1, 175–183 (Aug 5, 1967).*
The exact equations of motion for the space- and time-dependent coordinates of an arbitrary many-body system have been derived previously. These equations are integrodifferential equations whose kernels are generalizations of correlation functions and therefore are related to Green functions. In this paper an exact general expression for a flux operator is used to rewrite the equations. Then they become memory-retaining nonlocal generalizations of the diffusion equation. The formalism is applied to energy transport, and the usual expression for heat conductivity is derived without making the usual assumptions. Finally, a simple function is assumed for the kernel, and the equation then reduces to a well known heat conduction and wave equation.

Key Words: Equations of motion, nonequilibrium statistical mechanics, energy transport, heat conductivity, exact flux operator, heat wave equation.

Experimental determination of transition probabilities and Stark widths of S I and S II lines, J. M. Bridges and W. L. Wiese, *Phys. Rev.* **159,** *No. 1, 31–38 (July 5, 1967).*
Absolute transition probabilities and Stark widths for some prominent multiplets of S I and S II have been determined experimentally. A wall-stabilized arc was operated in SO_2 with a small hydrogen admixture. The spectroscopic measurements were performed photoelectrically. Side-on observations were transformed via the

Abel inversion to give the radial dependence of the measured quantities. Measurements of the absolute intensity of O I lines and the width of H_β served for the plasma analysis; the results of these measurements together with the application of equilibrium and conservation relations for arc plasmas enabled the determination of the temperature and various particle densities. Mass separation effects are taken into account. The measured Stark widths generally agree well with values calculated from Stark broadening theory; in the case of the S II lines the agreement with very recently calculated values is substantially better than that with earlier theoretical data.

Key Words: Arc, sulfur, transition probability, Stark broadening, atomic spectroscopy, plasma.

Hall mobility in $SrTiO_3$, H. P. R. Frederikse and W. R. Hosler, *Phys. Rev.* **161,** *No. 3, 822–827 (Sept. 15, 1967).*
Electron mobilities in reduced and doped $SrTiO_3$ have been deduced from measurements of conductivity and Hall coefficient between 1 and 1000 °K. Above room temperature scattering by the highest two longitudinal optical modes determines the mobility. Expressions based on intermediate electron-phonon coupling yield good agreement. Below 10 °K ionized impurity scattering is the dominant collision process. Using a screened Coulomb potential, one obtains mobility values of the right order of magnitude.

Key Words: Electron mobility, ionized impurity scattering, strontium titanate, temperature dependence of mobility, optical mode scattering.

Lifetimes of some 4*p* levels in argon I, J. Z. Klose, *J. Opt. Soc. Am.* **57,** *No. 10, 1242–1244 (Oct. 1967).*
Mean lives of four electronically excited atomic levels in Ar I have been determined using a method of delayed coincidence. The measured values of the mean lives of the $2p_1$ through $2p_4$ (Paschen notation) levels in neutral argon determined from transitions with associated wavelengths extending from 6677 to 7147 Å are as follows: $2p_1$, 21 ± 2 nanoseconds; $2p_2$, 25 ± 1 nsec; $2p_3$, 26 ± 1 nsec; and $2p_4$, 31 ± 2 nsec. The lifetimes were estimated to contain systematic errors varying from 5 to 15% and are presented in comparison with corresponding results of other workers.

Key Words: Lifetimes, atomic, argon, delayed coincidence, spectra, atomic.

Measurements of Stark profiles of C II and Ca II lines, J. R. Roberts and K. L. Eckerle, *Phys. Rev.* **159,** *No. 1, 104–107 (July 5, 1967).*
An electromagnetic T-tube was the source of a plasma used to measure line profiles of singly ionized atoms. The profiles of C II lines emitted from a plasma composed of He and CO_2 in the ratio 95:5 were scanned with a monochromator. The profile scans were accomplished by repeated firings of the T-tube while advancing the monochromator in wavelength steps. Also measured was the profile of the 3934 Å Ca II resonance line emitted from a plasma composed of He, H_2, CO_2 in the ratio 20:10:70 with Ca as an impurity. The profile of the 3889 Å He I line was also measured and its half-width was used to determine the plasma electron density in the case of the C II lines. Likewise H_α was used to determine the electron density in the case of the Ca II line. The experimental C II and Ca II Stark profile half-widths were compared with the theoretically calculated values.

Key Words: Stark profiles, C II, Ca II, T-tube, profile scans, monochromator, experimental stark-profile half-widths.

Mechanistic aspects of hearing, E. L. R. Corliss, *J. Acoust. Soc. Am.* **41,** *No. 6, 1500–1516 (June 1967).*
The results of a number of apparently diverse experiments on human hearing can be summarized via a simple model. Two mechanisms are required: One element emits unit responses whose number is proportional to the instantaneous amplitude of a sound. The other is a selector mechanism, analogous to a resonant circuit, that integrates the responses. Correspondingly, just two parameters are involved: the threshold of hearing and the "*Q*" of the selector mechanism. The system of equations representing the model makes it possible to derive the necessary parameters from the results of a number of different types of experiments. The theory of the selector mechanism is based upon a recent study of the limits of performance of a system capable of storing oscillatory energy reversibly, but the remainder of the theoretical description makes use of ordinary communication theory.
The discrimination ability of the normal ear is shown to be proportional to the one-fourth power of the level above threshold, and to relate closely to the sensation of loudness. Many features of the behavior of normal and impaired ears can be predicted by application of familiar network theory to the parameters derived from the model. The properties of the model may be used as criteria in the choice of experiments to develop explicit data on the way the ear performs its function.

Key Words: Hearing, mechanistic model of hearing, ear behavior, communication theory, auditory perception, resolving power of the ear, auditory analysis.

Nature of ionic deformations in crystals; application to an analysis of the magnetic properties of the alkali halide and alkaline-earth oxide crystals, A. R. Ruffa, *Phys. Rev.* **159,** *No. 3, 742–754 (July 15, 1967).*
Absolute diamagnetic susceptibilities for the alkali halide crystals are obtained theoretically and compared with the observed magnetic susceptibilities of these crystals in order to determine the crystalline paramagnetic susceptibilities. The paramagnetic susceptibilities obtained in this way are found to obey the linear relationship $\chi_{para} = 0.11\ \chi_{dia}$. Theoretical analysis confirms this relationship for the alkali halides and indicates, in addition, that (1) virtually all of the increased kinetic energy which the ions acquire in the process of crystallization takes the form of angular kinetic energy (2) the angular deformations of the ions in all the alkali halides are the same in that the average eigenvalue of the square of the angular momentum operator is constant for all these crystals (3) the general relationship between χ_{dia} and χ_{para} for an ionic crystal is of the form $\chi_{para} = C\chi_{dia}$, where C is very nearly proportional to the cohesive energy of the crystal. The last conclusion is confirmed in the alkaline earth oxides where $C \approx 0.5$, in accord with the fact that the cohesive energies of these crystals are about five times those of the alkali halides. Furthermore, this analysis indicates that an ionic crystal with a large enough cohesive energy is paramagnetic, in accord with observation.

Key Words: Ionic, deformation, paramagnetism, diamagnetism, kinetic energy, alkali halides, alkali earth oxides, ionic sizes, polarizabilities.

On the explanation of the so-called CN laser, D. R. Lide, Jr., and A. G. Maki, *Appl. Phys. Letters* **11,** *No. 2, 62–64 (July 15, 1967).*
It is shown that the major features of the far infrared "CN laser" are due to the HCN molecule. The intense line at 337 microns and other near-by lines are explained as transitions involving the 11^10 and 04^00 vibrational states, which are mixed by a Coriolis perturbation. The mechanism of the laser is discussed.

Key Words: CN, emission, far infrared, HCN, laser, spectra.

Second breakdown—A comprehensive review, H. A. Schafft, *Proc. IEEE* **55,** *No. 8, 1272–1288 (Aug. 1967).*
This paper is a comprehensive review of the published literature dealing with the phenomenon of second breakdown in semiconductor devices and the problems it creates in the design, fabrication, testing, and application of transistors.

Key Words: Review, semiconductor devices, transistors, diodes, second breakdown, thermal breakdown, transistor reliability, circuit realiability, failure modes, failure mechanisms.

Single- and double-quantum photodetachment of negative ions, E. J. Robinson and S. Geltman, *Phys. Rev.* **153,** *No. 1, 4–8 (Jan. 1967).*
The recent measurement of the transition probability for the double-quantum detachment of an electron from I^- has prompted a new theoretical study of this problem. A central field model for bound and free states is used, in which a parameter is adjusted in the potential to yield the observed binding energies of the negative ions. An implicit sum method, requiring the solution of inhomogeneous radial equations, is used to evaluate the sums over intermediate states.

The results for I^- lie within the experimental uncertainty. The single-quantum photodetachment and electron elastic scattering (from the neutral atom) cross sections are also given for the ions studied: C^-, O^-, F^-, Si^-, S^-, Cl^-, Br^-, I^-.

Key Words: Single-quantum, elastic scattering, double-quantum, negative ions, photodetachment.

Sporadic-*E* ionization, E. K. Smith, *Annual Suppl. Encyclopedic Dictionary of Physics, Ed. J. Therolis, Suppl. I, 239–331 (Pergamon Press Inc., New York, N.Y., 1966).*
A brief review is presented on the structure of the sporadic-*E* layer, its temporal characteristics, and finally of the current thinking of the cause of equatorial, temporate and auroral types of sporadic *E*.

Key Words: Auroral types of sporadic *E*, equatorial, ionization, sporadic-*E*.

Superconductive properties of ceramic mixed titanates, J. F. Schooley, H. P. R. Frederikse, W. R. Hosler, and E. R. Pfeiffer, *Phys. Rev.* **159,** *No. 2, 301–305 (July 10, 1967).*
The superconducting transition temperature of a series of mixed barium-strontium and calcium-strontium titanate ceramic specimens have been determined. For several of these samples the low-field magnetization has also been investigated. The results are compared with those obtained from single-crystal $SrTiO_3$.

Key Words: Barium strontium, calcium strontium, titanates.

Suppressed and accelerated spin-lattice relaxation, R. L. Peterson, *Phys. Rev.* **159,** *No. 2, 227–233 (July 10, 1967).*
The transient magnetic behavior of a paramagnetic substance, after an initial disturbance, is considered theoretically for a variety of situations in which the lattice temperature rises as a result of energy flow from the magnetic (electron spin) system. The direct and T^9 Raman spin-phonon processes are considered. Coupling between phonon modes, and leakage of energy into a bath are taken into account. Graphs of the resultant behavior are presented. Effects such as suppressed and accelerated spin relaxation, and rapid decay (phonon avalanche) after spin inversion, are discussed. It is pointed out that experiments performed without the usual helium bath may provide reliable measurements of inelastic phonon-boundary scattering.

Key Words: Spin-lattice relaxation, spin-phonon interactions, phonon avalanche, phonon bottleneck, inelastic phonon-boundary scattering.

Temperature dependence of the nuclear quadrupole resonance frequency of ^{35}Cl in $KClO_3$ between 12 and 90 °K, D. B. Utton, *J. Chem. Phys.* **47,** *No. 2, 371–373 (July 15, 1967).*
A precise measurement of the temperature dependence of the N.Q.R. frequency of Cl^{35} in $KClO_3$ has been made at constant pressure in the range 12 °K–90 °K. Analysis using the Bayer-Kushida theory predicts lattice modes at 60 cm^{-1} and 126 cm^{-1}. A comparison is made with the Raman spectrum.

Key Words: Chlorine, nuclear quadrupole resonance, potassium chlorate, temperature variation, 12 °K–90 °K, Bayer-Kushida Theory.

The radiative band pinch effect and temperature dependence of radiative recombination in GaAs, N. N. Winogradoff, K. Owen, and R. M. Curnutt, *Int. J. Electronics* **22,** *No. 3, 229–233 (Mar. 29, 1967).*
Localized heating of GaAs by intense ruby laser flashes cause a reduction or "pinching" of the band gap in the illuminated region. The increase in wavelength of the recombination radiation from this region permits the study of the temperature dependence of the internal quantum efficiency without absorption in the colder, wide band gap regions.
The results show that the internal quantum efficiency decrease with an increase in temperature.

Key Words: GaAs, radiative recombination, temperature dependence, quantum efficiency, ruby laser.

Other NBS Publications

J. Res. NBS 71B (Math. and Math. Phys.), No. 4 (Oct.–Dec. 1967), 75 cents.
Calibration designs based on solutions to the tournament problem. R. C. Bose and J. M. Cameron.
Bounds for the solutions of second-order linear difference equations. F. W. J. Olver.
Notes on automorphic functions: An entire automorphic form of positive dimension is zero. M. I. Knopp.
Solving equations exactly. M. Newman.
A system of equations having no nontrivial solutions. H. Gupta.
Remarks on cut-sets. J. W. Grossman.
A pseudo primal-dual integer programming algorithm. F. Glover.
Properties of a useful biorthogonal system. L. V. Spencer and P. Flusser.
On even matroids. W. T. Tutte.
Matrices of class J_2. J. S. Maybee.
Partially isometric matrices. J. Z. Hearon.
Symmetrizable generalized inverses of symmetrizable matrices. J. Z. Hearon.
Optimum branchings. J. Edmonds.
Systems of distinct representatives (SDR) and linear algebra. J. Edmonds.
Bounds for the number of generators of a finite group. M. Newman.

J. Res. NBS 72C (Engr. and Instr.), No. 1 (Jan.–Mar. 1968), 75 cents.
Acceleration due to gravity at the National Bureau of Standards. D. R. Tate.
Deflection of thin circular elastic plates under symmetrically distributed loading. A. F. Kirstein and R. M. Woolley.
A dynamic method for determining the vapor pressure of carbon dioxide at 0 °C. J. L. Edwards and D. P. Johnson.
An adiabatic saturation psychrometer. L. Greenspan and A. Wexler.
An injection method for self-calibration of inductive voltage dividers. W. C. Sze.
Bolometric voltage and current (Bolovac) standard for high and microwave frequencies. M. C. Selby.
An admittance meter technique to measure the complex permeability at VHF. A. L. Rasmussen and C. M. Allred.

Correlations for predicting leakage through closed valves, J. Hord, Tech. Note 355 (Aug. 1, 1967), 20 cents.
Loading factors and FDM–FM system performance calculations, E. F. Florman, Tech. Note 100–A (Sept. 1967), 20 cents. Supplement to Appendix C of Tech. Note 100.
Second breakdown in semiconductor devices—a bibliography, H. A. Schafft, Tech. Note 431 (Oct. 1967), 30 cents.
1967 Technical Highlights of the National Bureau of Standards, Annual Report, Fiscal Year 1967, Misc. Publ. 293 (Nov. 1967), 55 cents.
A comparison between solar X-ray emission and VLF sudden phase anomalies, C. J. Chilton, J. P. Conner, and F. K. Steele, Proc. IEEE **53,** No. 12, 2018–2026 (Dec. 1965).
A computer simulation model of railroad freight transportation systems, W. P. Allman, Intern. Railway Cong. Assoc. Mo. Bull. Cybernetics and Electronics **4,** No. 2, 45–57 (Feb. 1967).
A method of producing sturdy specimens of pressed powders for use in x-ray spectrochemical analysis, B. L. Bean, Appl. Spectry. **20,** No. 3, 191–193 (May–June 1966).
A modified Monte-Carlo quadrature. II, S. Haber, Math. Compt. **21,** No. 99, 388–397 (July 1967).
A novel, facile preparation of 1,1′-bipyrene, A. J. Fatiadi, J. Org. Chem. **32,** 2903–2904 (Sept. 1967).
A note on the evaluation of interference photographs, J. R. Meyer-Arendt, Acta Histochem. **22,** 58–61 (1965).
A precision noise power comparator, M. G. Arthur, C. M. Allred, and M. K. Cannon, IEEE Trans. Instr. Meas. **IM–4,** 301–305 (Dec. 1964).
A simple, inexpensive wavefront shearing interferometer, J. B. Saunders, Appl. Opt. **6,** No. 9 1581–1583 (Sept. 1967).
Angular scattering law for the moon at 6 meter wavelength, W. K. Klemperer, J. Geophys. Res. Letter **70,** No. 15, 3798–3800 (Aug. 1965).
Another method of synthesizing nonuniformly spaced antenna arrays, M. T. Ma, Trans. IEEE Ant. Prop. **AP–13,** No. 5, 833–834 (Sept. 1965).

Antennas, H. V. Cottony, Encyclopedia of Physics, Ed. R. M. Besancon, pp. 25–28 (Reinhold Publ. Corp., New York, N.Y., 1966).

Brief report of the XV URSI General Assembly, Commission I, on the status of international intercomparisons of high frequency and microwave electrical quantities, M. C. Selby (Proc. XV General Assembly of URSI, Munich, Germany, Sept. 5–15, 1966), Book, Progress in Radio Science 1963–1966, Part 1, pp. 113–116 (International Scientific Radio Union, Munich, Germany, Sept. 1966).

Characteristics of a slotted-sphere antenna immersed in a compressible plasma, J. R. Wait (Proc. Conf. Microwave Behavior of Ferrimagnetics and Plasmas), Conf. Publ. No. 13, pp. 1–4 (Inst. Electrical Engineers, London, England, 1965).

Comment on "paramagnetic resonance of alkyl nitroxides," R. E. Florin, J. Chem. Phys. **47,** No. 1, 345–346 (July 1, 1967).

Crystallization of natural rubber, N. Bekkedahl, Rubber Chem. Technol. **40,** No. 3, xxv-xlvii (June 1967).

C. S. Pierce on benefit-cost analysis of scientific activity, W. E. Cushen, Operations Res. **15,** No. 4, p. 641 (July–Aug. 1967).

Cyclotron harmonic emission from the abnormal negative glow plasma, K.-B. Persson, D. A. Uhlenbrock, and E. G. Johnson, Bull. Am. Phys. Soc. **12,** Series II, No. 5, 756 (May 1967).

Definitions of v, i, Z, Y, a, b Γ, and S, D. M. Kerns, Proc. IEEE **55,** No. 6, 892–900 (June 1967).

Development of an adhesive restorative material, R. L. Bowen (Proc. 2d Workshop, Adhesive Restorative Dental Materials, University of Virginia, Charlottesville, Va., Dec. 8–9, 1965), Book, Adhesive Restorative Dental Materials, No. 2, Chapt. 4, p. 225 (U.S. Public Health Service Publ. 1494, Supt. Doc. Government Printing Office, Washington, D.C. 20402, $1.00, 1966).

Editor and translator, H. J. Oser, Book, Functional Analysis and Numerical Mathematics, by L. Collatz, Academic Press, Inc., New York, N.Y., 1966.

Electronic computer applications in urban transportation planning, R. E. Schofer and F. F. Goodyear (Proc. 22d Natl. Conf. Association for Computing Machinery, Washington, D.C., Aug. 29–31, 1967), A. C. M. Publ. P–67, pp. 247–253 (Thompson Book Co., Washington, D.C., July 1967).

Equivalence between two formalisms of plasma fluctuations, J. Weinstock, Phys. Fluids **9,** No. 3, 621–622 (Mar. 1966).

F^{19} relaxation in AFM $KMnF_3$, P. T. Parrish, A. C. Daniel, and R. J. Mahler, Bull. Am. Phys. Soc. **12,** Series II, No. 3, 284 (Mar. 1967).

Identification of dyes in paper by extraction and chromatographic analysis, M. R. Wallace, L. T. Milliken, and S. D. Toner, TAPPI **50,** No. 9, 121A–124A (Sept. 1967).

Interpretation of de Grinberg's experiments on lateral surface fringes in sodium chloride, H. P. Utech, Phys. Stat. Solidi **20,** K41–K43 (1967).

Ionosphere, T. E. VanZandt, Encyclopedia of Physics, Ed. R. M. Besancon, pp. 348–349 (Reinhold Publ. Corp., New York, N.Y., 1966).

Linear measurements, T. R. Young, Book, Handbook of Industrial Metrology, Chapt. 3, pp. 55–81 (Prentice-Hall, Inc., Englewood Cliffs, N.J., 1967).

Localized-induction concept on a curved vortex and motion of an elliptic vortex ring, R. J. Arms and F. R. Hama, Phys. Fluids **8,** No. 4, 553–559 (Apr. 1965).

Lou Costrell of NBS speaks out on the revolution in instrument packaging, L. Costrell, EEE **15,** No. 8, 78–84 (Aug. 1967).

Measurement of density and specific gravity, J. K. Taylor, Book, Treatise on Analytical Chemistry, Ed. I. M. Kolthoff, P. J. Elving, and E. B. Sandell, Part 1, Theory and Practice, 7, Chapt. 81, 4561–4610 (Interscience Publ., New York, N.Y., 1967).

Metrology, essential of space age, A. G. McNish, George Washington University Mag. **1,** No. 4, 10–14 (1965).

Microprinting fills the bill, B. M. Fry, Business Graphics, pp. 21–25 (Jan 1967).

Note on paritions modulo 5, M. Newman, Math. Compt. **21,** No. 99, 481–482 (July 1967).

Nuclear magnetic acoustic resonance in $KTaO_3$, R. W. Mebs, L. H. Bennett, and J. R. Leibowitz, Physics Letters **24A,** No. 12, 665–666 (June 5, 1967).

On the structure of pyrazole, A. D. Mighell and C. W. Reimann, J. Phys. Chem. **71,** No. 7, 2375–2376 (June 1967).

Perturbation theorems for waveguide junctions, with applications, D. M. Kerns and W. T. Grandy, Jr., IEEE Trans. Microwave Theory Tech. **MTT–14,** No. 2, 85–92 (Feb. 1966).

Proof of a permanental inequality, R. A. Brualdi and M. Newman, Quart. J. Math. **17,** No. 67, 234–238 (Sept. 1966).

Remarks for XV URSI General Assembly session on progress at $f \leq 1$ GHz, M. C. Selby (Proc. XV General Assembly of URSI, Munich, Germany, Sept. 5–15, 1966), Book, Progress in Radio Science 1963–1966, Part 1, pp. 157–162 (International Scientific Radio Union, Munich, Germnay, Sept. 1966).

Reply by A. G. McNish, Phys. Today **19,** No. 4, 15–16 (Apr. 1966).

Reply to "Comments on Reed letter, by H. M. Otte," R. P. Reed, Acta. Met. **15,** No. 6, 1082–1083 (June 1967).

Robust estimation of location, E. L. Crow and M. M. Siddiqui, J. Am. Stat. Assoc. **62,** No. 318, 353–389 (June 1967).

Scanning the issue, R. W. Beatty and B. O. Weinschel, Proc. IEEE **55,** No. 6, 737–740 (June 1967).

Scheduling a vehicle between an origin and a destination to maximize traveler satisfaction, D. Young (Proc. 22nd Natl. Conf. Association for Computing Machinery, Washington, D.C., Aug. 29–31, 1967), A. C. M. Publ. P–67, pp. 233–245 (Thompson Book Co., Washington, D.C., July 1967).

Some radio-physical considerations in studies of the fine scale structure of the atmosphere, B. R. Bean and B. D. Warner, Proc. Intern. Conf. Fine Scale Structure of the Atmosphere, Moscow, USSR, June 1965, pp. 215–224 (1965).

Synchrotron radiation measurements near the magnetic equator, G. R. Ochs, Book, Radiation Trapped in the Earth's Magnetic Field, Ed. B. McCormac, pp. 703–713 (D. Riedel Publ. Co., Dordrecht, The Netherlands, 1966).

The application of the partial correlation analyses to the study of the occurrence probability of spread-F, T. Shimazaki (Proc. AGARD Conf. Spread F and Its Effects Upon Radiowave Propagation and Communication, Copenhagen, Denmark, Aug. 1964), AGARDograph 95, pp. 167–188 (W. and J. Mackay, London, England, 1966).

The aurora, A. G. McNish, Proc. NATO Advanced Study Institute, Bad Homburg, Germany, July 22–Aug. 2, 1963, Ed. D. S. Bliel, pp. 77–93 (Plenum Press Inc., New York, N.Y., 1964).

The development of an International atomic time scale, J. A. Barnes, Proc. IEEE **55,** No. 6, 822–826 (June 1967).

The effect of spread F on the propagation of radio waves near the equator, K. Davies and A. F. Barghausen (Proc. AGARD Conf. Spread F and Its Effects Upon Radio Wave Propagation and Communication, Copenhagen, Denmark, Aug. 1964), AGARDograph 95, pp. 437–466 (W. and J. Mackay, London, England, 1966).

The energies of N^+ fron the dissociative ionization of N_2(Abstract), K. J. Kieffer and R. J. Van Brunt (Proc. 18th Annual Gaseous Electronics Conf., Minneapolis, Minn., Oct. 21, 1965), Bull. Am. Phys. Soc. **11,** No. 4, 499 (1966).

The functions of Commission I of the International Scientific Radio Union, J. M. Richardson, Proc. IEEE **55,** No. 6, 743–745 (June 1967).

The role of NBS in motor vehicle safety research, P. J. Brown, Proc. Regional Meeting Society Automotive Engineers, Gaithersburg, Md., April 18, 1967, SAE 670204, p. 3 (June 1967).

The role of the NBS Radio Standards Laboratory, H. M. Altschuler, Proc. IEEE **55,** No. 6, 778–781 (June 1967).

The spheroidal method in satellite astronomy, J. P. Vinti, Book, Space Mathematics **5,** Part 1, 119–129 (American Mathematical Society, Providence, R.I., 1966).

The use of multiple antennas in studies of absorption at conjugate points, H. J. A. Chivers and J. K. Hargreaves, Proc. Symp. High Latitude Particles and the Ionosphere, Alpbach, Austria, 1964, p. 257–264 (Academic Press, Inc., New York, N.Y., 1965).

Vacuum-ultraviolet photolysis of acetylene in inert matrices. Spectroscopic study of the species C_2, D. E. Milligan, M. E. Jacox, and L. Abouaf-Marguin, J. Chem. Phys. **46,** No. 12, 4562–4570 (June 15, 1967).

Variational calculations for quartet states of three-electron atomic systems, S. Geltman and E. Holein, Phys. Rev. **153,** No. 1, 81 (1967).

**Publications for which a price is indicated are available by purchase from the Superintendent of Documents, U.S. Government Printing Office, Washington, D.C. 20402 (foreign postage, one-fourth additional). The NBS nonperiodical series are also available from the Clearinghouse for Federal Scientific and Technical Information, Springfield, Va. 22151. Reprints from outside journals and the NBS Journal of Research may often be obtained directly from the authors.*

U.S. GOVERNMENT PRINTING OFFICE : 1968 OL—289–015

SERIALS OCT 40129
UNIVERSITY MICROFILMS INC
ATTN SERIALS SECTION
300 NORTH ZEEB RD
ANN ARBOR MICH 48106

UNITED STATES
GOVERNMENT PRINTING OFFICE
DIVISION OF PUBLIC DOCUMENTS
WASHINGTON, D.C. 20402

OFFICIAL BUSINESS

POSTAGE AND FEES PAID
U.S. GOVERNMENT PRINTING OFFICE

JOURNAL OF RESEARCH of the National Bureau of Standards
A. Physics and Chemistry

Vol. 72A, No. 2 March–April 1968

Contents

Page

Constant pressure flame calorimetry with fluorine II. The heat of formation of oxygen difluoride. Reatha C. King and George T. Armstrong. 113

The heat of formation of boron carbide. E. S. Domalski and G. T. Armstrong.

Solubility of tris(hydroxymethyl)aminomethane in water-methanol solvent mixtures and medium effects in the dissociation of the protonated base. Paul Schindler, R. A. Robinson, and Roger G. Bates.

Calibration of the nickel dimethylglyoxime spectral shift at pressures to 20 kilobars for use in spectroscopic pressure measurement. Helen W. Davies.

Second virial coefficient of He^4 in the temperature range from 2 to 20 °K. Marjorie E. Boyd, Sigurd Y. Larsen, and Harmon Plumb.

Diffusion rates in organic nuclear materials. A. L. Dragoo.

Effect of oxide additions on the polymorphism of tantalum pentoxide. (system Ta_2O_5-TiO_2). J. L. Waring and R. S. Roth.

Effect of statistical counting errors on wavelength criteria for x-ray spectra. John S. Thomsen and F. Y. Yap.

Thermodynamic properties of ammonia as an ideal gas. Lester Haar.

Publications of the National Bureau of Standards.

Library of Congress Catalog Card Number: 62–37059

For sale by the Superintendent of Documents, U.S. Government Printing Office, Washington, D.C. 20402. Price $1.00 (single copy). Subscription price: $5 a year; $1.00 additional for foreign mailing.
UNITED STATES GOVERNMENT PRINTING OFFICE, WASHINGTON : 1968